FUNCTIONAL CHARACTERIZATION OF THE SHH RECEPTORSOME USING HUMAN INDUCED PLURIPOTENT STEM CELL MODELS

Inaugural-Dissertation
to obtain the academic degree
Doctor rerum naturalium (Dr. rer. nat.)

submitted to the Department of Biology, Chemistry, Pharmacy
of Freie Universität Berlin

by

MAIKE MARCZENKE

2021

The work was carried out from 09/2017 to 10/2021 under the supervision of Prof. Dr. Thomas E. Willnow at the Max Delbrück Center for Molecular Medicine in the Helmholtz Association in Berlin.

1st Reviewer: Prof. Dr. Thomas E. Willnow
Max Delbrück Center for Molecular Medicine in the Helmholtz Association

2nd Reviewer: Prof. Dr. Ursula Koch
Freie Universität Berlin

Date of defense: 12.04.2022

TABLE OF CONTENT

SUMMARY

The morphogen sonic hedgehog (SHH) regulates central patterning processes along the dorsoventral axis of the emerging forebrain. Secreted from the prechordal plate (PrCP), SHH targets neuroepithelial cells of the overlying forebrain organizer region in the rostral diencephalon ventral midline (RDVM), to establish and further specify ventral identity of the forebrain. Defects in this pathway result in severe developmental forebrain defects including holoprosencephaly (HPE). Besides the canonical SHH receptor patched 1 (PTCH1), several additional cell surface proteins have been identified as being essential for SHH signaling in the neuroepithelium. Jointly, they are referred to as the SHH receptorsome and include LRP2 and GAS1. Mutations in these co-receptors are the cause of familial forms of HPE and related phenotypes, such as in Donnai-Barrow syndrome (DBS), corroborating their importance for SHH-dependent forebrain development in humans. Intriguingly, the structure of SHH co-receptors is highly diverse and they show spatial and temporal differences in expression pattern, arguing for distinct functions of each receptor in SHH-dependent developmental processes. In this thesis, I used human induced pluripotent stem cell (iPSC)-based cell models to recapitulate early steps in neuroepithelial patterning and to elucidate unique roles for LRP2 and GAS1 in these processes. In the first project, I studied a unique missense mutation in *LRP2* in two siblings with DBS. To do so, I differentiated patient-derived iPSCs into neural progenitor cells (NPCs) and studied the impact of this mutation on receptor handling of SHH. I demonstrated that the mutant receptor was unable to discharge its ligand SHH, leading to enhanced lysosomal degradation of the mutant receptor bound to its ligand. These studies showed that ligand-induced decay of LRP2 is responsible for the disease phenotype in this family with DBS. Additionally, the results of this study verified the molecular function of LRP2 as SHH co-receptor as it mediates endocytosis and trafficking of the morphogen in forebrain neuroepithelial cells, a process essential for SHH signal reception in this cell type. In the second project, I uncovered a novel function for GAS1 in integrating SHH and NOTCH signaling during early forebrain development. Performing comparative analyses in GAS1-deficient mice and genetically engineered *GAS1* knockout (KO) iPSC-derived NPCs, I showed that loss of GAS1 impairs NOTCH-dependent facilitation of SHH signaling and results in a failure to maintain the SHH activity domain in the rostral ventral neuroepithelium. Thus, besides its known function as SHH co-receptor, GAS1 also acts as co-receptor for NOTCH1, enhancing pathway activation which, in turn, promotes maintenance of SHH signaling in the rostral ventral neuroepithelium during forebrain development.

ZUSAMMENFASSUNG

Das Morphogen sonic hedgehog (SHH) reguliert essenzielle Prozesse der Musterbildung während der embryonalen Vorderhirnentwicklung. SHH wird von der prächordalen Platte (PrCP) sezerniert und induziert die Ventralisierung und weitere Spezifizierung neuroepithelialer Zellen der ventralen Mittellinie. Störungen im SHH Signalweg sind Ursache schwerwiegender Entwicklungsstörungen des Vorderhirns, welche als Holoprosenzephalie (HPE) bezeichnet werden. Neben dem klassischen SHH Rezeptor patched 1 (PTCH1) wurden weitere Zelloberflächenproteine identifiziert, die ebenfalls SHH binden und die für die Aktivität dieses Signalweges essenziell sind. Hierzu zählen unter anderen die zwei Proteine LRP2 und GAS1. Mutationen in Co-Rezeptorengenen führen ebenfalls zu HPE und verwandten Entwicklungsstörungen, wie beim Donnai-Barrow Syndrom (DBS). Interessanterweise unterscheiden sich die einzelnen Co-Rezeptoren sowohl in ihrem strukturellen Aufbau als auch in ihrem embryonalen Expressionsmuster. Dies deutet auf distinkte Mechanismen hin, mittels derer einzelne Rezeptorspezies SHH-abhängige Entwicklungsprozesse kontrollieren. Im Rahmen meiner Doktorarbeit habe ich die Wirkungsweise der beiden SHH Co-Rezeptoren LRP2 und GAS1 mithilfe humaner induzierter pluripotenter Stammzellen (iPSCs) aufgeklärt. Im ersten Projekt konnte ich mittels iPSC-abgeleiteter Neuroepithelzellen (NPCs) zeigen, dass eine neuartige Missense-Mutation im LRP2-Gen zweier DBS Patienten die Rezeptorfunktion insofern beeinflusst, dass LRP2 nicht mehr fähig ist, sich im Endozytoseweg der Zelle von seinem Liganden SHH zu lösen. Dies hat zur Folge, dass der Rezeptor zusammen mit dem gebundenen Liganden in Lysosomen abgebaut wird. Der Liganden-induzierte Verlust an LRP2 Protein ist also die Ursache für das DBS in den betroffenen Patienten. Grundsätzlich konnte ich mit dieser Arbeit bestätigen, dass die wesentliche Funktion von LRP2 die eines Endozytoserezeptors für SHH ist und dass die LRP2-vermittelte Aufnahme und zelluläre Sortierung von SHH essenziell für die Übermittelung von SHH Signalen im sich entwickelnden Vorderhirns ist. In einem zweiten Projekt habe ich eine neuartige Funktion von GAS1 als Modulator in der Interaktion zwischen der Signalmoleküle SHH und NOTCH während der frühen Vorderhirnentwicklung aufgeklärt. So konnte ich mittels eines GAS1-defizienten Mausmodells und GAS1-defizienter iPSC-abgeleiteter NPCs zeigen, dass GAS1 auch als NOTCH Co-Rezeptor dient und essentiell ist für die Aktivierung des NOTCH Signalwegs im Neuroepithel. Die GAS1-abhängige Verstärkung der NOTCH Aktivität ist unabdingbar für die NOTCH-vermittelte Aufrechterhaltung der SHH Aktivitätsdomäne im ventralen Neuroepithel des sich entwickelnden Vorderhirns.

LIST OF PUBLICATIONS AND CONTRIBUTIONS

Publications related to this thesis

Flemming, J.*, **Marczenke, M.***, Rudolph, I-M., Nielsen, R., Storm, T., Christensen, E.I., Diecke, S., Emma, F. and Willnow, T.E. (2020). Induced pluripotent stem cell-based disease modeling identifies ligand-induced decay of megalin as cause of Donnai-Barrow syndrome. Kidney International 98, 259-267. doi: 10.1016/j.kint.2020.02.021.
* Flemming and Marczenke contributed equally to the study

Marczenke, M., Sunaga-Franze, D.Y., Popp, O., Althaus, I., Sauer, S., Mertins, P., Christ, A., Allen, B.L. and Willnow, T.E. (2021). GAS1 is required for NOTCH-dependent facilitation of SHH signaling in the ventral forebrain neuroepithelium. Accepted in Development, September 27, 2021. doi: 10.1242/dev.200080

Other publications

Christ, A., **Marczenke, M.** and Willnow, T.E. (2020). LRP2 controls sonic hedgehog-dependent differentiation of cardiac progenitor cells during outflow tract formation. Human Molecular Genetics. 29(19):3183-3196. doi: 10.1093/hmg/ddaa200

Conferences

Marczenke, M., Christ, A., Allen, B.L., Willnow, T.E. *Functional relevance of the sonic hedgehog receptorsome for neuroepithelial patterning and forebrain specification.* Poster presented at the International Society for Stem Cell Research Annual Meeting, Los Angeles, June 26-29, 2019, and at the European Developmental Biology Congress, Alicante, October 23-26, 2019.

LIST OF ABBREVIATIONS

ADAM17	A disintegrin and metalloprotease 17
ADE	anterior definitive endoderm
AME	axial mesendoderm
ANR	anterior neural ridge
AP	anterior-posterior
AP2	adaptor protein complex 2
ARH	LDLR adaptor protein 1
AVE	anterior visceral endoderm
BMP	bone morphogenetic proteins
BMPR	BMP receptor type
BOC	brother of CDO
C	carboxy
CDO	cell-adhesion molecule-related/downregulated by oncogenes
CER1	Cerberus 1
Ci	Cubitus interruptus
CK1α	casein kinase 1 α
CMZ	ciliary marginal zone
Cripto-1	teratocarcinoma-derived growth factor 1
CSF	cerebrospinal fluid
DAB2	disabled homolog 2
DBS	Donnai-Barrow syndrome
DHH	desert hedgehog
DISP1	dispatched 1
DKK1	Dickkopf-related protein 1
DLHP	dorsolateral hinge point
DLL1	delta-like protein 1
DPW	dorsal pericardial wall
Dvl	Dishevelled
E	embryonic day
EGF	epidermal growth factor
ER	endoplasmic reticulum
EVC	EvC ciliary complex subunit
FGF	fibroblast growth factor
FGFR	FGF receptor

Fn(III)	fibronectin-type III
FOXA2	forkhead box A2
Fz	Frizzled
GAS1	growth-arrest specific 1
GDNF	glial cell derived neurotrophic factor
GFRα	GDNF receptor family α
GIPC	GAIP interacting protein, C terminus
GLI	GLI family zinc finger
GPI	glycosylphosphatidylinositol
GPRK2	G protein coupled receptor kinase 2
GSK3β	glycogen synthase kinase 3 β
HES5	Hes family BHLH transcription factor 5
HESX1	homeobox expressed in ES cells 1
HH	hedgehog
HHIP	hedgehog interacting protein
HPE	holoprosencephaly
Ig	immunoglobulin
IHH	indian hedgehog
iPSC	induced pluripotent stem cell
kDa	kilodalton
KIF3A	kinesin-like protein 3A
KIF7	kinesin-like protein 7
LDLR	low density lipoprotein receptor
LGE	lateral ganglionic eminences
LRP	LDLR related proteins
LRP2	low-density lipoprotein receptor-related protein 2
MAPK	mitogen-activated protein kinase
MGE	medial ganglionic eminences
MHP	medial hinge point
MIH	middle interhemispheric
MSX1	Msh homeobox 1
N	amino
NICD	NOTCH intracellular domain
NKX2.1	NK2 homeobox 1
NKX2.2	NK2 homeobox 2
NKX6.1	NK6 homeobox 1

NOTCH1	NOTCH receptor 1
NPC	neural progenitor cell
OFT	outflow tract
OLIG2	oligodendrocyte transcription factor 2
OTX2	orthodenticle homeobox 2
PCP	planar cell polarity
PKA	protein kinase A
PrCP	prechordal plate
PTCH1	patched 1
PTCH2	patched 2
RBPJ	recombinant signal binding protein for Ig kappa J
RDVM	rostral diencephalon ventral midline
RND	resistance-nodulation-division
RP	roof plate
RPTEC	renal proximal tubule epithelial cell
SCUBE2	signal peptide CUB domain and EGF like domain containing 2
SHF	second heart field
SHH	sonic hedgehog
SIX3	SIX homeobox 3
SMO	smoothened
SUFU	suppressor of fused
SVZ	subventricular zone
TCF3	transcription factor E2-alpha
TGFβ	transforming growth factor β
TGIF	TGFβ induced factor homeobox
VE	visceral endoderm
WNT	Wingless-related integration site
ZIC2	ZIC family member 2

LIST OF FIGURES

1 INTRODUCTION

1.1 Forebrain development

The forebrain arises from a single-layered sheet of neuroectodermal cells at the rostral end of the neural plate. The interplay of several neural and non-neural signaling centers and morphogenic factors first induce neural fate in the gastrulating embryo and, subsequently, regulate the folding of the neural plate during the process of neurulation. Further tissue growth, patterning, and specification give rise to the forebrain consisting of diencephalon and telencephalon. These brain centers control complex functions like sensory perception, emotions, memory, thinking, motor as well as autonomic functions, and the endocrine system. The general induction and organization of the forebrain are highly conserved in all vertebrates (Stern and Downs, 2012).

1.1.1 Early forebrain induction

Forebrain development is initiated during the process of gastrulation that generates the three germ layers ectoderm, mesoderm, and endoderm from the epiblast (Solnica-Krezel and Sepich, 2012). In the course of gastrulation several so-called gastrula organizers are established. Their interplay is required for induction and maintenance of anterior neural identity by expression of agonists and antagonists of different morphogenic signaling pathways that protect anterior tissue from posteriorizing signals in a gradient-dependent manner (Andoniadou and Martinez-Barbera, 2013; Wilson and Houart, 2004). While initial anterior neural induction is promoted by fibroblast growth factors (FGFs), it is inhibited by caudalizing factors such as proteins of the transforming growth factor beta (TGFβ) family including bone morphogenetic proteins (BMPs) and proteins of the Wingless-related integration site (WNT) family (Hoch et al., 2009; Kudoh et al., 2004; Streit et al., 2000).

At the onset of mouse gastrulation at embryonic day (E) 5.5, cells of the extra-embryonic visceral endoderm (VE) at the distal tip of the embryo receive signals from the epiblast involving Nodal and mitogen-activated protein kinase (MAPK) to induce cells of the anterior visceral endoderm (AVE) organizer (Fig. 1A) (Brennan et al., 2001; Clements et al., 2011). These cells migrate anteriorly until they reach the boundary between extra-embryonic ectoderm and epiblast marking the anterior end of the embryo (Fig. 1B). The AVE primes the epiblast for anterior neural induction and neural plate formation by promoting the expression of anterior forebrain markers such as SIX homeobox 3 (SIX3), homeobox expressed in ES cells 1 (HESX1), orthodenticle homeobox 2 (OTX2), forkhead box A2 (FOXA2) and transcription factor E2-alpha (TCF3), all harboring anti-caudalizing activity (Andoniadou and

Martinez-Barbera, 2013; Hoch et al., 2009; Kimura et al., 2000; Klingensmith et al., 2010; Yang and Klingensmith, 2006).

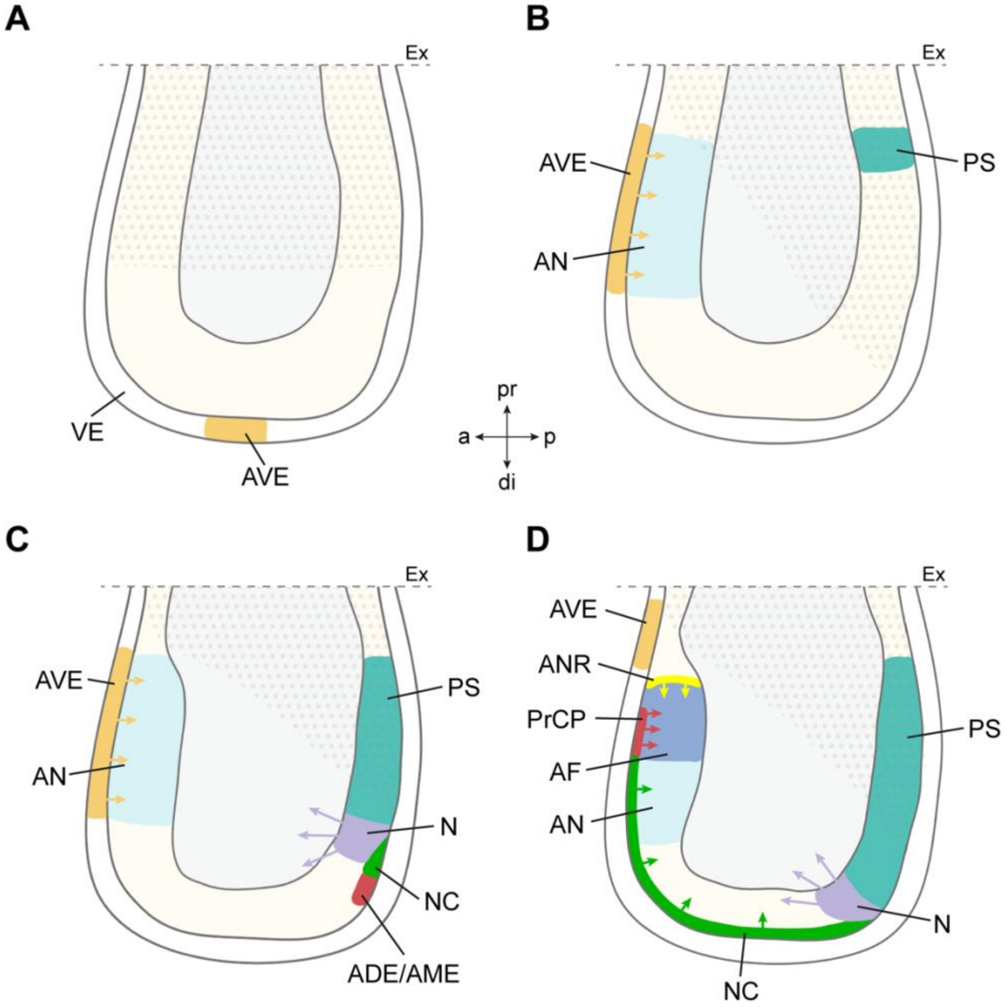

Figure 1 Early forebrain induction during mouse gastrulation. Schematized illustration of early anterior neural induction in the gastrulating mouse embryo. (**A**) At embryonic day (E) 5.5 the extra-embryonic visceral endoderm (VE) receives signals from the epiblast to induce the anterior VE (AVE, orange) at the distal tip of the embryo. (**B**) Between E6.0 to E6.5 the AVE migrates anteriorly and promotes anterior neural ectoderm (AN, light blue) formation by secreting anti-caudalizing signals to counteract BMP signaling (grey dots). The primitive streak (PS, turquoise) forms at the proximal posterior end establishing the anterior-posterior axis of the embryo. (**C**) At E7.0 the PS elongates towards the distal tip where it gives rise to the node (N, purple) at the most anterior part. Similar to the AVE the node secretes factors antagonizing BMP signaling. Anterior definitive endoderm (ADE) and anterior axial mesoderm (AME, red) originate in the node and move towards the anterior tip of embryo followed by the notochord (NC, green). (**D**) By E7.5 ADE/AME displace the AVE towards extraembryonic tissues, express anti-caudalizing factors and, additionally, induce the anterior neural ridge (ANR, yellow). AME gives rise to the prechordal plate (PrCP, red) which promotes formation of the anterior forebrain primordium (AF, dark blue) by secreting SHH as well as BMP antagonists. Ex, extraembryonic tissue; a, anterior; p, posterior; pr, proximal; di, distal. Adapted from Andoniadou and Martinez-Barbera, 2013, and Yang and Klingensmith, 2006; created with BioRender.com.

Subsequently at E6.5 the primitive streak forms at the posterior proximal end of the embryo establishing the anterior-posterior (AP) axis (Fig. 1B). The primitive streak elongates towards the distal tip of the embryo and gives rise to the organizer at the most anterior tip, in mice termed the node (Fig. 1C). The node comprises precursor cells of mesodermal and endodermal derivatives. AVE and node express antagonists of TGFβ signaling, including Lefty1, Chordin, Noggin and Follistatin as well as WNT signaling such as Cerberus 1 (CER1) and Dickkopf-related protein 1 (DKK1) (Bachiller et al., 2000; del Barco Barrantes et al., 2003; Belo et al., 1997; Khokha et al., 2005; Mukhopadhyay et al., 2001; Robb and Tam, 2004; Yang and Klingensmith, 2006). The two organizers cooperate to prevent caudalization of the anterior neuroectoderm by TGFβ and WNT signaling enabling the anterior neural tissue to form the forebrain primordium (Andoniadou and Martinez-Barbera, 2013).

Further morphogenic tissue rearrangements initiate the migration of the anterior definitive endoderm (ADE) and the anterior axial mesendoderm (AME), originating in the node, to its destination underlying the rostral neuroectoderm (Fig. 1C and D). Similar to the AVE, ADE and AME also express and secrete inhibitors of TGFβ and Wnt signaling (Andoniadou and Martinez-Barbera, 2013; Wilson and Houart, 2004; Yang and Klingensmith, 2006). At the most rostral end of the induced anterior neuroectoderm at the junction to non-neural surface ectoderm, ADE/AME induce cells from the anterior neural ridge (ANR) to express FGF3 and FGF8 that promote expression of telencephalic genes as well as growth, specification, and regionalization of the telencephalon (Meyers et al., 1998; Raible and Brand, 2001; Shimamura and Rubenstein, 1997; Ye et al., 1998). While the ADE gives rise to anterior foregut precursors and derivatives, the AME generates the prechordal plate (PrCP) consisting of endodermal and mesenchymal cells underlying the neuroepithelium of the prospective telencephalon, anterior hypothalamus, and eye field. Additionally, ADE/AME are followed by migrating cells forming the notochord that is established caudally from the PrCP (Fig. 1D) (Andoniadou and Martinez-Barbera, 2013). Besides anti-caudalizing signals, PrCP and notochord express Nodal and sonic hedgehog (SHH) that are essential for ventral midline specification (Chiang et al., 1996; Ohkubo et al., 2002).

At the end of the gastrulation period at E7.5 anti-caudalizing signals provided by antagonists of the TGFβ and WNT signaling pathways have established the formation of the AP axis, have induced anterior neural ectoderm including the anterior forebrain primordium, and then maintain anterior neural identity to assure further growth and development (Andoniadou and Martinez-Barbera, 2013).

1.1.2 Neurulation

After gastrulation, the neural plate is transformed into an elongated hollow tubular structure, the neural tube. To do so, the flat neural plate evaginates, undergoes bending to form neural groove and bilateral neural folds, which elevate, appose, and finally fuse along the dorsal midline (Fig. 2). This multistep process of neurulation is coordinated by many morphogenetic events, including changes in cell shape, migration, and proliferation. It requires the integration of various signaling pathways, actomyosin dynamics and cell-cell interactions (Nikolopoulou et al., 2017). Disruptions of these processes lead to neural tube closure defects including spina bifida, craniorachischisis and anencephaly (Lee and Gleeson, 2020).

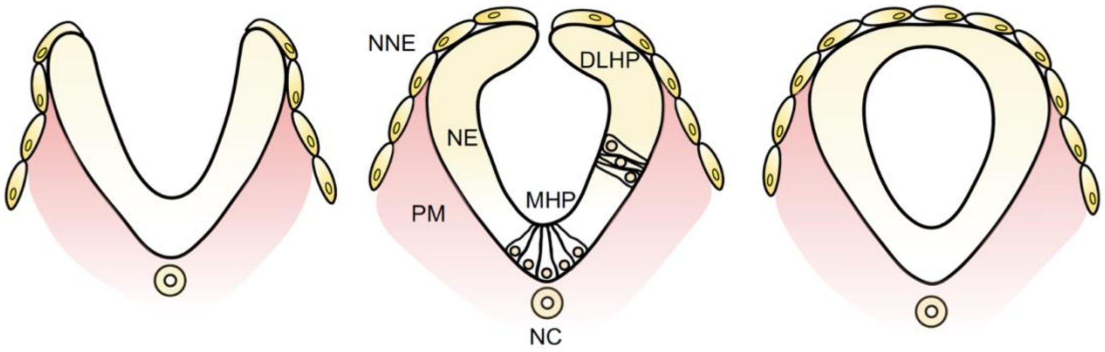

Figure 2 Neural tube closure. Neurulation is a multifactorial process involving the elevation (left) and bending (middle) of the neural folds. These processes start at the median hinge point (MHP), induced by the underlying notochord (NC), followed by the paired dorsolateral hinge points (DLHP). It is completed by the fusion of the neural fold tips at the dorsal midline (right). Cells of the MHP and DLHP undergo apica constriction and become wedge-shaped, driving the process of bending. Additionally, neural tube closure is supported by the pushing and pulling forces resulting from the expansion of the surrounding non-neural ectoderm (NNE) and paraxial mesoderm (PM). Tissue remodeling separates the inner neuroepithelium (NE) from the outer NNE which gives rise to the surface ectoderm of future epidermis. Adapted from Nikolopoulou et al., 2017.

Neural tube closure is initiated by convergent extension. The neural plate narrows along the mediolateral axis (convergence) while it elongates along the rostrocaudal body axis (extension) (Keller et al., 2000). Convergent extension is mainly driven by polarized cell rearrangements that are controlled by the non-canonical WNT/planar cell polarity (PCP) pathway (Curtin et al., 2003; Hamblet et al., 2002; Kibar et al., 2001; Montcouquiol et al., 2003; Murdoch et al., 2001, 2003). Mouse models deficient for components of the PCP pathway, such as Vangl2, Celsr1, Dishevelled 1 (Dvl1) and 2 (Dvl2) as well as Frizzled 3 (Fz3) and 6 (Fz6), develop neural tube closure defects. These defects include craniorachischisis due to failed convergent extension, leading to a short and widened neural plate and thus preventing the apposition and fusion of the neural folds (Curtin et al., 2003; Kibar et al., 2001; Murdoch et al., 2001, 2003; Wallingford and Harland, 2001, 2002; Wang et al., 2006).

Bending of the neural plate happens at different so-called hinge points (Fig. 2). Following shaping, the underlying PrCP/notochord induces the formation of the medial hinge point (MHP) through SHH (Smith and Schoenwolf, 1989). Cells within the MHP undergo apical constriction and become wedge-shaped, leading to the first bending event and the formation of the neural folds and neural grooves. Intrinsic cell movements and mediolateral cell proliferation drive elevation of the neural folds. Induced by integrative signals from BMP, secreted by the non-neural ectoderm, from PrCP/notochord-derived SHH as well as chordin and noggin, the bilateral dorsolateral hinge points (DLHPs) form (Ybot-Gonzalez et al., 2002, 2007). Similar to the MHP, cells within the DLHPs constrict apically and become wedge-shaped supporting further bending. Additionally, bending and closure of the cranial neural tube is dependent on the expansion of the surrounding non-neural ectoderm and head mesenchyme, as pushing and pulling forces result in biconvex shaped neural folds (Alvarez and Schoenwolf, 1992; Chen and Behringer, 1995; Hackett et al., 1997; Moury and Schoenwolf, 1995; Zhao et al., 1996).

After dorsolateral bending, the generated biconcave neural folds flip and their tips appose for fusion. The first fusion points are formed by filopodia and lamellipodia, cellular protrusions extending from the apical cells of the neural folds (Geelen and Langman, 1977, 1979; Rolo et al., 2016), and this process requires Eph-ephrin signaling (Abdul-Aziz et al., 2009; Holmberg et al., 2000). Once these fusion points approach each other, they interdigitate at the dorsal midline and establish the roof plate. Tissue remodeling separates the inner neuroectoderm, forming the neuroepithelium, from the outer non-neural ectoderm that gives rise to the surface ectoderm or epidermis (Copp et al., 2003; Yamaguchi and Miura, 2013).

Neural tube closure in mammals is a progressive process including multiple closing sites (zippering) (Fig. 3) (Copp, 2005; Copp et al., 2003; Geelen and Langman, 1977; Golden and Chernoff, 1993; Juriloff et al., 1991). While the neural tube in medial regions has already closed, it is still open at the most anterior and posterior regions generating the anterior and posterior neuropore, respectively. They will fuse at slightly later timepoints of development. Failure of anterior neuropore closure results in anencephaly, while failed posterior neuropore closure typically causes spina bifida (Copp, 2005; Copp et al., 2003; Matsumoto et al., 2002; Wood and Smith, 1984; Yamaguchi and Miura, 2013).

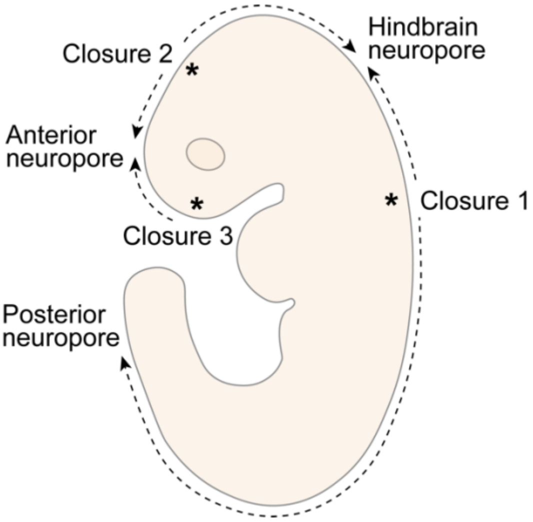

Figure 3 Multiple neural tube closure sites in the mouse embryo. Neural tube closure begins at the hindbrain cervical boundary (Closure 1) and spreads rostrally and caudally. Independently, closure follows at the forebrain midbrain boundary (Closure 2) and at the rostral forebrain (Closure 3). Neurulation exceeds caudally and rostrally from these closure sites by zipping, generating anterior, hindbrain, and posterior neuropores, respectively. These finally close at later developmental stages. Asterisks mark primary closing sites. Adapted from Copp et al., 2003.

1.1.3 Dorsoventral patterning

After the neural tube has closed, the formed brain vesicle expands. Subsequent patterning along the anterior-posterior as well as dorsal-ventral axis gives rise to different compartments of the future central nervous system. The most anterior part of the neural tube forms the forebrain, consisting of telencephalon (future cerebral hemispheres) and diencephalon (future thalamus), while more caudal regions develop into mesencephalon (midbrain) and rhombencephalon (hindbrain).

Genetic studies using mouse and zebrafish models have identified key local organizer regions in the forebrain that are established during neurulation and that are characterized by the expression and activity of distinct morphogenic signaling pathways regulating forebrain pattering and supporting the development of region-specific structures. These organizer regions include the ventral telencephalic midline and hypothalamus, the ANR rostrally as well as the roof plate (RP) dorsally. These organizers interact in forming and patterning the forebrain (Fig. 4) (Hébert and Fishell, 2008).

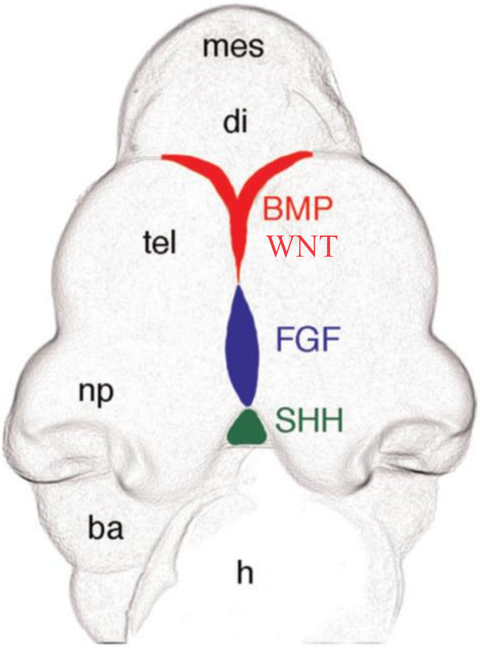

Figure 4 Key forebrain organizer regions in the developing mouse embryo. Local midline organizer regions in the mouse prosencephalon at E10.5 (frontal view) include the dorsal roof plate expressing BMP and WNT (red), the anterior neural ridge rostrally marked by the expression of FGFs (blue), and the ventral forebrain midline including hypothalamus and eye field expressing SHH (green). ba, branchial arch; di, diencephalon; h, heart; mes, mesencephalon; np, nasal process; tel, telencephalon. Adapted from Fernandes and Hébert, 2008.

Dorsal midline cells of the roof plate differentiate into the choroid plexus which secretes the cerebrospinal fluid, and into the adjacent cortical hem that induces the formation of the hippocampus (Grove et al., 1998; Lee et al., 2000; Takiguchi-Hayashi et al., 2004; Zhao et al., 2006). RP cells express BMP2, 4, 5, 6 and 7 (Furuta et al., 1997) as well as WNT2b, 3a, 5a and 8b (Grove et al., 1998; Lee et al., 2000). Treating cultured explants of the lateral telencephalon with BMP4-soaked beads induces dorsal midline features including a reduced rate of proliferation, a higher rate of cell death, and the expression of the dorsal midline marker Msh homeobox 1 (MSX1) (Furuta et al., 1997). In turn, disruption of BMP signaling causes the absence of apoptosis, loss of MSX1 expression, and the lack of the choroid plexus as seen in mouse models doubly deficient for BMP receptor type 1 a (BMPR1a) and b (BMPR1b) (Fernandes et al., 2007; Hébert et al., 2002). The cortical hem induces the development of the hippocampus via WNT3a. Mouse models lacking WNT3a in the cortical hem show severe defects in the formation and proliferation of hippocampal structures (Galceran et al., 2000; Lee et al., 2000). Additionally, BMPs and WNTs might act together to promote dorsal structures by directly regulating the expression of empty spiracles homeobox (EMX) genes including EMX2 (Theil et al., 2002).

The ANR functions in the patterning of telencephalic structures and the eye field through FGF8 and other FGFs (FGF3, 15, 17 and 18) (Crossley and Martin, 1995; Maruoka et al., 1998; McWhirter et al., 1997; Shinya et al., 2001). FGF8-soaked beads placed in dorsolateral areas of the chick telencephalon induce rostral midline features (Crossley et al., 2001). Deletion of FGF receptor 1 (FGFR1) leads to midline defects including the loss of the septum and midline glia cells as well as the inability of forebrain commissures to cross the midline (Tole et al., 2006). ANR specification requires antagonism of BMP and WNT signaling to restrict FGF8 spatially and temporally to the rostral patterning center, thereby inducing prosencephalic identity in the anterior neuroectoderm (Fukuchi-Shimogori and Grove, 2001; Shanmugalingam et al., 2000; Shimamura and Rubenstein, 1997). On the one hand, ectopic WNT signaling in the ANR induces midbrain marker expression and inhibits FGF8 and neocortical markers. On the other hand, FGF8 limits the expression of BMP and WNT to the dorsal RP. Thus, ectopic FGF8 signaling suppresses WNT3a and WNT5a in the cortical hem and inhibits the development of the hippocampus (Houart et al., 2002; Shimogori et al., 2004).

The ventral key organizer region in the developing forebrain is characterized by the expression of SHH. SHH from the PrCP induces the overlying rostral ventral forebrain midline, including hypothalamus and preoptic area, where it continues to be expressed. SHH signaling is essential for the specification of the ventral midline, eye field (Crossley et al., 2001) and, at later stages, the medial and lateral ganglionic eminences (MGE and LGE, respectively) (Huang et al., 2007). It does so mainly by antagonizing the dorsalizing effect of GLI family zinc finger 3 (GLI3) (Aoto et al., 2002; Corbin et al., 2003; Ericson et al., 1995; Ohkubo et al., 2002; Rallu et al., 2002; Rash and Grove, 2007) and by excluding lateral and dorsal markers from the midline (Houart et al., 2002). In addition, SHH is required for balancing proliferation versus apoptosis in the dorsal telencephalon and for the invagination of the rostral telencephalic midline resulting in two separated hemispheres (Hayhurst et al., 2008; Rash and Grove, 2007). In *Shh* mutant mice, ventral precursor cells and ventral midline structures are lost. These defects are accompanied by cyclopia and failed separation of the forebrain hemispheres (Chiang et al., 1996; Ohkubo et al., 2002). Signals by SHH from the ventral midline and by FGFs from the ANR cooperate in ventral patterning through a positive feedback loop (Ohkubo et al., 2002). Maintained expression of FGF8 depends on SHH signaling as SHH counteracts the inhibiting action of GLI3. FGF8 signals, likely mediated by receptors FGFR1 and FGFR3, are required for ventral SHH expression. Additionally, FGF signaling can compensate for the loss of SHH in rescue of ventral fates in *Shh;Gli3* compound null mutants (Aoto et al., 2002; Gutin et al., 2006; Rallu et al., 2002; Shanmugalingam et al., 2000; Take-uchi et al., 2003; Walshe and Mason, 2003).

Different feedback mechanisms are important in coordinating the actions of the four main signaling centers to establish, maintain, and refine regional identity in the developing forebrain. Imbalances or disruptions in any of these signaling pathways lead to a failure of midline formation and, consequently, in severe developmental forebrain defects such as holoprosencephaly (section 1.1.4).

1.1.4 Holoprosencephaly

Holoprosencephaly (HPE) is the most common forebrain anomaly in humans occurring in 1 of 250 human pregnancies and 1 of 10,000 live births (Cohen, 1989; Dubourg et al., 2007; Orioli and Castilla, 2010). HPE is caused by defects in the formation of midline structures leading to an incomplete separation of the prosencephalon into left and right hemispheres and in accompanying craniofacial malformations (Geng and Oliver, 2009). Clinical manifestations are highly variable and define three main types based on the degree of severity: alobar, semilobar, and lobar HPE. Alobar HPE is the most severe form with the lack of midline separation and a complete fusion of the hemispheres into one single ventricle (monoventricle). Affected individuals additionally lack the corpus callosum and olfactory bulbs. Semilobar HPE shows an incomplete interhemispheric fissure with partial separation in the posterior regions. Lobar HPE is characterized by an incomplete separation in the most rostral part of the frontal lobes. In addition, more mild forms have been described, such as middle interhemispheric (MIH) HPE, septopreoptic HPE as well as HPE microforms (Fig. 5A) (Fertuzinhos et al., 2009; Hahn and Barnes, 2010; Hahn et al., 2010; Marcorelles and Laquerriere, 2010; Monuki, 2007; Weaver et al., 2010). Severe craniofacial malformations include cyclopia and the formation of a proboscis while milder variants and microforms are associated with hypotelorism, single maxillary median incisor, single nostril, midface hypoplasia, and cleft lip (with and without cleft palate) (Fig. 5B) (Cohen and Sulik, 1992; Kauvar et al., 2010; Solomon et al., 2010a). A correlation between the severity of brain abnormalities and craniofacial defects has been described in up to 90% of cases (DEMYER et al., 1964; Orioli and Castilla, 2010; Petryk et al., 2015; Solomon et al., 2010a).

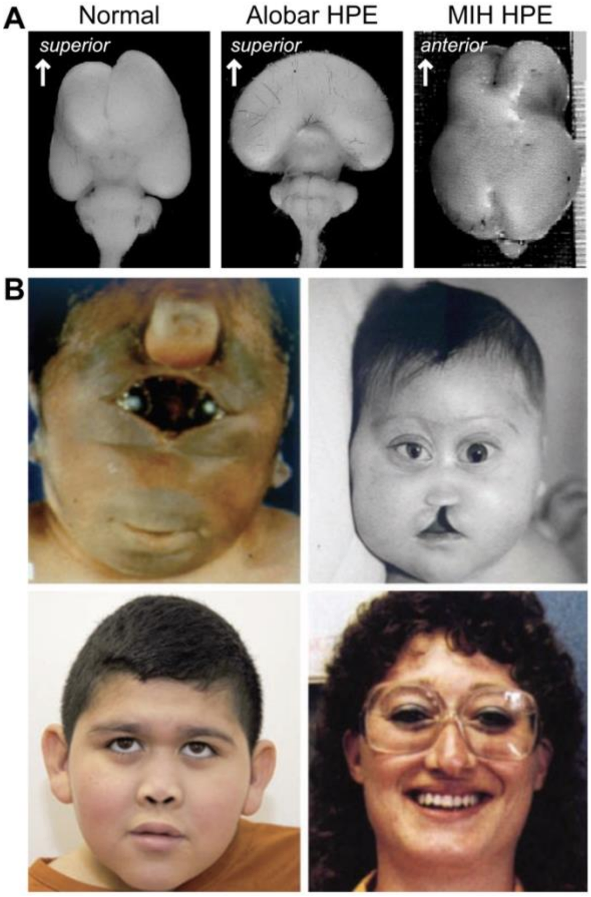

Figure 5 Brain and craniofacial abnormalities in holoprosencephaly. (**A**) Two types of HPE. Normal (left) brain and brains of two patients with alobar (middle) and MIH (right) HPE at 13-18-week gestation. Adapted from Monuki, 2007. (**B**) Variations in craniofacial manifestations showing cyclopia and proboscis (top left); hypotelorism, flat nasal bridge, colobomata and clefting (top right); hypotelorism and flat nasal brigde (bottom left); hypotelorism and single median incisor (bottom right). Adapted from Solomon et al., 2010.

The etiology of HPE is highly heterogenous and involves both environmental and genetic causes (Bendavid et al., 2010; Petryk et al., 2015; Pineda-Alvarez et al., 2010; Roessler and Muenke, 2010). The majority of cases are sporadic but familial HPE has been described as well (Ming and Muenke, 1998; Muenke et al., 1994). The exposure to teratogens increases the probability of HPE up to 200-fold (Muenke and Beachy, 2000). The most studied environmental factor is maternal diabetes with a risk for HPE of 1-2% (Barr et al., 1983; Correa et al., 2008). Other environmental risk factors include maternal consumption of alcohol (Bönnemann and Meinecke, 1990; Ronen and Andrews, 1991), smoking during pregnancy (Croen et al., 2000), or prenatal exposure to retinoic acid as prescribed for treatments of acne, sun-damaged skin, or psoriasis (Lammer et al., 1985; Sulik et al., 1995).

Up to 45% of HPE cases are due to chromosomal abnormalities, such as trisomy 13 or 18, which result in embryonic or perinatal mortality (Croen et al., 1996; Muenke and Beachy, 2000; Roessler and Muenke, 2010; Solomon et al., 2010b). So-called syndromic HPE belongs to the category of multiple malformation syndromes as described for Smith-Lemli-Opitz syndrome, Pallister-Hall syndrome, or Rubinstein-Taybi syndrome (Petryk et al., 2015). In addition, mutations in genes of at least 13 chromosomal loci have been identified in up to 25% of cases (Bendavid et al., 2009). One quarter of these variants affect four genes, namely SHH, ZIC family member 2 (ZIC2), SIX3, and TGFβ induced factor homeobox (TGIF) (Dubourg et al., 2004). Most of the identified genes act in morphogenic signaling pathways essential for early forebrain development, including SHH, Nodal, and FGF signaling (Arauz et al., 2010; Mercier et al., 2013).

Strikingly, *SHH* gene variants are the most common genetic cause of HPE, accounting for up to 37% of familial and up to 8% of sporadic cases (Nanni et al., 1999; Roessler et al., 1996). More than one hundred different mutations in the *SHH* gene have been implicated in HPE including frameshift, nonsense as well as missense mutations (Roessler et al., 2009a). Additionally, many other HPE-associated genes encode proteins that directly or indirectly regulate SHH expression or pathway activity, such as its receptor patched 1 (PTCH1) (Ming et al., 2002), the secretion factor dispatched 1 (DISP1) (Dubourg et al., 2016; Roessler et al., 2009b), or downstream transcription factors GLI2 (Roessler et al., 2003) and SIX3 (Wallis et al., 1999).

According to previous concepts, the pathology of HPE was believed to be caused by a single genetic insult but the incomplete penetrance and the variability in manifestation of the disease suggested other factors or several mutations to be involved as well. Meanwhile, HPE is described as a multifactorial disease with multiple inheritance modes including mutations in genes of the same pathway or in different pathways with genetic and functional interaction. In addition, genetic modifiers, epigenetic mechanisms as well as environmental factors impact severity and penetrance of the disease (Dipple and McCabe, 2000; Hong et al., 2017; Mercier et al., 2013; Ming and Muenke, 2002; Mouden et al., 2016; Odent et al., 1998).

Mouse and other animal models such as chicken and zebrafish helped to gain more insights into the molecular basis of HPE (Geng and Oliver, 2009; Gongal et al., 2011;

Schachter and Krauss, 2008). While gene haploinsufficiency in humans typically leads to the onset of HPE, homozygosity for the respective gene defect is required in mouse models to induce the mispatterning (Cohen, 1989). In mice, HPE has mostly been studied in transgenic lines deficient for components of SHH, BMP, FGF, and Nodal signaling pathways (Schachter and Krauss, 2008). For example, *Shh* depletion in mice results in severe alobar HPE with complete fusion of the hemispheres, cyclopia, and the formation of a proboscis (Chiang et al., 1996). However, similar to humans, the manifestation of phenotypes in mice is variable and additional effects on the penetrance of the HPE phenotype caused by the genetic background or strain-specific genetic modifiers recapitulate the concept of a multifactorial trait (Echevarría-Andino and Allen, 2020; Feinberg and Irizarry, 2010; Mecklenburg et al., 2021; Nadeau, 2001; Petryk et al., 2015; Seppala et al., 2014).

1.2 The sonic hedgehog signaling pathway

1.2.1 Hedgehog signaling in development

The hedgehog (HH) signaling pathway regulates various developmental processes. HH proteins act as morphogen and control growth, cell fate and survival, and they pattern almost every aspect of the vertebrate body plan. Initially, HH was identified in the developing *Drosophila melanogaster* larvae (Nüsslein-Volhard and Wieschaus, 1980). In mammals, three HH orthologues have been described, called Indian hedgehog (IHH), desert hedgehog (DHH), and SHH (Echelard et al., 1993). Like other morphogens, HH proteins are secreted from a local source and establish a concentration gradient throughout their target tissue. The dose and duration of HH signals define distinct responses and, hence, different fate in target cells (Tabata and Takei, 2004).

Although their physiological effects are thought to be similar, HH proteins show diverse expression patterns and perform different functions in development (McMahon et al., 2003; Varjosalo and Taipale, 2008). DHH is mainly expressed in gonads and is important for germ cell development. DHH-deficient mice are viable but males are infertile due to a lack of mature sperm (Bitgood et al., 1996). IHH is expressed in the primitive endoderm (Dyer et al., 2001) and the gut (van den Brink, 2007) and plays a role in bone and cartilage development and growth (Maeda et al., 2007; Razzaque et al., 2005; St-Jacques et al., 1999; Vortkamp et al., 1996). *Ihh* mutant mouse models show an impaired development of the extraembryonic vasculature and cortical bone defects (Colnot et al., 2005; St-Jacques et al., 1999). Mutations in humans lead to a congenital disorder called acrocapitofemoral dysplasia which is characterized by a short stature and bone defects (Hellemans et al., 2003).

The most broadly expressed mammalian HH protein is SHH. It is expressed in midline tissues including the node, notochord, floor plate, and prechordal plate and it controls left-right and dorsoventral patterning of the neural tube and the brain. Additionally, SHH regulates the development and patterning of the limb buds, smooth muscle, lung, kidney, hair follicle, tooth, inner ear, and eye (Varjosalo and Taipale, 2008). The best characterized SHH-dependent developmental process is the neuronal subtype specification in the ventral spinal cord. SHH is expressed and secreted from the notochord and the overlying floor plate creating a concentration gradient along the dorsoventral axis and specifying five neuronal progenitor subtypes in a precise spatial order (Briscoe et al., 2000; Dessaud et al., 2008; Jessell, 2000; Patten and Placzek, 2000). Loss of SHH activity causes severe developmental disorders including HPE, craniofacial malformations, and polydactyly (Hill et al., 2003; McMahon et al., 2003; Muenke and Beachy, 2000), while aberrant pathway activation has been associated with different kinds of cancer, including glioma (Kinzler et al., 1987), breast (Kubo et al., 2004), pancreatic (Thayer et al., 2003), gastric (Berman et al., 2003) as well as small-cell lung cancer (Watkins et al., 2003).

1.2.2 Processing and transport of sonic hedgehog ligands

Like all members of the HH family, SHH is synthesized as a 45 kilodalton (kDa) precursor that undergoes autocatalytic signal sequence cleavage in the endoplasmic reticulum (ER) catalyzed by its carboxy (C)-terminal region (Mann and Beachy, 2004; Perler, 1998). While the C-terminal fragment (HH-C, 25 kDa) exits the ER and is targeted for proteasomal degradation (Chen et al., 2011a), the amino (N)-terminal peptide (HH-N, 19 kDa) is further modified by the attachment of a cholesterol moiety at the C-terminus (Mann and Beachy, 2004) and an amide-linked palmitic acid group at the N-terminus (Pepinsky et al., 1998; Taylor et al., 2001). The dually lipid-modified HH-N is then transported through the constitutive secretory pathway to the plasma membrane and is released.

The most common secretory mechanism for SHH is mediated by a cooperative action of the multipass transmembrane protein DISP1 and glycoprotein signal peptide CUB domain and EGF like domain containing 2 (SCUBE2). Both proteins bind different parts of the cholesterol molecule to promote release of mature HH from the cell surface (Creanga et al., 2012; Tukachinsky et al., 2012). Loss of DISP1 leads to an accumulation of HH within the cell and a failure of long-range signaling (Burke et al., 1999; Ma et al., 2002). Independently, monomeric HH-N can self-assemble to large soluble multimers that are released from the plasma membrane (Chen et al., 2004a; Gallet et al., 2006). Alternatively, HH-N oligomers interact with heparan sulfate proteoglycans enabling their incorporation in lipoprotein particles (Eugster et al., 2007; Panáková et al., 2005). Furthermore, mature HH can be released via exovesicles (Thérond, 2012) or spread via filopodia like cell extensions (Ramírez-Weber and Kornberg, 1999; Rojas-Ríos et al., 2012). HH can travel and act up to 50 µm in the *Drosophila* imaginal wing disc and up to 300 µm in the vertebrate limb bud away from its secretion source (Zhu and Scott, 2004).

Both lipid modifications are important for morphogen distribution and signal transduction. Lack of cholesterol or palmitate moieties impacts long-range spread and signal activity. The cholesterol moiety tethers HH proteins to the plasma membrane and concentrates them within sterol-rich lipid-rafts facilitating the assembly of HH monomers into multimers (Vyas et al., 2008; Zeng et al., 2001). Unpalmitoylated HH shows little to no patterning activity in *Drosophila* and mammalian tissues (Chen et al., 2004a; Dawber et al., 2005; Lee et al., 2001b). In cultured mouse embryonic fibroblasts, palmitoylated SHH shows a 40 to 160-fold increase in signal activity compared to unmodified SHH (Pepinsky et al., 1998). Additionally, palmitate was suggested to play a role in the proteolytic removal of inhibitory N-terminal residues by ADAM17 to enable binding of SHH to its receptor PTCH1 (Ohlig et al., 2011).

1.2.3 Sonic hedgehog signal transduction

In the absence of ligand, the SHH signaling pathway is repressed through a cascade of inhibitory interactions that are released upon pathway activation. In vertebrates, the functionality of the pathway is linked to a cellular immotile organelle, called the primary cilium. Diseases affecting ciliary structure and function, summarized as ciliopathies, cause similar symptoms as defective HH signaling (Goetz and Anderson, 2010). The 12-pass transmembrane protein PTCH1 acts as the main cellular receptor for HH. It is localized in the ciliary pocket in and around the base of the primary cilium and inhibits the G protein coupled receptor and signal transducer smoothened (SMO) from ciliary entry (Rohatgi et al., 2007). How exactly PTCH1 acts on SMO remains unclear. PTCH1 contains a resistance-nodulation-division (RND) permease motif and a sterol-sensing domain (Kuwabara and Labouesse, 2002; Nikaido, 2011; Tseng et al., 1999). Mutations affecting the motif de-represses SMO suggesting that PTCH1 controls the availability of different ligands that regulate SMO activity (Taipale et al., 2002). The most promising candidates are oxysterols which directly bind SMO and promote SHH signaling (Corcoran and Scott, 2006; Dwyer et al., 2007; Nachtergaele et al., 2012). The identification of numerous SMO agonists and antagonists structurally related to sterol such as the steroidal alkaloid cyclopamine support the hypothesis that endogenous sterol-like molecules transported by PTCH1 regulate SMO and, thus, HH signaling (Chen et al., 2002; Mas and Ruiz i Altaba, 2010).

Binding of SHH to its receptor PTCH1 induces endocytosis and lysosomal degradation of PTCH1 (Incardona et al., 2002), releasing the inhibition of SMO. Full activation of SMO requires a conformational switch in the C-terminal domain from a closed, inactive to an open, active conformation through multiple sequential phosphorylation mediated by the G protein coupled receptor kinase 2 (GPRK2) and casein kinase 1 α (CK1α) (Chen et al., 2011b; Zhao et al., 2007). The change in conformation is essential for SMO to accumulate at the cell surface and to transduce signals (Chen et al., 2010; Zhao et al., 2007). The degree of phosphorylation and the corresponding gradual switch in conformation corresponds to the strength of HH signaling (Jia et al., 2004). Activated SMO enters the cilium either via lateral transport from the plasma membrane (Milenkovic et al., 2009) or directly via intracellular vesicles (Wang et al., 2009). Translocation of SMO is facilitated by direct interaction with β-arrestin and kinesin-like protein 3A (KIF3A) (Chen et al., 2004b; Kovacs et al., 2008). After entering the primary cilium, SMO associates with ciliary proteins EvC ciliary complex subunit 1 (EVC1) and 2 (EVC2) resulting in its accumulation distal to the basal body and enabling signal transduction (Dorn et al., 2012; Yang et al., 2012).

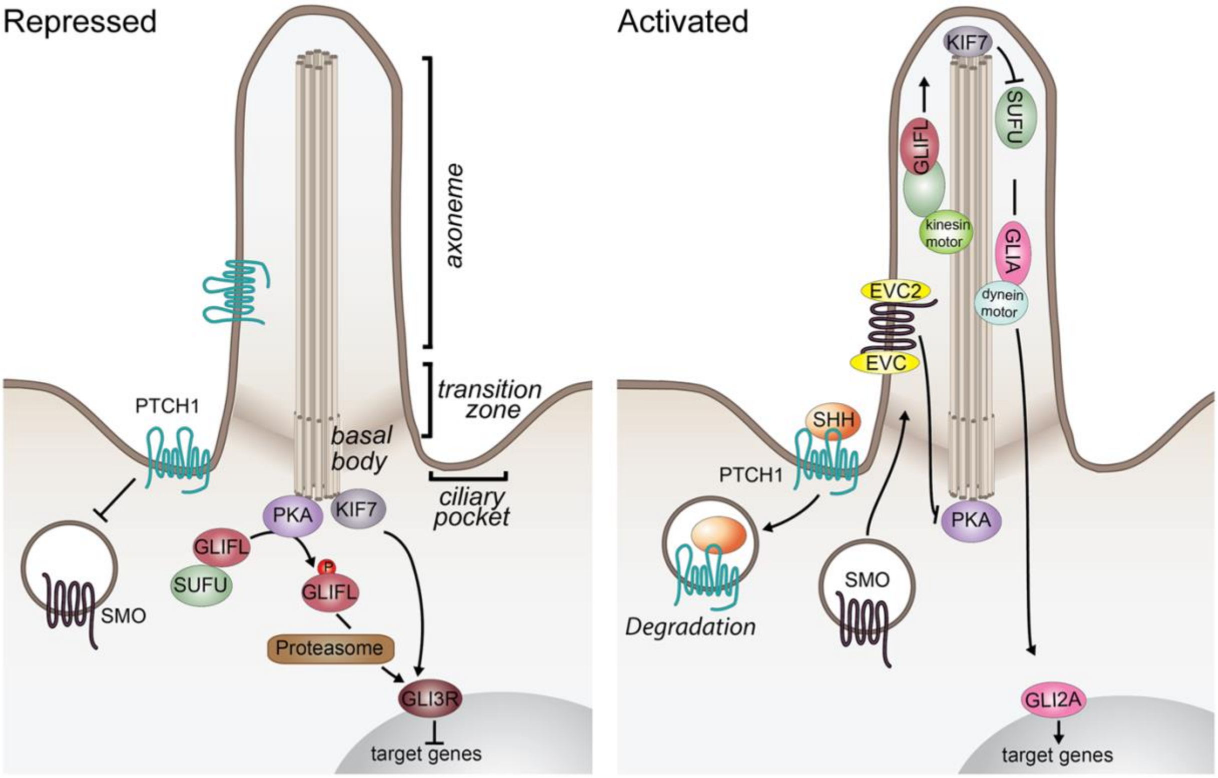

Figure 6 SHH signal transduction at the primary cilium. (**Left**) In absence of SHH, the signaling pathway is repressed through inhibition of SMO by PTCH1. Consequently, full length GLI transcription factors (GLIFL) are sequestered by SUFU, phosphorylated by PKA, and processed by the proteasome into GLI repressor forms (GLI3R) that inhibit expression of downstream target genes. (**Right**) SHH binding to PTCH1 induces the internalization and lysosomal degradation of the receptor, releasing the inhibition of SMO. SMO enters the primary cilium associated with EVC/EVC2. Jointly, they prevent GLIFL from getting phosphorylated. KIF7 facilitates the accumulation of the SUFU/GLIFL complex and inhibits SUFU. Unprocessed full length GLI activator forms (GLIA/GLI2A) dissociate from the complex and activate the expression of downstream target genes. Adapted from Christ et al., 2016.

Signal transduction in vertebrate cell types acts on GLI transcription factors (Hui and Angers, 2011) which are homologs of the transcription factor Cubitus interruptus (Ci) in *Drosophila melanogaster* (Von Ohlen et al., 1997). GLI proteins are members of the Kruppel family of zinc finger proteins with similar DNA binding specificities. They all contain a C-terminal activation domain whereas GLI2 and GLI3 additionally contain a N-terminal repressor domain (Dai et al., 1999; Sasaki et al., 1999). GLI2 mainly acts as pathway activator, while GLI3 primarily represses it (Ding et al., 1998; Wang et al., 2000). GLI1, in turn, is transcriptionally induced upon SHH pathway activation and exclusively induces the expression of downstream targets (Hynes et al., 1997). SHH signaling regulates a balance between GLI activator and repressor forms by mediating their proteolytic processing. In the absence of SHH, full-length GLIs are sequestered at the ciliary base via suppressor of fused (SUFU). There, they are phosphorylated by protein kinase A (PKA) and glycogen synthase kinase 3 β (GSK3β) at multiple sites (Ding et al., 1999; Kogerman et al., 1999; Tuson et al., 2011). Phosphorylation recruits an E3 ubiquitin ligase complex which ubiquitinates and targets GLI2/3 to the proteasome. The C-terminal activation domain is removed by degradation and the remaining protein fragment represses transcription of downstream target genes after translocating to the nucleus (Dai et al., 1999; Jia et al., 2005; Kise et al., 2009; Smelkinson and Kalderon, 2006; Tuson et al., 2011; Wang et al., 2000). The kinesin-like protein 7 (KIF7) additionally promotes the formation of GLI repressor forms (Endoh-Yamagami et al., 2009). Upon pathway activation, SMO inhibits the phosphorylation of GLI proteins on the one hand (Dorn et al., 2012), while KIF7 facilitates the accumulation of the full length GLI2/3/SUFU complexes at the tip of the primary cilium and inhibits SUFU on the other hand (Cheung et al., 2009; Endoh-Yamagami et al., 2009). GLI activator proteins dissociate from the complex and translocate to the nucleus activating target gene expression (Fig. 6) (Humke et al., 2010; Tukachinsky et al., 2010).

1.2.4 The sonic hedgehog receptorsome

Activation of the SHH signaling pathway requires the binding of the morphogen to PTCH1. However, recent studies in mouse models have identified several additional cell surface proteins that are essential for SHH signal reception and transduction in target cells, even in the presence of PTCH1. Collectively, these SHH binding proteins are referred to as the SHH receptorsome (Fig. 7). They are structurally diverse and show unique spatial and temporal expression patterns suggesting distinct functions in modulating SHH pathway activity (Christ et al., 2016). Depending on the physiological and cellular context, these co-receptors cooperate with PTCH1 or with each other to act redundantly, synergistically or even opposingly in SHH signal reception (Allen et al., 2007; Echevarría-Andino and Allen, 2020; Izzi et al., 2011; Xavier et al., 2016; Zhang et al., 2011). Mice deficient for these proteins show a range of phenotypes reminiscent of partial to complete SHH-deficiency or overactivity of the pathway, respectively (Allen et al., 2007, 2011; Cole and Krauss, 2003; Echevarría-Andino and Allen, 2020; Izzi et al., 2011; Willnow et al., 1996; Zhang et al., 2006, 2011). Additionally, mutations in several of these SHH binding proteins in patients have been linked to HPE or HPE-related phenotypes as in Donnai-Barrow syndrome (DBS) (Bae et al., 2011; Hong et al., 2017; Kantarci et al., 2007; Ribeiro et al., 2010) corroborating their importance for SHH-dependent forebrain development in humans.

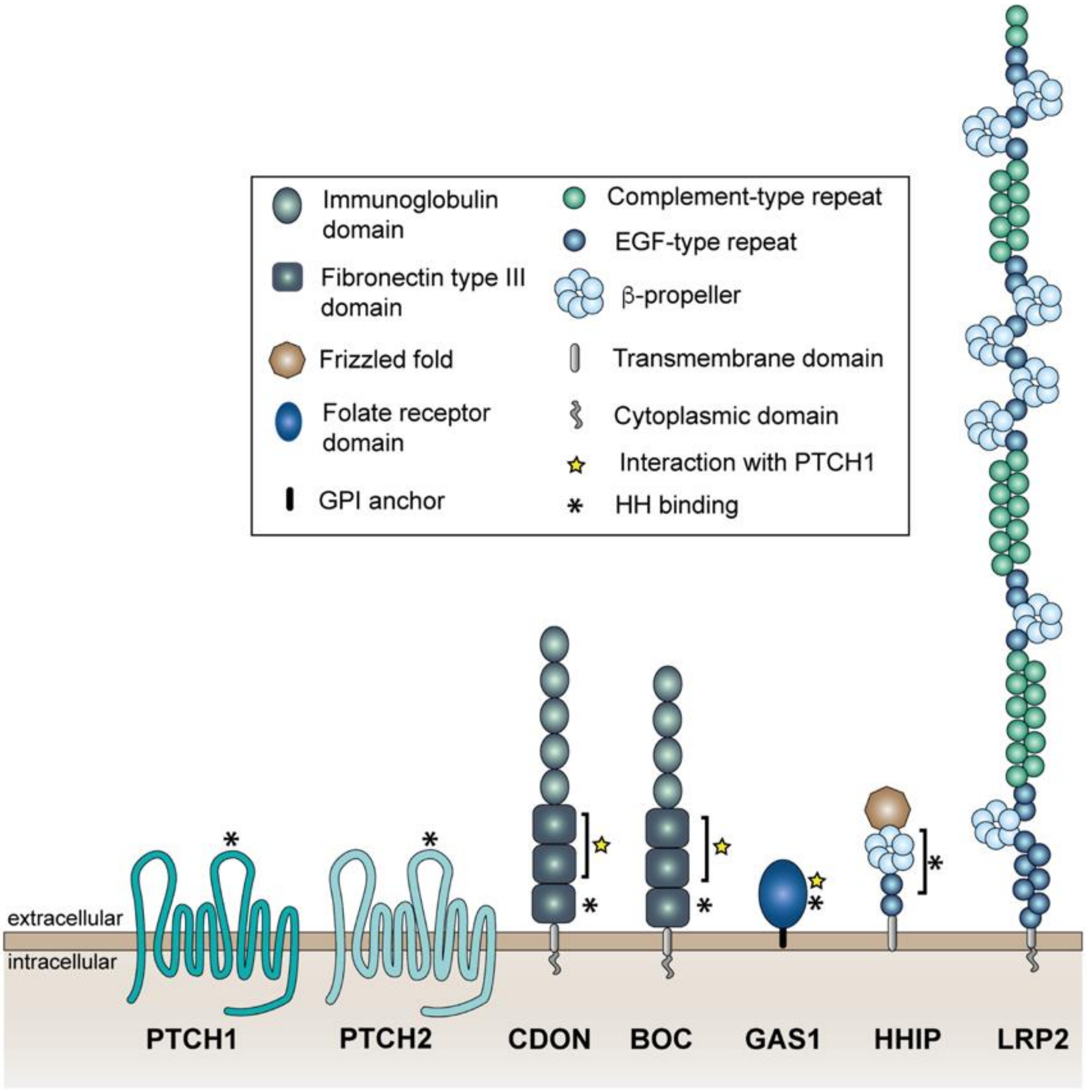

Figure 7 The SHH receptorsome. Structural organization of HH receptors and co-receptors in mammals. Adapted from Christ et al. 2016.

The first SHH co-receptor hedgehog interacting protein (HHIP) was identified in a screen for novel HH pathway components in the mouse limb bud (Chuang and McMahon, 1999). HHIP is an 80 kDa glycoprotein that is anchored to the cell surface by a single short hydrophobic C-terminal domain. It binds all three mammalian HH proteins and acts as a negative regulator by sequestering the morphogen at the cell surface (Chuang and McMahon, 1999; Holtz et al., 2013; Jeong and McMahon, 2005). Based on bone and cartilage formation defects in HHIP-deficient or overexpressing mouse models, HHIP is believed to play a role in regulating IHH function (Chuang and McMahon, 1999; Chuang et al., 2003).

Another negative regulator of SHH signaling is the PTCH1 homolog patched 2 (PTCH2) (Fig. 7). Both share only 56% of homology suggesting different functions in pathway modulation (Motoyama et al., 1998a, 1998b). PTCH2 also binds all three HH protein variants and interacts with SMO (Carpenter et al., 1998) but the strength of pathway inhibition in absence of ligands is weaker than that described for PTCH1 (Rahnama et al., 2004). PTCH2 mutant mice are viable and fertile and do not exhibit neural tube defects (Goodrich et al., 1997; Nieuwenhuis et al., 2006). However, a combined loss of PTCH1 and PTCH2 leads to an increase in the amount of ventral neural progenitor cells due to overactive SHH signaling (Holtz et al., 2013; Jeong and McMahon, 2005).

Finally, four other SHH co-receptors have been described to interact with PTCH1 in modulating morphogen signaling. This class of proteins encompasses cell-adhesion molecule-related/downregulated by oncogenes (CDO), brother of CDO (BOC), growth-arrest specific 1 (GAS1), and low-density lipoprotein receptor-related protein 2 (LRP2) (Christ et al., 2016) (Fig. 7). CDO and BOC are homologs of Ihog and Boi in *Drosophila melanogaster*. They are receptors of the immunoglobulin (Ig) super family and consist of four or five Ig repeats, three fibronectin-type III (Fn(III)) repeats, and a short intracellular domain (Kang et al., 1997, 2002). Both bind all three HH proteins and positively regulate SHH signaling (Tenzen et al., 2006; Yao et al., 2006) by forming a co-receptor complex with PTCH1 (Izzi et al., 2011). Loss of CDO in mouse models (Cole and Krauss, 2003; Echevarría-Andino and Allen, 2020; Zhang et al., 2006) or *CDON* mutations in humans (Bae et al., 2011) have been associated with HPE or related phenotypes. BOC is important for SHH-dependent guidance of commissural axons in the spinal cord (Okada et al., 2006). BOC alone does not affect forebrain development but its loss worsens or weakens SHH signaling defects and forebrain phenotypes when combined with CDO- or GAS1-deficiencies in mice (Allen et al., 2011; Echevarría-Andino and Allen, 2020; Seppala et al., 2014; Zhang et al., 2011). Also, BOC acts as a silent HPE modifier gene influencing the severity of HPE phenotypes in the context of other HPE causing mutations (Hong and Krauss, 2018; Hong et al., 2017). CDO and GAS1 cooperate to promote SHH signaling during vertebrate development (Allen et al., 2007). Mouse embryos lacking GAS1, CDO, and BOC show complete abrogation of SHH signal activity leading to prenatal lethality, severe heart defects, mispatterning of the neural tube, and HPE (Allen et al., 2011).

1.3 GAS1

GAS1 is a 45 kDa glycoprotein attached to the plasma membrane via a glycosylphosphatidylinositol (GPI) anchor (Fig. 7) (Stebel et al., 2000). It is structurally related to glial cell derived neurotrophic factor (GDNF) receptor family α (GFRα) (Cabrera et al., 2006).

GAS1 was first described as being upregulated in NIH3T3 cells arrested in cell cycle by serum starvation (Schneider et al., 1988). Among the six identified GAS proteins, only GAS1 was able to suppress cell cycle progression in NIH3T3 cells when overexpressed. It does so by blocking G_0 to S phase transition (Del Sal et al., 1992, 1994; Evdokiou and Cowled, 1998a) mostly via tumor suppressor gene p53 (Del Sal et al., 1995; Ruaro et al., 1997). Since senescent fibroblasts do not show any GAS1 upregulation, it was hypothesized that GAS1 negatively regulates cell growth rather than inducing cellular senescence (Cowled et al., 1994). Additionally, GAS1 overexpression in C6 glioma cells induces apoptosis via caspase 3 and reduces the tumorigenicity of these cells when injected into nude mice (Zamorano et al., 2003, 2004). A similar effect of ectopic GAS1 expression was seen in lung adenocarcinoma cells (Evdokiou and Cowled, 1998b). Consistently, several gene expression profiling studies on different cancer cells showed a downregulation of GAS1 expression (Huang et al., 2001; Lapouge et al., 2005). By contrast, expression analyses in mouse and chick embryos documented high levels of GAS1 in proliferative regions suggesting a positive rather than a negative regulation of cell proliferation during development *in vivo*. This assumption is supported by the fact that *Gas1* mutant mice are smaller in size and do not display tissue overgrowth (Lee and Fan, 2001; Lee et al., 2001c).

An unbiased expression screen for new SHH binding proteins in early mouse embryos uncovered GAS1 to associate with SHH and IHH suggesting a potential role in regulating HH signaling (Lee et al., 2001a). In the developing embryo, GAS1 is initially expressed in the notochord and throughout the neural tube but its expression becomes progressively restricted to dorsal regions correlating with regions distant from the SHH source. This fact indicates repression of GAS1 expression by SHH (Allen et al., 2007; Martinelli and Fan, 2007).

It was first believed that GAS1 negatively regulates SHH pathway activity to sequester excessive SHH and to prevent its activity at long distances (Cobourne et al., 2004; Lee et al., 2001a). However, GAS1-deficient embryos showed phenotypes consistent with a reduction of SHH signaling including compromised floor plate specification and loss of ventral neural tube cell identities, defects in digit patterning as well as skeletal abnormalities (Allen et al 2007, Echevarria-Andino and Allen 2020, Khonsari et al 2013, Martinelli and Fan 2007, Seppala 2007, Seppala 2014, Carreno 2017, Zhao 2012). These phenotypes worsened after reducing SHH dosage in *Shh* haploinsufficient mouse embryos indicating a genetic interaction between GAS1 and SHH in morphogen signaling (Allen et al., 2007; Khonsari et al., 2013; Martinelli and Fan, 2007). Along the same lines, reduction of GAS1 activity in NIH3T3 cells by RNA interference led to decreased GLI1-reporter gene activation (Martinelli and Fan, 2007). Ectopic GAS1 expression in the chick neural tube facilitated SHH signaling and induced the expression of target genes, such as NK2 homeobox 2 (NKX2.2), NK6 homeobox 1 (NKX6.1), oligodendrocyte transcription factor 2 (OLIG2), and FOXA2 at farther distance (Allen et al., 2007; Martinelli and Fan, 2007). These data proved that GAS1 acts cell autonomously to enhance SHH responsiveness mostly at long distance and low concentrations in the caudal neural tube and limb buds instead of negatively regulating pathway activity. Co-immunoprecipitation analyses in overexpressing COS7 cells uncovered that GAS1 promotes SHH signal activity by forming a co-receptor complex with the receptor PTCH1 essential for SHH signal transduction (Izzi et al., 2011).

Loss of GAS1 activity in mutant mouse models (Allen et al., 2007; Echevarría-Andino and Allen, 2020; Khonsari et al., 2013; Martinelli and Fan, 2007; Seppala et al., 2007, 2014) or in patients carrying mutations in *GAS1* (Pineda-Alvarez et al., 2012; Ribeiro et al., 2010) result in a range of forebrain and craniofacial malformations including hypoplastic midface, defective eyes, hypotelorism, single median maxillary central incisor, cleft palate, fusion of the nasal processes, the telencephalic vesicle and the frontal lobes as well as lobar and semilobar HPE. Some identified missense mutations in HPE patients reduce the affinity of GAS1 for binding SHH (Pineda-Alvarez et al., 2012). Because *Gas1* mutant embryos showed impaired expression of *Shh* (Seppala et al., 2014) and downstream target genes, such as *Gli1* (Echevarría-Andino and Allen, 2020; Khonsari et al., 2013; Seppala et al., 2007) and NK2 homeobox 1 (*Nkx2.1*) (Allen et al., 2007; Echevarría-Andino and Allen, 2020) in the ventral forebrain midline, impaired SHH signaling in the developing forebrain was held responsible for malformations in GAS1-deficient mouse models and human patients mentioned above.

1.4 LRP2

The most recently identified member of the SHH receptorsome is the 600 kDa endocytic receptor LRP2, also known as megalin (Fig. 7). Its extracellular domain consists of modules characteristic for a group of receptors structurally related to the low density lipoprotein receptor (LDLR), so called LDLR related proteins (LRPs). The ectodomain of LRP2 is composed of four repetitive modules consisting in total of 17 epidermal growth factor (EGF)-type repeats, eight β-propellers and four cysteine-rich complement type-repeats (Rudenko et al., 2002; Saito et al., 1994). These elements are required for ligand binding (complement-type repeats) or for pH dependent-release of cargo in the acidic milieu of the endosome (β-propellers and EGF-type repeats).

The intracellular tail of LRP2 harbors interaction sites for cytosolic adaptor proteins and kinases controlling shuttling of the receptor and its ligand between the plasma membrane and endocytic compartments. These interaction sites include three NPxY/NPxY-like motifs and two PDZ domain binding sites (Takeda et al., 2003). In mammals, LRP2 is predominantly expressed on the apical site of absorptive epithelia in kidney, lung, reproductive organs, eyes, spinal cord, and brain (Argraves and Morales, 2004; Assémat et al., 2005; Christ et al., 2015; Christensen et al., 1995; Gajera et al., 2010; Lundgren et al., 1997; Wicher et al., 2006). Most internalized receptor ligands are directed to lysosomal compartments for catabolism (Christensen et al., 1999; Nykjaer et al., 1999). However, some ligands resist lysosomal degradation and are recycled back to the cell surface for resecretion (Christ et al., 2012; Morales et al., 2006), while others are transported from the apical to basolateral membrane via transcytosis (Marinò et al., 2003; Ortega et al., 2012).

LRP2 was initially characterized as an endocytic receptor in renal proximal tubular cells of the kidney essential for clearance of low-molecular weight plasma proteins from the glomerular filtrate. Ligands include plasma carriers for vitamins A, B12, and D. (Birn et al., 2002; Christensen et al., 1999; Nykjaer et al., 1999). In addition to glomerular reabsorption defects, patients with mutations in *LRP2* (Rosenfeld et al., 2010) or LRP2-deficient mouse models (Spoelgen et al., 2005; Willnow et al., 1996) show HPE and craniofacial malformations reminiscent of defective SHH signaling in the developing forebrain.

An essential role for LRP2 in control of SHH signaling in different developmental processes in the embryo as well as in adult homeostasis was subsequently confirmed using mutant mouse models (Christ et al., 2012, 2015, 2020; Gajera et al., 2010; Ortega et al., 2012). These studies identified LRP2 as an auxiliary SHH co-receptor in the rostral diencephalon ventral midline (RDVM) during neurulation. It is highly expressed in the ciliary pocket of neuroepithelial cells and forms a co-receptor complex with PTCH1 facilitating binding and endocytosis of SHH secreted from the underlying PrCP. Internalized SHH and LRP2 colocalize within Ras-related protein RAB 11 (RAB11)-positive recycling endosomes suggesting a role for LRP2 in promoting the resecretion of SHH to sequester the morphogen in this forebrain organizer region (Christ et al., 2012). In *Lrp2* mutant mice, the induction of the SHH expression domain in the RDVM is delayed leading to aberrant dorsoventral patterning and defective ventralization. These defects cause the fusion of cerebral hemispheres and craniofacial malformations (Christ et al., 2012; Spoelgen et al., 2005; Willnow et al., 1996).

In the adult brain, LRP2 is expressed in polarized epithelial cells of the ependyma covering the luminal surface of the brain ventricles (Gajera et al., 2010). Although not belonging to the neural stem cell population of the subventricular zone (SVZ), ependymal cells are important for maintaining the microenvironment of the neurogenic stem cell niche by impacting the distribution of the cerebrospinal fluid (CSF) and providing neurogenic factors that enable and sustain adult neurogenesis (Colak et al., 2008; Ihrie and Alvarez-Buylla, 2011; Lim et al., 2000). Loss of *Lrp2* in mouse models reduce the number of neural stem cells in the SVZ indicating a role of LRP2 in regulating neurogenesis in this niche (Gajera et al., 2010).

Similar to the neurogenic niche of the SVZ, LRP2 impacts SHH-dependent proliferation of progenitor cells of the anterior second heart field (SHF) located in the dorsal pericardial wall (DPW) of the embryonic heart. These cells contribute to outflow tract (OFT) development and septation. Impaired SHH signaling in the DPW of *Lrp2* mutant mice coincides with a decreased number of SHH-dependent progenitor cells in this tissue due to their premature differentiation into cardiomyocytes. As a consequence, the OFT is shortened, the likely cause of OFT formation defects (i.e., common arterial trunk) seen in humans (Zaidi et al., 2013) and mouse models (Baardman et al., 2016; Li et al., 2015) lacking the receptor gene. Similar phenotypes are seen in *Shh* mutant mice (Goddeeris et al., 2007; Washington Smoak et al., 2005).

Contrary to its agonistic action in the forebrain neuroepithelium, LRP2 operates as SHH antagonist in the ciliary marginal zone (CMZ) of the retina during eye development (Christ et al., 2015). Here, SHH is produced by retinal ganglion cells and acts on retinal progenitor cells to pattern the retina in a central to peripheral direction (Wang et al., 2002). SHH is absent from the CMZ at the distal margin of the retina leaving retinal progenitor cells in a quiescent state (Cho and Cepko, 2006; Zhao et al., 2002) and restricting growth of the eye. LRP2 is exclusively expressed in the CMZ where it acts as a clearance receptor for SHH. LRP2-mediated uptake and lysosomal degradation of SHH protects progenitor cells of the CMZ from mitogenic stimuli by this factor. In the absence of LRP2, retinal progenitor cells experience increased SHH signals leading to hyperproliferation and expansion of the progenitor cell pool in the mutant CMZ (Christ et al., 2015). As a consequence, LRP2-deficient animal models show massive overgrowth of the eye globes (Cases et al., 2015; Christ et al., 2015; Storm et al., 2014; Veth et al., 2011) providing a molecular explanation for the development of buphthalmia in patients with mutated *LRP2*.

1.4.1 Donnai-Barrow/Facio-oculo-acoustico renal syndrome

Mutations in the *LRP2* gene have been identified as cause of Donnai-Barrow/Facio-oculo-acoustico renal syndrome (herein referred to as DBS) in humans (Kantarci et al., 2007; Pober et al., 2009). DBS is a rare autosomal recessive disorder characterized by a broad range of clinical features such as low-molecular weight proteinuria, congenital diaphragmatic hernia, hearing impairments, high myopia, mental retardation, developmental delay, craniofacial malformations, and brain abnormalities. The latter include absence of the corpus callosum, hypertelorism, enlarged anterior fontanelle as well as microforms of HPE (Avunduk et al., 2000; Chassaing et al., 2003; Donnai and Barrow, 1993; Gripp et al., 1997; Kantarci et al., 2007, 2008; Khalifa et al., 2015; Pober et al., 2009; Rosenfeld et al., 2010). So far, less than 50 patients from consanguineous families have been diagnosed with DBS. Twenty-two *LRP2* mutant gene variants have been documented, including nonsense and missense mutations, small deletions and insertions in gene coding regions. In addition, mutations in conserved splice sites, mostly within the extracellular domain, result in a complete absent or nonfunctional LRP2 protein (Anglani et al., 2018; Dachy et al., 2015; Kantarci et al., 2007, 2008; Khalifa et al., 2015; Khan and Ghazi, 2018; Pober et al., 2009; Schrauwen et al., 2014; Shaheen et al., 2010; Stora et al., 2009; Storm et al., 2013). However, no apparent genotype-phenotype correlation has been identified (Kantarci et al., 2007; Pober et al., 2009). LRP2-deficiency in mouse models recapitulate many features seen in DBS patients, for example proximal tubular reabsorption defects and low-molecular weight proteinuria, enlarged eye globes, buphthalmia and glaucoma, craniofacial anomalies as well as forebrain defects like agenesis of the corpus callosum and HPE (Cases et al., 2015; Christ et al., 2012, 2015; Leheste et al., 1999; Nykjaer et al., 1999; Spoelgen et al., 2005; Storm et al., 2014; Veth et al., 2011; Willnow et al., 1996).

1.5 Aim

Besides the canonical SHH receptor PTCH1, several additional cell surface proteins have been identified as being essential for proper SHH signaling in the developing forebrain neuroepithelium. Mutations in these co-receptors have been identified in familial forms of HPE in patients and mouse models corroborating their importance for SHH-dependent forebrain development. However, the distinct functions of these receptors in cellular SHH action remain enigmatic. The aim of my work was to elucidate the cellular function of two such SHH co-receptors, LRP2 and GAS1 in forebrain development using human disease modeling in induced pluripotent stem cells (iPSCs). In the first project, I focused on a unique missense mutation in *LRP2* in two siblings with DBS. Here, I queried how this mutation impacts receptor functions in iPSC-derived neural progenitor cells (NPCs) and renal proximal tubule epithelial cells (RPTECs). In the second project, I studied the molecular mechanism of GAS1 action during forebrain development by performing comparative studies in GAS1-deficient mice and iPSC-based models of the human forebrain neuroepithelium.

2 RESULTS

2.1 Paper 1: Induced pluripotent stem cell-based disease modeling identifies ligand-induced decay of megalin as a cause of Donnai-Barrow syndrome.

Authors

Julia Flemming*, Maike Marczenke*, Ina-Maria Rudolph, Rikke Nielsen, Tina Storm, Erik Ilsoe Christensen, Sebastian Diecke, Francesco Emma, Thomas E. Willnow

*Flemming and Marczenke contributed equally to this study

Published in Kidney International, 2020 July, 98(19):159-167
doi: 10.1016/j.kint.2020.02.021
https://doi.org/10.1016/j.kint.2020.02.021

Personal contribution

Together with the co-authors I designed and performed experiments, collected, analyzed and interpreted the data, prepared the visualization of the work and arranged the figures, and wrote the manuscript. In detail, I performed experiments that contributed to the following figures: 4c and d, 5, 6e, 7, S2B and D, S5C and D, S7, and S8.

Induced pluripotent stem cell-based disease modeling identifies ligand-induced decay of megalin as a cause of Donnai-Barrow syndrome

see commentary on page 54

OPEN

Julia Flemming[1,5], Maike Marczenke[1,5], Ina-Maria Rudolph[1], Rikke Nielsen[2], Tina Storm[2], Ilsoe Christensen Erik[2], Sebastian Diecke1, Francesco Emma[3] and Thomas E. Willnow1,2

[1]*Max-Delbrueck-Center for Molecular Medicine, Berlin, Germany;* [2]*Department of Biomedicine, Faculty of Health Science, Aarhus University, Aarhus C, Denmark; and* [3]*Division of Nephrology, Department of Pediatric Subspecialties, Bambino Gesù Children's Hospital – IRCCS, Rome, Italy*

Donnai-Barrow syndrome (DBS) is an autosomal-recessive disorder characterized by multiple pathologies including malformation of forebrain and eyes, as well as resorption defects of the kidney proximal tubule. The underlying cause of DBS are mutations in *LRP2*, encoding the multifunctional endocytic receptor megalin. Here, we identified a unique missense mutation R3192Q of *LRP2* in an affected family that may provide novel insights into the molecular causes of receptor dysfunction in the kidney proximal tubule and other tissues affected in DBS. Using patient-derived induced pluripotent stem cell lines we generated neuroepithelial and kidney cell types as models of the disease. Using these cell models, we documented the inability of megalin R3192Q to properly discharge ligand and ligand-induced receptor decay in lysosomes. Thus, mutant receptors are aberrantly targeted to lysosomes for catabolism, essentially depleting megalin in the presence of ligand in this affected family.

Kidney International (2020) 98, 159–167; https://doi.org/10.1016/j.kint.2020.02.021

KEYWORDS: endocytosis; low-molecular-weight proteinuria; proximal tubule dysfunction; renal Fanconi syndrome

Donnai-Barrow/Facio-oculo-acoustico-renal syndrome (herein referred to as DBS) is an autosomal recessive disorder caused by inheritable mutations in *LRP2* (low-density lipoprotein receptor–related protein 2)1, This gene encodes the endocytic receptor megalin that acts as a high-capacity clearance pathway for numerous ligands in absorptive epithelia, most notably in the developing forebrain and retina[3-5] and in the proximal tubules of the adult kidney.6,[7] Some variability exists in the extent of malformation of forebrain and facial structures in patients with DBS, defects attributed to the loss of receptor expression in neuroepithelial cells of the developing central nervous system.2,[8-10] By contrast, patients with DBS invariably suffer from renal resorption defects (renal Fanconi syndrome) characterized by urinary loss of megalin ligands, including vitamins D, A, and B12 bound to their plasma carrier proteins.1,[11,12] This observation underscores the central role played by megalin in proximal tubular retrieval processes in humans.

Despite its importance for renal (patho)physiology, little is known about the functional organization of the giant 600 kDa receptor megalin and the molecular mechanisms that define its ability to act as a clearance pathway in the kidney and other tissues of the human body. Naturally occurring muta- tions in DBS may shed light on essential protein domains altered in the mutant receptors. However, most known *LRP2* mutations encode truncated soluble fragments offering little conceptual advance on the functional organization of the receptor polypeptide.[1] Here, we report the identification of a novel missense mutation *LRP2*$^{\text{R3192Q}}$ in 2 siblings with DBS. Using human disease modeling in neuroepithelial and renal cell types generated from induced pluripotent stem cells (iPSCs) of both individuals, we document that mutation *LRP2*$^{\text{R3192Q}}$ disrupts the ability of megalin to properly discharge internalized ligand. As a consequence, mutant receptors are aberrantly targeted to lysosomes for catabolism, essentially depleting DBS cells for megalin in the presence of ligand.

RESULTS

iPSC-derived cell lines for disease modeling of DBS

We identified 2 siblings who presented with clinical symptoms of renal Fanconi syndrome, including hypercalciuria and abnormal urinary excretion of low-molecular-weight

---

Correspondence: *Thomas E. Willnow, Max-Delbrueck-Center for Molecular Medicine, Robert-Roessle-Str. 10, D-13125 Berlin, Germany. E-mail: willnow@mdc-berlin.de*

[5]These authors contributed equally to the study.

Received 29 May 2019; revised 11 February 2020; accepted 13 February 2020; published online 24 March 2020

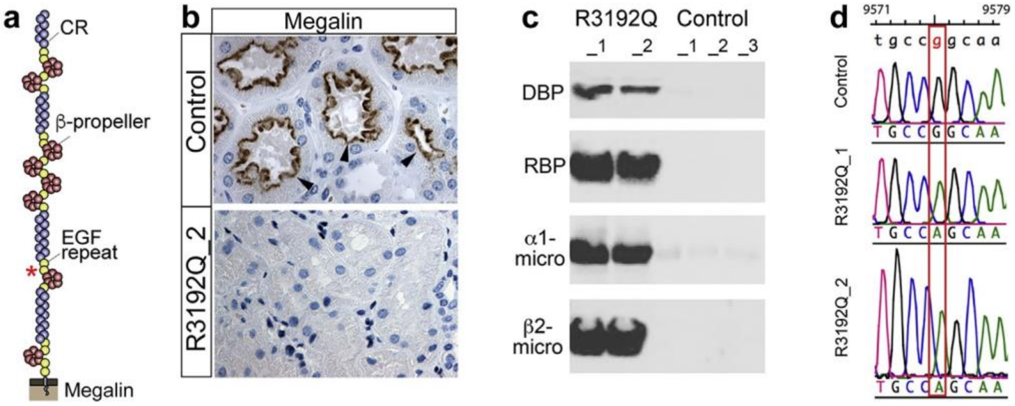

Figure 1 | Mutation c:G9575A in Donnai-Barrow syndrome disrupts renal megalin^{R3192Q} expression. (a) Structural organization of the megalin polypeptide composed of complement-type repeats (CR), epidermal growth factor (EGF)–type repeats, and β-propellers. Mutation R3192Q (encoded by c:G9575A) in an EGF-type repeat is indicated by the red asterisk. (b) Immunohistological detection of megalin (arrowheads) in proximal tubule cells of kidney biopsies from a control subject but not from patient R3192Q_2. (c) Western blot analysis of spot urine documenting urinary loss of the megalin ligands vitamin D–binding protein (DBP), retinol-binding protein (RBP), α_1-microglobulin, and β_2-microglobulin in patients R3192Q_1 and R3192Q_2, but not in 3 control subjects. (d) Sequence analysis showing a homozygous mutation c:G9575A (red box) in *LRP2* in induced pluripotent stem cell lines derived from patients R3192Q_1 and R3192Q_2 as compared with a control cell line. Sequences were aligned to the *LRP2* reference sequence given above (NCBI reference sequence: NM_004525.2). To optimize viewing of this image, please see the online version of this article at www.kidney-international.org.

proteins at the age of 7 and 9, respectively (see the Patient information section for more clinical details). Exome sequencing identified homozygosity for mutation c:G9575A in *LRP2* in both individuals, resulting in amino acid alteration R3192Q in an epidermal growth factor–type repeat in the extracellular megalin domain (Figure 1a). Megalin deficiency as the underlying cause of renal Fanconi syndrome was confirmed by the absence of receptor expression in renal biopsies (Figure 1b) and by aberrant urinary excretion of known receptor ligands (Figure 1c) in the affected individuals R3192Q_1 and R3192Q_2.

To elucidate the mechanism impairing megalin^{R3192Q} expression, we generated iPSC lines by reprogramming peripheral blood mononuclear cells from both patients. Homozygosity for c:G9575A in the iPSC lines was confirmed by DNA sequencing (Figure 1d). Karyotyping of peripheral blood mononuclear cells, and iPSC lines derived thereof, identified copy neutral loss of heterozygosity at 2q23.3-q31.1 as the reason for homozygosity for c:G9575A (Supplementary Figure S1A and B). Minor alterations in other chromosomal regions common to peripheral blood mononuclear cells and iPSC lines were considered irrelevant to explain the loss of renal megalin expression in the affected individuals (Supplementary Figure S1C and D).

iPSC lines from patients R3192Q_1 and R3192Q_2 showed robust expression of pluripotency markers (Supplementary Figure S2A and B) and the expected potential to differentiate into all 3 germ layers (Supplementary Figure S2C and D). To derive a cell model for studying the molecular mechanism underlying loss of megalin^{R3192Q} expression, we initially applied a protocol whereby iPSCs were differentiated into neural precursor cells (NPCs), the progenitor cell population for various cell types of the developing central nervous system (Supplementary Figure S3A).[13] We chose this differentiation protocol for our initial studies because of its robustness and reproducibility, and because it recapitulates expression of megalin in this cell type *in vivo*.[4,14] Both patient cell lines faithfully recapitulated neuroectodermal differentiation as exemplified by induction of neuroectodermal markers PAX6 and SOX1, and by a concomitant loss of pluripotency marker OCT4 (Supplementary Figure S3B–E).

When expression of megalin during neuroectodermal differentiation was tested by immunocytochemistry, robust induction of receptor levels was seen in R3192Q_1 and control cell lines at day 5 of differentiation (Figure 2a). However, megalin levels decreased significantly by day 9 in patient as compared with control cells (Figure 2a). Loss of megalin^{R3192Q} at later stages of differentiation was not due to a decrease in gene transcription, as *LRP2* transcript levels were similar to control cells at days 5 and 9 of differentiation (Figure 2b). The reduced level of megalin protein, but not transcript at day 9 of differentiation, was substantiated by Western blot (Figure 2c and d) and quantitative real-time polymerase chain reaction analysis (Figure 2e), respectively. Post-transcriptional loss of megalin expression was reproduced in an iPSC line from patient R3192Q_2 using immunocytochemistry and quantitative real-time polymerase chain reaction (Supplementary Figure S4A, B, and E), as well as Western blotting (Supplementary Figure S4C and D).

Mutation R3192Q does not abolish the endocytic activity of megalin

To interrogate the impact of mutation R3192Q on the activity of megalin, we established an endocytosis assay in NPCs using the amino terminal fragment of sonic hedgehog (SHH-N) fused to glutathione S-transferase, a megalin ligand in several

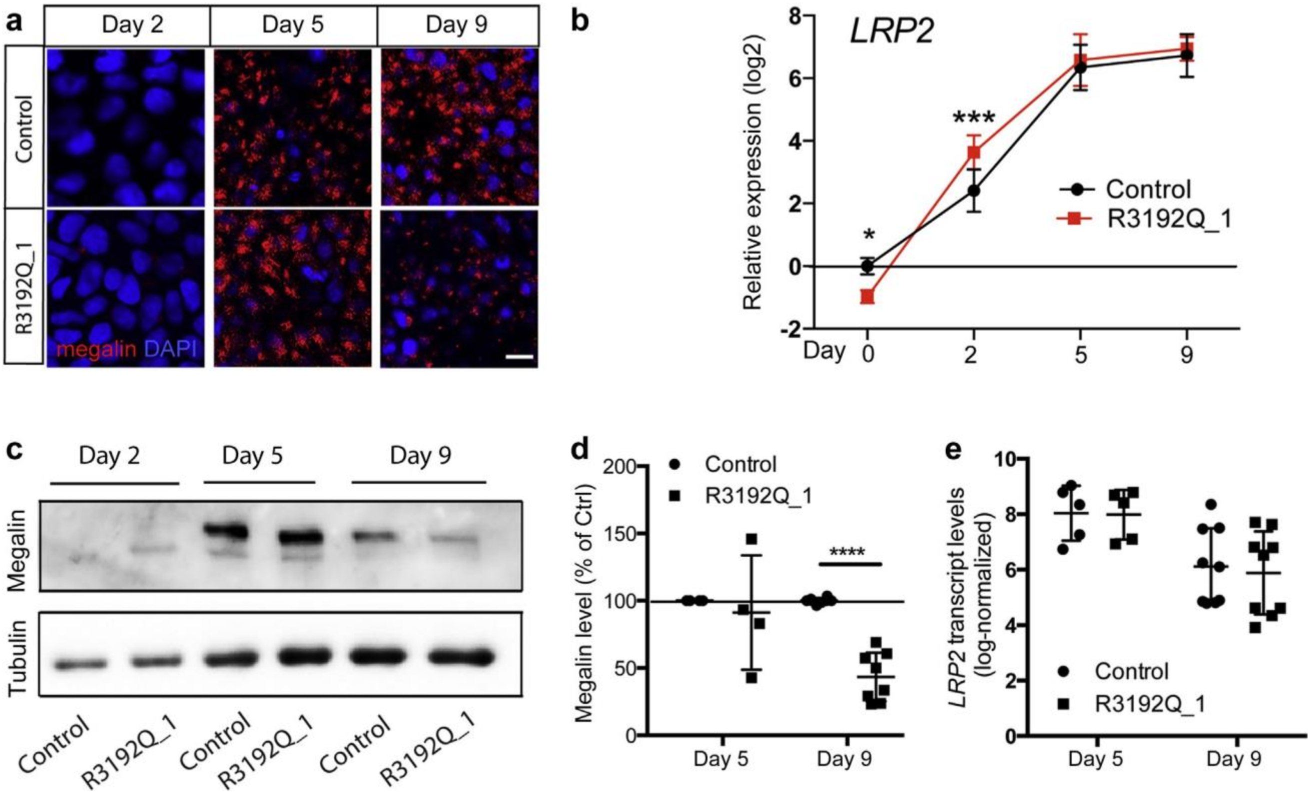

Figure 2 | Cellular expression of megalin^{R3192Q} is impacted by a post-transcriptional mechanism. (a) Immunodetection of megalin (red) in induced pluripotent stem cell (iPSC) lines at the indicated time points of neuroectodermal differentiation. Cells were counterstained with 4^{0},6-diamidino-2-phenylindole (DAPI) (blue). Megalin expression was induced from day 5 onward in both genotypes. At day 9, receptor levels decreased in patient-derived cells as compared with control cells. Bar ¼ 10 mm. (b) Transcript levels of *LRP2* during differentiation into neuroectoderm cells in the control subject and patient R3192Q_1. Data are depicted as Dct normalized to day 0 of the control cells (DDct) ± SD; n ¼ 4 experiments with 2–3 biological replicates/experiment. Statistical analyses were performed by 2-way analysis of variance with the Bonferroni post-test. **P* < 0.05; ****P* < 0.001. (c) Western blot analysis of megalin in R3192Q_1 and control iPSC lines at the indicated time points of neuroectodermal differentiation. The detection of a-tubulin served as loading control. (d) Megalin levels were quantified by densitometric scanning of replicate Western blots (exemplified in panel c) in control and R3192Q_1 neural precursor cells (NPCs) at days 5 and 9 of differentiation (n ¼ 2–3 independent experiments, 2–4 biological replicates/experiment). Megalin levels in R3192Q_1 cells were comparable with control cells at day 5, but significantly decreased at day 9 of differentiation. Values are given as relative levels of expression compared with controls (set to 100% ± SD). Statistical significance was determined by Student's *t* test (day 9) or 1-paired *t* test (day 5). *****P* < 0.0001. (e) Quantitative real-time polymerase chain reaction analysis of *LRP2* transcript levels in a control and R3192Q_1 NPCs at days 5 and 9 of differentiation. (n ¼ 3 independent experiments, 2–4 biological replicates/experiment). Levels are depicted as ct values normalized to transcript levels of *GAPDH* (Dct ± SD) used as an internal control. Transcript levels for *LRP2* are unchanged at days 5 and 9 comparing genotypes (Student's *t* test). To optimize viewing of this image, please see the online version of this article at www.kidney-international.org.

tissues.[4,15] To first establish the validity of this assay for scoring megalin activity, we used a CRISPR/Cas9 strategy to disrupt the megalin coding sequence in the control cell line used in this study and to generate a cell clone genetically deficient for this receptor ($LRP2^{-/-}$; Supplementary Figure S5A). Deletion of the ATG codon in the *LRP2* gene locus completely ablated megalin expression in this cell clone as shown by Western blot analysis (Supplementary Figure S5B). The absence of megalin severely reduced the uptake of GST-SHH-N in $LRP2^{-/-}$ NPCs as compared with parental cells ($LRP2^{b/b}$) as documented by immunocyto- chemistry (Supplementary Figure S5C), identifying megalin as the major endocytic route for SHH-N in NPCs. To more accurately assess the quantitative contribution of megalin to SHH-N uptake in these cells, we treated $LRP2^{-/-}$ and control NPCs with GST-SHH-N and determined the amount of cell-associated ligand thereafter using Western blotting (Supplementary Figure S5B). Megalin deficiency reduced the amount of GST-SHH-N in the $LRP2^{-/-}$ cell fraction by 50% as compared with control cells, underscoring the significance of megalin as the SHH receptor in NPCs (Supplementary Figure S5D). The residual amount of GST-SHH-N associ- ated with $LRP2^{-/-}$ NPCs likely reflected adherence of the ligand to the cellular surface, although the existence of other uptake mechanisms, such as through the receptor Patched1, cannot be excluded.

Next, we used the GST-SHH-N uptake assay to assess the receptor activity in the patient cell line R3192Q_1. Ligand uptake was reduced in these cells as compared with control NPCs as documented by immunocytochemistry (Figure 3a) and quantitative Western blotting (Figure 3b and c). Still, the megalin-mediated uptake of GST-SHH-N in the cell line

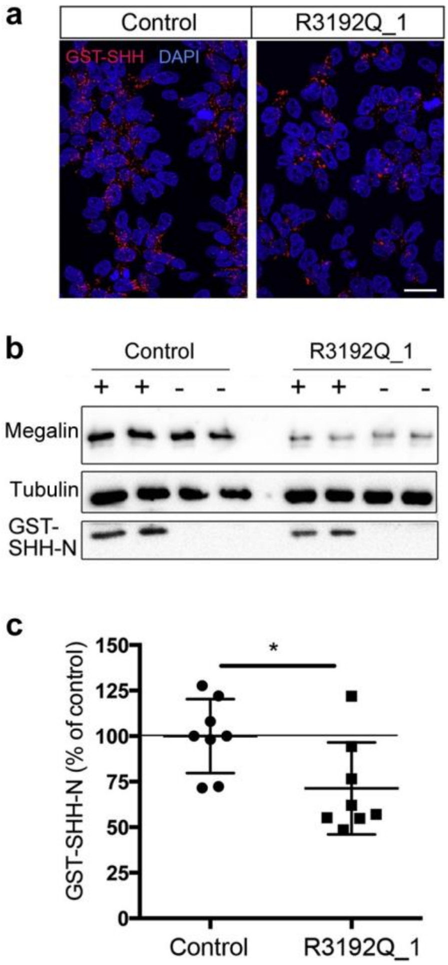

Figure 3 | Mutation c:G9575A does not impact the endocytic activity of megalin^{R3192Q}. (a) Neural precursor cells (NPCs) from a control or from patient R3192Q_1 were treated for 2 hours in medium containing 10 mg/ml recombinant GST-SHH-N. Subsequently, cells were immunostained for GST-SHH-N (red) using anti-GST antisera and counterstained with 4^0,6-diamidino-2-phenylindole (DAPI) (blue). Bar ¼ 25 mm. (b) NPCs from a control or from patient R3192Q_1 at day 9 of differentiation were treated overnight in medium with (þ) or without (–) 10 mg/ml recombinant GST-SHH-N. Thereafter, levels of megalin and GST-SHH-N in cell extracts were determined by Western blotting. Detection of a-tubulin served as loading control. (c) Quantification of GST-SHH-N uptake in control and R3192Q_1 cells by densitometric scanning of replicate Western blots (exemplified in panel b). Levels are given relative to control cells (set to 100% ± SD). The amount of internalized GST-SHH-N is significantly lower in cells from patients R3192Q_1 as compared with control cells (n ¼ 3 independent experiments, 2–4 biological replicates/experiment; Student's *t* test). **P* < 0.05. To optimize viewing of this image, please see the online version of this article at www.kidney-international.org.

R3192Q_1 was apparent and substantially higher than in receptor null cells (75% of control in Figure 3c vs. 50% of control in Supplementary Figure S5D). These findings indicated that impaired expression of megalin^{R3192Q} reduced but did not abolish the ability of NPCs to internalize receptor ligands.

SHH induces loss of megalin^{R3192Q} expression in neuroepithelial and renal cell types

Our data revealed the surprising finding that mutation R3192Q did not ablate expression or endocytic activity of megalin but impacted receptor levels by a post-transcriptional mechanism. As our differentiation protocol entailed the addition of SHH at day 5 of differentiation (Supplementary Figure S3A), we reasoned that this ligand may trigger the decline in megalin^{R3192Q} levels seen at day 9. To test this hypothesis, we used NPCs at day 5 of differentiation and incubated them with or without GST-SHH-N. The addition of ligand resulted in significantly lower megalin levels in the patient cell line R3192Q_1 (Figure 4a and b) as compared with the untreated cells. Similarly, levels of mutant megalin were also decreased on ligand exposure in the patient cell line R3192Q_2, although an increase in wild-type receptor contributed to the difference in megalin levels seen between patient 2 and control cells (Supplementary Figure S6A and B). Decreased levels of megalin^{R3192Q} in the presence of GST-SHH-N were due to a reduced half-life of the mutant re- ceptor as shown by determining protein stability in NPCs treated with cycloheximide, an inhibitor of protein translation (Figure 4c and d).

To substantiate that ligand-induced decay of megalin^{R3192Q} was also seen in renal cell types and potentially responsible for renal Fanconi syndrome in affected individuals, we applied an established protocol to differentiate iPSCs into renal proximal tubule epithelial-like cells (RPTECs)[16] (Supplementary Figure S7A). Differentiation into the proper renal cell type was documented by transient expression of mesodermal marker *T*/*Brachyury* and early proximal renal vesicle marker *JAG1*, as well as by stable induction of proximal tubule markers *AQP1* and *LRP2* (Supplementary Figure S7B). Coexpression of AQP1 and megalin in the differentiated cells was substantiated by immunocytochemistry (Supplementary Figure S7C). As shown for NPCs above, the addition of GST-SHH-N resulted in lower megalin levels in R3192Q_1 as compared with control cells (Figure 5a and b). To query whether other receptor ligands may also impact expression of megalin^{R3192Q} in RPTECs, we tested the effect of lysozyme, a protein cleared from the glomerular filtrate by megalin.[17] Contrary to SHH-N, the addition of lysozyme to the cell medium did not impact levels of megalin^{R3192Q} (Supplementary Figure S8).

Aberrant lysosomal targeting of receptor/SHH complexes induces catabolism of megalin^{R3192Q}

To explore the reasons for the reduced stability of megalin^{R3192Q} in the presence of GST-SHH-N, we studied the subcellular localization of the receptor and ligand. When the subcellular localizations of megalin and internalized GST-SHH-N were tested by immunocytochemistry in NPCs, an increased colocalization of megalin^{R3192Q} with this ligand was observed in both patients' cell lines as compared with the wild-type receptor (Figure 6a and b; Supplementary Figure S9A and B). As shown by co-

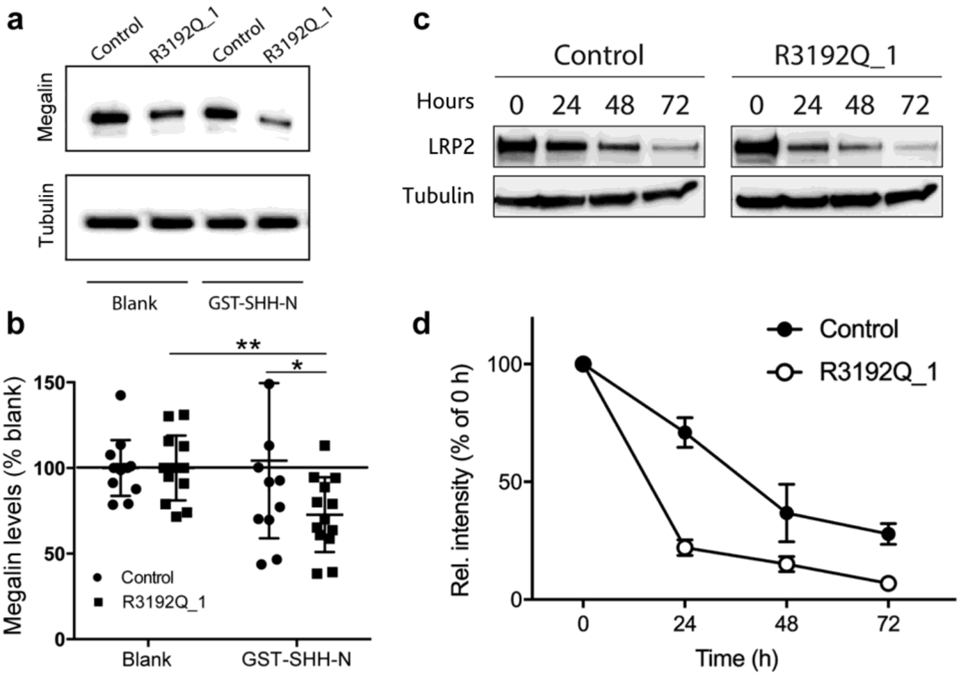

Figure 4 | The addition of SHH-N decreases stability of megalin^{R3192Q} in neural precursor cells (NPCs). (a) NPCs at day 5 of differentiation were treated with 10 mg/ml GST-SHH-N or blank medium overnight, and levels of megalin were determined in cell lysates by Western blotting thereafter. Detection of a-tubulin served as a loading control. (b) Quantification of megalin levels in control and R3192Q_1 NPC lines by densitometric scanning of replicate Western blots (exemplified in panel a). Levels are given as relative to the untreated condition (set to 100% ± SD). In the presence of GST-SHH-N, levels of megalin^{R3192Q} were significantly lower compared with that of the wild-type receptor (n ¼ 4 independent experiments, 2–3 biological replicates/experiment). This difference was not seen in the control medium (blank) lacking the receptor ligand. Statistical significance was determined using Student's *t* test. *$P < 0.05$; **$P < 0.01$. (c) Replicate layers of control and R3192Q_1 NPCs at day 5 of differentiation were treated with 10 mg/ml GST-SHH-N and 7.5 mg/ml cycloheximide. Cells were harvested at the indicated time points, and expression levels of megalin were determined by Western blotting. Detection of a-tubulin served as a loading control. (d) Megalin levels were quantified by densitometric scanning of replicate Western blots (exemplified in panel c) in control and R3192Q_1 NPCs after treatment with GST-SHH-N and cycloheximide (mean of 3 independent experiments). Receptor levels are given as a percentage of levels at time point 0 of treatment for each cell line. In the presence of a ligand, a significantly faster decay was observed for megalin^{R3192Q} as compared with the wild-type receptor ($P < 0.0001$ for genotype and time, unmatched 2-way analysis of variance).

immunostaining with lysosomal marker LAMP1, the addition of ligand provided a protective effect to wild-type megalin reducing its localization to LAMP1þ lysosomes. This protective effect was not seen with megalin^{R3192Q}, resulting in enhanced lysosomal trapping in the presence of ligand as compared with the wild-type receptor (Figure 6c and d; Supplementary Figure S9C and D). No difference in lysosomal targeting of megalin was seen between mutant and control cells when treated with GST only (Figure 6 c and d; Supplementary Figure S9C and D). Triple immunostaining substantiated enhanced colocalization of megalin^{R3192Q} and GST-SHH-N in LAMP1þ lysosomes (Figure 6e).

To further corroborate ligand-induced lysosomal catabolism of megalin^{R3192Q} as a molecular cause of DBS, we treated control and mutant NPCs with GST-SHH-N in the presence or absence of lysosomal inhibitors. Lysosomal blockade did not alter the levels of wild-type megalin, but it significantly increased levels of the mutant receptor (Figure 7). These findings further substantiated that lysosomal degradation significantly contributes to the reduced stability of megalin^{R3192Q} in DBS.

DISCUSSION

Megalin is the main endocytic receptor in the proximal convoluted tubules for bulk clearance of plasma proteins from the glomerular filtrate.6,7[17,18] Megalin-mediated clear- ance of ligands has also been shown in other absorptive epithelia, including the neural tube,4 the epididymis,[19] and the retinal pigment epithelium.5 So far, the inability to recombinantly express full-length megalin has hampered at- tempts to dissect functional domains in the receptor poly- peptide. Now, the availability of naturally occurring *LRP2* mutations in patients with DBS and the ability to recapitulate mutant phenotypes in iPSC-derived cell models significantly advance our abilities to study megalin in human health and disease. This assumption is substantiated by our studies of individuals homozygous for a novel *LRP2* mutation c:G9575A. Based on the absence of megalin in renal biopsies (Figure 1b), the inability to properly fold and express mega- lin^{R3192Q} may have been anticipated as a consequence of this mutation. However, studies in iPSC-derived cell lines docu- ment proper expression of the mutant receptor in the absence of ligands in neuroepithelial (Figure 2a and Supplementary Figure S4A) and proximal tubule (Supplementary

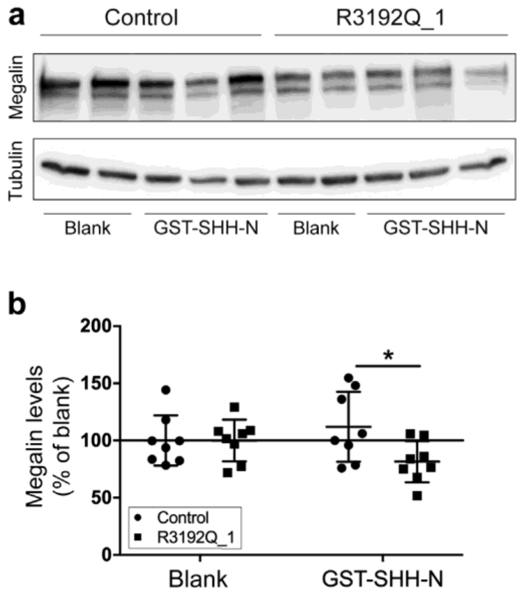

Figure 5 | Ligand-induced decay of megalin^{R3192Q} in induced pluripotent stem cell (iPSC)–derived renal proximal tubule epithelial-like cells (RPTECs). (a) Control and patient iPSC-derived RPTECs at day 8 of differentiation were treated with 10 mg/ml GST-SHH-N or blank (10 mg/ml GST) medium overnight. Subsequently, megalin levels in cell lysates were determined by Western blotting. Detection of a-tubulin served as a loading control. (b) Megalin levels in a control and R3192Q_1 RPTECs were quantified by densitometric scanning of replicate Western blots (exemplified in panel a). Levels are given as relative to the untreated condition (set at 100% ± SD). In the presence of GST-SHH-N, levels of megalin^{R3192Q} were significantly lower as compared with the wild-type receptor (n ¼ 3 independent experiments, 2–3 biological replicates/experiment). Statistical significance was determined using Student's *t* test. *$P < 0.05$.

Figure S7C) cell types. Also, the ability to perform endocytosis does not seem to be overtly impacted as judged from the ability of the mutant receptor to clear the ligands SHH-N (Figure 3) and lysozyme (Supplementary Figure S8). Rather, extended retention of receptor/ligand complexes (Figure 6a and b; Supplementary Figure S9AB and B) and enhanced accumulation of the receptor to lysosomal compartments in the presence of ligands (Figure 6c–e; Supplementary Figure S9C and D) argue for the induced decay of megalin^{R3192Q} because of an inability to properly discharge some ligands in the endocytic pathway. Blockade of lysosomal activity significantly increases levels of megalin^{R3192Q} but not of the wild-type receptor (Figure 7). This finding supports targeting to lysosomes as a factor that specifically contributes to the impaired stability of the mutant receptor in neuroepithelial and renal cells types. Remarkably, a similar mechanism has been identified as a cause of low-density lipoprotein receptor deficiency in familial hypercholesterolemia (class 5 mutations).[20] Our hypothesis is backed by the localization of R3192Q in an epidermal growth factor–type repeat, a domain required for endosomal discharge of ligands by the low-density lipoprotein receptor.[21]

Much of our cell biological studies have focused on the interaction of megalin with its ligand SHH-N in NPCs, an interaction considered crucial to the role of this receptor in the development of forebrain and eyes.3,4 Individuals homozygous for *LRP2*^{R3192Q} do not present with obvious craniofacial malformations, recapitulating earlier observations that missense mutations in *LRP2* feature mild forms or even the absence of forebrain anomalies.8,9 However, both individuals present with severe myopia (þ7 and þ9 dioptres, respectively), indicating massive overgrowth of the eyes as a consequence of potentially impaired uptake of SHH-N[3] and other megalin ligands5 in the retinal pigment epithelium. Although aberrant targeting of megalin^{R3192Q} to lysosomes has only been shown directly in NPCs, the ability of SHH-N to induce the decay of the mutant receptor in iPSC-derived RPTECs strongly argues that a similar disease mechanism is operable in the kidney and responsible for renal Fanconi syndrome in this family with DBS.

As megalin acts as a high-capacity clearance receptor for numerous ligands in the renal proximal tubule, the question remains whether only SHH-N or also other receptor ligands destine megalin^{R3192Q} to lysosomal catabolism. Conceivably, the induced decay of the mutant receptor may be caused by ligands, which binding sites are altered by c:G9575A, but not by others not impacted by this mutation. In our hands, lysozyme did not decrease the stability of the mutant receptor in RPTECs (Supplementary Figure S8), documenting that the proposed disease mechanism is not applicable to every ligand. Unfortunately, little is known about the exact binding sites for SHH, lysozyme, or most other receptor ligands that may guide our choice of alternative ligands to be tested. Still, irrespective of the number of ligands that may cause the lysosomal decay of megalin^{R3192Q}, our findings highlight an important new concept in receptor cell biology, relevant for pathophysiology of the kidney and other tissues that require the endocytic activity of megalin.

METHODS

Patient information

The patients are son and daughter of apparently unrelated parents originating from the same small town in Italy. They were diagnosed with proteinuria when aged 7 and 9 years, respectively. The brother presented first, after discovering proteinuria in a spot urine analysis (30 mg/dl) performed during a varicella zoster infection. Further investigations revealed mild kidney insufficiency (estimated glomerular filtration rate: 86 ml/min per 1.73 m^2), increased urinary protein/creatinine ratio (1.35 mg/mg [n.v. < 0.2 mg/mg]), hypercalciuria (urinary calcium/creatinine ratio: 0.31 mg/mg [n.v. < 0.2 mg/mg]), and abnormal urinary excretion of low-molecular-weight proteins (urinary beta 2 microglobulin/creatinine ratio: 0.48 mg/mg [n.v. absent]). Other tests showed normal serum bicarbonate levels, normal renal phosphate handling (serum phosphate: 5.1 mg/dl [n.v. > 3.5 mg/dl]; TmP/GFR: 4.2 mg/dl [n.v. > 2.9 mg/dl]), and normal excretion of amino acids, glucose, uric acid, sodium, and magnesium. The urine sediment was normal. Renal ultrasound showed normal sized kidneys (approximately 10th percentile), with very mild hyperechogenicity. The physical examination was unremarkable, except for

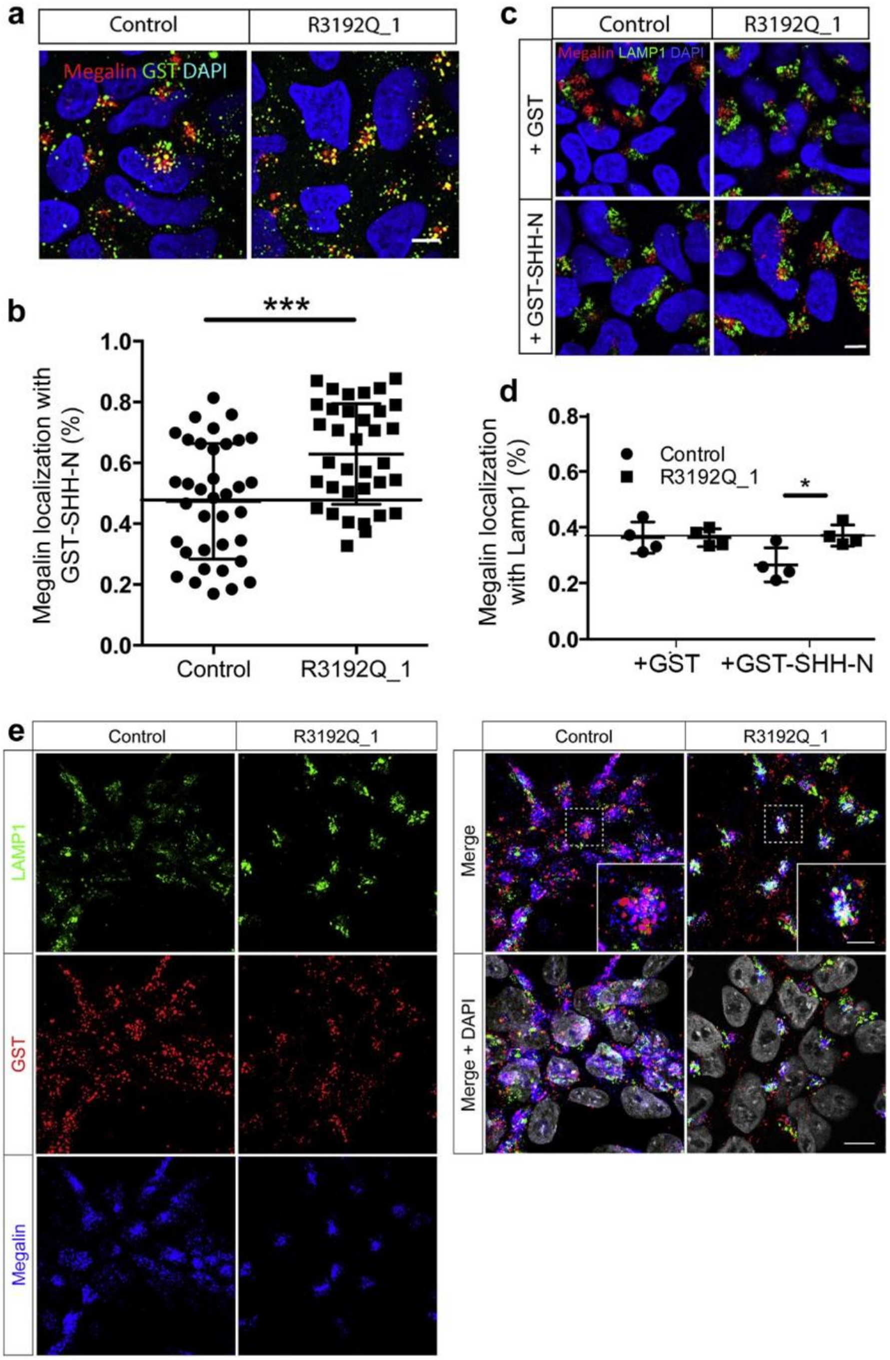

Figure 6 | Binding of GST-SHH-N directs megalin^{R3192Q} to lysosomes. (a) Immunofluorescence detection of megalin (red) and GST-SHH-N (green) in control and patient neural precursor cells (NPCs) at day 7 of differentiation treated with 10 mg/ml GST-SHH-N for 2 hours. Cells were counterstained with 4^0,6-diamidino-2-phenylindole (DAPI) (blue). Bar ¼ 8 mm. (b) Extent of colocalization of megalin with GST-SHH-N as determined by Mander's colocalization coefficient is increased for megalin^{R3192Q} as compared with wild-type megalin, suggesting the prolonged interaction of the mutant receptor with its ligand. One representative experiment is shown with data given as mean ± SD. This experiment was repeated 4 times with 25–40 cells/experiment analyzed. All 4 experiments showed statistical significance (Student's *t* test). ***$P < 0.0001$. (c) Immunofluorescence detection of megalin (red) and lysosomal marker LAMP1 (green) in control and patient NPCs at day 7 of differentiation treated with 10 mg/ml GST or GST-SHH-N for 2 hours. Cells were counterstained with DAPI. Bar ¼ 8 mm. (d) Mander's colocalization coefficient documents increased colocalization of megalin^{R3192Q} with LAMP1 in NPCs treated with GST-SHH-N (but not GST) as compared with wild-type megalin (n ¼ mean of 4 experiments with 15–40 cells/experiment analyzed ± SD; Student's *t* test). (e) Immunodetection of lysosomal marker LAMP1 (green), GST-SHH-N (red), and megalin (blue) in control and patient NPCs at day 7 of differentiation. Cells were treated with 10 mg/ml GST-SHH-N for 2 hours and counterstained with DAPI (gray). Bar ¼ 10 mm. Higher magnifications of overview pictures are given as insets (bars ¼ 4 mm). Increased colocalization of megalin with GST-SHH-N in LAMP1þ lysosomal vesicles (white signals) was noted in patient as compared with control NPC lines. To optimize viewing of this image, please see the online version of this article at www.kidney-international.org.

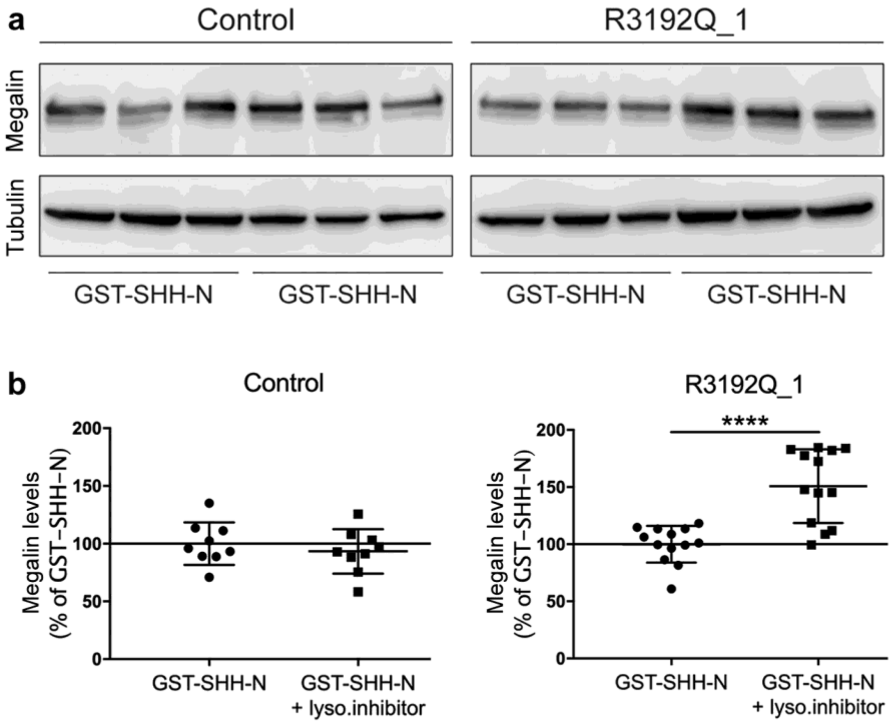

Figure 7 | Inhibition of lysosomal proteases prevents the ligand-induced decay of megalin^{R3192Q}. (a) Neural precursor cells (NPCs) at differentiation day 5 were treated overnight with 10 mg/ml GST-SHH-N in the absence or presence of lysosomal protease inhibitors (þ lyso. inhibitor; see Supplementary Methods for details). Subsequently, megalin levels in cell lysates were determined by Western blotting. Detection of a-tubulin served as a loading control. (b) Quantification of megalin levels in control and R3192Q_1 NPCs by densitometric scanning of replicate Western blots (exemplified in panel a). Levels are given relative to GST-SHH-N without lysosomal inhibitors (set to 100% ± SD). Treatment with lysosomal inhibitors significantly increased levels of megalin^{R3192Q} as compared with nontreated cells (right panel). No effect of lysosomal inhibition was seen on levels of the wild-type receptor in control NPCs (left panel) (n ¼ 4 independent experiments, 2–3 biological replicates/experiment). Statistical significance was determined using Student's *t* test. ****$P < 0.0001$.

severe bilateral myopia (þ7 dioptres). His sister was diagnosed at age 9 by family screening. Her renal function was normal (estimated glomerular filtration rate: 93 ml/min per 1.73 m^2). Urine evaluation showed similar findings to her brother, including high urinary protein/creatinine ratio (2.26 mg/mg), abnormal urinary excretion of low-molecular-weight proteins (urinary beta 2 microglobulin/creatinine ratio: 1.31 mg/mg), and mild hypercalciuria (urinary calcium/creatinine ratio: 0.25 mg/mg). A small phosphate leak was also noticed (serum phosphate: 3.4 mg/dl; TmP/GFR: 2.7 mg/dl) without evidence of hyperparathyroidism (intact parathyroid hormone 31 pg/ml). No other serum or urinary abnormalities were noticed. Renal ultrasound showed normal sized kidneys (approximately 50th percentile) with discrete cortical hyperechogenicity. Her physical examination showed normal blood pressure and was significant for severe bilateral myopia (þ9 dioptres), short stature (height SD: –2.13), and mild overweight (body mass index: 26.7).

Analysis of human specimen and cell lines

The study of human specimens and cell lines was approved by the Ethics Committee of Ospedale Pediatrico Bambino Gesù (approval no.: 1235_OPBG_2016). All subjects gave written informed consent before participating in this study. Generation of iPSCs was performed using the CytoTune-iPS 2.0 Sendai Reprogramming Kit. Differentiation of iPSCs to NPCs or RPTECs was performed according to published protocols[13,16] and detailed in Supplementary Methods. Differentiation into the 3 germ layers was carried out using a commercial kit according to the supplier's recommendations (Trilineage Differentiation Kit, Miltenyi Biotec, Bergisch Gladbach, Germany, No. 130-115-660). Immunodetection of megalin in renal biopsies and documentation of urinary loss of receptor ligands in spot urine of patients and control subjects shown here were performed as reported earlier.[11]

Cell studies

Studies were conducted in NPCs or RPTECs using the experimental conditions described in the respective figure legends. GST and GST-SHH-N used as ligands were affinity purified from bacterial cultures using glutathione affinity chromatography as described previously.[4] Lysozyme purified from hen egg white was obtained commercially (Abcam, Cambridge, UK, 10837059001). Experimental details for immunodetection of proteins using Western blotting or immunocytochemistry are given in the Supplementary Methods section.

Quantitative real-time polymerase chain reaction

Total RNA was extracted from cell cultures using the RNeasy Mini Kit (QIAGEN, Hilden, Germany) according to the manufacturer's instructions with an additional step of treating the RNA with RNase-free DNase I for 15 minutes at room temperature. RNA (500 ng to 1 mg) was reverse transcribed using the High Capacity RNA to cDNA Kit (Applied Biosystems, Foster City, CA). For cDNA amplification, TaqMan-Oligonucleotide probes were used with the TaqMan Gene Expression Master Mix (Applied Biosystems) on a 7900 HT Fast Real time PCR System (Thermo Fisher Scientific, Waltham, MA) and the Sequence detection system V2.4 (Thermo Fisher Scientific). Results were analyzed using the comparative cycle threshold method normalized to *GAPDH*.[22]

Statistical analysis

All statistical analysis was performed using the GraphPad Prism 7.0 software (San Diego, CA). The applied statistical tests are indicated in the respective figure legend. Data are presented as mean ± SD. To determine the degree of colocalization between megalin and LAMP1 or GST-SHH-N, images with comparable background were taken for analysis and background correction was performed. Images were converted to 8-bit pixel images and individual cells were automatically outlined to define a region of interest. ImageJ was used to assess the Mander's colocalization coefficient, indicating the fraction of megalin colocalizing with LAMP1 or GST-SHH-N.[23]

DISCLOSURE

FE is a consultant to Otsuka Pharmaceuticals and Kiowa Kirin Pharmaceuticals. All the other authors declared no competing interests.

ACKNOWLEDGMENTS

The authors are indebted to Christine Kruse, Kristin Kampf, and Norman Krüger for expert technical assistance. The authors also acknowledge the Wellcome Trust Sanger Institute as the source of human induced pluripotent cell line HPSI1113i-wetu_2, which was generated under the human iPSC Initiative funded by a grant from the Wellcome Trust and the Medical Research Council, supported by the Wellcome Trust (WT098051) and the NIHR/Wellcome Trust Clinical Research Facility, and acknowledge Life Science Technologies Corporation as the provider of Cytotune.

SUPPLEMENTARY MATERIAL

Supplementary File (PDF)

Supplementary Methods.

Supplementary References.

Figure S1. Karyotypes of iPSC lines from patients with Donnai-Barrow syndrome.

Figure S2. Pluripotency markers and differentiation potential of iPSCs from Donnai-Barrow patients.

Figure S3. Neuroectodermal differentiation of iPSC lines from Donnai-Barrow patients.

Figure S4. Megalin^{R3192Q} expression is impaired post-transcriptionally in a second patient.

Figure S5. Generation of iPSCs genetically deficient for *LRP2.*

Figure S6. Ligand-induced decay of megalin^{R3192Q} in NPCs from a second patient.

Figure S7. Differentiation of iPSCs into renal proximal tubular epithelial-like cells.

Figure S8. Lysozyme does not induce decay of megalin^{R3192Q} in RPTECs.

Figure S9. Binding of GST-SHH-N directs megalin^{R3192Q} to lysosomes in NPCs from a second patient.

REFERENCES

1. Kantarci S, Al-Gazali L, Hill RS, et al. Mutations in LRP2, which encodes the multiligand receptor megalin, cause Donnai-Barrow and facio-oculo-acoustico-renal syndromes. *Nat Genet*. 2007;39:957–959.
2. Pober BR, Longoni M, Noonan KM. A review of Donnai-Barrow and facio-oculo-acoustico-renal (DB/FOAR) syndrome: clinical features and differential diagnosis. *Birth Defects Res A Clin Mol Teratol*. 2009;85:76–81.
3. Christ A, Christa A, Klippert J, et al. LRP2 acts as SHH clearance receptor to protect the retinal margin from mitogenic stimuli. *Dev Cell*. 2015;35:36–48.
4. Christ A, Christa A, Kur E, et al. LRP2 is an auxiliary SHH receptor required to condition the forebrain ventral midline for inductive signals. *Dev Cell*. 2012;22:268–278.
5. Cases O, Obry A, Ben-Yacoub S, et al. Impaired vitreous composition and retinal pigment epithelium function in the FoxG1::LRP2 myopic mice. *Biochim Biophys Acta Mol Basis Dis*. 2017;1863:1242–1254.
6. Verroust PJ, Birn H, Nielsen R, et al. The tandem endocytic receptors megalin and cubilin are important proteins in renal pathology. *Kidney Int*. 2002;62:745–756.
7. Christensen EI, Birn H. Megalin and cubilin: multifunctional endocytic receptors. *Nat Rev Mol Cell Biol*. 2002;3:256–266.
8. Schrauwen I, Sommen M, Claes C, et al. Broadening the phenotype of LRP2 mutations: a new mutation in LRP2 causes a predominantly ocular phenotype suggestive of Stickler syndrome. *Clin Genet*. 2014;86:282–286.
9. Anglani F, Terrin L, Brugnara M, et al. Hypercalciuria and nephrolithiasis: expanding the renal phenotype of Donnai-Barrow syndrome. *Clin Genet*. 2018;94:187–188.
10. Longoni M, Kantarci S, Donnai D, Pober BR. Donnai-Barrow Syndrome. Published August 28, 2008. Updated November 21, 2018. In: Adam MP, Ardinger HH, Pagon RA, et al., eds. *GeneReviews* [Internet]. Seattle, WA: University of Washington; 1993–2020. Available at: https://www.ncbi.nlm.nih.gov/books/NBK1878/. Accessed May 3, 2020.
11. Storm T, Tranebjaerg L, Frykholm C, et al. Renal phenotypic investigations of megalin-deficient patients: novel insights into tubular proteinuria and albumin filtration. *Nephrol Dial Transplant*. 2013;28:585–591.
12. Dachy A, Paquot F, Debray G, et al. In-depth phenotyping of a Donnai-Barrow patient helps clarify proximal tubule dysfunction. *Pediatr Nephrol*. 2015;30:1027–1031.
13. Chambers SM, Fasano CA, Papapetrou EP, et al. Highly efficient neural conversion of human ES and iPS cells by dual inhibition of SMAD signaling. *Nat Biotechnol*. 2009;27:275–280.
14. Assemat E, Chatelet F, Chandellier J, et al. Overlapping expression patterns of the multiligand endocytic receptors cubilin and megalin in the CNS, sensory organs and developing epithelia of the rodent embryo. *Gene Expr Patterns*. 2005;6:69–78.
15. McCarthy RA, Barth JL, Chintalapudi MR, et al. Megalin functions as an endocytic sonic hedgehog receptor. *J Biol Chem*. 2002;277:25660–25667.
16. Hariharan K, Stachelscheid H, Rossbach B, et al. Parallel generation of easily selectable multiple nephronal cell types from human pluripotent stem cells. *Cell Mol Life Sci*. 2019;76:179–192.
17. Leheste JR, Rolinski B, Vorum H, et al. Megalin knockout mice as an animal model of low molecular weight proteinuria. *Am J Pathol*. 1999;155:1361–1370.
18. Nykjaer A, Dragun D, Walther D, et al. An endocytic pathway essential for renal uptake and activation of the steroid 25-(OH) vitamin D3. *Cell*. 1999;96:507–515.
19. Morales CR, Zeng J, El Alfy M, et al. Epithelial trafficking of Sonic hedgehog by megalin. *J Histochem Cytochem*. 2006;54:1115–1127.
20. Hobbs HH, Brown MS, Goldstein JL. Molecular genetics of the LDL receptor gene in familial hypercholesterolemia. *Hum Mutat*. 1992;1:445–466.
21. van der Westhuyzen DR, Stein ML, Henderson HE, et al. Deletion of two growth-factor repeats from the low-density-lipoprotein receptor accelerates its degradation. *Biochem J*. 1991;277(Pt 3):677–682.
22. Schmittgen TD, Livak KJ. Analyzing real-time PCR data by the comparative C(T) method. *Nat Protoc*. 2008;3:1101–1108.
23. Dunn KW, Kamocka MM, McDonald JH. A practical guide to evaluating colocalization in biological microscopy. *Am J Physiol Cell Physiol*. 2011;300:C723–C742.

SUPPLEMENTARY METHODS

Generation of induced pluripotent stem cells

Human induced pluripotent stem cell line HPSI1113i-wetu_2 used as a control line was kindly provided by the Wellcome Trust Sanger Institute, UK. Generation of iPSCs from patients was performed using the CytoTune®-iPS 2.0 Sendai Reprogramming Kit. In brief, $2x10^5$ cells/cm^2 were transduced with the non-transmissible Sendai virus harbouring the genetic factors SOX2, KLF4, OCT4 and c-MYC in the presence of 10 µg/ml Polybrene. Subsequently, the cells were cultured in StemPro®-34SFM medium supplemented with StemPro®-34 Nutrient Supplement, 2 mM glutamine, 100 ng/ml stem cell factor, 100 ng/ml fms-like tyrosine kinase 3, 20 ng/ml interleukin-3, 20 ng/ml interleukin-6 and 2 U/ml erythropoietin. After two days, the transduced cells were transferred onto Matrigel-coated plates and the medium was successively switched from StemPro®-34SFM medium supplemented with StemPro®-34 Nutrient Supplement and 2 mM glutamine to Essential 7 (E7) medium (DMEM/F12, 64 µg/ml L-ascorbic acid 2-phosphate, 20 µg/ml insulin, 5 µg/ml transferrin, 14 ng/ml sodium selenite, 100 ng/ml fibroblast growth factor 2), and finally to Essential 8 (E8) medium (E7 medium with 2 ng/ml transforming growth factor ß1). Ultimately, the cells were cultured in E8 medium. Undifferentiated colonies were picked and cultured in E8 supplemented with 10 µg/ml Y27632.

For experimentation, all iPSC lines were cultured on Matrigel-coated culture dishes in Essential 8 medium. The culture medium was changed daily. Cells were recovered and passaged at a density of 70 – 80% using accutase or 0.5M EDTA/DPBS. For SNP karyotyping, iPSC pellets were resuspended in 200 µl of PBS and genomic DNA was isolated using the DNeasy blood and tissue kit (Qiagen, Valencia, CA). DNA samples were SNP karyotyped using the Infinium OmniExpressExome-8 Kit and the iScan system from Illumina. CNV and SNP visualization were performed using KaryoStudio v1.4 (Illumina).

Sequencing

To verify the presence of the *LRP2* mutation in patient-derived iPSC lines, primer were generated using the DNAStar Seqbuilder Software Version 13.0.0 that flank the mutation at position c:G9575A. Primer sequences were as follows:

LRP2fw: AAGCTCATGTCTGACAAGCGGACT,

LRP2rev: TACAATCTCTTCTCTACTCGGTC.

The Phire Animal Tissue Direct PCR kit (Thermo Fisher Scientific) was used to amplify a genomic DNA fragment containing the *LRP2* mutation. The PCR products were purified using the ExoSAP-IT^{Tm}PCR Product Cleanup reagent (Thermo Fisher Scientific). DNA sequencing was performed by LGC Genomics GmbH (Germany) and data analysed using the DNAStar SeqMan Software Version 13.0.0.

LRP2 gene disruption in iPSCs

The deletion of *LRP2* gene in human iPSC line HPSI1113i-wetu_2 was achieved by using the CRISPR/Cas9 system. Single guide RNA (sgRNA) targeting the start codon of *LRP2* gene was designed using the online software tool provided by Zhang lab (crispr.mit.edu). sgRNA sequences were as follows: sense: CCGTCGCGGAGATGGATCGC and antisense: GCGATCCATCTCCGCGACGG. Annealed sgRNA oligonucleotides were cloned into the expression vector pSpCas9(BB)-2A-GFP (PX458, Addgene plasmid #48138) following digesting with FastDigest BbsI (Thermo Fisher Scientific). Human iPSCs were transfected with the final sgRNA-plasmid construct using Lipofectamine3000 (Thermo Fisher Scientific) according to manufacturer's protocol. Transfected cells were selected with 0.1 µg/ml puromycin for one week before seeding them at low density for single cell colony expansion. Clones were analyzed for successful deletion using the Phire Animal Tissue Direct PCR kit. Primer sequences used were: LRP2KOfw: AGGGCTTTATGCACTGTCTGG; LRP2KOrev: AGGCTCTGGCTGGGCTCTT. DNA sequencing to confirm genome editing was performed by LGC Genomics GmbH and data analyzed using the DNAStar SeqMan Software Version 13.0.0.

Differentiation of iPSCs to NPCs

The neuroectodermal differentiation protocol was adapted from a published protocol [1]. In detail, iPSCs were dissociated with accutase to single cell suspension and 20.000 cells/cm^2 plated on Matrigel-coated dishes in E8 medium supplemented with 10 µg/ml of Rock inhibitor Y27632. Cells were allowed to grow for 3 days until they were nearly confluent, after which the medium was changed to N2B27 differentiation medium containing 100 ng/ml noggin, 200 nM dorsomorphin (inhibitor of the bone morphogenetic/activin pathway) and 10 µM SB431542 (inhibitor of transforming growth factor ß/activin pathway). Medium change was performed daily. At day 5, the medium was replaced by N2B27 containing noggin, dorsomorphin, and 200 ng/ml sonic hedgehog, and cells were grown for up to 4 more days. For rosette formation, cells were re-plated at day 5 at high density (1:2) on Matrigel-coated plates and fixed at day 7 for immunocytochemistry.

Differentiation of iPSC to RPTECs

The differentiation protocol was adapted from [2]. Briefly, iPSCs were dissociated into single cells using accutase and 10.000 cells/cm^2 were plated on Matrigel-coated dishes in E8 medium supplemented with 10 µg/ml Rock inhibitor Y27632. When cells reached 75-80% confluence depicted as day 0 of differentiation, medium was changed to STEMdiff™ APEL™ 2 medium (Stem Cell Technologies) supplemented with 10 ng/ml Activin A, 30 ng/ml BMP4 and 1 µM retinoic acid to induce mesodermal fate. At day 4, medium was changed to APEL supplemented with 150 ng/ml GDNF to induce renal vesicle differentiation. Upon differentiation day 8, renal epithelial growth medium (REGM, Lonza) was utilized for tubular epithelial specification. During the course of differentiation, medium was replaced every other day.

Fluorescence immunocytochemistry

Cells were fixed in 4% paraformaldehyde for 10 minutes at room temperature, washed with PBS, blocked and permeabilised in PBS containing 0.2% gelatine, 0.1% saponin and 5 mg/ml BSA for 10 minutes. Primary antibodies were diluted in washing solution (PBS containing 0.2% gelatine and 0.01% saponin) and cells incubated over night at 4°C. Then, the cells were washed with washing solution and incubated with the secondary antibodies coupled to Alexa fluorophores for 1 hour at room temperature. Cells were mounted in Prolong Diamond Antifade Mountant containing DAPI (Thermo Fisher Scientific). Antibodies used were directed against OCT4 (Abcam, ab19857; 1:100), SOX2 (Abcam, ab97959; 1:100), Nanog (R&D, 1:100), SSEA4 (Abcam, ab16287; 1:100), megalin (produced in-house; 1:250), LAMP1 (Cell Signaling, 9091P; 1:700), GST (Cell Signaling, 624S; 1:100), PAX6 (BioLegend, 9019301; 1:100), SOX1 (Abcam, ab109290; 1:100), and AQP1 (Proteintech, 20333-1-AP, 1:100). For assessing germ layer differentiation, the human germ layer 3-Color Immunocytochemistry kit (R&D) was used.

Ligand treatment

For analysis of ligand impact on megalin activity, cells were starved in blank medium for 2 hours before addition of 10 µg/ml GST-SHH-N or GST, or 20 µg/ml lysozyme in DMEM/1.5% BSA. After ligand incubation for the time points indicated in the respective figure legends, cells were either fixed in 4% paraformaldehyde for immunofluorescence analysis or lysed for western blotting. Antibodies used for Western blotting were goat anti-rabbit megalin (produced in-house; 1:500), anti-GST (Cell Signaling; 624S, 1:1000), anti-lysozyme (Abcam, ab391, 1:500), and anti-tubulin (Calbiochem; CP06, 1:1000).

Cycloheximide experiments

To determine megalin stability, replicate layers of cells were treated with 10 µg/ml GST-SHH-N and 7.5 µg/ml cycloheximide in N2B27 medium from day 5 of neuroectodermal differentiation onwards. During incubation time, the cell culture medium with freshly added ligand and cycloheximide was changed daily. Cells were lysed for analysis of megalin levels by western blotting at the indicated time points.

Lysosomal inhibition

Replicate cell layers were differentiated into NPCs until day 5. Activity of lysosomal proteases was blocked by adding a cocktail of 100 µM leupeptin, 10 µM pepstatin and 50 µM chloroquine for 1 hour. Afterwards, cells were incubated with 10 µg/ml GST-SHH-N and lysosomal inhibitors overnight before analyzing megalin levels by western blotting.

SUPPLEMENTARY REFERENCES

1. Chambers SM, Fasano CA, Papapetrou EP, *et al.* Highly efficient neural conversion of human ES and iPS cells by dual inhibition of SMAD signaling. *Nat Biotechnol* 2009; **27:** 275-280.

2. Hariharan K, Stachelscheid H, Rossbach B, *et al.* Parallel generation of easily selectable multiple nephronal cell types from human pluripotent stem cells. *Cell Mol Life Sci* 2019; **76:** 179-192.

SUPPLEMENTARY FIGURE LEGENDS

Figure S1: Karyotypes of iPSC lines from patients with Donnai-Barrow syndrome

(A, B) Chromosome 2 ideogram from peripheral blood mononuclear cells (PBMC) of patients R3192Q_1 (A) and R3192Q_2 (B). The logR ratio (red data points) depicts single nucleotide polymorphism intensity signals indicative of potential duplications or deletions in this chromosome locus. The B allele frequency (blue data point) gives the relative frequency of one allele compared to the other. Both patients are characterized by CN-LOH at 2q23.3-q31.1 encompassing *LRP2*. **(C, D)** Virtual karyotypes of PBMC and iPSC from patients R3192Q_1 (C) and R3192Q_2 (D). Insertions (green), deletions (red), and regions with copy neutral loss of heterozygosity (CN-LOH; grey) are indicated.

Figure S2: Pluripotency markers and differentiation potential of iPSCs from Donnai-Barrow patients

(**A**) Bright field images and immunocytochemical detection of pluripotency markers OCT4 (red), SOX2 (red), NANOG (red), and SSEA4 (green) in iPSCs from patients R3192Q_1 and R3192Q_2 compared to control cells. Cells were counterstained with DAPI (blue). Scale bars: 100 µm (bright field) or 25 µm (immunostainings). **(B)** Quantitative (q) RT-PCR analysis of the indicated pluripotency markers in patient and control iPSCs. Data are depicted as ct values normalized to transcript levels of *GAPDH* (Δct ± SD) as internal control. This experiment was performed in 3 independent biological replicates. No statistically significant differences in transcript levels of these pluripotency markers were seen comparing cell lines (Student's *t*-test). (**C**) iPSCs were differentiated into the three germ layers and differentiation assessed by immunocytochemical detection of ectoderm marker OTX2 (red) and SOX2 (red), endoderm marker GATA4 (green) and SOX17 (red), as well as mesoderm marker HAND1 (red). Cells were counterstained with DAPI (blue). Scale bar: 10 µm. (**D**) qRT-PCR analysis of the indicated markers in differentiated patient and control cells as exemplified in (C). Data are depicted as ct values normalized to internal *GAPDH* transcript levels (Δct ± SD). This experiment was performed in 3 independent biological replicates. No statistically significant differences in transcript levels of these marker genes were seen comparing cell lines (Student's *t*-test).

Figure S3: Neuroectodermal differentiation of iPSC lines from Donnai-Barrow patients

(A) Protocol for neuroectodermal differentiation of iPSCs to neural progenitor cells (NPCs). The protocol used was adapted from [1] (see supplementary methods for details). **(B, C)** Immunocytochemical detection of early neuroectodermal markers PAX6 (green; B) and SOX1 (green; C) in iPSC lines from patients R3192Q_1 and R3192Q_2 as compared to control cells at day 2, 5, and 9 of differentiation. Cells were counterstained with DAPI (blue). Scale bar: 25 µm. **(D, E)** Quantitative RT-PCR analysis of the pluripotency marker *OCT4* and early neuroectodermal marker *PAX6* in iPSCs from patients R3192Q_1 (D) and R3192Q_2 (E) as compared to control cells at day 2, 5, and 9 of differentiation. Data are depicted as Δct values normalized to the mean of the control cells at day 0 (ΔΔct) ± SD (n=1-4 experiments with 2-3 biological replicates/experiment). Statistical analysis was determined by Two-way Anova. No statistically significant differences were found using Bonferroni post-test comparing genotypes at the given time points.

Figure S4: Megalin^{R3192Q} expression is impaired post-transcriptionally in a second patient

(**A**) Immunodetection of megalin (red) in iPSCs from control and Donnai-Barrow patient R3192Q_2 at the indicated time points of neuroectodermal differentiation. Cells were counterstained with DAPI (blue). Megalin expression is induced from day 5 onwards in both genotypes. At day 9, megalin levels are decreased in patient-derived NPCs as compared to control cells. Scale bar: 10 µm. (**B**) Transcript levels of *LRP2* during differentiation were analyzed in iPSCs from a control subject and patient R3192Q_2. Data are depicted as Δct normalized to day 0 of the control cells (ΔΔct) ± SD (n=1 experiment with 2 biological replicates per genotype). Statistical analysis was performed by Two-way Anova with a Bonferroni post-test. **, p<0.01 (**C**) Representative western blot analysis of megalin levels in control and R3192Q_2 iPSC lines at the indicated time points of differentiation. Detection of tubulin served as loading control. (**D**) Megalin levels were quantified by densitometric scanning of replicate western blots (as exemplified in panel C) in control and R3192Q_2 NPCs at day 5 and at day 9 of neuronal differentiation (n=3 independent experiments with 3 biological replicates/experiment). Values are given as relative levels of expression compared to control (set to 100% ± SD). Megalin levels in R3192Q_2 cells are comparable to control cells at day 5, but significantly decreased at day 9 of differentiation. Statistical significance was determined by Student´s *t*-test. ****, p<0.0001. **(E)** Quantitative RT-PCR analysis of *LRP2* transcript levels in control and R3192Q_2 NPCs cells at day 5 and 9 of differentiation. (n=3 independent experiments with 3 biological replicates/experiment). Levels are depicted as ct values normalized to transcript levels of *GAPDH* (Δct ± SD) used as internal control. Transcript levels for *LRP2* are unchanged comparing the two genotypes as determined by Student´s *t*-test.

Figure S5: Generation of iPSCs genetically deficient for *LRP2*

(A) Sequence analysis showing homozygosity for a 13 nucleotides deletion including the ATG start codon (highlighted in blue) in a $LRP2^{-/-}$ cell clone derived from the parental control cell line ($LRP2^{+/+}$) by CRISPR/Cas9-mediated genome editing (see supplementary methods for details). Sequences for cell lines $LRP2^{-/-}$ and $LRP2^{+/+}$were aligned to the *LRP2* reference sequence given above (NCBI Reference Sequence: NM_004525.2). (**B**) NPCs from cell lines $LRP2^{-/-}$ and $LRP2^{+/+}$ at day 9 of differentiation were treated overnight in medium containing

10 µg/ml recombinant GST-SHH-N. Thereafter, levels of megalin and GST-SHH-N in cell lysates were analyzed by western blotting. Two biological replicates are shown for each cell line. Detection of tubulin served as loading control. Expression of megalin is readily detected in control cells but absent from the receptor null clone *LRP2*$^{-/-}$. (**C**) NPCs from cell lines *LRP2*$^{-/-}$ and *LRP2*$^{+/+}$ at day 7 of differentiation were treated for 2 h in medium containing 10 µg/ml recombinant GST-SHH-N. Subsequently, the cells were immunostained for GST-SHH-N (red) using anti-GST antisera and counterstained with DAPI (blue). Scale bar: 25 µm. (**D**) Uptake of GST-SHH-N in NPCs from cell lines *LRP2*$^{-/-}$ and *LRP2*$^{+/+}$ at day 9 of differentiation was quantified by densitometric scanning of replicate western blots (as exemplified in panel B). Levels are given relative to control cells (set to 100% ± SD). The amount of internalized GST-SHH-N is significantly lower in *LRP2*$^{-/-}$ cells as compared to control cells (n= 2 independent exemplary experiments, 1-2 biological replicates/experiment; Student´s *t*-test). **, p<0.01.

Figure S6: Ligand-induced decay of megalin^{R3192Q} in NPCs from a second patient

(A) NPCs at day 5 of differentiation were treated with 10 µg/ml GST-SHH-N or blank medium overnight and levels of megalin were determined in cell lysates thereafter. Detection of α-tubulin served as loading control. **(B)** Quantification of megalin levels in control and R3192Q_2 NPC lines by densitometric scanning of replicate western blots (as exemplified in panel A). Levels are given as relative to the untreated condition (set at 100% ± SD). In the presence of GST-SHH-N, levels of megalin^{R3192Q} were significantly lower compared to that of the wild-type receptor (n= 4 independent experiments, 2-3 biological replicates/experiment). This difference was not seen in control medium (blank) lacking the receptor ligand. Statistical significance was determined using Student´s *t*-test. *, p<0.05.

Figure S7: Differentiation of iPSCs into renal proximal tubular epithelial-like cells

(A) Protocol for differentiation of iPSCs into renal proximal tubular epithelial-like cells (RPTECs). The protocol was adapted from [2]. **(B)** Quantitative RT-PCR analysis of mesodermal marker *T*/*Brachyury*, renal vesicle marker *JAG1*, proximal tubule marker *AQP1*, and *LRP2* in iPSCs from R3192Q_1 as compared to control cells at day 4, 8, 10, 12 and 14 of differentiation. Data are depicted as Δct values normalized to control cells at day 0 (ΔΔct ± SD; n=3 experiments). Statistical analysis was performed by Two-way Anova with Bonferroni post-test. No statistically significant differences in gene transcript levels were seen comparing genotypes. **(C)** Immunofluorescence detection of aquaporin-1 (AQP1, green) and megalin (red) in control and R3192Q_1 cells at day 10 of differentiation. Cells were counterstained with DAPI (blue). Scale bar: 10 μm.

Figure S8: Lysozyme does not induced decay of megalin^{R3192Q} in RPTECs

(A) Control and iPSC-derived RPTECs at differentiation day 8 were treated with 20 μg/ml lysozyme or with blank medium overnight. Subsequently, megalin levels were determined by western blotting of cell lysates. Detection of α-tubulin served as loading control. **(B)** Megalin levels in control and R3192Q_1 were quantified by densitometric scanning of replicate western blots (exemplified in panel A). Levels are given as relative to the untreated condition (set at 100% ± SD). No statistical significance of data was seen with blank or lysozyme-treatment condition comparing the two genotypes (n=3 independent experiments, 2-3 biological replicates/experiment; Student's *t*-test).

Figure S9: Binding of GST-SHH-N directs megalin^{R3192Q} to lysosomes in NPCs from a second patient

(A) Immunofluorescence detection of megalin (red) and GST-SHH-N (green) in control and patient NPCs at day 7 of differentiation. Cells were treated with 10 µg/ml GST-SHH-N for 2 hours. Scale bar: 8 µm. **(B)** Co-localization of megalin with GST-SHH-N as determined by Mander's co-localization coefficient is increased for megalin^{R3192Q} as compared to wild-type megalin, suggesting prolonged interaction of the mutant receptor with ligands. One representative experiment is shown with data given as mean ± SD. This experiment was repeated 4 times with 25-40 cells/experiment analyzed. Two experiments showed statistical significance and one experiment a clear trend (Student's *t* test). *, p<0.05. **(C)** Immunofluorescence detection of megalin (red) and lysosomal marker LAMP1 (green) in control and patient NPC at day 7 of differentiation. Cells were treated with 10 µg/ml GST or GST-SHH-N for 2 hours. Scale bar: 8 µm. **(D)** Mander's co-localization coefficient documents increased co-localization of megalin^{R3192Q} with LAMP1 in NPC treated with GST-SHH-N as compared to wild-type megalin (n=mean of 4 experiments with 10-40 cells/experiment analyzed ± SD; Student's *t* test). **, p<0.01.

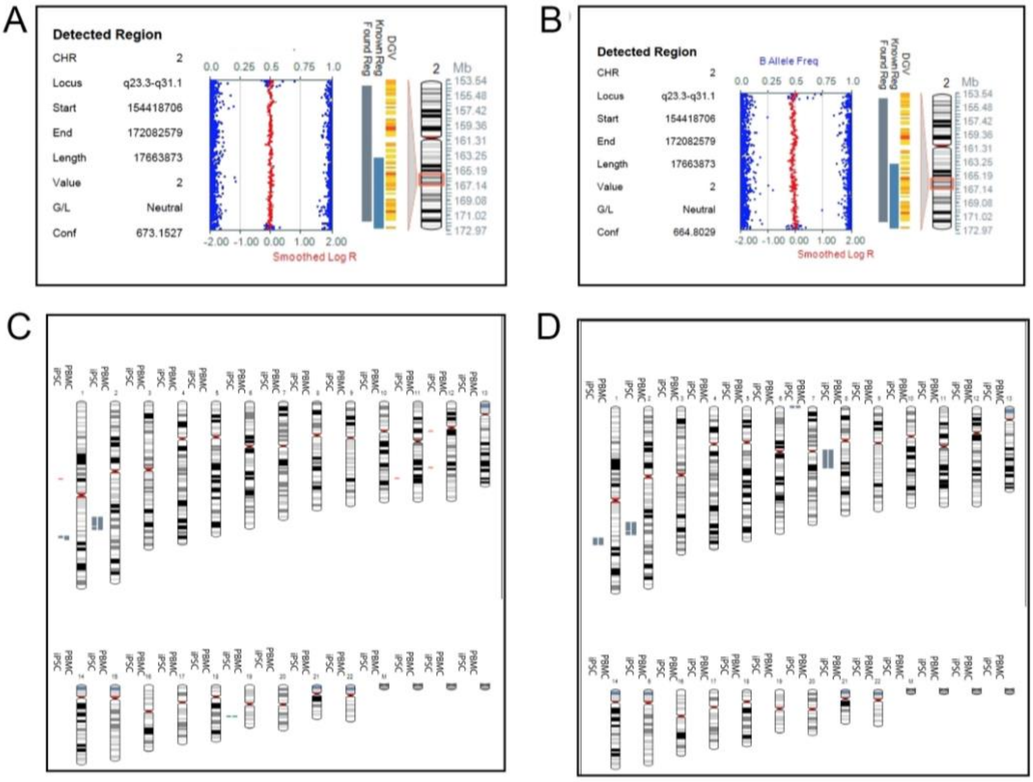

Detected Region

CHR 2
Locus q23.3-q31.1
Start 154418706
End 172082579
Length 17663873
Value 2
G/L Neutral
Conf 673.1527

Detected Region

CHR 2
Locus q23.3-q31.1
Start 154418706
End 172082579
Length 17663873
Value 2
G/L Neutral
Conf 664.8029

Flemming et al., Figure S1

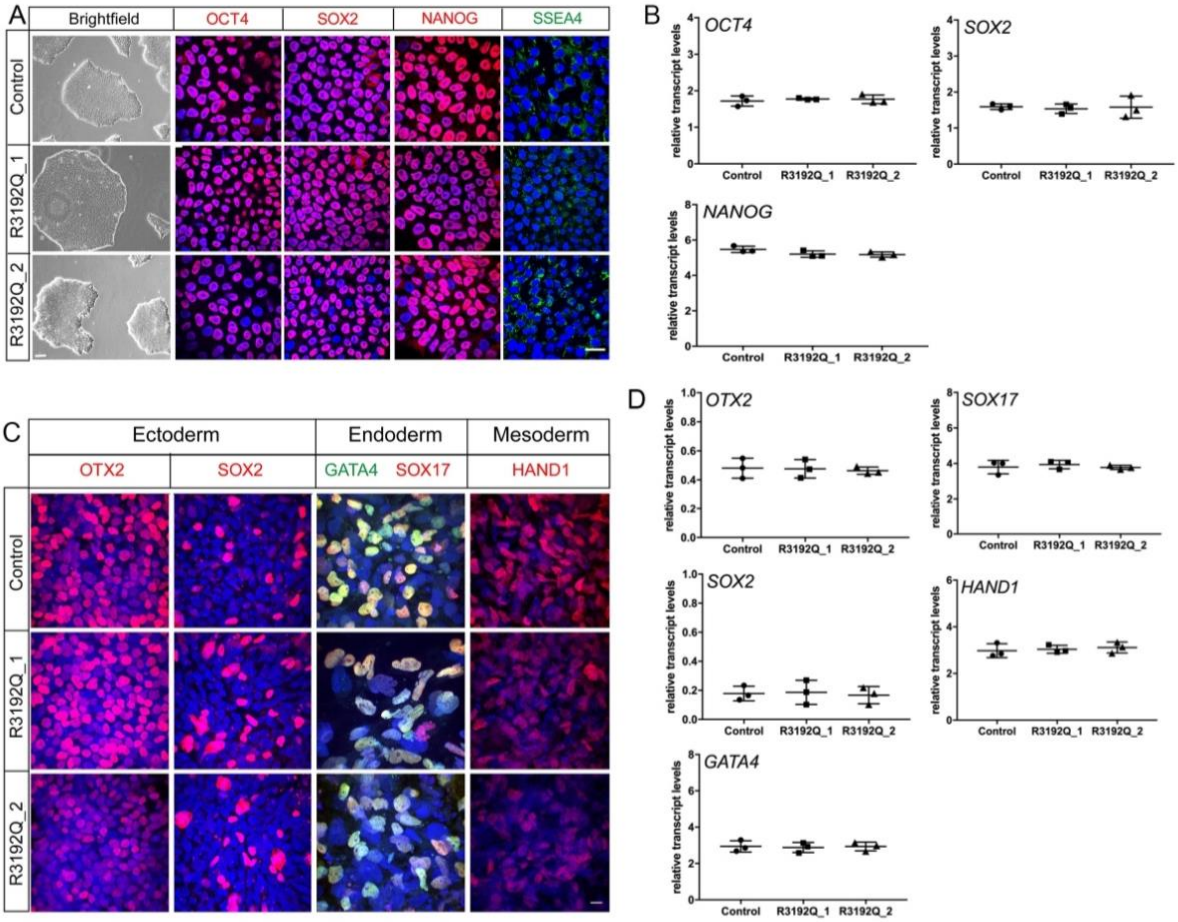

Flemming et al., Figure S2

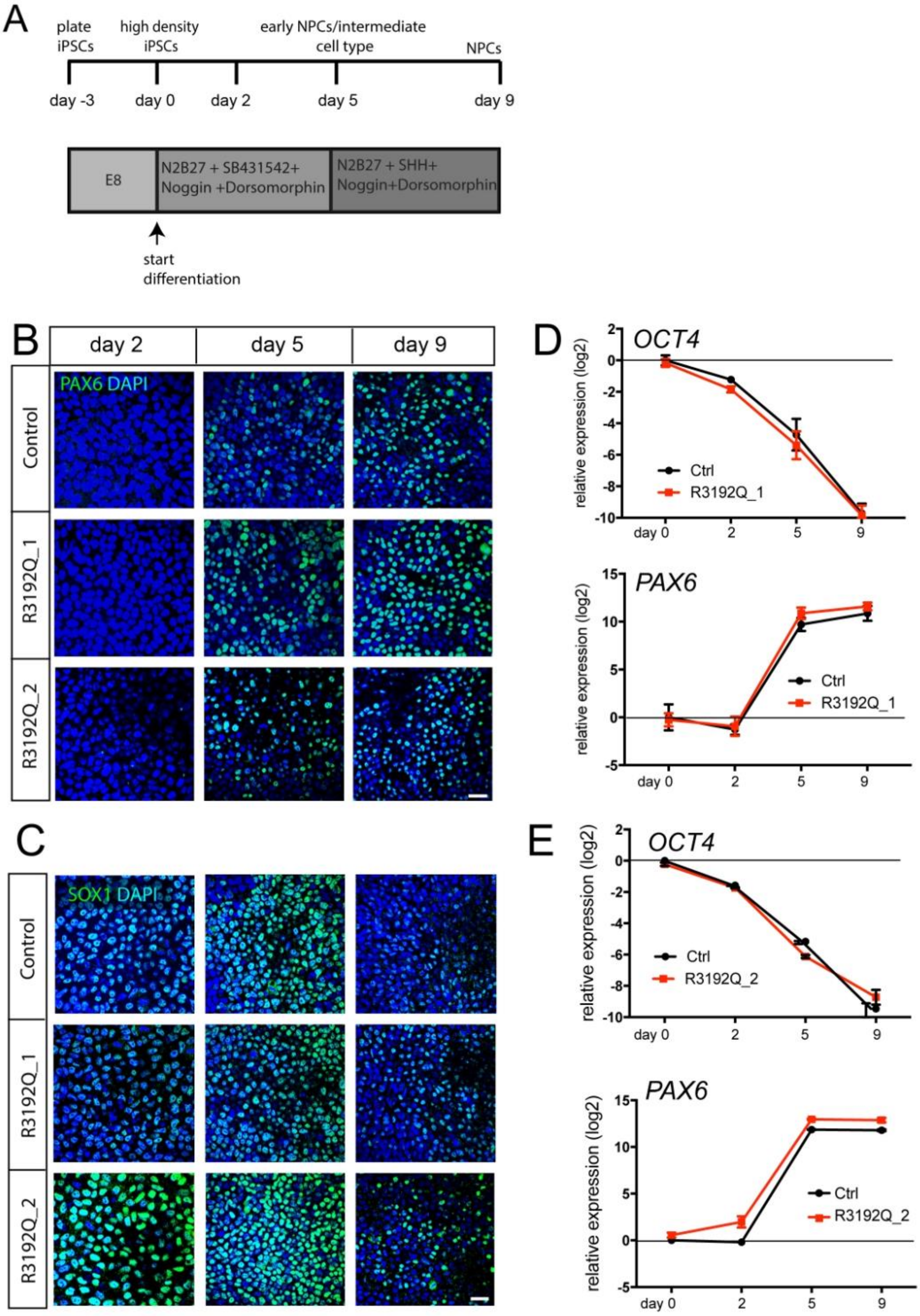

Flemming et al., Figure S3

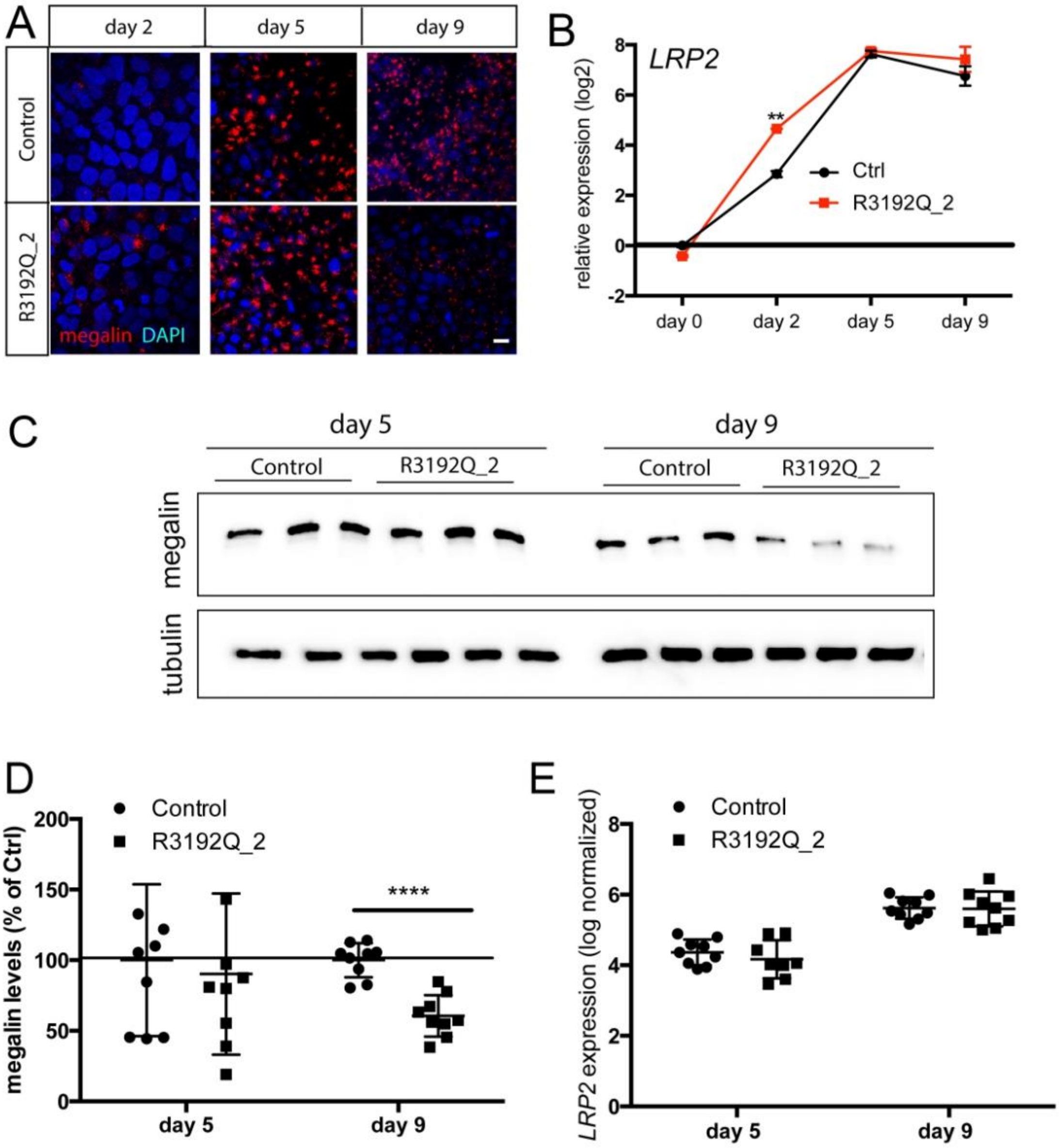

Flemming et al., Figure S4

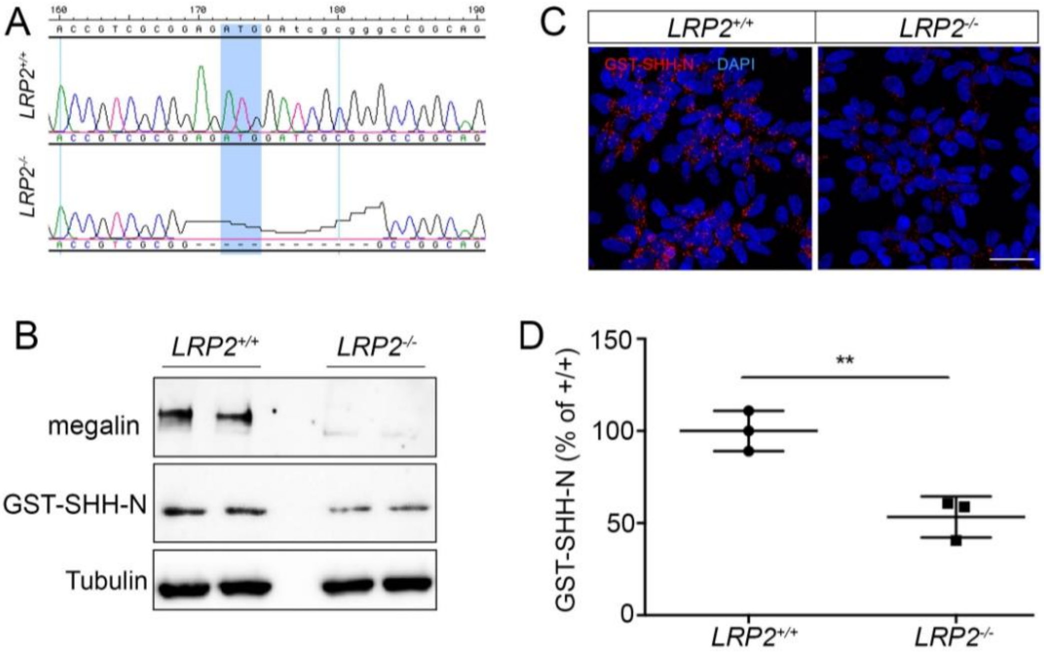

Flemming et al., Figure S5

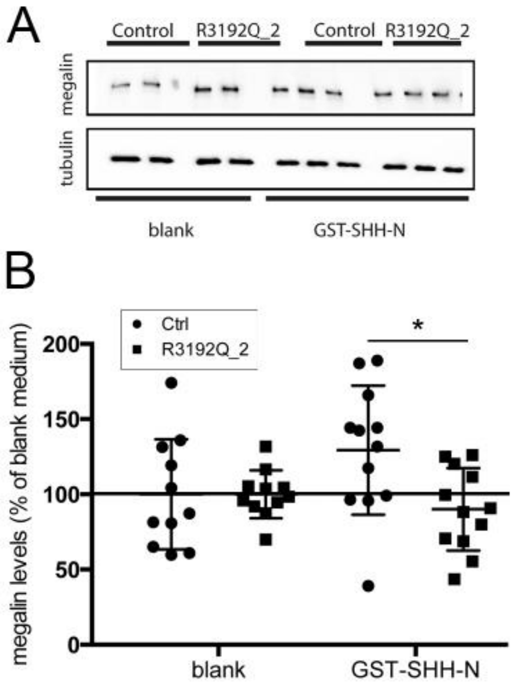

Flemming et al., Figure S6

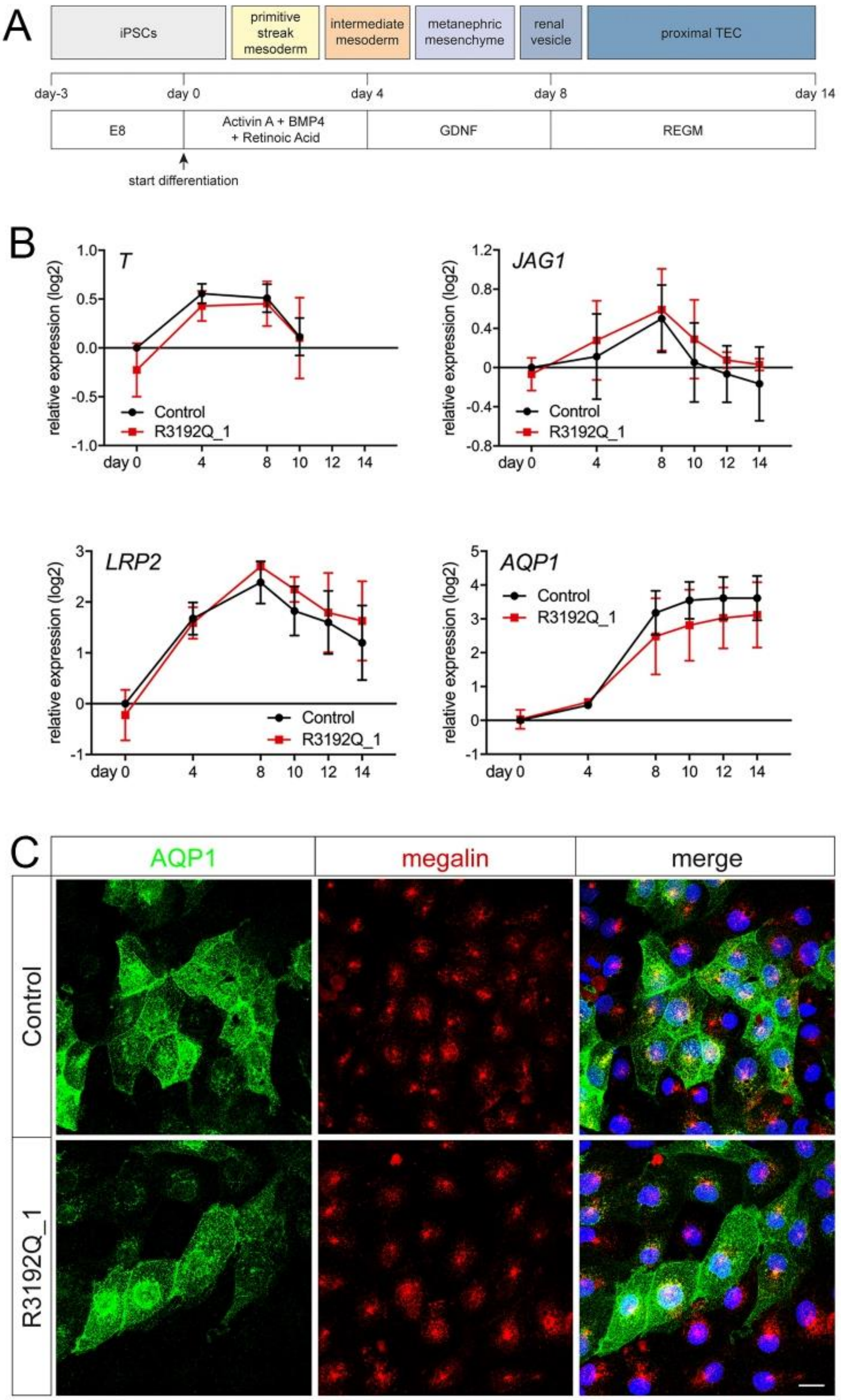

Flemming et al., Figure S7

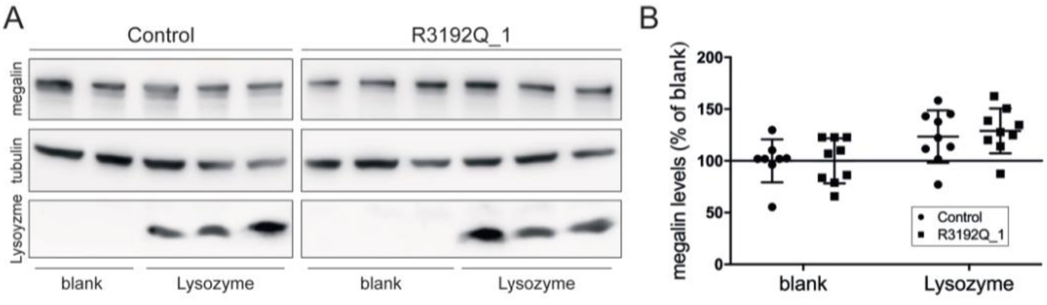

Flemming et al., Figure S8

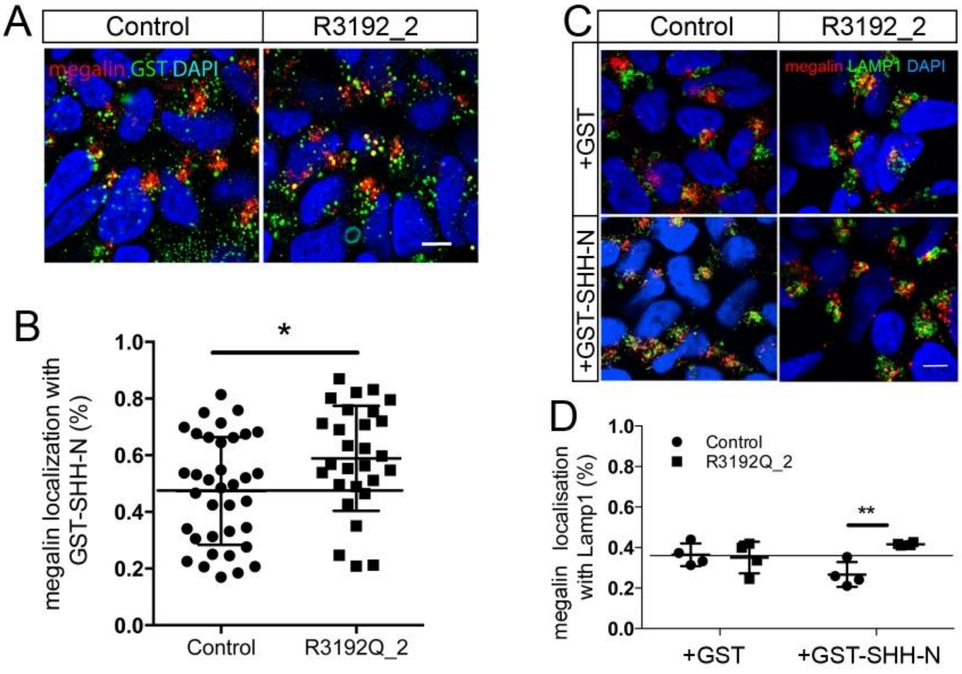

Flemming et al., Figure S9

corrigendum www.kidney-international.org

Corrigendum to Flemming J, Marczenke M, Rudolph I-M, et al. Induced pluripotent stem cell-based disease modeling identifies ligand-induced decay of megalin as a cause of Donnai-Barrow syndrome. *Kidney Int*. 2020;98:159–167

Kidney International (2021) 100, 482; https://doi.org/10.1016/j.kint.2021.06.014

Julia Flemming[1,5], Maike Marczenke[1,2,5], Ina-Maria Rudolph[1], Rikke Nielsen[3], Tina Storm[3], Erik Ilsoe Christensen[3], Sebastian Diecke[1], Francesco Emma[4] and Thomas E. Willnow[1,3]

[1]Max-Delbrueck-Center for Molecular Medicine, Berlin, Germany; [2]Department of Biology, Chemistry and Pharmacy, Freie Universitaet Berlin, Berlin, Germany; [3]Department of Biomedicine, Faculty of Health Science, Aarhus University, Aarhus C, Denmark; and [4]Division of Nephrology, Department of Pediatric Subspecialties, Bambino Gesù Children's Hospital – IRCCS, Rome, Italy

[5]These authors contributed equally to the study.

In the above-stated article, the given name and surname one of the authors, Erik Ilsoe Christensen, was presented inaccurately. The given name is Erik and the surname is Ilsoe Christensen. In addition, an additional affiliation of Maike Marczenke was omitted. The additional affiliation is the Department of Biology, Chemistry and Pharmacy, Freie Universitaet Berlin, Berlin, Germany.

The authors would like to apologize for any inconvenience caused.

2.2 Paper 2: GAS1 is required for NOTCH-dependent facilitation of SHH signaling in the ventral forebrain neuroepithelium.

Authors

Maike Marczenke, Daniele Yumi Sunaga-Franze, Oliver Popp, Irene W. Althaus, Sascha Sauer, Philipp Mertins, Annabel Christ, Benjamin L. Allen, Thomas E. Willnow.

Accepted in Development (2021) 148; September 27, 2021
doi: 10.1242/dev.200080
https://doi.org/10.1242/dev.200080

Personal contribution

Together with the co-authors I conceptualized the project and developed methodologies, designed and performed the experiments, collected, analyzed and interpreted the data, prepared the visualization of the work and arranged the figures, and wrote the manuscript. In detail, I conducted almost all of the experimental work on my own. As for my co-authors, Daniele Yumi Sunaga-Franze and Sascha Sauer from the MDC Genomics Platform performed the RNA sequencing run and first bioinformatic data analysis (shown in Fig. 2B and C). Irene W. Althaus provided the mutant human *GAS1* constructs used by me (Fig. 6C-G), while Benjamin L. Allen provided the *Gas1* mutant mouse line. Annabel Christ acquired funding. Oliver Popp and Philipp Mertins from the MDC Proteomics Core Unit performed mass spectrometry analysis which was not included in the manuscript in the end.

MS ID#: DEVELOP/2021/199583

GAS1 is required for Notch-dependent facilitation of SHH signaling in the ventral forebrain neuroepithelium

Maike Marczenke[1,2*], Daniele Yumi Sunaga-Franze[3], Oliver Popp[4], Irene W. Althaus[5], Sascha Sauer[3], Philipp Mertins[4], Annabel Christ[1], Benjamin L. Allen[5], and Thomas E. Willnow[1,6]*

[1]Molecular Physiology, Max-Delbrueck-Center for Molecular Medicine, 13125 Berlin, [2]Department of Biology, Chemistry and Pharmacy, Freie Universitaet Berlin, 12169 Berlin, Germany, [3]Genomics and [4]Proteomics Platforms, Max-Delbrueck-Center for Molecular Medicine, 13125 Berlin, Germany; [5]Department of Cell and Developmental Biology, University of Michigan Medical School, Ann Arbor, MI 48109, USA; and [6]Department of Biomedicine, Aarhus University, 8000 Aarhus, Denmark.

Running title: GAS1 facilitates NOTCH signaling

Keywords: forebrain organizer region, holoprosencephaly, NOTCH intracellular domain, neuroepithelial precursor cells, HH co-receptors

* Correspondence to: Maike Marczenke
Max-Delbrueck-Center for Molecular Medicine
Robert-Roessle-Str. 10, D-13125 Berlin, Germany
Phone: +49-30-9406-3414
Email: maike.marczenke@mdc-berlin.de

Thomas Willnow
Max-Delbrueck-Center for Molecular Medicine
Robert-Roessle-Str. 10, D-13125 Berlin, Germany
Phone: +49-30-9406-2569
Email: willnow@mdc-berlin.de

SUMMARY STATEMENT

GAS1 acts as co-receptor that integrates signaling by sonic hedgehog and NOTCH in neural progenitor cells, essential to control differentiation of the forebrain neuroepithelium.

ABSTRACT

Growth arrest-specific 1 (GAS1) acts as a co-receptor to Patched 1 promoting sonic hedgehog (SHH) signaling in the developing nervous system. *GAS1* mutations in humans and animal models result in forebrain and craniofacial malformations, defects ascribed to a function for GAS1 in SHH signaling during early neurulation. Here, we confirm loss of SHH activity in the forebrain neuroepithelium in GAS1-deficient mice and in iPSC-derived cell models of human neuroepithelial differentiation. However, our studies document that this defect can be attributed, at least in part, to a novel role for GAS1 in facilitating Notch signaling, essential to sustain a persistent SHH activity domain in the forebrain neuroepithelium. GAS1 directly binds NOTCH1, enhancing ligand-induced processing of the NOTCH1 intracellular domain, which drives Notch pathway activity in the developing forebrain. Our findings identify a unique role for GAS1 in integrating Notch and SHH signal reception in neuroepithelial cells, and they suggest that loss of GAS1-dependent NOTCH1 activation contributes to forebrain malformations in individuals carrying *GAS1* mutations.

INTRODUCTION

The mammalian forebrain develops from a simple neuroepithelial sheet at the anterior end of the neural plate, the anterior neuroectoderm. Several morphogen pathways provide instructive signals during early neurulation, including sonic hedgehog (SHH) which governs patterning processes along the dorso-ventral axis of the developing neural tube (reviewed in (Dessaud et al., 2008)). In the embryonic forebrain, SHH is initially produced from the prechordal plate (PrCP) at the anterior tip of the embryo. It acts on the overlying rostral diencephalon ventral midline (RDVM) to induce its own production and the expression of ventral forebrain markers. SHH transcriptional targets, such as NK2 homeobox 1 (NKX2.1), specify ventral midline identity and counteract dorsalizing signals by bone morphogenetic protein 4 (BMP4) (Hoch et al., 2009; Sousa and Fishell, 2010). In line with a prominent role for SHH in forebrain development, defects in SHH signaling in humans (Roessler et al., 1996) and in mouse models (Chiang et al., 1996) result in midline formation defects, ultimately causing craniofacial malformation and holoprosencephaly (HPE). HPE is the most frequent forebrain anomaly in humans and may include improper division of the forebrain hemispheres, as well as cyclopia and formation of a proboscis (Muenke and Beachy, 2000). Inheritable mutations in components of the SHH signaling pathway have been associated with human HPE, including mutations in *SHH*, in its receptor Patched 1 (*PTCH1*), or in downstream transcription factors, like GLI family zinc finger 2 (*GLI2*), SIX homeobox 3 (*SIX3*), and zinc finger protein of the cerebellum 2 (*ZIC2*) (Roessler and Muenke, 2010).

Besides the canonical SHH receptor PTCH1, previous studies have identified additional cell surface proteins that facilitate SHH signal reception in the neuroepithelium and that cause midline malformations and HPE when mutated (reviewed in (Christ et al., 2016)). One of these auxiliary SHH receptors is growth arrest-specific 1 (GAS1), a 45 kDa glycoprotein attached to the plasma membrane via a glycosylphosphatidylinositol (GPI) anchor. Among other cell types, GAS1 is expressed in progenitor cells of the developing central nervous system (Allen et al., 2007; Lee and Fan, 2001). GAS1 facilitates interaction of SHH with PTCH1 under limiting SHH concentrations by forming co-receptor complexes, promoting SHH signaling in the cerebellum (Izzi et al., 2011) and spinal cord (Allen et al., 2011; Allen et al., 2007; Martinelli and Fan, 2007).

Loss of GAS1 in gene-targeted mice (Allen et al., 2007; Khonsari et al., 2013; Martinelli and Fan, 2007; Seppala et al., 2007; Seppala et al., 2014) or in patients with *GAS1* missense mutation (Pineda-Alvarez et al., 2012; Ribeiro et al., 2010) result in a range of craniofacial and forebrain malformations, including small eyes, cleft palate, fusion of nasal processes, and HPE. These malformations are believed to originate from defects in early development of the rostral forebrain neuroepithelium as judged from impaired expression of *Shh* (Seppala et al., 2014) as well as its targets *Nkx2.1* (Allen et al., 2007; Echevarria-Andino and Allen, 2020) and *Gli1* (Echevarria-Andino and Allen, 2020; Khonsari et al., 2013; Seppala et al., 2007) in this tissue in *Gas1* mutant mice.

Our findings now corroborate loss of SHH activity in the GAS1-deficient forebrain neuroepithelium *in vitro* and *in vivo*. Surprisingly, this defect may be attributed, at least in part, to a novel role for GAS1 in promoting Notch signaling, required to sustain the SHH activity domain in this forebrain organizer region. Loss of GAS1 impairs Notch-mediated facilitation of SHH signaling in neural progenitors and results in a failure to permanently establish the ventral SHH activity domain in the embryonic forebrain, the ultimate cause of forebrain and craniofacial anomalies in individuals lacking GAS1.

RESULTS

Reduced SHH and Notch pathway activities in the rostral ventral neuroepithelium of *Gas1* mutant mouse embryos

To dissect the contribution of GAS1 to SHH signaling during early neuroepithelial differentiation, we compared expression of *Shh* and its target *Gli1* (Lee et al., 1997) in *Gas1*$^{-/-}$

mouse embryos and their littermate controls. No differences were detected in *Shh* transcript and SHH protein in the PrCP and overlying RDVM, a major forebrain organizer region, at E8.5 (8-9 and 10-11 somites; Fig. 1A-B and Fig. S1A). By contrast, *Shh* and *Gli1* transcripts in the rostral ventral neuroepithelium of *Gas1*$^{-/-}$ embryos were decreased by E9.5 (Fig. 1C) and SHH protein was completely lost by E10.5, when compared to controls (Fig. 1D). These findings extended earlier observations of reduced expression of *Shh* (Seppala et al., 2014) at E12.5 or *Nkx2.1* (Allen et al., 2007; Echevarria-Andino and Allen, 2020) and *Gli1* (Echevarria-Andino and Allen, 2020; Khonsari et al., 2013; Seppala et al., 2007) at E9.5 - 10.5 in the ventral forebrain neuroepithelium of *Gas1* mutant mice. Importantly, our findings uncovered that GAS1 is not essential for SHH signaling in this tissue. Rather it promotes persistence of this SHH activity domain, initially established in the absence of this receptor.

At E8.5, expression of *Shh* in the PrCP provides the major source of the morphogen to pattern the overlying RDVM (Dale et al., 1997). To exclude a primary defect in this source as the reason for loss of SHH activity in *Gas1*$^{-/-}$ embryos at later embryonic stages, we quantified the size of the mutant PrCP based on *Shh* fluorescence *in situ* hybridization (FISH) on E8.5 coronal forebrain sections. These studies failed to detect any difference in the size of the *Shh* expression domain in the PrCP comparing control and *Gas1*$^{-/-}$ embryos (Fig. S1B-C).

To elucidate the reasons for loss of SHH activity in *Gas1*$^{-/-}$ embryos at later stages of development, we performed comparative bulk RNAseq of the microdissected rostral ventral neuroepithelium from E10.0 *Gas1*$^{+/+}$ and *Gas1*$^{-/-}$ embryos (Fig. 2A). Global changes in the transcriptomes were determined by principal component analysis (Fig. 2B) and by hierarchical clustering of 324 identified differentially expressed genes (DEGs; Fig. 2C and Supplementary Excel file). Gene ontology (GO) term enrichment analysis identified the expected changes in gene expression related to nervous system development, neurulation, and Hedgehog signaling (Fig. 2D). Changes in DEGs included decreased levels of transcripts for *Shh*, *Ptch1*, and *Nkx2.2* (Fig. 2E and Table S1). In addition, manual query of the RNAseq data for established down-stream targets of the SHH signaling pathway identified statistically significant decreases in expression of *Isl1*, *Pomc1*, *Nkx2.1*, and *Wnt5a (*Fig. S2*)*, as well as a concordant upregulation of *Fgf10*, *Tbx2* (Fig. 2E-F), and *Tbx3* (Fig. S2). These changes recapitulated phenotypes seen in *Shh* mutant mice (Carreno et al., 2017; Corman et al., 2018; Crane-Smith et al., 2021; Szabo et al., 2009) and further substantiated a role for GAS1 in control of SHH activity in the developing forebrain neuroepithelium.

In addition to the anticipated change in SHH target gene expression, global transcriptomics identified unexpected alterations in NOTCH signaling in the ventral forebrain midline of *Gas1* mutants (Fig. 2D). NOTCH pathway components have been shown to be expressed in the rostral ventral neuroepithelium of the mouse embryo from E8.5 onwards (Ware et al., 2014), but no function for GAS1 in modulating NOTCH signaling in this domain had been described so far. In detail, our RNAseq data revealed decreased transcript levels for the DEGs NOTCH receptor 1 (*Notch1*), Delta-like protein 1 (*Dll1*) and 3 (*Dll3*), Hes family bHLH transcriptions factor 5 (*Hes5*), NOTCH regulated ankyrin repeat protein (*Nrarp*), and maniac fringe (*Mfng*) (Fig. 2F and Table S2). Alterations in NOTCH activity in *Gas1*$^{-/-}$ embryos were further supported by expression analyses of genes affected by NOTCH deficiency in other models (Ratie et al., 2013; Ware et al., 2016). Genes also downregulated in the rostral forebrain neuroepithelium of *Gas1* mutant mice included the transcription factor *Hey1*, a NOTCH target in the murine forebrain neuroepithelium (Ware et al., 2014) (Fig. S3). Of note, some targets, upregulated upon NOTCH pathway disruption in mouse and chick models (Ratie et al., 2013; Ware et al., 2016), were downregulated in the *Gas1*$^{-/-}$ ventral midline, including *Ascl1*, *Stmn2*, and *Slit1* (Fig. S3).

Impaired NOTCH pathway activity was further validated by expression analyses in *Gas1*$^{-/-}$ embryos. In detail, *Hes5* expression in the rostral neuroepithelium was reduced as early as E8.5 (10-11 somites; Fig. 3B), a time point coinciding with *Gas1* expression in this tissue (Fig. S4A). Transcripts for *Hes5*, but also for *Notch1* and *Dll1* in the rostral ventral neuroepithelium of mutants were further reduced at E9.5 (Fig. 3C) and E10.5 (Fig. 3D). Notably, a reduction in *Hes5* expression at E8.5 preceded defects seen in the SHH pathway in *Gas1* mutants at E9.5 (Fig. 1C); and they were specific to the forebrain neuroepithelium as no changes in expression of *Notch1*, *Dll1*, or *Hes5* were detected in the spinal cord of mutant as compared with control embryos (Fig. S4B).

GAS1 promotes activation of NOTCH1 to facilitate SHH-dependent ventral neuroepithelial cell fate specification

To further dissect the molecular mechanism underlying GAS1 function in the rostral neuroepithelium, we established isogenic human induced pluripotent stem cell (iPSC) lines, either wild-type (WT) or genetically deficient for *GAS1* (*GAS1* KO; Fig. S5A-B). Loss of *GAS1* did not impact pluripotency of iPSCs as shown by normal expression of pluripotency markers (Fig. S5C-F) and by their ability to generate all three germ layers (Fig. S5G-J).

Next, WT and *GAS1* KO iPSCs were subjected to differentiation into neural progenitor cells (NPCs) of dorsal or ventral cell identity using established protocols (Fig. 4A) (Chambers et al., 2009; Flemming et al., 2020). When treated with noggin, dorsomorphin, and small molecule SB431542 to block BMP and TGFβ signaling, both WT and *GAS1* KO iPSCs downregulated the pluripotency marker OCT4 and induced the neuroectodermal marker PAX6 (Fig. 4B-C; Fig. S6A-B). Consistent with adopting a dorsal neural progenitor fate, both genotypes induced *GLI3*, an inhibitor of the SHH pathway (Fig. 4D). Also, WT, but not KO cells, induced expression of *GAS1* (Fig. 4E-F), a negative SHH transcription target (Allen et al., 2007). By contrast, when iPSCs were treated with SHH, instead of SB431542, to induce a ventral neural progenitor fate (schematic in Fig. 4A), *GAS1* KO cells failed to efficiently repress *PAX6* and *GLI3* (Fig. 4C-D), or to induce the ventral markers *FOXG1*, *NKX2.1*, *NKX2.2*, *DLX2*, and *LHX6* (Fig. 4G-K). Such a cellular response to SHH was readily seen in WT cells adopting a ventral cell fate (day 11, ventral; Fig. 4C-K). Loss of SHH-dependent repression of PAX6 or induction of NKX2.1 in mutant NPCs was confirmed by immunocytochemistry (Fig. S6B-C). These data documented the inability of GAS1-deficient NPCs to adopt a ventral cell fate, likely due to their impaired response to ventralizing signals provided by SHH.

To substantiate the inability of *GAS1* KO cells to respond to SHH, we tested *GLI1* transcript levels in NPCs treated with conditioned medium from HEK293 cells secreting SHH-Np (Christ et al., 2012). SHH-Np induced *GLI1* transcription in WT NPCs to a much greater extent than in *GAS1* KO NPCs (SHH-Np; Fig. 4L), a response blocked by the hedgehog inhibitor cyclopamine-KAAD in both cell types (SHH-Np + CKAAD; Fig. 4L). Treatment with Smoothened agonist (SAG) resulted in a similar induction of *GLI1* in both genotypes, indicating pathway integrity in *GAS1* KO cells downstream of SMO (SAG; Fig. 4L). Taken together, our findings substantiated iPSC-derived NPCs as a faithful model to study neural progenitor fate decisions, and the importance of GAS1 for interpreting ventralizing signals provided by SHH to this cell type.

In line with our gene expression data from *Gas1* mutant embryos, *GAS1* KO NPCs also failed to activate the NOTCH pathway during neuroectodermal differentiation. Thus, despite normal expression of *NOTCH1* and *DLL1* transcripts and proteins (Fig. 5A-B and D), induction of *HES5* transcript and protein levels was much lower in *GAS1* KO as compared with WT NPCs (Fig. 5C and E). This defect was seen for dorsal and ventral cell fates alike, documenting a SHH-independent role for GAS1 in NOTCH signaling. GAS1 deficiency impacted *Notch1* and *Dll1* expression in E9.5-10.5 embryos (Fig. 3C-D) but not in NPCs (Fig. 5A-B). This distinction likely reflected the fact that iPSC-derived NPCs recapitulate an early stage of neuroepithelial differentiation. Importantly, enhancing or abrogating SHH activity by SHH-Np and SAG or by cyclopamine, respectively, did not impact *HES5* transcript levels in WT NPCs (Fig. S7). These findings confirmed that SHH does not control expression of

NOTCH pathway components in neural progenitors and that loss of SHH activity was not the primary cause of NOTCH pathway deficiency in *GAS1* KO NPCs.

The impact of GAS1 on NOTCH signaling manifested at the level of ligand-induced processing of the receptor polypeptide as shown by quantification of the NOTCH1 intracellular domain (NICD) produced in response to treatment with its ligand DLL1. In WT NPCs, treatment with recombinant DLL1 increased NICD levels as compared to the control condition (Fig. 5F and G). NICD formation in WT NPCs was blocked by addition of the γ-secretase inhibitor DAPT (Fig. 5F and G). DLL1-induced NICD production correlated with increased levels of *HES5* transcripts in WT cells, faithfully recapitulating established NICD actions in this cell type (Fig. 5H). By contrast, DLL1-induced NICD generation and down-stream signal transduction was completely lost in *GAS1* KO NPCs as the levels of NICD (Fig. 5F-G) as well as *HES5* transcripts (Fig. 5H) did not increase above the levels seen in cells in the absence of the ligand. These findings documented a complete loss of ligand-induced NOTCH activity in NPCs lacking GAS1.

To investigate the molecular mechanism of GAS1 action in NOTCH signaling, we performed proximity ligation assays, demonstrating the close proximity of GAS1 and NOTCH1 in WT NPCs (Fig. 6A). Immunoprecipitation (IP) assays further showed that GAS1 co-IPs with PTCH1 (a known interaction) but also with NOTCH1 (Fig. 6B), further arguing that GAS1 and NOTCH1 physically interact. To further dissect the domain requirements for GAS1 in NOTCH1 activation, we transfected HEK293 cells with hemagglutinin (HA)-tagged full length or truncated variants of GAS1 (Fig. 6C) and determined endogenous NICD production in response to DLL1 application. Whereas full length GAS1 induced DLL1-dependent NICD production, GAS1 lacking the GPI anchor did not (Fig. 6D-E). Also, deletion of the extracellular DN or DC domains in GAS1 eliminated the ability of the receptor to induce NICD production (Fig. 6F-G). These findings documented that full length, membrane tethered GAS1 is required to promote NOTCH1 signaling in neural progenitors.

Ectopic NOTCH signaling rescues loss of SHH activity in the GAS1-deficient forebrain neuroepithelium

NOTCH has been shown to facilitates SHH signaling in retina and spinal cord of mouse, chick, and zebrafish models (Huang et al., 2012; Jacobs and Huang, 2019; Kong et al., 2015; Ringuette et al., 2016; Stasiulewicz et al., 2015). To investigate a similar role for NOTCH in the rostral neuroepithelium, and the relevance for GAS1 in this process, we studied the interdependency of SHH and NOTCH pathways in NPCs. Levels of *HES5* were always lower in *GAS1* KO as compared to WT NPCs, irrespective of the presence or absence of SHH-Np (Fig. 7A), consistent with the notion that GAS1 activation of NOTCH is SHH-independent. By contrast, induction of *GLI1* and *NKX2.1* expression in WT NPCs by addition of SHH-Np was reduced (*GLI1*) or even completely lost (*NKX2.*1) by blockade of NOTCH signaling using DAPT (Fig. 7B-C). In fact, *GLI1* and *NKX2.1* transcript levels in WT cells treated with SHH-Np and DAPT were comparable to levels in *GAS1* KO cells treated with SHH-Np in the absence of DAPT. These findings further argued that GAS1-dependent activation of NOTCH1 is a major contributor to SHH signal strength in neural progenitors.

To further substantiate the relevance of GAS1-dependent activation of NOTCH1 for SHH signaling, we tested SHH activity in GAS1 mutant cells following ectopic induction of NOTCH1 activity. In these experiments, lentiviral overexpression of NICD rescued the defect in *HES5* induction in *GAS1* KO NPCs independent of SHH as levels of this transcript were comparable in NICD-treated WT and KO NPCs; both in the presence or absence of SHH-Np (Fig. 7D). Importantly, NICD overexpression partially rescued SHH-dependent *GLI1* and *NKX2.1* induction in *GAS1* KO NPCs treated with SHH-Np and NICD as compared to treatment with SHH-Np only (Fig. 7E-F).

So far, our findings corroborated a role for GAS1 in NOTCH-dependent facilitation of SHH signaling in cultured NPCs. To confirm the relevance of this activity for SHH action in the developing forebrain, we tested the ability of NOTCH signaling to rescue loss of SHH activity in the *Gas1*$^{-/-}$ rostral ventral neuroepithelium. To do so, we used cephalic explants, a utilitarian model to study neuroepithelial differentiation *ex vivo* (Christ et al., 2012; Echevarria et al., 2001). In the protocol used here, cephalic explants were isolated from E9.5 WT and *Gas1*$^{-/-}$ embryos and cultured for 48h, followed by gene expression analyses using ISH (Fig. 8A). In *Gas1* mutant explants, correct albeit slightly reduced expression of *Shh* was seen at E9.5 in the rostral ventral neuroepithelium (t = 0 hr; Fig. 8B). This expression domain was completely lost after two days in culture (t = 48 hr; Fig. 8B). By contrast, *Shh* expression sustained in the rostral ventral neuroepithelium of WT explants (Fig. 8B). These findings recapitulated our *in vivo* data that GAS1 was required to sustain the *Shh* expression domain, initially established normally around E8.5 in the G*as1* mutant forebrain. Thus, cephalic explants represented a faithful model to recapitulate *Shh* defects observed in the GAS1-deficient rostral neuroepithelium *in vivo.*

Next, we treated cephalic explants with lentiviral constructs encoding NICD to ectopically induce NOTCH signaling. In line with this strategy, expression of *Hes5*, absent from GAS1-deficient explants treated with control virus, was rescued in mutants by ectopic expression of NICD (Fig. 8C). Importantly, overexpression of NICD also increased *Shh* transcript levels in the rostral ventral neuroepithelium in approximately half of the *Gas1*$^{-/-}$ explants to levels similar to that in WT tissue (Fig. 8D). Similarly, NICD expression also partially rescued levels of *Nkx2.1* in the rostral ventral neuroepithelium of mutant explants (Fig. 8E). As a negative control, no rescue of *Shh* or *Nkx2.1* expression was detected in *Gas1*$^{-/-}$ explants treated with a control virus (Fig. 8D-E).

In conclusion, our findings identified a novel role for GAS1 in integrating SHH and NOTCH signaling pathways, a function specific to neural progenitors in the rostral forebrain neuroepithelium destined to adopt a ventral cell fate (Fig. 8F). According to our model, GAS1 interacts with PTCH1 to promote SHH-dependent gene expression, including induction of

Shh, *Nkx2.1*, or *Gli1*. However, GAS1 also interacts with NOTCH1 to facilitate ligand-induced production of NICD. GAS1-dependent NICD production induces prototypic NOTCH targets, such as *Hes5* and *Hey1*; but it also acts on the SHH pathway to increase strength and persistence of SHH signal reception. The latter mode of action is unclear at present but, based on work by others, may act at the level of several HH pathway components, including PTCH1, SMO, or GLI2.

DISCUSSION

Previous studies have identified multiple developmental abnormalities in mouse models and patients carrying mutations in *GAS1*. These defects have been phenotypically characterized in great detail in *Gas1*$^{-/-}$ mice and include microforms of HPE, but also a range of craniofacial anomalies, such as midfacial hypoplasia, premaxillary incisor fusion, cleft palate, or malformation of the anterior pituitary (Allen et al., 2007; Echevarria-Andino and Allen, 2020; Khonsari et al., 2013; Martinelli and Fan, 2007; Seppala et al., 2007; Seppala et al., 2014). Malformations phenocopy aspects of SHH deficiency, including hypothalamic defects and pituitary hypoplasia (Carreno et al., 2017; Zhao et al., 2012). Phenotypes increase in severity with haploinsufficiency for *Shh* (Allen et al., 2007; Khonsari et al., 2013; Martinelli and Fan, 2007; Seppala et al., 2007), documenting interaction of *Gas1* and *Shh* in formation of the midline and structures derived thereof. Increasing or decreasing GAS1 activity in the neural tube of chick or mouse positively correlates with SHH pathway activity, corroborating an agonistic role for GAS1 in the graded response of neuroepithelial cells to ventralizing signals by this morphogen (Allen et al., 2007; Khonsari et al., 2013; Martinelli and Fan, 2007; Seppala et al., 2007). Although studies on the cellular response to SHH mainly concern a role for GAS1 in patterning of the caudal neural tube and limbs (Allen et al., 2011; Allen et al., 2007; Martinelli and Fan, 2007), they also serve as an explanatory model for GAS1 action in SHH signaling in the rostral neuroepithelium. This assumption is supported by loss of expression of *Shh* and downstream targets in this tissue around E9.5 - 12.5. (Allen et al., 2007; Echevarria-Andino and Allen, 2020; Khonsari et al., 2013; Seppala et al., 2014).

Our studies aimed at corroborating a role for GAS1 in the cellular response of neural progenitors of the forebrain neuroepithelium to SHH signals. To do so, we applied unbiased as well as targeted approaches of molecular phenotyping of the forebrain neuroepithelium during early neurulation (E8.5 to E10.5), and we queried our findings by modeling of morphogen actions in iPSC-derived NPCs. NPCs faithfully recapitulate the *in vivo* response of neuroepithelial cells to morphogen signals and the consequential dorsal versus ventral cell fate choices (Fig. 4B-K). Also, this cell model faithfully recapitulates defects in the immediate cellular response to SHH signals observed in the GAS1-deficient forebrain neuroepithelium *in vivo* and *ex vivo*. Importantly, this cell model enables quantitative assessment of the cellular response to morphogen signals using agonists and antagonists, an experimental strategy difficult to apply to forebrain patterning *in vivo*.

Concerning the presumed role for GAS1 in the cellular response of the forebrain neuroepithelium to SHH, our studies extended previous work by confirming loss of morphogen expression and activity around E9.5 (Fig. 1C). These defects are consistent with SHH deficiency at early neurulation as seen in *Shh* mutant mouse embryos (Carreno et al., 2017; Corman et al., 2018; Crane-Smith et al., 2021; Szabo et al., 2009). However, contrary to prior analysis that focused on developmental stages after E9.5, our data uncovered that GAS1 is not required for initial establishment of the SHH domain in the RDVM at E8.5, but to sustain its activity at later stages of neurulation. The same effect is also seen in cephalic explants (Fig. 8B). This mode of action distinguishes GAS1 from other SHH binding proteins, such as LRP2, required for initial establishment of the SHH activity domain in the RDVM at E8.5 (Christ et al., 2012). A faciliatory role for GAS1 in SHH signal reception in neural progenitors is substantiated by quantitative assessment of their response to pathway stimulation. In these experiments, the response of *GAS1* KO cells to SHH-Np is lower than in

WT cells, yet significant as compared to non-treated cells, and comparable to the extent of pathway stimulation seen with SAG in either genotype. Still, baseline stimulation of the SHH pathway in the absence of GAS1 is clearly insufficient to trigger a ventral cell fate decision (Fig. 4B-K), providing a molecular correlate for ventralizing defects seen in the *Gas1* mutant neural tube *in vivo* (Allen et al., 2007; Khonsari et al., 2013; Martinelli and Fan, 2007; Seppala et al., 2007).

While a role for GAS1 in the response of the forebrain neuroepithelium to SHH may have been anticipated based on previous work, a role for this receptor in NOTCH signaling in this cell type is novel and surprising. In NPCs, loss of GAS1 completely abrogates the ability to induce the NOTCH target *HES5,* an effect independent of dorsal or ventral cell fate decisions (Fig. 5C and E). Also, GAS1-deficient NPCs fail to respond to the NOTCH ligand DLL1 with induction of NICD production and *HES5* transcription (Fig 5F-H). Deficiency in NOTCH signaling is confirmed in GAS1-deficient embryos as early as E8.5 (Fig. 3B). Phenotypes include features observed in mice with targeted disruption of the NOTCH pathway component RBPJ, such as loss of *Hes5* in the rostral ventral diencephalon (Ware et al., 2016). Some targets, such as *Ascl1*, upregulated upon NOTCH pathway disruption in the RBPJ KO mouse model (Ratie et al., 2013; Ware et al., 2016), were downregulated in the *Gas1*$^{-/-}$ ventral midline (Fig. S3). These distinctions are likely due to the fact that *Gas1*$^{-/-}$ mice still retain the activity of RBPJ, that acts as a transcriptional repressor in the absence of NICD (Castel et al., 2013). NOTCH signaling promotes progenitor cell maintenance in the developing CNS and controls neuronal/glial cell fate decisions (reviewed in (Gaiano and Fishell, 2002)). Specifically, recent work identified the importance of NOTCH signaling for maintenance and differentiation of prosencephalic structures, including hypothalamic neurons and pituitary gland. Consequently, NOTCH signaling defects in the RBPJ KO mouse model causes malformation of the pituitary gland (Aujla et al., 2015; Aujla et al., 2013), a defect shared by GAS1-deficient mice (Khonsari et al., 2013). Although not explored in this study in detail, loss of NOTCH activity in the rostral neuroepithelium of *Gas1*$^{-/-}$ embryos may be expected to cause additional phenotypes related to NOTCH deficiency.

Concerning the molecular mechanism whereby GAS1 promotes NOTCH activation, this action likely involves direct interaction with NOTCH1, a co-receptor concept also operable for GAS1 action on PTCH1 (Izzi et al., 2011). At present, we can only speculate about the mode of GAS1 action in this context. Because the ability of GAS1 to promote NOTCH1 activation is lost when the GPI anchor is deleted, one may argue that GPI-anchored GAS1 targets NOTCH1 to specialized lipid raft compartments where secretases or ligands reside. Such a NOTCH-sorting function has been shown for GPI-anchored Cripto-1 (Watanabe et al., 2009). Whatever the mode of action, it is operable in the rostral but not the caudal neural tube, supporting a unique role for GAS1 in NOTCH signaling during early forebrain patterning.

Conceptually, GAS1 deficiency phenotypes may represent a combination of NOTCH and SHH defects, originating from independent functions of GAS1 in activation of PTCH1 and NOTCH1. More exciting is the hypothesis that both functions for GAS1 converge on its ability to promote SHH signal strength and persistence in the forebrain neuroepithelium (see schematic in Fig. 8F). NOTCH is known to exerts some of its actions by facilitating SHH signal reception and maintaining SHH responsiveness in target cells. These actions may work through different mechanisms. On the one hand, NOTCH signaling has been shown to regulate the availability and stability of GLI proteins in mouse retinal progenitor cells (Ringuette et al., 2016) as well as in neural progenitor cells of the zebrafish spinal cord (Jacobs and Huang, 2019). On the other hand, NOTCH signals prime neural progenitor cells of the mouse and chick neural tube for response to SHH by regulating trafficking of PTCH1 and SMO (Huang et al., 2012; Kong et al., 2015; Stasiulewicz et al., 2015).
Haploinsufficiency for NOTCH pathway components in some patients with HPE further suggests that NOTCH-dependent facilitation of SHH signaling is required for forebrain

formation (Dupe et al., 2011). This conclusion is supported by loss of NOTCH-dependent SHH activity in the embryonic mouse and chick forebrains following pharmacological or genetic perturbation of NOTCH activity, defects that include disruption of the hypothalamo-pituitary axis (Hamdi-Roze et al., 2020).

While dissection of NOTCH-dependent versus NOTCH-independent effects of GAS1 on SHH signaling will be challenging *in vivo*, iPSC-based modelling of neural progenitor differentiation enables quantitative assessment of the contribution of both pathways to SHH signal strength. In WT NPCs, SHH-Np induced gene expression is largely reduced (*GLI1*) or even completely abolished (*NKX2.1*) by blockade of NOTCH using DAPT (Fig. 7B and C). In support of a prominent role for NOTCH in SHH signal strength, SHH signaling defects in GAS1 mutant NPCs can be partially rescued *in vitro* (Fig. 7E-F) and in cephalic explants *ex vivo* (Fig. 8D-E) by NICD. Although this experimental approach does not formally rule out a GAS1-independent role for NOTCH in SHH signal transduction, SHH-Np induced expression of *GLI1* is comparable in WT and *GAS1* KO cells in the presence of DAPT, arguing that a major contribution to SHH signal strength in WT cells stems from the action of GAS1 on NOTCH (Fig. 7B).

In conclusion, our findings suggest a new concept concerning the role of SHH co-receptors in control of morphogen signaling in forebrain neuroepithelial cells. Specifically, they document that GAS1 acts as a co-receptor for both PTCH1 and NOTCH1 to integrate instructive signals by SHH and NOTCH ligands in this cell type; and they argue that loss of GAS1-dependent NOTCH activation may contribute to forebrain malformations in individuals carrying *GAS1* mutations.

MATERIALS AND METHODS

Mouse models

Mice carrying a targeted disruption of *Gas1* (Martinelli and Fan, 2007) have been described. The *Gas1* mutant line was kept by breeding of *Gas1*$^{+/-}$ animals on a C57BL/6N genetic background. As no phenotypic differences in forebrain formation were observed between *Gas1*$^{+/+}$ and *Gas1*$^{+/-}$ embryos in this study, both genotypes were used as matched littermate controls for GAS1-deficient embryos. All animal experimentation was performed following approval by authorities of the State of Berlin (X9007/17). *In situ* hybridization (ISH) and immunohistology on mouse tissues were performed according to published protocols (Christ et al., 2012) and as detailed in the supplementary method section.

GAS1-deficient human iPSC model

Human induced pluripotent stem cell line HPSI1113i-wetu_2 was kindly provided by the Wellcome Trust Sanger Institute, UK and used as wild-type control cell line (WT). iPSCs were cultured on Matrigel (354277, Corning) -coated culture plates in Essential 8 (E8) or E8 Flex medium (Gibco). Culture medium was changed daily. Cells were passaged every three to four days at a density of 70-80% using StemPro Accutase (Gibco) and 10 µM of Rock inhibitor Y27632 (SEL-S1049, Selleck Chemicals). A GAS1-deficient subclone of HPSI1113i-wetu_2 (*GAS1* KO) was generated by targeting the *GAS1* gene using the CRISPR/Cas9 system. Single guide RNA (sgRNA) was designed using the online software tool CHOPCHOP (Labun et al., 2019). sgRNA sequences were sense: CTCAACGACTGCGTGTGCGA and antisense: TCGCACACGCAGTCGTTGAG. Annealed sgRNA oligonucleotides were cloned into the expression vector pSpCas9(BB)-2A-Puro V2.0 (PX459, Addgene plasmid #62988). Human iPSCs were transfected with the final sgRNA-plasmid construct using Lipofectamine3000 (Invitrogen) according to manufacturer's instructions. Transfected cells were selected with 0.1 µg/ml puromycin for one week before seeding them at low density for single cell colony expansion. Clones were analyzed for successful deletion using the Phire Animal Tissue Direct PCR Kit (Thermo Fisher Scientific). Primer sequences used were CAAAGTCTTCAACGGGCTGC (forward) and CGGGCCATGTTCTCCTTGA (reverse). To confirm deletion of the targeted *GAS1* region, DNA sequencing was performed by LGC Genomics GmbH and data analyzed using the DNAStar SeqMan Software Version 13.0.0. Analysis of pluripotency by scorecard assay and differentiation in neuroepithelial progenitor cells is described in the supplementary method section. All iPSC lines were regularly tested negative for mycoplasma.

SHH signaling in NPCs

NPCs of differentiation day 7-9 were incubated with 5-10% conditioned medium from control or SHH-Np secreting HEK293 cells (Christ et al., 2012), 200 nM SAG (SML1314, Sigma-Aldrich), 50 nM cyclopamine-KAAD (239804, Calbiochem), or 25 µM DAPT (565770, Sigma-Aldrich) diluted in N2B27 medium overnight or for 3 days (for studies including DAPT). The medium was changed daily with freshly added compounds. For rescue experiments, NPCs of differentiation day 5 were dissociated using Accutase and seeded onto Matrigel-coated 24-well-plates at a density of 400000 cells/well. Cells were transduced with 20 µl/well NICD or GFP control expressing lentivirus solutions and 8 µg/ml polybrene overnight. 48 hours after transduction, cells were incubated overnight with 5-10% conditioned medium from control or SHH-Np secreting HEK293 cells. Following, cells were subjected to gene expression analysis by quantitative real-time PCR.

Analysis of NOTCH1 signaling in NPCs and HEK293

NPCs at differentiation day 7-9 were treated with recombinant DLL1-Fc (10184-DL, R&D Systems) or Fc control (110-HG, R&D Systems) coupled to Pierce Protein G Magnetic Beads (Thermo Fisher Scientific) and, where applicable, additionally with 25 µM DAPT overnight.

Human GAS1 constructs (HA-hGAS1, HA-hGAS1ΔGPI, HA-hGAS1ΔDN, and HA-hGAS1ΔDC) were generated by PCR-based cloning into the pCIG vector (Megason and McMahon, 2002) and confirmed by sanger sequencing. HEK293T cells were transfected with the various GAS1 constructs using Lipofectamine2000. Forty-eight hours after transfection, cells were incubated with DLL1-Fc or Fc control magnetic beads overnight. Cells were washed with PBS to remove beads and subjected to protein analysis by western blotting. For each reaction, 20 µl protein G magnetic beads were first equilibrated in PBS and then incubated with 500 ng DLL1-Fc or Fc control overnight at 4°C on a rotator. Next day, the beads were washed and stored in PBS at 4°C until use.

Rescue of SHH signaling in explants

Cephalic explants were prepared as described (Christ et al., 2012; Echevarria et al., 2001) with minor modifications. Briefly, E9.5 embryos were dissected in DMEM without phenol red supplemented with 1x GlutaMAX and 1x penicillin-streptomycin (Gibco). Embryonic heads were opened along the dorsal midline and the floor plate was cut at the level of the cephalic flexure. Explants were placed on polycarbonate membrane filters of 0.8-1 µm pore size (Millipore) with the ventricular side facing up and transferred to 24-well-plates containing DMEM supplemented with 10% FCS, 1x GlutaMAX and 1x penicillin-streptomycin (Gibco). Explants were recovered for 2-3 hours at 37°C with 5% CO_2 and 95% humidity. 20 µl lentivirus solution containing NICD or GFP encoding lentivirus particles was applied on top and explants were further cultivated for 48 hours. After gently washing with culture medium and subsequently with PBS, the explants were fixed in 4% PFA at 4°C overnight before subjecting to whole mount ISH for *Shh*, *Nkx2.1* or *Hes5*.

Statistical Analysis

Data are represented as mean + standard deviation (SD). All statistical analyses were performed using GraphPad Prism 7.0. The applied statistical tests are indicated in the respective figure legends.

Author contribution

Conceptualization: M.M., D.Y.S.-F., O.P., I.W.A., S.S., P.M., B.L.A., T.E.W.

Software: D.Y.S.-F.

Formal analysis: M.M., D.Y.S.-F., O.P., I.W.A., S.S., P.M., B.L.A., T.E.W.

Investigation: M.M., D.Y.S.-F., O.P., I.W.A., S.S., P.M., B.L.A., T.E.W.

Data curation: M.M., D.Y.S.-F., T.E.W.

Writing - original draft: M.M., B.L.A., T.E.W.

Supervision: S.S., P.M., B.L.A., T.E.W.

Funding acquisition: A.C., T.E.W.

Competing interest statement

The authors have no competing interest to declare.

ACKNOWLEDGMENTS

We are indebted to C. Kruse, K. Kampf, and M. Kamprath for technical assistance and to S. Diecke (MDC) for expert advice. The authors acknowledge the Wellcome Trust Sanger Institute as the source of human iPSC line HPSI1113i-wetu_2 which was generated under the human iPSC Initiative funded by a grant from the Wellcome Trust and the Medical Research Council, supported by the Wellcome Trust (WT098051) and the NIHR/Wellcome Trust Clinical Research Facility, and acknowledge Life Science Technologies Corporation as the provider of Cytotune. Studies were funded in part by grants from the German Research Foundation/DFG (GRK 2318/0; CH 1838/1-1).

REFERENCES

Allen, B. L., Song, J. Y., Izzi, L., Althaus, I. W., Kang, J. S., Charron, F., Krauss, R. S. and McMahon, A. P. (2011). Overlapping roles and collective requirement for the coreceptors GAS1, CDO, and BOC in SHH pathway function. *Dev Cell* **20**, 775-787.

Allen, B. L., Tenzen, T. and McMahon, A. P. (2007). The Hedgehog-binding proteins Gas1 and Cdo cooperate to positively regulate Shh signaling during mouse development. *Genes Dev* **21**, 1244-1257.

Aujla, P. K., Bogdanovic, V., Naratadam, G. T. and Raetzman, L. T. (2015). Persistent expression of activated notch in the developing hypothalamus affects survival of pituitary progenitors and alters pituitary structure. *Dev Dyn* **244**, 921-934.

Aujla, P. K., Naratadam, G. T., Xu, L. and Raetzman, L. T. (2013). Notch/Rbpjkappa signaling regulates progenitor maintenance and differentiation of hypothalamic arcuate neurons. *Development* **140**, 3511-3521.

Carreno, G., Apps, J. R., Lodge, E. J., Panousopoulos, L., Haston, S., Gonzalez-Meljem, J. M., Hahn, H., Andoniadou, C. L. and Martinez-Barbera, J. P. (2017). Hypothalamic sonic hedgehog is required for cell specification and proliferation of LHX3/LHX4 pituitary embryonic precursors. *Development* **144**, 3289-3302.

Castel, D., Mourikis, P., Bartels, S. J., Brinkman, A. B., Tajbakhsh, S. and Stunnenberg, H. G. (2013). Dynamic binding of RBPJ is determined by Notch signaling status. *Genes Dev* **27**, 1059-1071.

Chambers, S. M., Fasano, C. A., Papapetrou, E. P., Tomishima, M., Sadelain, M. and Studer, L. (2009). Highly efficient neural conversion of human ES and iPS cells by dual inhibition of SMAD signaling. *Nat Biotechnol* **27**, 275-280.

Chiang, C., Litingtung, Y., Lee, E., Young, K. E., Corden, J. L., Westphal, H. and Beachy, P. A. (1996). Cyclopia and defective axial patterning in mice lacking Sonic hedgehog gene function. *Nature* **383**, 407-413.

Christ, A., Christa, A., Kur, E., Lioubinski, O., Bachmann, S., Willnow, T. E. and Hammes, A. (2012). LRP2 is an auxiliary SHH receptor required to condition the forebrain ventral midline for inductive signals. *Dev Cell* **22**, 268-278.

Christ, A., Herzog, K. and Willnow, T. E. (2016). LRP2, an auxiliary receptor that controls sonic hedgehog signaling in development and disease. *Dev Dyn* **245**, 569-579.

Corman, T. S., Bergendahl, S. E. and Epstein, D. J. (2018). Distinct temporal requirements for Sonic hedgehog signaling in development of the tuberal hypothalamus. *Development* **145**.

Crane-Smith, Z., Schoenebeck, J., Graham, K. A., Devenney, P. S., Rose, L., Ditzell, M., Anderson, E., Thomson, J. I., Klenin, N., Kurrasch, D. M., et al. (2021). A Highly Conserved Shh Enhancer Coordinates Hypothalamic and Craniofacial Development. *Front Cell Dev Biol* **9**, 595744.

Dale, J. K., Vesque, C., Lints, T. J., Sampath, T. K., Furley, A., Dodd, J. and Placzek, M. (1997). Cooperation of BMP7 and SHH in the induction of forebrain ventral midline cells by prechordal mesoderm. *Cell* **90**, 257-269.

Dessaud, E., McMahon, A. P. and Briscoe, J. (2008). Pattern formation in the vertebrate neural tube: a sonic hedgehog morphogen-regulated transcriptional network. *Development* **135**, 2489-2503.

Dupe, V., Rochard, L., Mercier, S., Le Petillon, Y., Gicquel, I., Bendavid, C., Bourrouillou, G., Kini, U., Thauvin-Robinet, C., Bohan, T. P., et al. (2011).

NOTCH, a new signaling pathway implicated in holoprosencephaly. *Hum Mol Genet* **20**, 1122-1131.

Echevarria, D., Vieira, C. and Martinez, S. (2001). Mammalian neural tube grafting experiments: an in vitro system for mouse experimental embryology. *Int J Dev Biol* **45**, 895-902.

Echevarria-Andino, M. L. and Allen, B. L. (2020). The hedgehog co-receptor BOC differentially regulates SHH signaling during craniofacial development. *Development* **147**.

Flemming, J., Marczenke, M., Rudolph, I. M., Nielsen, R., Storm, T., Erik, I. C., Diecke, S., Emma, F. and Willnow, T. E. (2020). Induced pluripotent stem cell-based disease modeling identifies ligand-induced decay of megalin as a cause of Donnai-Barrow syndrome. *Kidney Int* **98**, 159-167.

Gaiano, N. and Fishell, G. (2002). The role of notch in promoting glial and neural stem cell fates. *Annu Rev Neurosci* **25**, 471-490.

Hamdi-Roze, H., Ware, M., Guyodo, H., Rizzo, A., Ratie, L., Rupin, M., Carre, W., Kim, A., Odent, S., Dubourg, C., et al. (2020). Disrupted Hypothalamo-Pituitary Axis in Association With Reduced SHH Underlies the Pathogenesis of NOTCH-Deficiency. *J Clin Endocrinol Metab* **105**.

Hoch, R. V., Rubenstein, J. L. and Pleasure, S. (2009). Genes and signaling events that establish regional patterning of the mammalian forebrain. *Semin Cell Dev Biol* **20**, 378-386.

Huang, P., Xiong, F., Megason, S. G. and Schier, A. F. (2012). Attenuation of Notch and Hedgehog signaling is required for fate specification in the spinal cord. *PLoS Genet* **8**, e1002762.

Izzi, L., Levesque, M., Morin, S., Laniel, D., Wilkes, B. C., Mille, F., Krauss, R. S., McMahon, A. P., Allen, B. L. and Charron, F. (2011). Boc and Gas1 each form distinct Shh receptor complexes with Ptch1 and are required for Shh-mediated cell proliferation. *Dev Cell* **20**, 788-801.

Jacobs, C. T. and Huang, P. (2019). Notch signalling maintains Hedgehog responsiveness via a Gli-dependent mechanism during spinal cord patterning in zebrafish. *Elife* **8**.

Khonsari, R. H., Seppala, M., Pradel, A., Dutel, H., Clement, G., Lebedev, O., Ghafoor, S., Rothova, M., Tucker, A., Maisey, J. G., et al. (2013). The buccohypophyseal canal is an ancestral vertebrate trait maintained by modulation in sonic hedgehog signaling. *BMC Biol* **11**, 27.

Kong, J. H., Yang, L., Dessaud, E., Chuang, K., Moore, D. M., Rohatgi, R., Briscoe, J. and Novitch, B. G. (2015). Notch activity modulates the responsiveness of neural progenitors to sonic hedgehog signaling. *Dev Cell* **33**, 373-387.

Labun, K., Montague, T. G., Krause, M., Torres Cleuren, Y. N., Tjeldnes, H. and Valen, E. (2019). CHOPCHOP v3: expanding the CRISPR web toolbox beyond genome editing. *Nucleic Acids Res* **47**, W171-W174.

Lee, C. S. and Fan, C. M. (2001). Embryonic expression patterns of the mouse and chick Gas1 genes. *Mech Dev* **101**, 293-297.

Lee, J., Platt, K. A., Censullo, P. and Ruiz i Altaba, A. (1997). Gli1 is a target of Sonic hedgehog that induces ventral neural tube development. *Development* **124**, 2537-2552.

Martinelli, D. C. and Fan, C. M. (2007). Gas1 extends the range of Hedgehog action by facilitating its signaling. *Genes Dev* **21**, 1231-1243.

Megason, S. G. and McMahon, A. P. (2002). A mitogen gradient of dorsal midline Wnts organizes growth in the CNS. *Development* **129**, 2087-2098.

Muenke, M. and Beachy, P. A. (2000). Genetics of ventral forebrain development and holoprosencephaly. *Curr Opin Genet Dev* **10**, 262-269.

Pineda-Alvarez, D. E., Roessler, E., Hu, P., Srivastava, K., Solomon, B. D., Siple, C. E., Fan, C. M. and Muenke, M. (2012). Missense substitutions in the GAS1 protein present in holoprosencephaly patients reduce the affinity for its ligand, SHH. *Hum Genet* **131**, 301-310.

Ratie, L., Ware, M., Barloy-Hubler, F., Rome, H., Gicquel, I., Dubourg, C., David, V. and Dupe, V. (2013). Novel genes upregulated when NOTCH signalling is disrupted during hypothalamic development. *Neural Dev* **8**, 25.

Ribeiro, L. A., Quiezi, R. G., Nascimento, A., Bertolacini, C. P. and Richieri-Costa, A. (2010). Holoprosencephaly and holoprosencephaly-like phenotype and GAS1 DNA sequence changes: Report of four Brazilian patients. *Am J Med Genet A* **152A**, 1688-1694.

Ringuette, R., Atkins, M., Lagali, P. S., Bassett, E. A., Campbell, C., Mazerolle, C., Mears, A. J., Picketts, D. J. and Wallace, V. A. (2016). A Notch-Gli2 axis sustains Hedgehog responsiveness of neural progenitors and Muller glia. *Dev Biol* **411**, 85-100.

Roessler, E., Belloni, E., Gaudenz, K., Jay, P., Berta, P., Scherer, S. W., Tsui, L. C. and Muenke, M. (1996). Mutations in the human Sonic Hedgehog gene cause holoprosencephaly. *Nat Genet* **14**, 357-360.

Roessler, E. and Muenke, M. (2010). The molecular genetics of holoprosencephaly. *Am J Med Genet C Semin Med Genet* **154C**, 52-61.

Seppala, M., Depew, M. J., Martinelli, D. C., Fan, C. M., Sharpe, P. T. and Cobourne, M. T. (2007). Gas1 is a modifier for holoprosencephaly and genetically interacts with sonic hedgehog. *J Clin Invest* **117**, 1575-1584.

Seppala, M., Xavier, G. M., Fan, C. M. and Cobourne, M. T. (2014). Boc modifies the spectrum of holoprosencephaly in the absence of Gas1 function. *Biol Open* **3**, 728-740.

Sousa, V. H. and Fishell, G. (2010). Sonic hedgehog functions through dynamic changes in temporal competence in the developing forebrain. *Curr Opin Genet Dev* **20**, 391-399.

Stasiulewicz, M., Gray, S. D., Mastromina, I., Silva, J. C., Bjorklund, M., Seymour, P. A., Booth, D., Thompson, C., Green, R. J., Hall, E. A., et al. (2015). A conserved role for Notch signaling in priming the cellular response to Shh through ciliary localisation of the key Shh transducer Smo. *Development* **142**, 2291-2303.

Szabo, N. E., Zhao, T., Cankaya, M., Theil, T., Zhou, X. and Alvarez-Bolado, G. (2009). Role of neuroepithelial Sonic hedgehog in hypothalamic patterning. *J Neurosci* **29**, 6989-7002.

Ware, M., Hamdi-Roze, H. and Dupe, V. (2014). Notch signaling and proneural genes work together to control the neural building blocks for the initial scaffold in the hypothalamus. *Front Neuroanat* **8**, 140.

Ware, M., Hamdi-Roze, H., Le Friec, J., David, V. and Dupe, V. (2016). Regulation of downstream neuronal genes by proneural transcription factors during initial neurogenesis in the vertebrate brain. *Neural Dev* **11**, 22.

Watanabe, K., Nagaoka, T., Lee, J. M., Bianco, C., Gonzales, M., Castro, N. P., Rangel, M. C., Sakamoto, K., Sun, Y., Callahan, R., et al. (2009). Enhancement of Notch receptor maturation and signaling sensitivity by Cripto-1. *J Cell Biol* **187**, 343-353.

Zhao, L., Zevallos, S. E., Rizzoti, K., Jeong, Y., Lovell-Badge, R. and Epstein, D. J. (2012). Disruption of SoxB1-dependent Sonic hedgehog expression in the hypothalamus causes septo-optic dysplasia. *Dev Cell* **22**, 585-596.

FIGURE LEGENDS

Figure 1: GAS1 deficiency impedes persistence of the SHH activity domain in the murine embryonic forebrain.

SHH and *Gli1* expression patterns in control (Control) and GAS1-deficient (*Gas1*$^{-/-}$) embryos at the indicated embryonic stages. Analyses were performed on whole mount preparations (for *Shh* in panels A and B), or coronal sections thereof (as indicated in the respective insets adapted from BioRender.com). (**A, B**) *Shh* transcript (blue; upper panels) and SHH protein (red; middle panels) are detectable in prechordal plate (PrCP) and rostral diencephalon ventral midline (RDVM), while *Gli1* transcripts are seen in the rostral ventral neuroepithelium (green; lower panels) at 8-9 (A) and 10-11 (B) somite stages in both genotypes. (**C, D**) Levels of *Shh* transcript (blue; upper panels) and SHH protein (red; middle panels), as well as *Gli1* transcript (green; lower panels) are decreased at E9.5 (C) and completely lost at E10.5 (D) in the rostral ventral neuroepithelium of *Gas1*$^{-/-}$ embryos compared with controls. Dotted lines demarcate PrCP, RDVM, or rostral ventral neuroepithelium, respectively. n=4-5 embryos per genotype and embryonic stage. Scale bars: 50 µm.

Figure 2: Global transcriptomics indicate defects in NOTCH signaling in the GAS1-deficient rostral ventral forebrain.

(**A**) The SHH expression domain (as highlighted by immunodetection of SHH) in the rostral ventral midline of murine E10.0 forebrain sections was isolated by laser capture microdissection and subjected to bulk RNA sequencing as detailed in supplementary methods. (**B, C**) Principal component analysis (PCA; B) and column-based hierarchical clustering heatmap (C) for all 324 identified differentially expressed genes (DEGs) of replicate pools (5 embryos per pool) of control (n=5) and *Gas1*$^{-/-}$ (n=4) tissue samples are shown. (**D**) Gene ontology (GO) term enrichment analysis including the categories biological process, enriched pathway sets, and associated phenotypes. The 5 top hits for each category are shown in decreasing order of evidence based on GO term enrichment test q-value. Numbers indicate the quantity of DEGs related to the respective term. (**E, F**) Heatmap of DEGs associated with the GO term "smoothened signaling pathway" (E) and "NOTCH signaling pathway" (F).

Figure 3: GAS1 deficiency disrupts NOTCH signaling in the murine embryonic forebrain.

Detection of *Notch1*, *Dll1*, and *Hes5* transcripts on coronal sections of control and *Gas1*$^{-/-}$ embryos at the indicated embryonic stages (plane of section indicated in the insets adapted from BioRender.com). (**A, B**) While *Notch1* (green; upper panels) and *Dll1* (purple; middle panels) transcript levels in the rostral neuroepithelium are comparable between genotypes, transcript levels for *Hes5* (red; lower panels) are normal at 8-9 (A) but decreased at 10-11 (B) somites in *Gas1*$^{-/-}$ embryos compared with controls. n=4-6 embryos per genotype and somite stage (**C**, **D**) Transcript levels for *Notch1* (green; upper panels), *Dll1* (purple; middle panels), and *Hes5* (red; lower panels) are reduced in the rostral ventral diencephalon of E9.5 (C) and E10.5 (D) *Gas1*$^{-/-}$ embryos as compared with controls. n=8 embryos per genotype and embryonic stage. Scale bars: 50 µm. Dotted lines demarcate rostral ventral neuroepithelium.

Figure 4: Failure to induce SHH-dependent ventral neuroepithelial cell fate in GAS1-deficient human iPSCs.

(**A**) Protocol for neuroectodermal differentiation of human iPSCs to neural progenitor cells (NPCs). Cells received either SB431542 for 11 days (dorsal fate) or for only 5 days, followed by treatment with SHH for 6 days (ventral fate). (**B-E**) Quantitative (q) RT-PCR analysis of transcript levels for *OCT4* (B), *PAX6* (C), *GLI3* (D), and *GAS1* (E) at the indicated time points of dorsal or ventral neuroectodermal differentiation. n=3 biological replicates per genotype. (**F**) Immunodetection of GAS1 (red) in WT but not *GAS1* KO NPCs. Inset depicts a higher magnification of the boxed region in the overview image. Scale bars: 10 µm. (**G-K**) qRT-PCR analysis of transcript levels for *FOXG1* (G), *NKX2.1* (H), *NKX2.2* (I), *DLX2* (J), and *LHX6* (K) at the indicated time points of dorsal or ventral neuroectodermal differentiation. n=3 biological replicates per genotype. (**L**) Relative transcript levels of *GLI1* as determined by qRT-PCR in NPCs at day 8-10 of neuroectodermal differentiation. Cells had been treated overnight with control medium, or with medium containing 200 nM smoothened agonist (SAG) or SHH-Np, in the absence or presence of 50 nM cyclopamine-KAAD (CKAAD). n=4 biological replicates per genotype and condition. Levels in (B-E) and (G-L) are given as CT values normalized to transcript levels of *GAPDH* ($2^{-\Delta CT}$ ± standard derivation (SD). Statistical analyses were performed by two-way ANOVA with Bonferroni post hoc test. * $p < 0.05$, ** $p < 0.01$, **** $p < 0.0001$

Figure 5: GAS1 promotes NOTCH1 signaling in NPCs.

(**A-C**) Quantitative (q) RT-PCR analysis of relative transcript levels for *NOTCH1* (A), *DLL1* (B), and *HES5* (C) in WT and *GAS1* KO iPSCs at the indicated time points of dorsal or ventral neuroectodermal differentiation. Levels are depicted as CT values normalized to transcript levels of *GAPDH* ($2^{-\Delta CT}$ ± SD). n=3 biological replicates per genotype and time point. Statistical differences were analyzed by two-way ANOVA with Bonferroni post hoc test. **** $p < 0.0001$. (**D**) Immunodetection of NOTCH1 (red; upper panels) and DLL1 (red; lower panels) in WT and *GAS1* KO NPCs. Nuclei were counterstained with DAPI. Scale bar: 10 µm. (**E**) Detection of *HES5* transcripts in WT and *GAS1* KO NPCs at the indicated time points of dorsal or ventral neuroectodermal differentiation. Nuclei were counterstained with DAPI. Scale bar: 25 µm. (**F**) Western blot analysis of levels of full length NOTCH1 and the NOTCH1 intracellular domain (NICD) in total lysates of WT and *GAS1* KO NPCs. Prior, cells were treated overnight with control Fc (Fc) or with recombinant DLL1-Fc-conjugated (DLL1-Fc) magnetic beads in the presence or absence of 25 µM γ-secretase inhibitor DAPT.

Detection of tubulin served as loading control. (**G**) NICD levels in WT and *GAS1* KO NPCs treated with control Fc or with DLL1-Fc were determined by densitometric scanning of replicate western blots as exemplified in (F). Levels are given as relative to the control condition (set to 1 ± SD). n=3 experiments with 2-3 replicates/experiment. (**H**) *HES5* transcript levels in WT and *GAS1* KO NPCs treated overnight with control Fc or DLL1-Fc-conjugated magnetic beads were determined by qRT-PCR. Levels are given as ΔCT values normalized to Fc treated cells ($2^{-\Delta\Delta CT}$ ± SD). n=3 experiments. Statistical significances in (G) and (H) were determined using unpaired *t* test. ** $p < 0.01$.

Figure 6: GAS1 interacts with NOTCH1 to enhance NICD processing.

(A) Proximity ligation assay documenting proximity of GAS1 and NOTCH1 (red signal; left panels) as well as GAS1 and PTCH1 (red signal, right panels) in WT NPCs. No PLA signal was detected in *GAS1* KO cells. (**B**) Co-immunoprecipitation experiments using WT NPCs. The presence of GAS1, PTCH1, and NOTCH1 in total cell lysates is shown in the panel Input. In panel αGAS1, co-immunoprecipitation of NOTCH1 and PTCH1 using anti-GAS1 antiserum is documented. Detection of tubulin served as loading control (in Input) and as negative control for specificity of the antiserum (in αGAS1). No proteins were immunoprecipitated using control anti-IgG antiserum (panel αIgG). The molecular weights of protein standards (kDa) are shown in lane M. (**C**) HA-tagged expression constructs for full-length human GAS1 (HA::GAS1) or truncated variants lacking the GPI anchor (HA::GAS1ΔGPI), or DC (HA::GAS1ΔDC) or DN (HA::GAS1ΔDN) domains. Constructs were transiently transfected into HEK293 cells to analyze their effect on NOTCH1 activation. (**D, E**) Parental HEK293 cells (Control) or cells expressing HA::GAS1 or HA::GAS1ΔGPI were treated with Fc or recombinant DLL1-Fc-conjugated magnetic beads. Levels of NICD were quantified 16 hours later by western blot analysis (D) and densitometric scanning of replicate blots (E). Detection of tubulin and NOTCH1 served as loading controls, detection of HA as GAS1 expression control. Data in E are given as mean ± SD of NICD levels (normalized to tubulin) relative to controls treated with DLL1-Fc (set at 1). n=3 experiments with 2-3 replicates/experiment. DLL1-induced production of NICD is higher in HA::GAS expressing as compared to HA::GAS1ΔGPI expressing or control cells. (**F, G**) Experiment as in (D) and (E) but using control or HEK293 cells expressing HA::GAS1, HA::GAS1ΔDC, or HA::GAS1ΔDN. n=3 experiments with 2-3 replicates/experiment. DLL1-induced production of NICD is higher in HA::GAS1 as compared to control cells or cells expressing HA::GAS1ΔDC or HA::GAS1ΔDN. Statistical differences in (E) and (G) were determined by one-way ANOVA with Bonferroni post hoc test. * p < 0.05, ** p < 0.01, *** p < 0.001.

Figure 7: GAS1 enhances SHH activity in iPSC-derived NPCs by facilitating NOTCH signaling.

(**A-C**) Relative transcript levels of *HES5* (A), *GLI1* (B), and *NKX2.1* (C) were determined by qRT-PCR in WT and *GAS1* KO NPCs at day 10 of neuroectodermal differentiation. Cells were treated either with control or SHH-Np-conditioned medium (in the absence or presence of DAPT) or with DAPT alone for 3 days. n=3 biological replicates per genotype and condition. (**D-F**) Relative transcript levels of *HES5* (D), *GLI1* (E), and *NKX2.1* (F) in WT or *GAS1* KO NPCs at day 8 of neuroectodermal differentiation. Cells were treated with control or SHH-Np-conditioned medium overnight in the absence or presence of lentiviral-induced NICD overexpression. n=3 biological replicates per genotype and condition. Levels in (A-F) are depicted as CT values normalized to transcript levels of *GAPDH* ($2^{-\Delta CT}$ ± SD) Statistical analyses were performed by two-way ANOVA with Bonferroni post hoc test. *** p < 0.001, **** p < 0.0001.

Figure 8: Ectopic expression of NICD rescues loss of the SHH activity in GAS1-deficient rostral ventral forebrain explants.

(**A**) Preparation of cephalic explants as detailed in the supplementary method section (Christ et al., 2012; Echevarria et al., 2001). (**B**) Cephalic explants of E9.5 control and *Gas1*$^{-/-}$ embryos were fixed 2 hours (t = 0 hr) or 48 hours (t = 48 hr) after dissection and subjected to in *situ* hybridization (ISH) for *Shh*. The expression domain for *Shh* in the rostral ventral neuroepithelium (marked by dotted circles) is seen in *Gas1*$^{-/-}$ embryos at t = 0 hr, albeit slightly reduced as compared to WTs. This expression domain is, however, completely lost in *Gas1*$^{-/-}$ embryos at t = 48 hr. (**C-E**) Cephalic explants of E9.5 control or *Gas1*$^{-/-}$ embryos were treated with lentiviral constructs encoding EF.PGK.GFP (GFP control) or NICD-pcw107-V5 (NICD), and subjected to ISH for *Hes5* (C), *Shh* (D), or *Nkx2.1* (E) 48 hours later. Expression domains for *Hes5, Shh*, and *Nkx2.1* in the rostral ventral neuroepithelium (circled by dotted lines) are absent from EF.PGK.GFP-treated *Gas1*$^{-/-}$ as compared to WT explants, but are partially rescued in *Gas1*$^{-/-}$ explants by NICD-pcw107-V5. The number of explants with robust signal for *Hes5, Shh*, or *Nkx2.1* in the rostral ventral neuroepithelium, out of all explants analyzed, are given for each condition and genotype. Scale bar: 500 µm. (**F**) Model for GAS1 integrating SHH and **NOTCH** signaling pathways in neural progenitor cells.

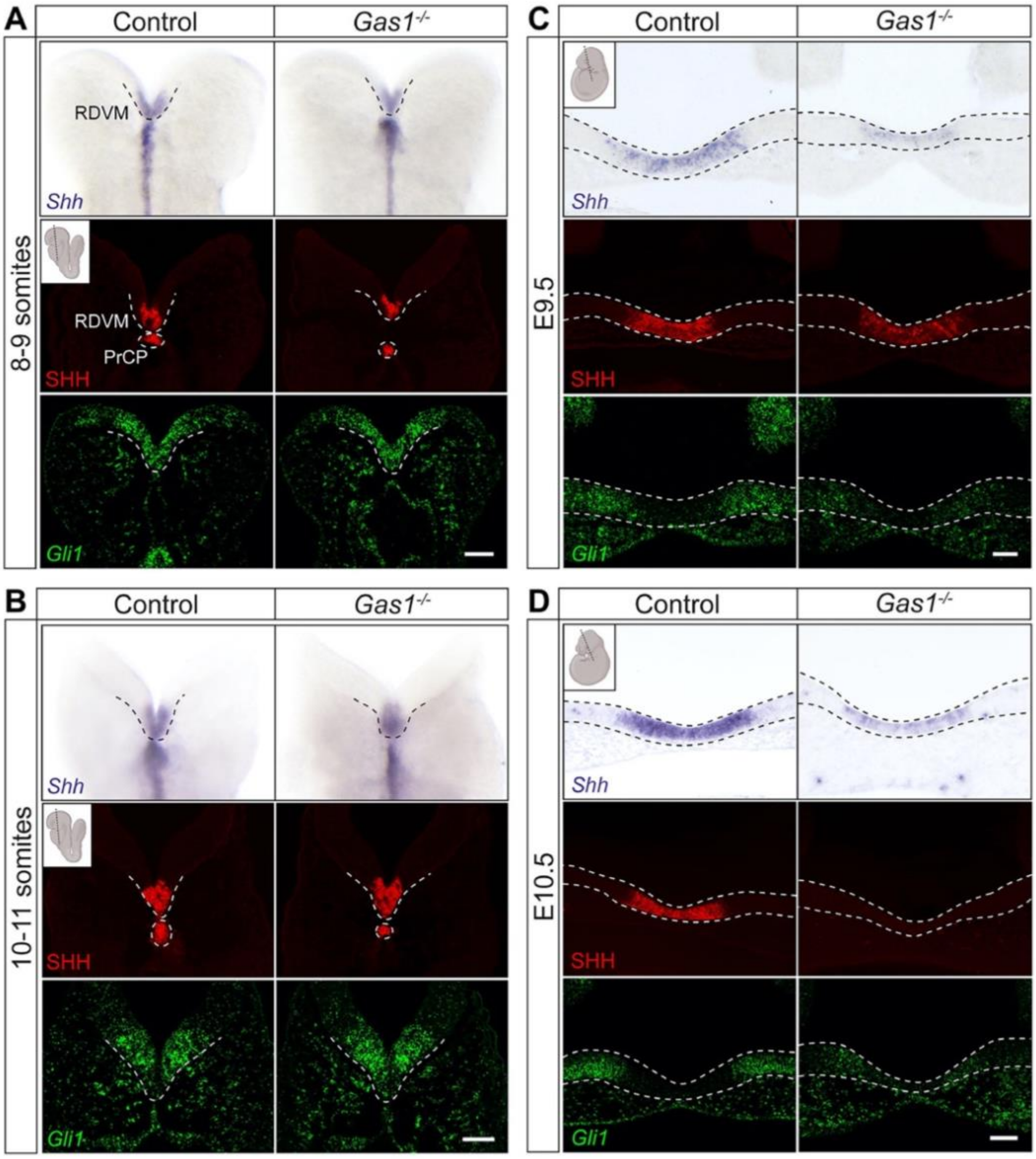

Marczenke et al., Figure 1

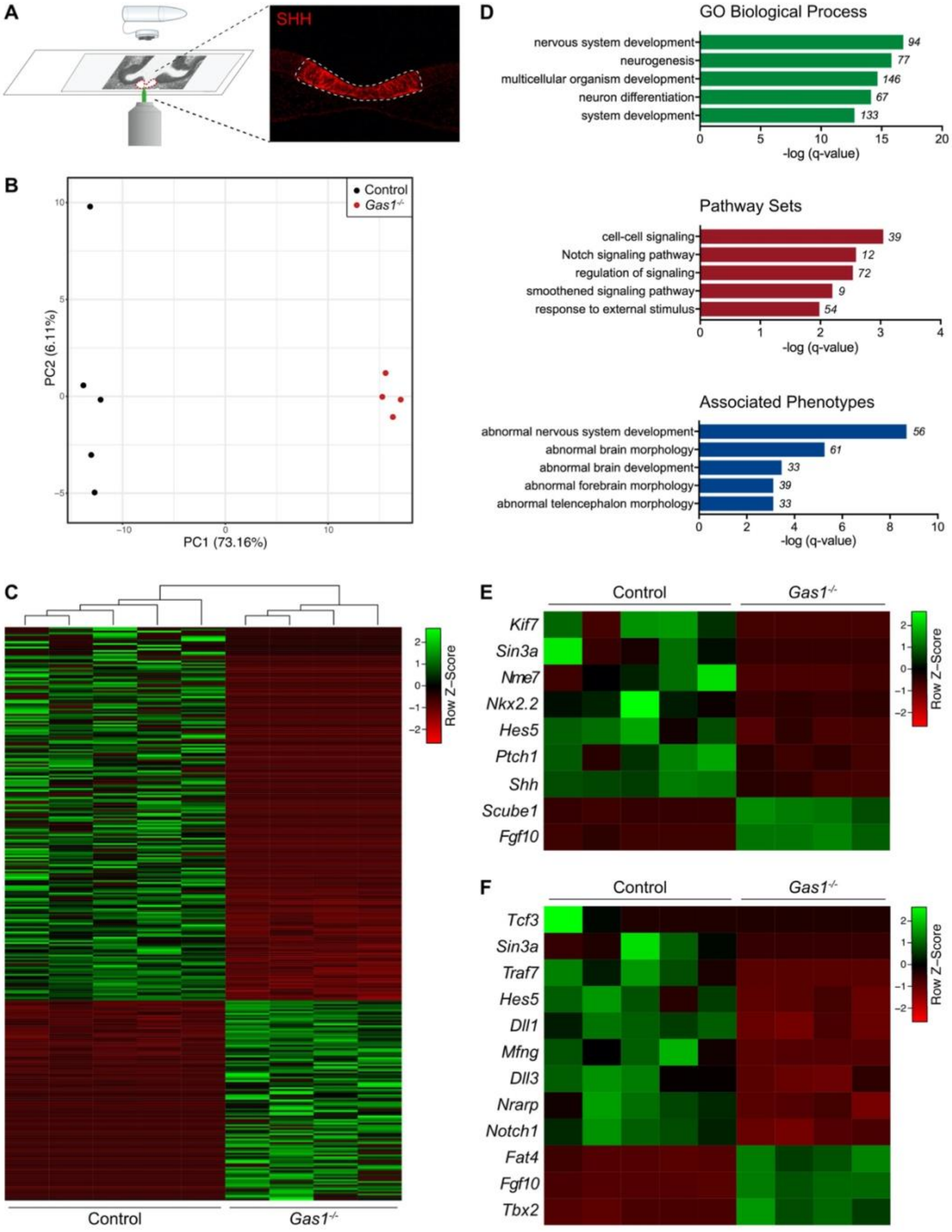

Marczenke et al., Figure 2

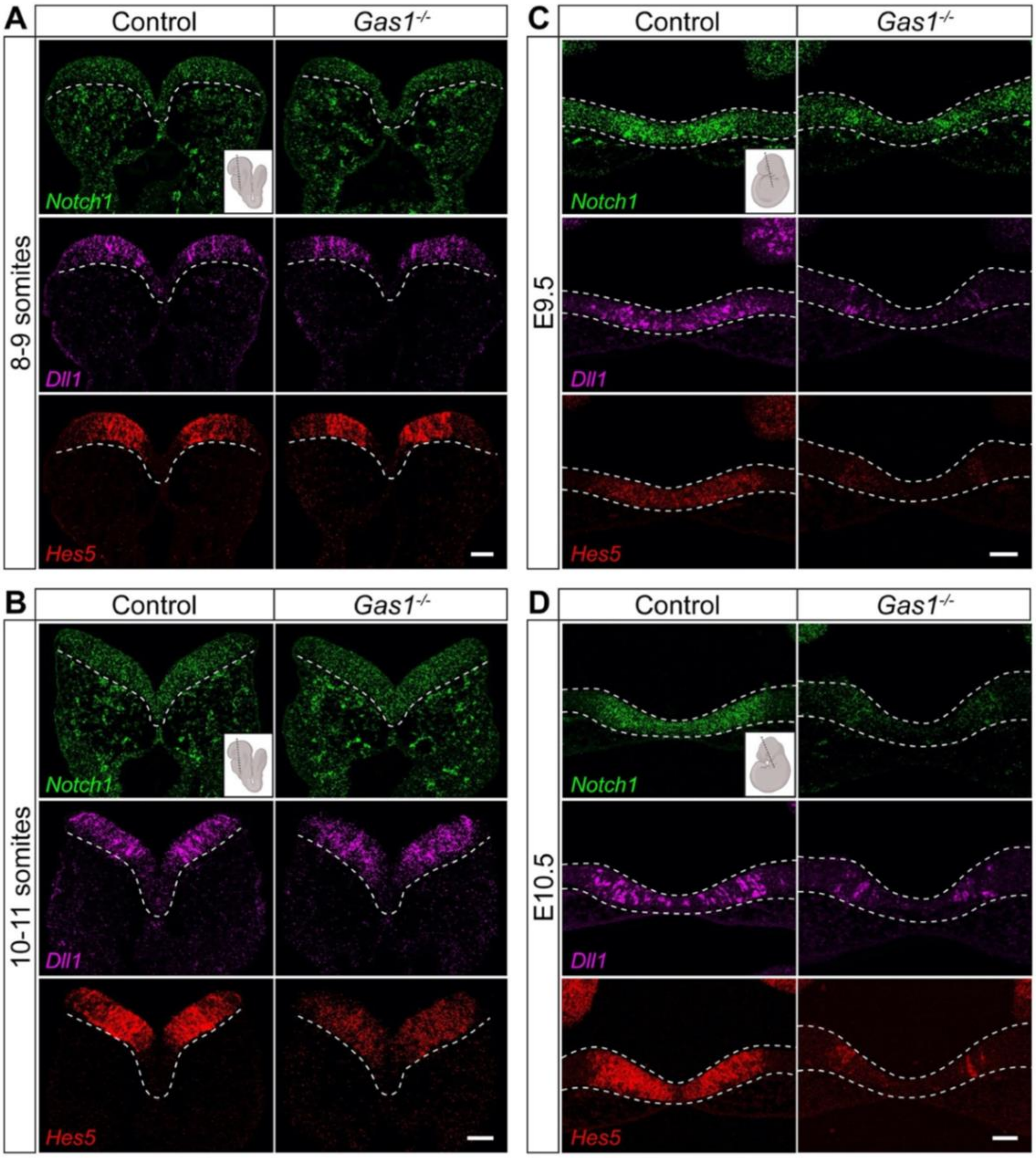

Marczenke et al., Figure 3

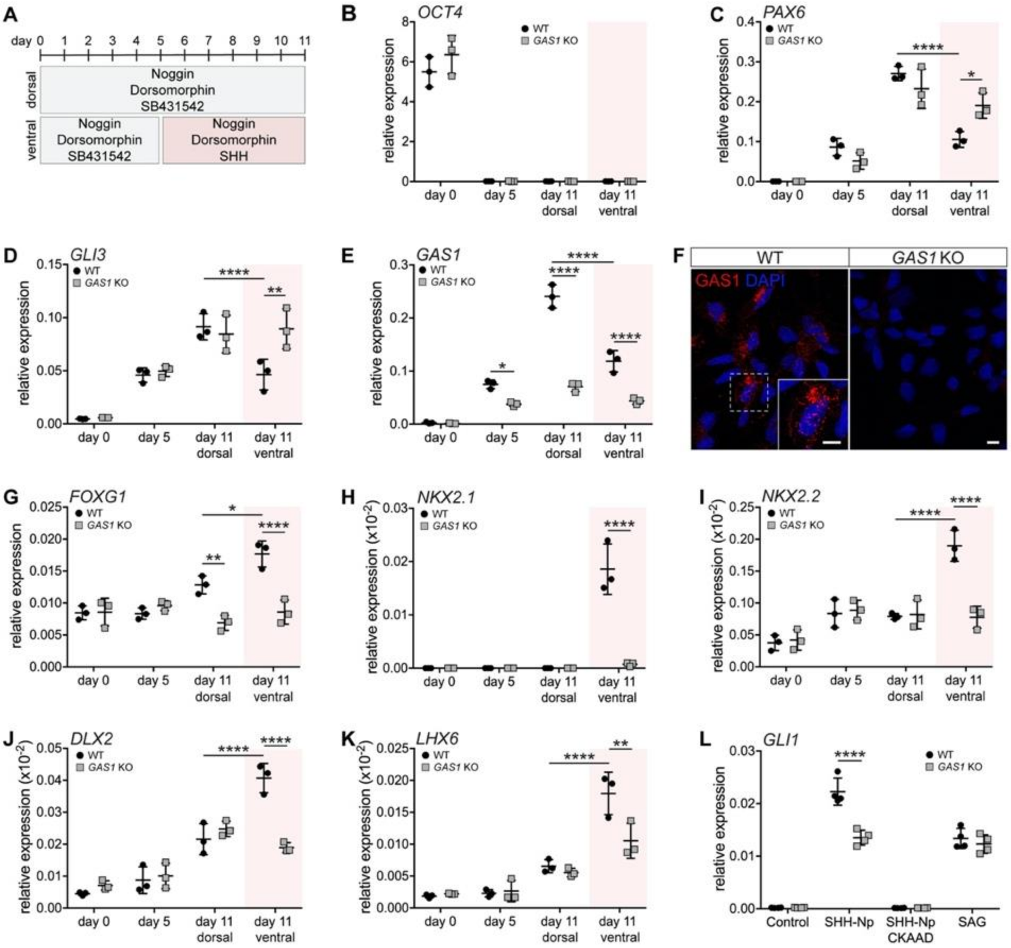

Marczenke et al., Figure 4

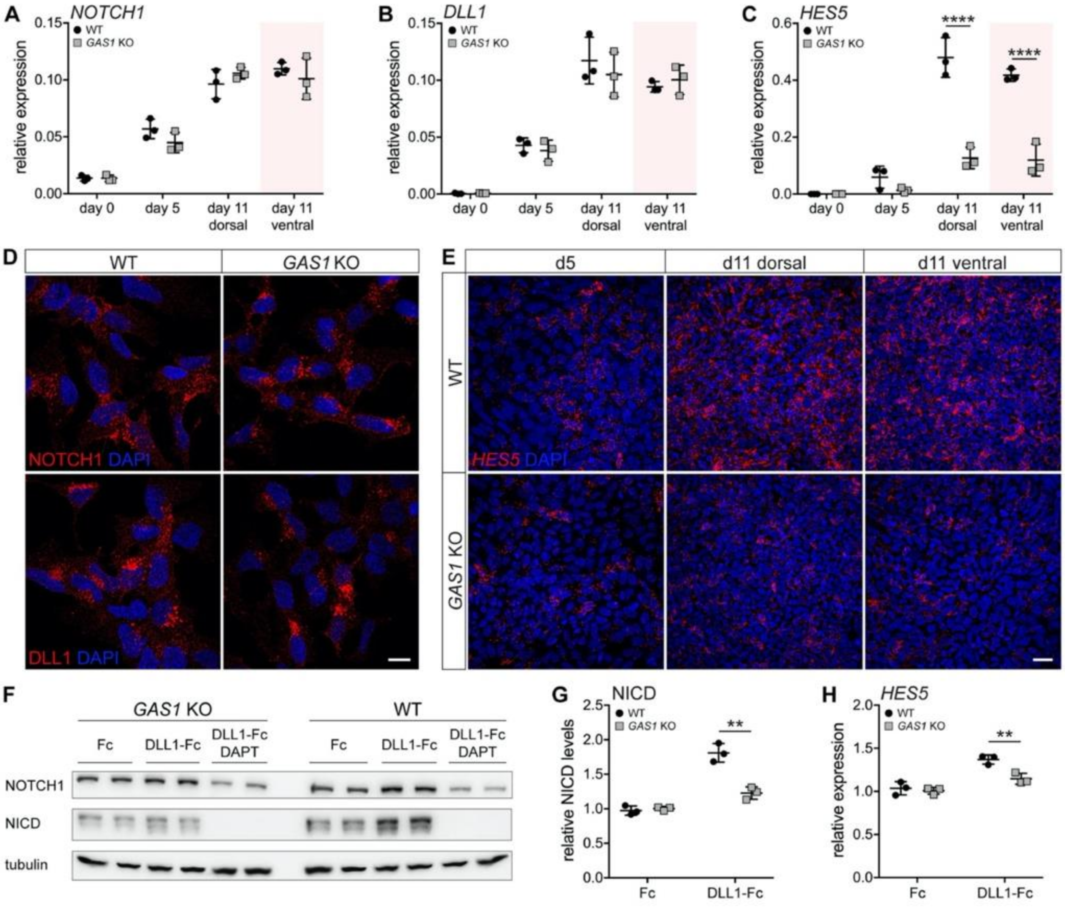

Marczenke et al., Figure 5

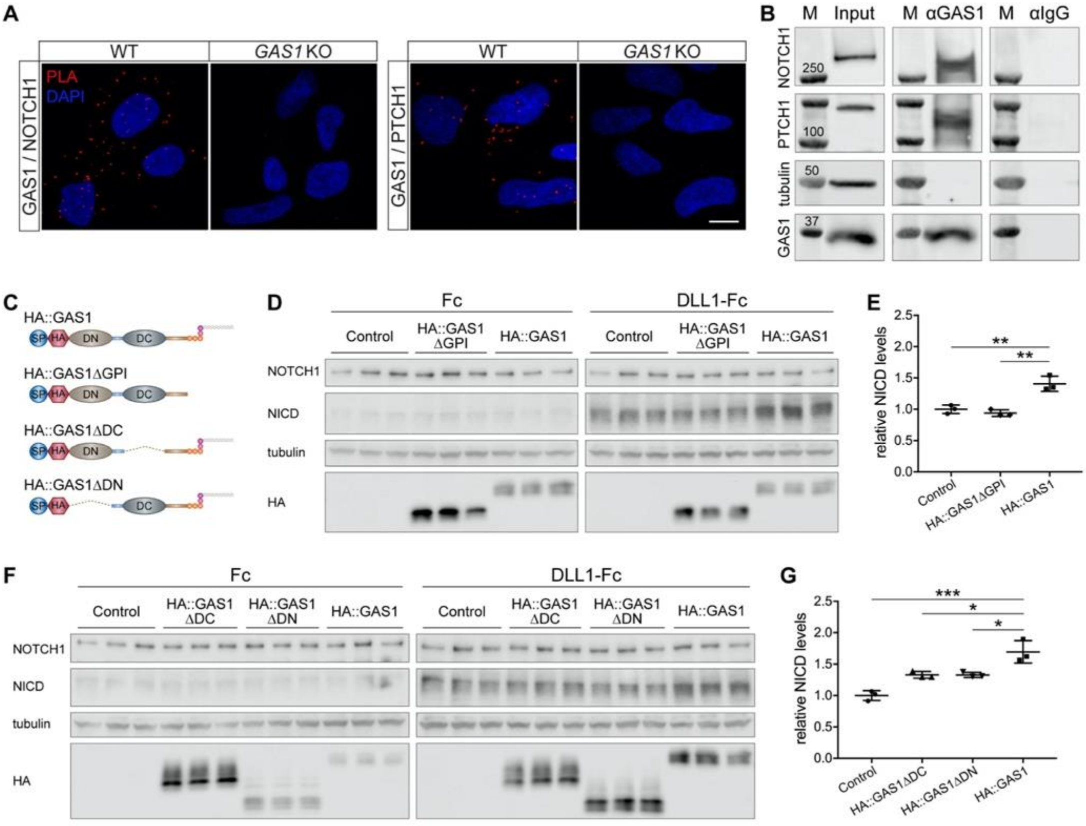

Marczenke et al., Figure 6

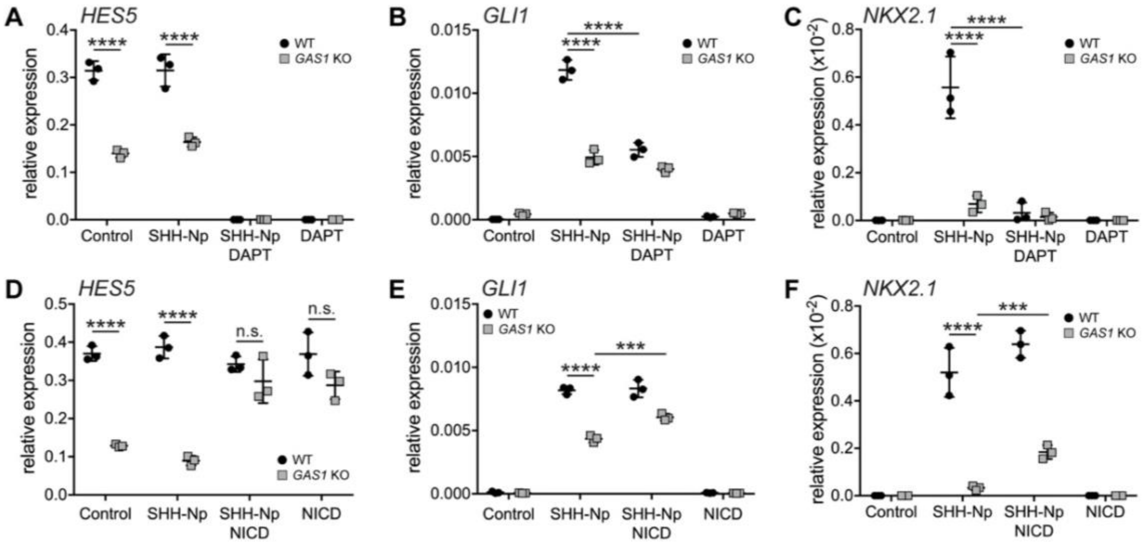

Marczenke et al., Figure 7

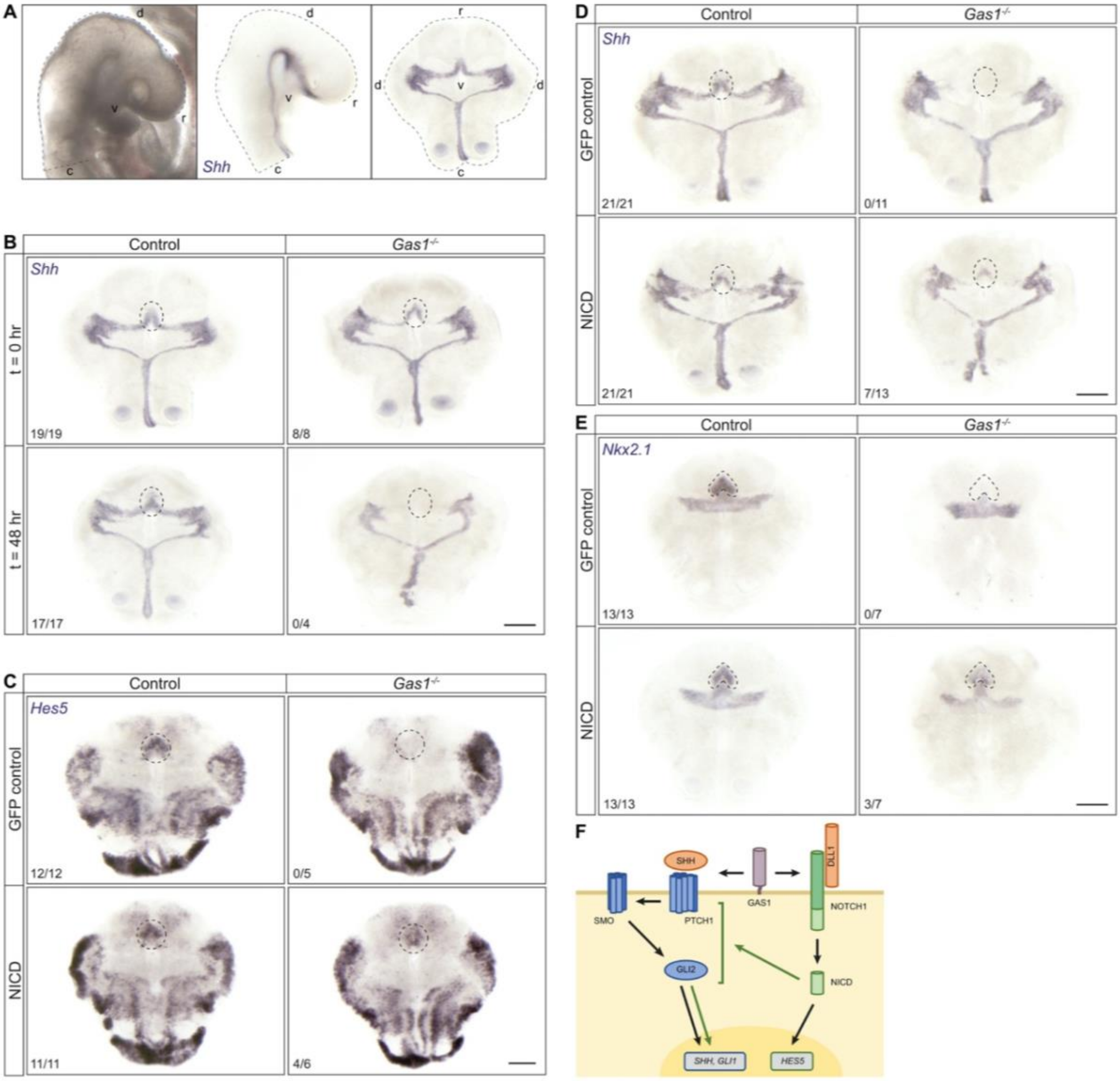

Marczenke et al., Figure 8

SUPPLEMENTARY METHODS

In situ hybridization and immunohistology on mouse tissue

The plasmid for generating the *in situ* hybridization (ISH) probe targeting *Shh* was kindly provided by A. P. McMahon (University of Southern California, Los Angeles). ISH probes detecting *Hes5* and *Nkx2.1* were generated in house targeting basepairs 573-1271 for *Hes5* (reference NM_010419.3) and basepairs 2032-2813 for *Nkx2.1* (reference NM_009385.2). Immunofluorescence staining was carried out using rabbit anti-SHH (1:50, sc-9024, Santa Cruz Biotechnology) or goat anti-GAS1(1:50, AF2644, R&D Systems), respectively, and secondary antibodies conjugated with Alexa Fluor fluorophores (1:1000, Invitrogen). RNAscope fluorescent ISH (FISH) on 6 µm paraffin sections was performed according to manufacturer's protocols using the Multiplex Fluorescent Reagent Kit v2 (ACD) with standard conditions for manual target retrieval and Protease Plus treatment. Following probes from ACD were used: *Shh* (3143661) or *Shh*-C2 (3143661-C2), *Gli1* (311011) or *Gli1*-C2 (311011-C2), *Notch1*-C2 (404641-C2), *Dll1*-C3 (425071-C3), *Hes5* (400991) or *Hes5*-C2 (400991-C2). Bound probes were visualized using Opal dyes 520 (FP1487001KT), 570 (FP1488001KT) or 620 (FP1495001KT, all from Akoya Biosciences) at a dilution of 1:1500.

Microdissection and bulk RNAseq

For laser capture microdissection (LCM), E10.0 embryos (30-33 somites) were dissected on ice and fixed in 2% paraformaldehyde (PFA) for two hours at 4°C. After washing with PBS twice, embryos were infiltrated with 30% sucrose in PBS for two hours at 4°C, sequentially incubated with 25%, 50%, and 75% Tissue Tek O.C.T. compound (Sakura) in 30% sucrose solution for 30 minutes at 4°C each before embedding in Tissue Tek O.C.T. Coronal 12 µm cryosections were collected on membrane slides (MembraneSlide NF 1.0 PEN, 415190-

9081-000, Zeiss), shortly washed in water, and dehydrated in cold 70% and 100% ethanol. Dried sections were stored in membrane slide chambers at -80°C. Before microdissection, slides were gradually chilled to room temperature (RT) by incubating at -20°C, 4°C, and RT for 20 minutes each. LCM was performed by using the Zeiss Axio Observer Z1. Dissected rostral ventral forebrain midlines were collected in AdhesiveCap 500 tubes (415190-9201-000, Zeiss), directly lysed in RNA lysis buffer, shortly stored on dry ice, and then transferred to -80°C. For processing, samples were thawed on ice and RNA was isolated using the RNeasy FFPE Kit (Qiagen) according to the manufacturer's manual. RNA integrity and yield were assessed using the Bioanalyzer 2100 (Agilent Technologies) and Qubit fluorometric quantification (Thermo Fisher Scientific), respectively. RNA with RNA integrity number (RIN) > 6.5 was used for cDNA library preparation using the SMARTer Stranded Total RNA-Seq Pico Kit (Takara), and libraries were sequenced in a 2 x 75 bp paired end run on an Illumina HiSeq 4000 system with 20 million reads per sample. The analysis involved five replicates for control and four replicates for *Gas1*$^{-/-}$ embryos. Each replicate consisted of a pool of five embryos of the respective genotype.

Salmon v0.12.0 (Patro et al., 2017) was used to quantify the expression of transcripts against the Ensembl release 94 of the *Mus musculus* transcriptome. The multiple forms of noncoding RNA present in the total RNA sequencing were removed from the GTF file provided by the same Ensembl release. Only "protein_coding" and lincRNA transcript types were kept. Transcripts quantified by Salmon but not present in the filtered GTF file were removed for the downstream analysis. DESeq2 R package (Love et al., 2014) was used with default parameters to find the differentially expressed genes (DEGs). Transcripts with less than 5 read counts were filtered and p-values were corrected for multiple testing using the Benjamini-Hochberg procedure. DEGs recorded in at least two genotypic replicates were subjected to gene ontology (GO) term enrichment analysis using AmiGO (Carbon et al.,

2009) and ConsensusPathDB (Kamburov et al., 2011; Kamburov et al., 2009), over-representation analysis and default parameters, while only GO terms with q-value ≤ 0.05 were considered. Heatmaps and PCA were generated using the heatmap.2 and prcomp function from the ggplot2 library in RStudio, respectively.

The RNA-seq data have been deposited in the ArrayExpress database at EMBL-EBI under accession number E-MTAB-10207.

Scorecard assay

Pluripotency and the ability of generating all three germ layers were assessed by TaqMan Scorecard Assay (Applied Biosystems) on spontaneously differentiated embryoid bodies (EB) (Tsankov et al., 2015). For EB formation, iPSCs were dissociated with Accutase, seeded into Nucleon Sphera 96-well U-shaped-bottom plates (Thermo Fisher Scientific) at a density of 8000 cells/well in E8 medium supplemented with 10 µg/ml Y27632, and centrifuged for 3 minutes at 200 g. Next day, the medium was replaced by DMEM/F12 supplemented with 10% KnockOut Serum Replacement and 1% penicillin-streptomycin (Gibco). The medium was changed every 3 days. iPSCs (day 0) and EBs (day 14, pool of 20 EBs per genotype) were subjected to RNA isolation followed by cDNA reverse transcription using the RNeasy Mini (Qiagen) and High-Capacity RNA-to-cDNA Kit (Applied Biosystems), respectively, before performing the Scorecard assay according to the manufacturer’s protocols. Gene expression data were analyzed via the web-based hPSC Scorecard Analysis Software (Thermo Fisher Scientific).

Generation of neural progenitor cells

The protocol for differentiating WT and *GAS1* KO cells into NPCs was published before (Flemming et al., 2020). Briefly, iPSCs were dissociated with Accutase and 20.000 cells/cm^2

were plated on Matrigel-coated plates in E8 medium supplemented with 10 µg/ml Y27632 for 24 hours. Cells were allowed to grow for 3 days in E8 medium until they were nearly confluent, after which the medium was changed to N2B27 differentiation medium containing 100 ng/ml noggin (6057-NG, R&D Systems), 200 nM dorsomorphin (sc-361173A, Santa Cruz Biotechnology) inhibiting BMP signaling and 10 µM SB431542 (Cay13031, Cayman Chemical) for the inhibition of TGFβ signaling. The medium was changed daily. For ventral-like NPC induction, the medium was replaced by N2B27 containing noggin, dorsomorphin, and 200 ng/ml SHH at day 5 of differentiation, and cells were grown for up to 6 more days.

Immunofluorescence staining and immunohistology of iPSCs/NPCs

Cells were washed with PBS to remove cell debris and fixed in 4% PFA for 15 minutes at RT. After washing with PBS, cells were permeabilized in blocking buffer containing 5% BSA and 0.5% Triton X100 for 1 hour at RT before incubating with primary antibodies diluted in blocking buffer at 4°C overnight. After washing in TBS with 1% Triton X-100 for 30 minutes and subsequently in TBS with 0.1% Tween 20, cells were incubated with secondary antibodies conjugated with Alexa Fluor fluorophores (Invitrogen) diluted 1:1000 in blocking buffer for 1-2 hours at RT. Cells were counterstained with DAPI and mounted with ProLong Gold Antifade Mountant (Life Technologies). Following primary antibodies were used: sheep anti-DLL1 (1:100, AF5026, R&D Systems), goat anti-GAS1 (1:50, AF2636, R&D Systems), goat anti-NANOG (1:100, AF1997, R&D Systems), rabbit anti-NKX2.1 (1:40, MAB94581, R&D Systems), sheep anti-NOTCH1 (1:200, AF5267, R&D Systems), rabbit anti-PAX6 (1:200, 901301, BioLegend), rabbit anti-OCT4 (1:400, sc-5279, Santa Cruz Biotechnology) and rabbit anti-SOX2 (1:100, ab97959, Abcam).

RNAscope FISH of *HES5* transcripts was performed using the Multiplex Fluorescent Reagent Kit v2 (ACD) according to manufacturer’s protocol and the technical note

"RNAscope Assay for Adherent Cells Cultured on Coverslips". Bound human *HES5* probe (521391) was visualized using Opal dye 570 (FP1488001KT) at a dilution of 1:1000.

Proximity ligation assay

Proximity ligation assay (PLA) was performed according to the manufacturer's instructions (Duolink PLA Fluorescence). PFA-fixed NPCs at differentiation day 7-9 were incubated with directly conjugated primary antibodies at a dilution of 1:100 generated with Duolink In Situ Probemaker PLUS and MINUS Kits. PLA signals were visualized using the Duolink In Situ Detection Reagent Kit Orange (all Sigma-Aldrich). Following primary antibodies were used: goat anti-GAS1 (AF2636, R&D Systems), sheep anti-NOTCH1 (AF5267, R&D Systems) and rabbi anti-PTCH1 (homemade).

Quantitative real-time-PCR

Total RNA was isolated using the RNeasy Mini Kit (Qiagen) according to the manufacturer's instructions with additionally treating the samples with RNase-free DNAse I (Qiagen) for 15 minutes at RT. One µg total RNA was reverse transcribed using the High-Capacity RNA-to-cDNA Kit (Applied Biosystems). The resulting cDNA was amplified using TaqMan oligonucleotide probes and the TaqMan Gene Expression Master Mix on a 7900HT Fast Real time PCR System and the Sequence detection system V2.4 (all Applied Biosystems). Results were analyzed using the comparative cycle threshold (CT) method. TaqMan probes from Applied Biosystems were *DLL1* (Hs00194509_m1), *DLX2* (Hs00269993_m1), *FOXG1* (Hs01850784_s1), *GAPDH* (Hs02758991_g1), *GAS1* (Hs00266715_s1), *GLI1* (Hs00171790_m1), *GLI3* (Hs00609233_m1), *HES5* (Hs01387463_g1), *LHX6* (Hs01030943_m1), *NANOG* (Hs02387400_g1), *NKX2.1* (Hs00968940_m1), *NKX2.2*

(Hs00159616_m1), *NOTCH1* (Hs01062014_m1), *OCT4* (Hs00999632_g1), *PAX6* (Hs00240871_m1) and *SOX2* (Hs01053049_s1).

Co-immunoprecipitation

NPCs were differentiated until day 6, seeded onto Matrigel-coated 6-well-plates at a density of 250000 cells/well, and transfected with pCIG-hGAS1-IRES-GFP (kindly provided by F. Charron, McGill University, Canada) using Lipofectamine2000 (Invitrogen) according to manufacturer's protocol. 48 hours after transfection, cells were fixed in 1% formaldehyde (Thermo Fisher Scientific) for 5 minutes at RT and quenched with cold 1.25 M glycine. Co-immunoprecipitation (Co-IP) was performed using the Pierce Crosslink Magnetic IP/Co-IP Kit (Thermo Fisher Scientific). For each reaction, 10 µg/ml goat anti-GAS1 antibody (AF2636, R&D Systems) or a non-immmune goat IgG control (01-6202, Invitrogen) were bound to 50 µl magnetic beads for 1 hour and crosslinked for 30 minutes. Cells were lysed with IP Lysis/Wash Buffer supplemented with cOmplete Protease Inhibitor Cocktail (Roche) for 1-2 hours on ice on a vertical shaker. The Pierce BCA Protein Assay Kit (Thermo Fisher Scientific) was used to determine protein concentration in cell lysates. Thirty µg protein lysate was used as input control and 200-300 µg protein lysate was incubated with crosslinked beads at 4°C overnight. Elution was performed for 30 minutes at RT on a rotator. Samples were incubated with Novex Tris-Glycine SDS Sample buffer (Invitrogen) supplemented with 2.5% 2-Mercaptoethanol for 5 minutes at 60°C, before subjecting to protein analysis by western blotting.

Western blot analysis

Protein expression in cells was evaluated by western blot analysis using standard procedures. Primary antibodies used for immunodetection were goat anti-GAS1 (1:500, AF2636, R&D

Systems), mouse anti-HA.11 (1:1000, 901513, BioLegend), rabbit anti-NOTCH1 (1:1000, 4380, Cell Signaling Technology), rabbit anti-cleaved NOTCH1 (1:500, 4147, Cell Signaling Technology) and mouse anti-tubulin (1:1000, CP06, Calbiochem). Primary antibodies were detected using secondary antibodies conjugated with horseradish peroxidase (diluted 1:1500; Sigma-Aldrich) and SuperSignal West Femto Maximum Sensitivity Substrate (Thermo Fisher Scientific). Protein levels were quantified by densitometric scanning of western blots using the Odyssey Fc Imaging System and Image Studio Lite Software (LI-COR Biosciences).

Lentivirus production

For producing NICD or GFP overexpressing lentivirus particles, HEK293TN cells were cultivated on 0.0025% poly-L-Lysin (Sigma-Aldrich) coated culture flasks in Opti-MEM (Gibco). Cells were transfected with lentivirus envelope and packaging plasmids pMD2.D, pMDLg/pRRE and pRSV-Rev (Addgene plasmids #12259, #12251 and #12253, respectively, and the control plasmid EF.PGK.GFP (Addgene plasmid #17618) or the NICD expressing plasmid NOTCH1 intracellular domain-pcw107-V5 (Addgene plasmid #64622) using Lipofectamine2000 according to manufacturer’s instructions in Opti-MEM supplemented with 25 µM chloroquine (Sigma-Aldrich). After 6 hours, the medium was changed to Opti-MEM supplemented with 10 µM sodium butyrate (Sigma-Aldrich). Cells were further cultivated for 2-3 days and the medium replaced and collected every day. The collected medium was centrifuged for 15 minutes at 500 g at 4°C to remove cell debris and every 3 volumes of lentivirus containing supernatant was incubated with 1 volume of cold Lenti-X Concentrator (Clontech Laboratories) on ice at 4°C overnight. The mixture was centrifuged at 4°C for 45 minutes at 1500 g and lentiviral pellets were resuspended in 1:100 of the original volume using cold and sterile PBS. Lentiviral particle containing solutions were aliquoted and stored at -80°C.

SUPPLEMENTARY EXCEL FILE

The supplementary excel file lists all 324 differentially expressed genes (DEGs) identified by comparative bulk RNA sequencing of the microdissected rostral ventral neuroepithelium from E10.0 *Gas1*$^{+/+}$ and *Gas1*$^{-/-}$ embryos. Fold change in transcript levels are given as *Gas1*$^{-/-}$ compared to *Gas1*$^{+/+}$ embryos. q values represent p values corrected for multiple testing using the Benjamini-Hochberg procedure.

SUPPLEMENTARY TABLES

Table S1: Expression values of differentially expressed genes related to the gene ontology term “smoothened signaling pathway” comparing *Gas1*$^{-/-}$ with control embryos

MGI symbol	log2 fold change	q value
Kif7	-8.515	3.794E-04
Sin3a	-7.752	7.008E-03
Nme7	-5.377	3.881E-02
Nkx2.2	-4.422	2.636E-03
Hes5	-3.788	1.350E-02
Ptch1	-1.957	4.501E-02
Shh	-1.825	8.659E-06
Scube1	2.288	1.404E-10
Fgf10	3.054	3.467E-16

Table S2: Expression values of differentially expressed genes related to the gene ontology term “NOTCH signaling pathway” in *Gas1*$^{-/-}$ embryos as compared to controls

MGI symbol	log2 fold change	q value
Tcf3	-22.727	1.566E-09
Sin3a	-7.752	7.008E-03
Traf7	-7.743	3.745E-07
Hes5	-3.788	1.350E-02
Dll1	-3.376	2.040E-05
Mfng	-2.859	6.735E-04
Dll3	-2.619	4.743E-02
Nrarp	-2.011	1.851E-02
Notch1	-1.694	4.825E-04
Fat4	2.063	8.931E-09
Fgf10	3.054	3.467E-16
Tbx2	3.426	1.114E-05

SUPPLEMENTARY REFERENCES

Carbon, S., Ireland, A., Mungall, C. J., Shu, S., Marshall, B., Lewis, S., Ami, G. O. H. and Web Presence Working, G. (2009). AmiGO: online access to ontology and annotation data. *Bioinformatics* **25**, 288-289.

Flemming, J., Marczenke, M., Rudolph, I. M., Nielsen, R., Storm, T., Erik, I. C., Diecke, S., Emma, F. and Willnow, T. E. (2020). Induced pluripotent stem cell-based disease modeling identifies ligand-induced decay of megalin as a cause of Donnai-Barrow syndrome. *Kidney Int* **98**, 159-167.

Kamburov, A., Pentchev, K., Galicka, H., Wierling, C., Lehrach, H. and Herwig, R. (2011). ConsensusPathDB: toward a more complete picture of cell biology. *Nucleic Acids Res* **39**, D712-717.

Kamburov, A., Wierling, C., Lehrach, H. and Herwig, R. (2009). ConsensusPathDB--a database for integrating human functional interaction networks. *Nucleic Acids Res* **37**, D623-628.

Love, M. I., Huber, W. and Anders, S. (2014). Moderated estimation of fold change and dispersion for RNA-seq data with DESeq2. *Genome Biol* **15**, 550.

Patro, R., Duggal, G., Love, M. I., Irizarry, R. A. and Kingsford, C. (2017). Salmon provides fast and bias-aware quantification of transcript expression. *Nat Methods* **14**, 417-419.

Tsankov, A. M., Akopian, V., Pop, R., Chetty, S., Gifford, C. A., Daheron, L., Tsankova, N. M. and Meissner, A. (2015). A qPCR ScoreCard quantifies the differentiation potential of human pluripotent stem cells. *Nat Biotechnol* **33**, 1182-1192.

SUPPLEMENTARY FIGURE

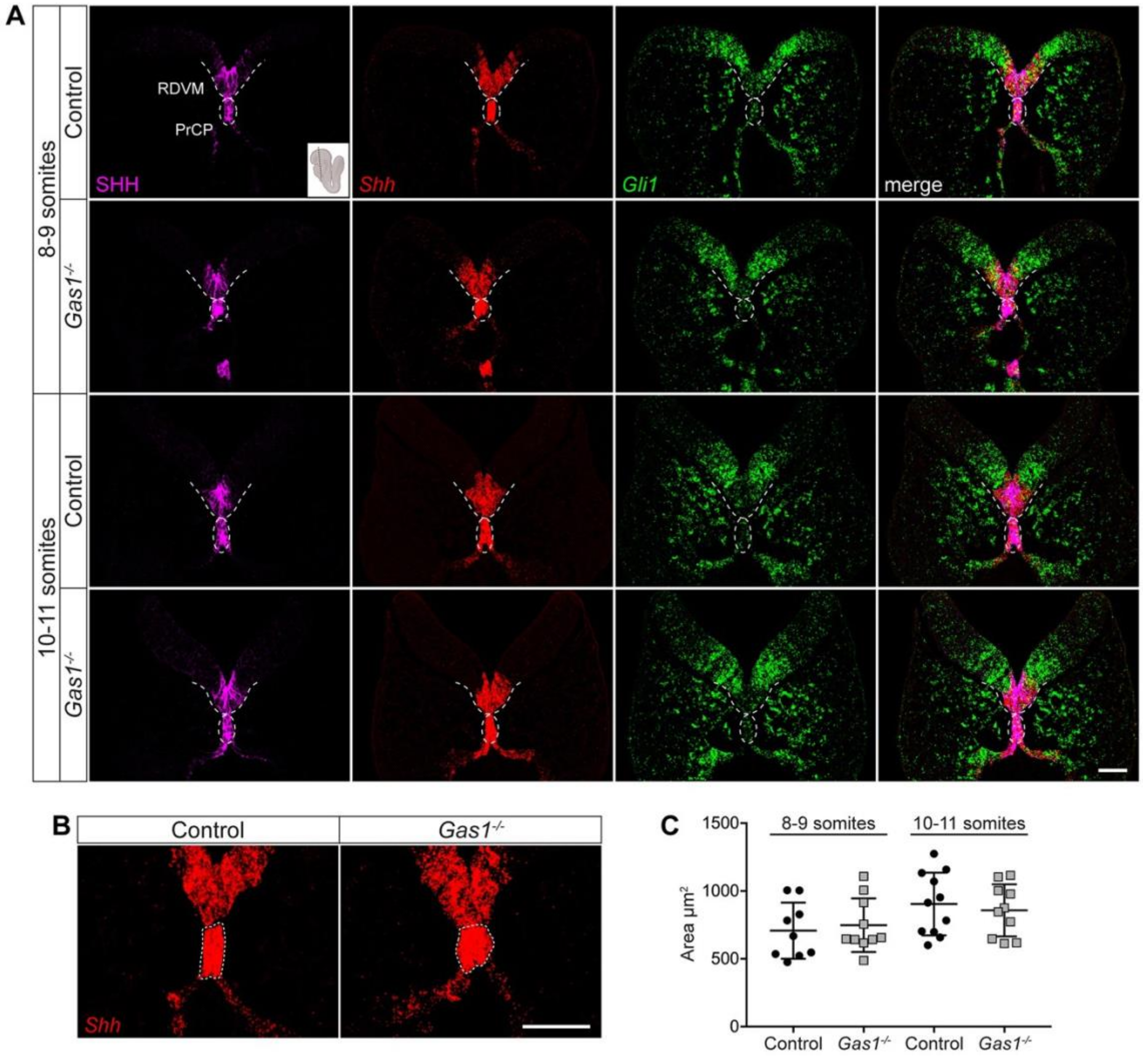

Supplementary figure S1: Expression and activity of SHH are not impacted in *Gas1*$^{-/-}$ embryos during early neurulation.

(**A**) SHH protein (magenta; left panels) as well as *Shh* (red; middle left panels) and *Gli1* transcripts (green; middle right panels) were co-detected on coronal sections from E8.5 control or *Gas1*$^{-/-}$ embryos (8-9 and 10-11 somite stages) using immunohistology or fluorescence *in situ* hybridization (FISH), respectively. Both single and merged channel (right panels) configurations are shown for each section. Dotted lines demarcate prechordal plate (PrCP) and rostral diencephalon ventral midline (RDVM). The inset (adapted from BioRender.com) illustrates the plane of section for all panels. n=3 embryos per somite stage and genotype. (**B**) Detection of *Shh* transcripts on coronal sections of E8.5 control and *Gas1*$^{-/-}$ embryos using FISH. Image magnified from panel (A). Dotted lines demarcate the PrCP. (**C**) The area of the *Shh* expression domain in the PrCP of control and *Gas1*$^{-/-}$ embryos at 8-9 and 10-11 somites was quantified using FISH (as exemplified in B). Areas are given as mean values of 3-4 consecutive sections per embryo. No significant differences in PrCP area was seen comparing *Gas1*$^{-/-}$ and control embryos using unpaired *t* test. n=9-11 embryos per somite stage and genotype. Scale bars: 50 µm.

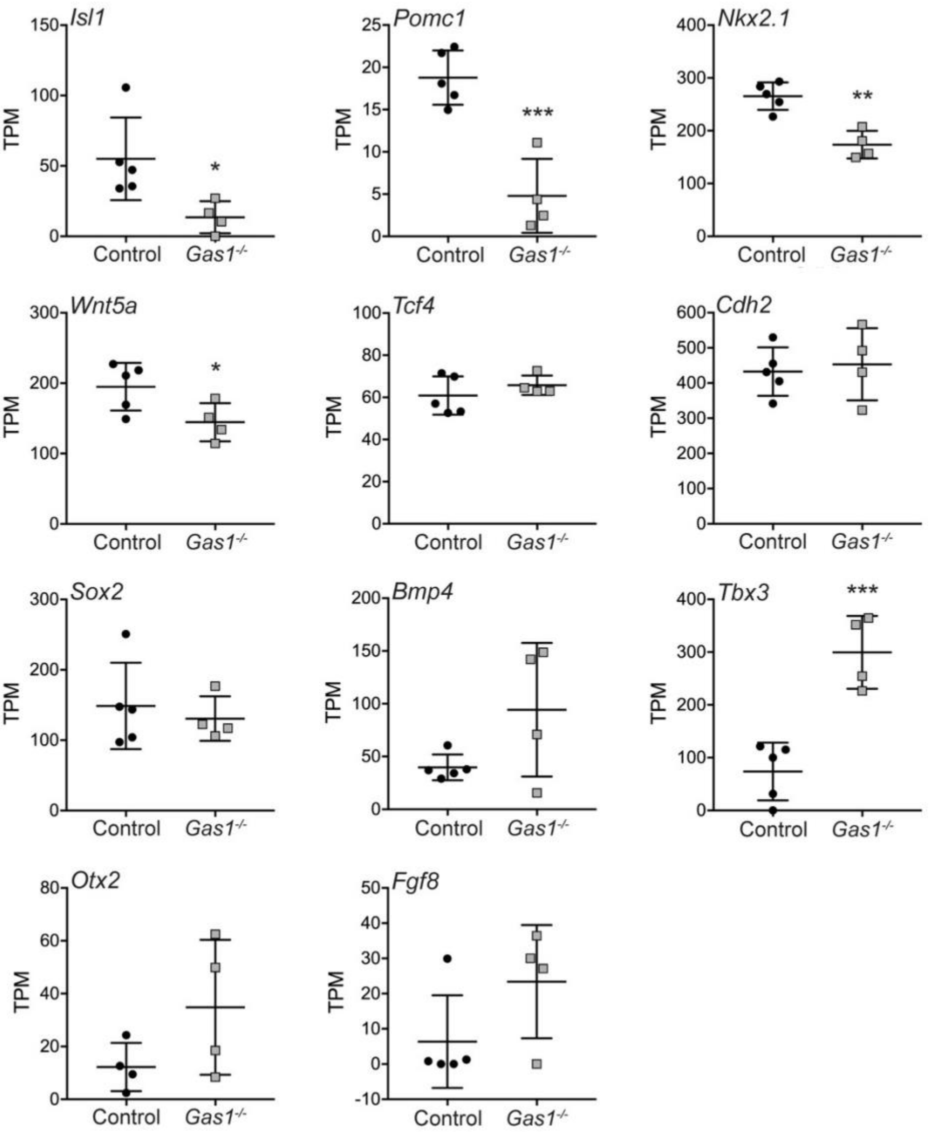

Supplementary figure S2: Global RNA sequencing indicates dysregulated expression of SHH target genes in the rostral ventral forebrain midline of *Gas1*$^{-/-}$ embryos.

RNA expression data for the indicated SHH target genes in the isolated rostral ventral forebrain midline of control and *Gas1*$^{-/-}$ embryos at E10.0 are shown. Levels are given as transcripts per million (TPM). n=5 (Control) and n=4 (*Gas1*$^{-/-}$) samples of 5 embryos per replicate pool. Significant differences were determined using unpaired *t*-test. * $p < 0.05$, ** $p < 0.01$, *** $p < 0.001$.

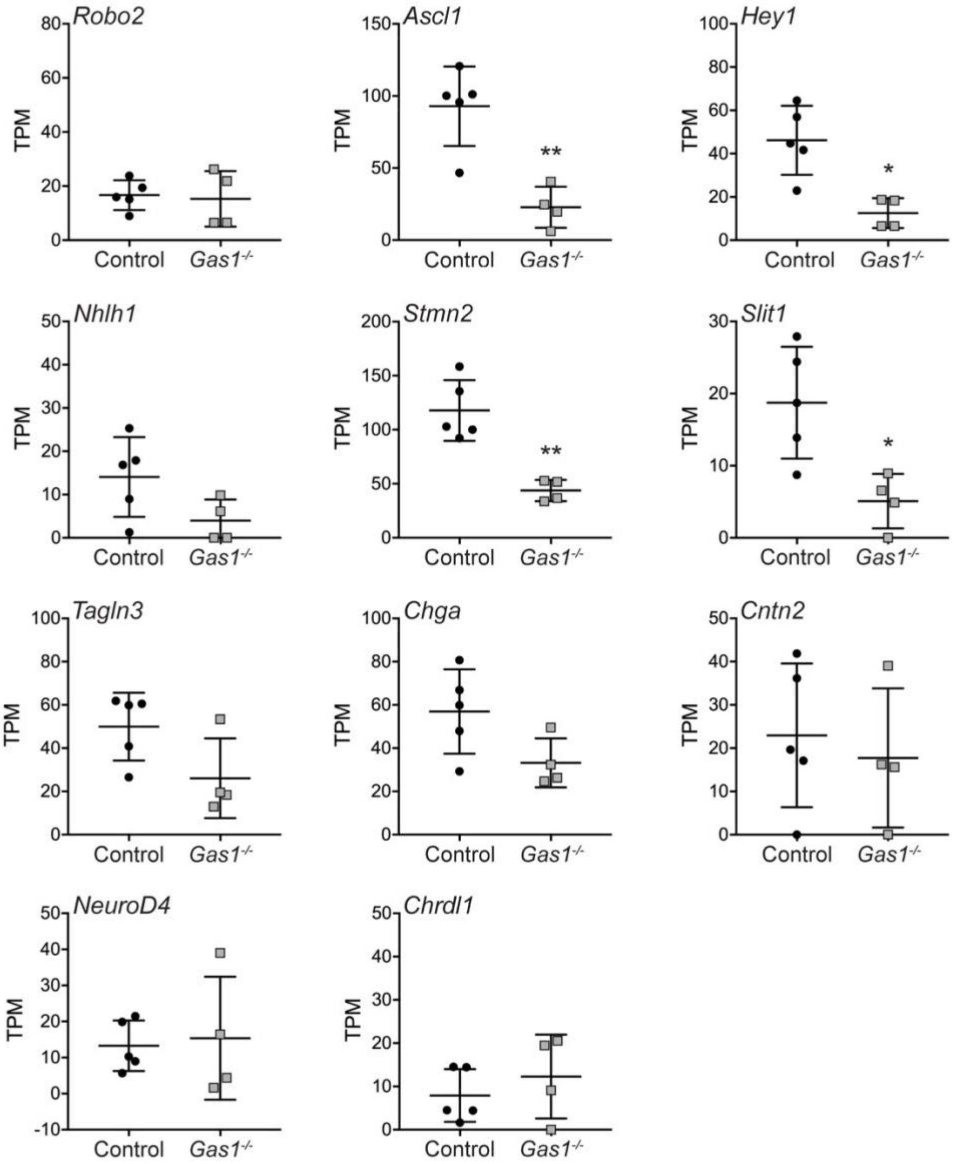

Supplementary figure S3: Global RNA sequencing indicates dysregulated expression of NOTCH target genes in the rostral ventral forebrain midline of *Gas1*$^{-/-}$ embryos.

RNA expression data for the indicated **NOTCH** target genes in the isolated rostral ventral forebrain midline of control and *Gas1*$^{-/-}$ embryos at E10 are shown. Levels are given as transcripts per million (TPM). n=5 (Control) and n=4 (*Gas1*$^{-/-}$) replicate pools with 5 embryos per pool. Significant differences were determined using unpaired *t*-test. * $p < 0.05$, ** $p < 0.01$.

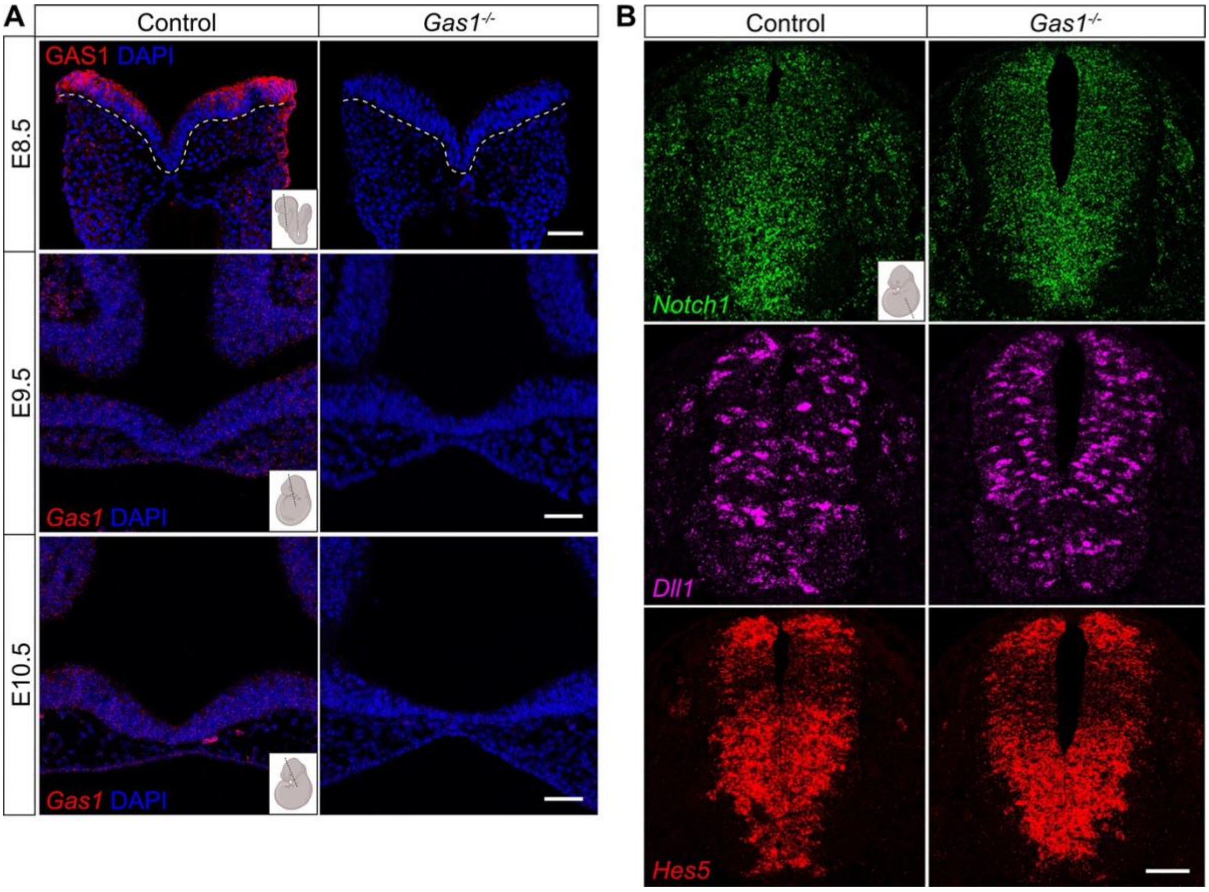

Supplementary figure S4: *Gas1* deficiency does not impact NOTCH activity in the caudal neural tube.

(**A**) Immunodetection of GAS1 protein (upper panel, red) and *Gas1* transcripts (middle and lower panels, red) in the rostral neuroepithelium of control but not *Gas1*$^{-/-}$ embryos at the indicated stages of development. Nuclei are counterstained with DAPI. In the E8.5 image, dotted lines indicate the rostral neuroepithelium. (**B**) Detection of *Notch1* (green; upper panels), *Dll1* (magenta; middle panels), and *Hes5* (red; lower panels) transcripts on coronal sections of E10.5 spinal cord using FISH. Transcript levels in *Gas1*$^{-/-}$ embryos are similar to those in controls. Scale bars: 50 µm. n=3 embryos per somite stage and genotype. Insets demonstrate plane of sections (adapted from BioRender.com).

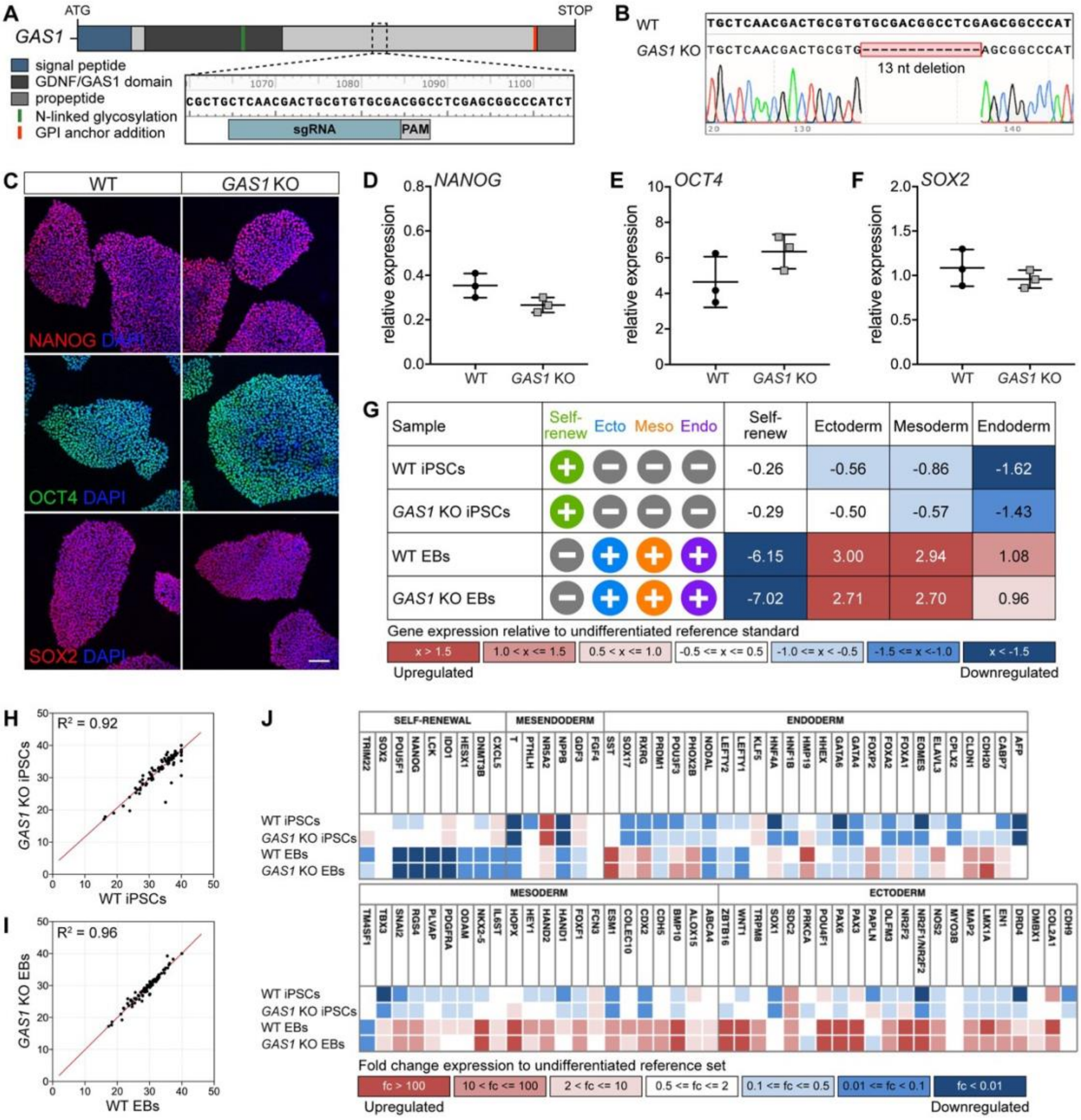

Sample	Self-renew	Ecto	Meso	Endo	Self-renew	Ectoderm	Mesoderm	Endoderm
WT iPSCs	+	−	−	−	-0.26	-0.56	-0.86	-1.62
GAS1 KO iPSCs	+	−	−	−	-0.29	-0.50	-0.57	-1.43
WT EBs	−	+	+	+	-6.15	3.00	2.94	1.08
GAS1 KO EBs	−	+	+	+	-7.02	2.71	2.70	0.96

Gene expression relative to undifferentiated reference standard

x > 1.5	1.0 < x <= 1.5	0.5 < x <= 1.0	-0.5 <= x <= 0.5	-1.0 <= x < -0.5	-1.5 <= x <-1.0	x < -1.5
Upregulated						Downregulated

Supplementary figure S5: iPSC-derived neuroepithelial cells to model GAS1 function in the RDVM

(**A**) CRISPR/Cas9 strategy for disrupting *GAS1*. Structural organization of human *GAS1* indicating the coding sequence targeted by the single guide (sg) RNA. Nucleotide numbers according to human *GAS1* sequence NM_002048.3. PAM, protospacer adjacent motif. (**B**) Disruption of the *GAS1* coding sequence by a 13 nucleotides long deletion in iPSC line *GAS1*

KO. The respective wild-type *GAS1* sequence is shown above (WT). (**C**) Immunofluorescence detection of pluripotency markers NANOG, OCT4 and SOX2 in WT and *GAS1* KO iPSC lines. Nuclei were counterstained with DAPI. Scale bar: 50 µm. (**D-F**) qRT-PCR of relative transcript levels for *NANOG* (D), *OCT4* (E), and *SOX2* (F) in WT and *GAS1* KO iPSCs. Levels in (D-F) are given as CT values normalized to transcript levels of *GAPDH* ($2^{-\}\mathrm{CT}}$ ± standard derivation (SD). No statistically significant differences were seen comparing genotypes (unpaired *t* test, n=3 biological replicates). (**G-J**) TaqMan Scorecard analysis of WT and *GAS1* KO iPSCs and spontaneously differentiated embryoid bodies (EBs) after 14 days, respectively. (G) WT and *GAS1* KO iPSCs and EBs showed similar scores for self-renewal, ectoderm, mesoderm and endoderm differentiation compared to the expression profile of the reference standard. EBs downregulated self-renewal genes indicated by (-), while upregulating ectoderm, mesoderm and endoderm genes as indicated by (+). (H, I) Correlation plots depict comparable expression rates of the 96 analyzed genes between iPSCs (H) and EBs (I) of different genotypes. Corresponding correlation coefficients (R^2) are shown in the upper left corner. (J) Heatmaps of the analyzed genes related to self-renewal, mesendoderm, endoderm, mesoderm and ectoderm fate. Values and colors correlate to the fold changes (FC) of each gene relative to the undifferentiated reference set.

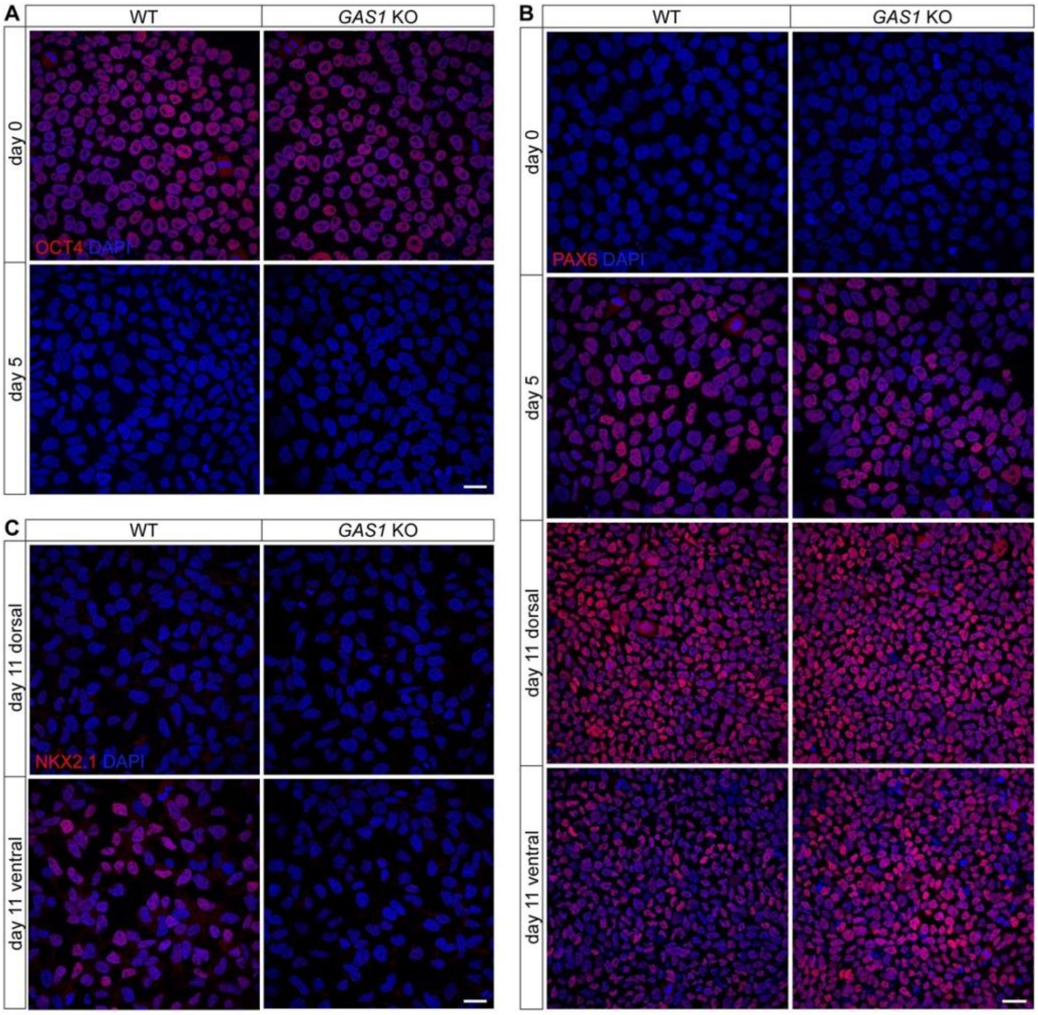

Supplementary figure S6*: GAS1* KO iPSCs fail to induce a SHH-dependent ventral neuroepithelial cell fate.

(**A**) WT and *GAS1* KO iPSCs (day 0), and day 5 NPCs derived thereof, were stained for multipotency marker OCT4 (red). (**B**) Immunodetection of PAX6 (red) in WT and *GAS1* KO iPSCs at the indicated timepoints of neuroepithelial differentiation. The dorsal marker PAX6 is downregulated in WT, but not in *GAS1* KO NPCs, upon SHH-dependent ventral cell fate induction (panel day 11 ventral). (**C**) Immunodetection of NKX2.1 (red) in WT and *GAS1* KO NPCs at day 11 of dorsal or ventral neuroepithelial differentiation. The ventral marker NKX2.1 is upregulated in WT, but not in *GAS1* KO NPCs, upon SHH-induced ventralization. Nuclei in (A-C) were counterstained with DAPI. Scale bars: 25 µm.

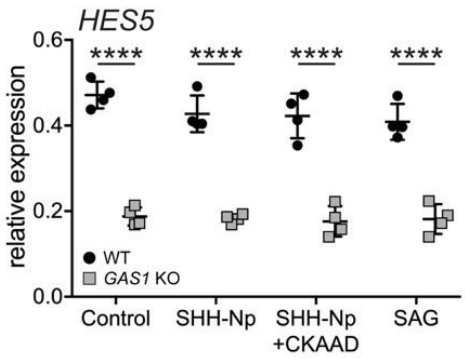

Supplementary figure S7: Loss of SHH signaling does not impact *HES5* expression in NPCs.

Relative transcript levels of *HES5* were determined by qRT-PCR in NPCs at day 8-10 of differentiation. Cells had been treated overnight with control medium, or with medium containing 200 nM smoothened agonist (SAG) or SHH-Np, in the absence or presence of 50 nM cyclopamine-KAAD (CKAAD). n=4 biological replicates per genotype and condition. Levels are given as CT values normalized to transcript levels of *GAPDH* ($2^{-\Delta CT}$ ± standard derivation (SD). Statistical analyses were performed by two-way ANOVA with Bonferroni post hoc test. **** $p < 0.0001$.

Ensemble ID	MGI symbol	log2 fold change	q value
ENSMUST00000233729	Vmn2r73	23,0388729	6,52E-11
ENSMUST00000066509	Etl4	9,772502535	0,000545849
ENSMUST00000170109	Slit2	9,752889788	0,000430853
ENSMUST00000178134	Mdn1	9,604241033	0,000593057
ENSMUST00000105251	R3hdm2	9,257716177	0,000775811
ENSMUST00000112836	Amot	9,256358886	5,76E-10
ENSMUST00000187389	Matr3	9,176571943	0,001365088
ENSMUST00000052629	Igsf9	9,047239397	3,36E-11
ENSMUST00000087864	Uvssa	8,971597375	0,001887413
ENSMUST00000076091	Ctf2	8,85036478	0,001597157
ENSMUST00000145567	Cul7	8,666925237	0,003242495
ENSMUST00000120847	Lrrc8d	8,520440722	0,00281618
ENSMUST00000187584	Tns1	8,344808519	0,007593907
ENSMUST00000114656	Fmr1	8,268191076	0,004326576
ENSMUST00000170002	Papola	8,23860062	8,66E-09
ENSMUST00000075916	Zfp12	8,206981288	0,00456521
ENSMUST00000176383	Zfhx4	8,18774408	0,007219252
ENSMUST00000087195	Ociad2	8,088802576	3,71E-09
ENSMUST00000217642	Olfr720	8,067553517	0,000412167
ENSMUST00000110085	Bicd2	8,056114901	0,00913799
ENSMUST00000211638	Tubgcp2	8,004355326	0,01145264
ENSMUST00000130313	Plagl1	7,919645	0,010694645
ENSMUST00000227192	Elf1	7,897394592	0,010694645
ENSMUST00000176114	Zfp536	7,835043996	1,78E-08
ENSMUST00000168828	Zfp385a	7,778624816	2,70E-07
ENSMUST00000055539	Timeless	7,737299193	0,014395154
ENSMUST00000182539	Ccnd3	7,718829864	0,020476492
ENSMUST00000138157	Frmd5	7,705106815	0,012626308
ENSMUST00000119254	Zfp827	7,689870849	1,13E-07
ENSMUST00000102842	Rtn4	7,652100111	0,000104374
ENSMUST00000170017	Glod4	7,515695865	0,024839415
ENSMUST00000233830	Vmn2r108	7,480526921	0,017688127
ENSMUST00000163969	Tro	7,467771789	0,024175398
ENSMUST00000232952	Vmn2r8	7,46288917	0,023973857
ENSMUST00000119523	Fbxl5	7,428256346	0,019950895

ENSMUST00000185524	Armc8	7,374488479	0,029493418
ENSMUST00000151952	Mgat4a	7,306076064	0,038497555
ENSMUST00000155272	Ppat	7,281375449	0,000135916
ENSMUST00000209139	Ptov1	7,224003845	1,40E-05
ENSMUST00000012161	Scarf2	7,206248264	2,96E-06
ENSMUST00000182622	Polq	7,193211412	0,038851165
ENSMUST00000147214	Prmt5	7,165579684	0,038497555
ENSMUST00000153970	Fbxo22	7,165091331	0,04081434
ENSMUST00000102822	Nrp2	7,141014905	3,62E-05
ENSMUST00000223982	Ptprm	7,138935347	0,039899463
ENSMUST00000168164	Pcid2	7,11337628	0,044618201
ENSMUST00000174152	Xpo4	6,932998495	3,57E-05
ENSMUST00000100794	Myo18a	6,842290068	0,006447953
ENSMUST00000084354	Spata6	6,670097544	0,00057943
ENSMUST00000226437	Laptm4b	6,567785083	0,000947901
ENSMUST00000196852	Prom1	6,505042488	0,001146238
ENSMUST00000172697	Mecom	6,497207298	0,043252968
ENSMUST00000106225	Tepsin	6,470203277	0,001664335
ENSMUST00000205806	Kif22	6,451162549	0,000994943
ENSMUST00000113250	Impg1	6,404310535	0,00081783
ENSMUST00000054368	Gimap1	6,363823385	0,000275106
ENSMUST00000043865	Mpst	6,345328339	0,012394782
ENSMUST00000118429	Tmem41b	6,23801774	0,041032643
ENSMUST00000224378	Dennd6a	6,213877041	0,000455247
ENSMUST00000102541	Gale	6,12141055	0,048060047
ENSMUST00000178226	Ankrd44	6,114074627	0,001854816
ENSMUST00000053459	Pxdc1	6,075757882	0,021976137
ENSMUST00000222699	Gm49384	6,002688592	0,003306241
ENSMUST00000225894	Nup153	5,993243494	0,018677243
ENSMUST00000225170	Mrps30	5,886474224	0,002872406
ENSMUST00000114607	Etl4	5,676088121	0,008793449
ENSMUST00000129304	Rufy1	5,584923307	0,002520641
ENSMUST00000172727	Vdac2	5,576242546	0,013966734
ENSMUST00000110947	Arhgap11a	5,554306458	0,020274512
ENSMUST00000197987	Zzz3	5,509976921	0,003157731
ENSMUST00000064364	Rnf185	5,440582582	0,007393589

ENSMUST00000146385	Ccdc85a	5,298591664	0,029493418
ENSMUST00000088627	Zic3	5,243114	0,000160099
ENSMUST00000226005	Fbxo16	5,101679458	0,030361828
ENSMUST00000159813	Zdhhc4	4,914245684	0,013966734
ENSMUST00000136870	Etl4	4,827729281	0,041778511
ENSMUST00000208023	Slc35a2	4,751001996	0,017836952
ENSMUST00000126931	Mrc2	4,604477737	0,025009042
ENSMUST00000077925	Unc5b	4,090940476	0,01026614
ENSMUST00000121707	Adgrl3	4,01553679	0,043716943
ENSMUST00000232303	Ppil2	3,926000521	0,044140401
ENSMUST00000102728	Fign	3,867433336	0,039365526
ENSMUST00000036992	Lmo1	3,471777634	0,009517765
ENSMUST00000000095	Tbx2	3,425590796	1,11E-05
ENSMUST00000016907	Scube1	3,40879513	0,029501541
ENSMUST00000028665	Patl2	3,356822906	0,027194169
ENSMUST00000144773	Scube1	3,224940225	1,06E-06
ENSMUST00000144238	Ewsr1	3,116340301	0,006642067
ENSMUST00000104955	Sowaha	3,096762103	4,68E-07
ENSMUST00000022246	Fgf10	3,053940783	3,47E-16
ENSMUST00000038107	Cited2	3,035681121	1,31E-05
ENSMUST00000030372	Col9a2	2,862694735	0,002332657
ENSMUST00000025778	Gldc	2,317492708	0,003242921
ENSMUST00000054294	Fzd1	2,309699677	0,004653212
ENSMUST00000229057	Scube1	2,288399683	1,40E-10
ENSMUST00000106236	Unc5c	2,261050582	0,001407661
ENSMUST00000216150	Zbtb16	2,199324005	0,000299757
ENSMUST00000023610	Adamts1	2,170374534	0,02034423
ENSMUST00000124768	Hexdc	2,150466008	0,020083517
ENSMUST00000188952	Epha4	2,122635474	0,042693027
ENSMUST00000061260	Fat4	2,062554716	8,93E-09
ENSMUST00000171496	Scube1	2,046321923	0,013237359
ENSMUST00000162056	Mff	2,022490425	0,030087143
ENSMUST00000031668	Col1a2	2,008074154	2,57E-05
ENSMUST00000006614	Epha2	1,912310187	0,001030905
ENSMUST00000054178	Nrip1	1,854930641	0,027413236
ENSMUST00000023749	Tmbim6	1,78671745	0,002388602

ENSMUST00000225316	Epb41l3	1,532444584	0,003373433
ENSMUST00000093852	Zbtb16	1,511694551	0,038349211
ENSMUST00000037287	Cdkn1c	1,485017856	0,000178337
ENSMUST00000142877	Grb10	1,36641594	0,02629184
ENSMUST00000023123	Col2a1	1,333494305	0,030903593
ENSMUST00000096053	Slf2	1,299046455	0,000353456
ENSMUST00000180353	Sox1	-1,118574908	0,00425178
ENSMUST00000021810	Id4	-1,21922269	0,03152511
ENSMUST00000105845	Ephb2	-1,264599605	0,012878834
ENSMUST00000034279	Gse1	-1,266077318	0,024947924
ENSMUST00000114013	Map2	-1,33736891	0,037743438
ENSMUST00000096441	Morc2a	-1,38040294	0,044608778
ENSMUST00000029002	Stmn2	-1,423696692	0,029501541
ENSMUST00000186247	Ank3	-1,438396037	0,007123519
ENSMUST00000017288	Rnd3	-1,498532498	0,027131634
ENSMUST00000121805	Dpysl3	-1,510774339	0,018247619
ENSMUST00000035471	Lama1	-1,516963593	0,000259899
ENSMUST00000002412	Ncan	-1,52133076	3,55E-05
ENSMUST00000021519	Six6	-1,536898211	0,002430754
ENSMUST00000028944	Acss1	-1,564376689	0,026512419
ENSMUST00000035208	Bsn	-1,604235603	0,006682059
ENSMUST00000028288	Notch1	-1,693543281	0,000482494
ENSMUST00000075774	Tubb2b	-1,746439793	0,005149891
ENSMUST00000002708	Shh	-1,825180608	8,66E-06
ENSMUST00000053491	Pou3f1	-1,836848578	0,036727663
ENSMUST00000151894	Pfkp	-1,844338833	0,031650761
ENSMUST00000194663	Ptch1	-1,956683729	0,045012404
ENSMUST00000046687	Spon1	-1,96752922	0,002606206
ENSMUST00000104999	Nrarp	-2,010565656	0,018505365
ENSMUST00000113470	Prdm12	-2,035334711	0,000269561
ENSMUST00000071134	Tubb3	-2,043173907	9,35E-06
ENSMUST00000140558	2310057J18Rik	-2,096332155	0,013792575
ENSMUST00000001304	Ckb	-2,142976561	0,018804479
ENSMUST00000020537	Nsg2	-2,242954682	0,021612503
ENSMUST00000069520	Syp	-2,249507477	0,046228187
ENSMUST00000108315	Dll3	-2,618740465	0,047425878

ENSMUST00000028727	Snap25	-2,678450195	0,009639682
ENSMUST00000170662	Sox21	-2,801193909	0,00513065
ENSMUST00000102963	Dnaic1	-2,843009915	0,038497555
ENSMUST00000018313	Mfng	-2,859190874	0,000673528
ENSMUST00000147604	Aim2	-2,961101792	0,046873404
ENSMUST00000156158	Trafd1	-2,979599086	0,048162478
ENSMUST00000147363	Ptgr2	-3,014039637	0,046228187
ENSMUST00000044297	Igfbpl1	-3,037724562	0,039355408
ENSMUST00000134865	Pde6b	-3,113637898	0,029493418
ENSMUST00000035129	Ephb1	-3,224478188	0,019376856
ENSMUST00000014917	Dll1	-3,375873406	2,04E-05
ENSMUST00000103045	Stmn3	-3,379915589	0,014395154
ENSMUST00000040001	Galnt9	-3,434371413	0,023973857
ENSMUST00000071201	Ntng2	-3,532441013	0,025258612
ENSMUST00000166668	Vwa3a	-3,595451906	0,043615857
ENSMUST00000073394	Usp17ld	-3,728180942	0,024096781
ENSMUST00000145366	Sestd1	-3,75888848	0,037858004
ENSMUST00000049621	Hes5	-3,787535462	0,01349704
ENSMUST00000066197	Asic2	-3,837785354	0,006130911
ENSMUST00000172821	Vax1	-3,987189875	0,010082404
ENSMUST00000037636	Ina	-4,289401207	3,12E-09
ENSMUST00000131835	Srgap3	-4,297805584	0,003774548
ENSMUST00000133247	Arhgap26	-4,318131078	0,019551676
ENSMUST00000067075	Nkx2-2	-4,421798037	0,002635953
ENSMUST00000199312	Rufy3	-4,428035309	0,038851165
ENSMUST00000054819	Sox14	-4,57639379	0,006162991
ENSMUST00000198326	Gbp8	-4,599124411	0,017745677
ENSMUST00000226742	Ptk2	-4,645135073	0,045897451
ENSMUST00000215345	Dync1li1	-4,670491388	0,029598424
ENSMUST00000098906	Pate2	-4,955647984	0,008793449
ENSMUST00000113679	Gmcl1	-4,986834793	0,015893386
ENSMUST00000126833	Smpd2	-5,07793971	0,034543889
ENSMUST00000050149	Mical2	-5,242441742	0,005936117
ENSMUST00000139949	Selenbp1	-5,260307067	0,014773853
ENSMUST00000171033	Luc7l3	-5,373042384	0,001178711
ENSMUST00000193808	Nme7	-5,377130661	0,03880604

ENSMUST00000202048	Limch1	-5,429796364	0,031930515
ENSMUST00000155059	D430042O09Rik	-5,457881467	0,00860091
ENSMUST00000145285	P2rx3	-5,711366813	0,018328912
ENSMUST00000070649	Ccdc70	-5,722421262	0,010059675
ENSMUST00000111757	Tor1aip2	-5,854914176	9,34E-06
ENSMUST00000170796	Nob1	-5,90719483	0,010670657
ENSMUST00000079881	Zfp398	-5,974538224	0,037025029
ENSMUST00000168458	Gm3727	-6,001587124	0,016919126
ENSMUST00000030265	Dph2	-6,026885599	0,000305188
ENSMUST00000106335	Sez6l2	-6,050788304	0,035936002
ENSMUST00000123930	Bcat1	-6,0748778	0,003306241
ENSMUST00000156173	Gga3	-6,090171039	0,002633143
ENSMUST00000160071	Auts2	-6,103180747	0,047121736
ENSMUST00000126336	St3gal3	-6,105755451	0,00239662
ENSMUST00000188205	Tmem183a	-6,110800312	0,006421939
ENSMUST00000183209	Celf2	-6,162045615	0,011720363
ENSMUST00000084616	Anks6	-6,231958497	0,046856968
ENSMUST00000182951	Safb	-6,264474058	0,044513115
ENSMUST00000135398	Adcy1	-6,264836023	0,044652834
ENSMUST00000085289	Impg1	-6,267204569	0,002776783
ENSMUST00000154827	Alg13	-6,306317103	0,043773717
ENSMUST00000074541	Jazf1	-6,344063915	0,000656541
ENSMUST00000233860	Rab44	-6,354008054	0,001135583
ENSMUST00000167740	Zfp946	-6,355196548	0,000142465
ENSMUST00000145227	Mapt	-6,362608614	0,000418187
ENSMUST00000108810	Trim11	-6,395328333	0,039365526
ENSMUST00000173696	Kpna1	-6,40867667	0,039365526
ENSMUST00000141135	Abca4	-6,443764005	0,04679772
ENSMUST00000063635	Radil	-6,457652329	0,00012336
ENSMUST00000201535	Snx17	-6,473786767	0,030903593
ENSMUST00000160724	Tle3	-6,505098702	0,029501541
ENSMUST00000200342	Celf3	-6,511003138	0,000107276
ENSMUST00000038141	Slfn8	-6,55423003	0,033362343
ENSMUST00000229694	Micall1	-6,555929395	0,02965356
ENSMUST00000046656	Tasp1	-6,591467055	0,00039496
ENSMUST00000174050	Dnm2	-6,597296602	0,048358768

ENSMUST00000215660	Pkm	-6,617777336	0,02629184
ENSMUST00000053666	Slc12a6	-6,627710173	0,039358631
ENSMUST00000070200	Pla2g4a	-6,651260153	0,0237588
ENSMUST00000186415	Rnf2	-6,668479092	0,001290139
ENSMUST00000065373	Tmem70	-6,677983913	0,020083517
ENSMUST00000026442	Tepsin	-6,689588109	0,020398425
ENSMUST00000165609	Pick1	-6,706690173	0,030087143
ENSMUST00000218088	Eea1	-6,727657007	1,38E-05
ENSMUST00000007733	Tinf2	-6,738774555	0,018125394
ENSMUST00000193625	Aida	-6,744205059	0,017836952
ENSMUST00000185715	Psmc3	-6,758877024	0,014390082
ENSMUST00000028801	Spef1	-6,784225798	0,0237588
ENSMUST00000116434	Zkscan3	-6,801729974	0,034885367
ENSMUST00000171711	Mtdh	-6,802163986	0,024119872
ENSMUST00000021900	Sema4d	-6,827080007	0,043807348
ENSMUST00000226124	Arfgap3	-6,835148403	0,036727663
ENSMUST00000218384	Klhl29	-6,880836696	0,022580008
ENSMUST00000124196	Dll1	-6,89033328	0,025820527
ENSMUST00000205116	Magi1	-6,904795872	4,28E-05
ENSMUST00000154166	Enpp5	-6,921379924	0,020595674
ENSMUST00000188332	Usp40	-6,954185566	0,019551676
ENSMUST00000139853	Rnf10	-6,969582322	0,035393217
ENSMUST00000204682	Prokr1	-7,005899677	0,013966734
ENSMUST00000103110	Atp6v0a1	-7,053156854	7,32E-06
ENSMUST00000197211	Tet2	-7,061532971	0,049863993
ENSMUST00000117177	Rnft2	-7,078204973	0,011289881
ENSMUST00000208682	Ptov1	-7,098306216	2,08E-06
ENSMUST00000105827	Hp1bp3	-7,10973891	0,034543889
ENSMUST00000115749	Dnm1l	-7,132522489	0,014747814
ENSMUST00000138455	Fgfr1	-7,14024835	0,011613018
ENSMUST00000160894	Ctnna2	-7,14838142	0,009639682
ENSMUST00000229981	Nell2	-7,153423473	1,32E-05
ENSMUST00000004057	Fam162a	-7,165030736	0,009047737
ENSMUST00000170176	Wdr4	-7,186881073	0,008793449
ENSMUST00000114823	Mkrn1	-7,238449855	0,010666003
ENSMUST00000200132	St7l	-7,242739888	8,75E-07

ENSMUST00000188495	Myb	-7,259837007	4,36E-05
ENSMUST00000111124	Hipk3	-7,260226581	0,008676081
ENSMUST00000089311	Sun2	-7,281599339	0,015811564
ENSMUST00000149537	Fastk	-7,3010041	3,57E-06
ENSMUST00000173369	Trim39	-7,362895708	0,008408215
ENSMUST00000077078	Rnf185	-7,408478202	3,43E-07
ENSMUST00000169059	Xpo6	-7,44614874	0,005559828
ENSMUST00000136203	Ldb1	-7,492838643	0,010418969
ENSMUST00000107377	Tnc	-7,537741993	0,014867629
ENSMUST00000115736	Paip2	-7,543340484	0,003984865
ENSMUST00000110221	Col14a1	-7,556063453	0,004326576
ENSMUST00000105244	Timeless	-7,56830175	2,97E-05
ENSMUST00000186694	Tgfbrap1	-7,695276246	4,26E-08
ENSMUST00000084705	Tead1	-7,708116901	0,002521606
ENSMUST00000031815	Krba1	-7,730137595	1,53E-05
ENSMUST00000088464	Traf7	-7,743178066	3,74E-07
ENSMUST00000166713	Cpeb2	-7,743715645	0,002404986
ENSMUST00000168678	Sin3a	-7,752304652	0,007007737
ENSMUST00000114537	Myo1b	-7,783243833	0,004512195
ENSMUST00000114158	Crmp1	-7,815617574	0,005852718
ENSMUST00000140076	Ppat	-7,893395575	1,15E-06
ENSMUST00000197827	Csde1	-7,896541561	0,001756906
ENSMUST00000112883	Nr5a1	-7,957474206	0,001597157
ENSMUST00000221074	Ppp2r5c	-7,9728797	0,001923585
ENSMUST00000200776	Ociad2	-7,988629384	0,003448764
ENSMUST00000116133	Fzd5	-8,034978743	0,002243628
ENSMUST00000177950	Rnf44	-8,047163035	0,001662954
ENSMUST00000112363	Eml4	-8,132851201	0,00425178
ENSMUST00000127482	Igsf9	-8,21874031	0,001046015
ENSMUST00000078050	Rnf114	-8,330997486	7,72E-08
ENSMUST00000095666	Nin	-8,336520411	0,004335691
ENSMUST00000103111	Zhx3	-8,343615321	2,71E-07
ENSMUST00000191758	Tmem131l	-8,418857614	1,44E-06
ENSMUST00000161132	Cep295	-8,504939177	0,045964908
ENSMUST00000178048	Kif7	-8,514639203	0,00037944
ENSMUST00000035237	Usp4	-8,57265912	8,66E-10

ENSMUST00000079934	Mga	-8,630690895	0,039981302
ENSMUST00000191601	Apbb1	-8,637469025	6,70E-10
ENSMUST00000059647	Rbm12	-8,665062485	0,033236592
ENSMUST00000023057	Nptxr	-8,792026239	0,02942065
ENSMUST00000200393	Ints1	-8,818315364	0,00217865
ENSMUST00000176637	Gnb1	-8,838910885	0,031642622
ENSMUST00000204168	Gimap1	-8,886911389	5,76E-10
ENSMUST00000211687	Sorcs1	-8,914606742	0,026686196
ENSMUST00000074552	Ncaph2	-8,914756345	1,27E-09
ENSMUST00000173839	Nnat	-8,929605631	0,000679048
ENSMUST00000191606	Msh4	-9,013854568	0,026842759
ENSMUST00000152117	Ttc3	-9,183959334	1,33E-10
ENSMUST00000166811	Ncam1	-9,305072159	0,000142603
ENSMUST00000220346	Cep290	-9,317064251	2,67E-10
ENSMUST00000049941	Scn3b	-9,337890868	0,000223294
ENSMUST00000108239	Atad5	-9,348205859	0,000579522
ENSMUST00000044783	Eif4g1	-9,706549065	5,47E-05
ENSMUST00000227566	Vmn1r90	-9,713298774	0,015347181
ENSMUST00000134458	Macf1	-10,41122579	8,66E-09
ENSMUST00000082170	Fat3	-10,79576866	0,00385437
ENSMUST00000215087	Lars2	-12,54928463	1,22E-07
ENSMUST00000140312	Son	-22,01677591	3,37E-09
ENSMUST00000053927	Erbin	-22,09670413	3,22E-09
ENSMUST00000092777	Spag9	-22,26825347	2,93E-09
ENSMUST00000071487	Larp1	-22,5009357	2,02E-09
ENSMUST00000108068	Ubap2	-22,51468011	3,00E-09
ENSMUST00000231989	Vmn2r99	-22,59263268	2,07E-09
ENSMUST00000134465	Phldb1	-22,62387556	1,23E-09
ENSMUST00000105340	Tcf3	-22,72652813	1,57E-09
ENSMUST00000034611	Phldb1	-22,90207527	7,61E-10
ENSMUST00000113157	Setd5	-22,99676949	9,97E-10
ENSMUST00000233955	Vmn2r26	-23,00151837	6,70E-10
ENSMUST00000099479	Ddx46	-23,00919058	7,43E-10
ENSMUST00000108307	Virma	-23,01592744	6,70E-10
ENSMUST00000110773	Mga	-23,05139853	6,70E-10
ENSMUST00000154356	Ctnnb1	-23,07805978	6,70E-10

ENSMUST00000233802	Pot1b	-23,21697258	6,70E-10

3 DISCUSSION

The SHH signaling pathway regulates central patterning processes in the embryo including the specification of the emerging forebrain along the dorsoventral axis. Pathway activation requires the binding of SHH to its canonical receptor PTCH1. However, recent studies have shown that PTCH1 alone is not sufficient for SHH signal reception and transduction. Rather, additional cell surface proteins have been identified as being essential for proper SHH signaling referred to as the SHH receptorsome. Two members of this SHH receptorsome are LRP2 and GAS1. Mutations in SHH co-receptors recapitulate the spectrum of the loss of *Shh* phenotype and have been linked to familial forms of HPE in patients and mouse models further corroborating their importance for SHH-dependent forebrain development (Allen et al., 2007, 2011; Bae et al., 2011; Cole and Krauss, 2003; Echevarría-Andino and Allen, 2020; Hong et al., 2017; Izzi et al., 2011; Kantarci et al., 2007; Ribeiro et al., 2010; Willnow et al., 1996; Zhang et al., 2006, 2011).

Interestingly, members of the SHH receptorsome are structurally diverse and show unique spatial and temporal expression patterns, suggesting distinct functions in SHH-dependent developmental processes (Christ et al., 2016). Although the use of receptor mutant mouse models has been instrumental in identifying members of the SHH receptorsome in the first place, dissecting their distinct cellular and molecular functions may be technically challenging *in vivo*. In the past, *in vitro* studies using COS7 or NIH3T3 cells have helped to overcome such technical hurdles by providing easy means to elucidate receptor functions including their capability to bind SHH, to interact with PTCH1, or to impact intracellular SHH signal transduction (Christ et al., 2012; Izzi et al., 2011; Seppala et al., 2007). However, these *in vitro* studies required the ectopic overexpression of the SHH co-receptors which turned out impossible for the giant receptor LRP2 or created an unphysiological milieu, potentially leading to irrelevant interactions. Thus, how exactly these co-receptors modulate SHH action at the cellular level remained understudied.

In the present thesis, I applied a novel experimental approach using human iPSC-based modeling of early neurogenesis to elucidate the role of the two SHH co-receptors LRP2 and GAS1 in forebrain development and the reasons for HPE in patients lacking either receptor. In 2007, work by Yamanaka and colleagues documenting the ability to reprogram human iPSCs from somatic cells provided a seminal breakthrough in biomedical research (Takahashi et al., 2007). Nowadays, the potential to direct differentiation of iPSCs into almost any cell type of the human body enables a wide range of applications including stem cell and developmental research, high throughput drug screening, autologous cell therapy as well as disease modeling. iPSC-based cellular models faithfully recapitulate complex features of *in vivo* development as well as respective disease phenotypes and pathophysiological manifestations. Additionally, iPSCs can be easily accessed in terms of genetic manipulations as well as distinct modulations of cellular and molecular processes such as cell signaling. Clearly, iPSC-based modeling of human diseases has its limitations as iPSC-derived cell types mostly resemble immature and juvenile cell fates complicating the study of late-onset diseases. Furthermore, the reprogramming strategy as well as longer cultivation may have an impact on the genetic stability (Doss and Sachinidis, 2019; Moradi et al., 2019; Singh et al., 2015). However, in the present study, iPSC-based cell models represented a faithful and powerful research tool to uncover molecular mechanisms whereby LRP2 and GAS1 control SHH action during early forebrain development and why HPE ensues in patients carrying receptor gene mutations.

3.1 SHH-induced decay of LRP2 is a molecular cause for HPE

The multi-ligand endocytic receptor LRP2, also known as megalin, is expressed on the apical surface of absorptive epithelial tissue including the embryonic neural tube (Christ et al., 2012) where it directs internalization and cellular trafficking of different ligands. While most receptor ligands are directed to lysosomal compartments for catabolism (Christ et al., 2015; Christensen et al., 1999; Nykjaer et al., 1999), some resist degradation and are recycled for resecretion (Christ et al., 2012; Morales et al., 2006), while others are targeted for transcytosis (Marinò et al., 2003; Ortega et al., 2012). Shuttling of the LRP2/ligand complex are controlled by various cytosolic adaptor proteins and kinases including adaptor protein complex 2 (AP2) and disabled homolog 2 (DAB2) as well as LDLR adaptor protein 1 (ARH) and GAIP interacting protein, C terminus (GIPC), and GSK3β and PKA (Gallagher et al., 2004; Keyel et al., 2008; Li et al., 2001; Morris et al., 2002; Naccache et al., 2006; Nagai et al., 2005; Shah et al., 2013; Takeda et al., 2003; Yuseff et al., 2007).

Mutations in *LRP2* in humans and LRP2-deficiency in mouse models result in developmental forebrain defects that include HPE and HPE-related phenotypes such as DBS. These features recapitulate phenotypic aspects of SHH-deficiency (Avunduk et al., 2000; Chassaing et al., 2003; Donnai and Barrow, 1993; Gripp et al., 1997; Kantarci et al., 2007, 2008; Khalifa et al., 2015; Pober et al., 2009; Rosenfeld et al., 2010). Subsequently, LRP2 was shown to act as SHH co-receptor in the RDVM prior to neural tube closure (Christ et al., 2012). There, it forms a co-receptor complex with PTCH1 and facilitates binding and endocytosis of SHH secreted from the underlying PrCP. Internalized SHH and LRP2 predominantly co-localize with recycling endosomes suggesting a role of LRP2 in directing internalized SHH trafficking to resecretion in the forebrain organizer region and to further increase local SHH concentrations. However, due to the difficulty to recombinantly express full length LRP2, the cellular mechanisms of receptor function (and dysfunction in DBS) remained unexplored.

The establishment of iPSC-derived cell models from two DBS patients enabled me now to study mutant *LRP2* variants in health and disease. In a collaboration with Julia Flemming, another PhD student in the lab, I studied the impact of a unique missense mutation identified in a family with DBS on receptor function in patient-derived iPSCs differentiated into NPCs. The two patients analyzed showed homozygosity for a point mutation in an EGF repeat in the extracellular region of *LRP2* (megalin^{R3192Q}) (Paper 1, Fig. 1a and d). Besides renal resorption defects, low-molecular weight proteinuria, and severe bilateral myopia, both patients presented with the absence of megalin^{R3192Q} immunoreactivity in the proximal tubules of renal biopsies (Paper 1, Fig. 1b and c) suggesting either instability of the mutant transcript or improper folding and premature degradation of the mutant receptor polypeptide. iPSC-derived NPCs endogenously expressed LRP2/megalin comparable to the expression dynamics of the receptor seen *in vivo* (Paper 1, Fig. 2a and b, Fig. S4 A and B, Fig. S7B and C). These findings proved iPSCs as a suitable cell model to elucidate the molecular cause of DBS in these two patients. Our studies failed to document any difference in RNA level comparing wild-type and *LRP2* mutant cell lines (Paper 1, Fig. 2b and S4B). Also, expression of mutant megalin^{R3192Q} in the absence of any ligands was comparable to the wild-type receptor in control cell lines (Paper 1, Fig. 2 and S4). However, exposure to its ligand SHH caused aberrant retention of the megalin^{R3192Q} bound to SHH (Paper 1, Fig. 6a and b, S9A and B) and an enhanced sorting of the megalin^{R3192Q}/SHH complex to lysosomes as judged by increased colocalization with LAMP1-positive vesicles (Paper 1, Fig. 6c-e, Fig. S9C and D). In line with this hypothesis, lysosomal inhibition increased the levels of the mutant receptor in iPSC-derived NPCs treated with SHH (Paper 1, Fig. 7). Since the missense mutation was located in an EGF-type repeat, required for endosomal discharge of ligands at acidic pH (van der Westhuyzen et al., 1991), we suspected ligand-induced decay of megalin^{R3192Q} based on its inability to properly release SHH in the endocytic pathway. As a consequence, the liganded mutant receptor would be subjected to lysosomal degradation. A similar disease mechanisms has been described in familial hypercholesterolemia caused by mutations in the gene encoding the low density lipoprotein receptor (Hobbs et al., 1992; Miyake et al., 1989; van der Westhuyzen et al., 1991). Although we have only showed receptor degradation via lysosomes in iPSC-derived NPCs, SHH also induced degradation of mutant megalin^{R3192Q} in iPSC-derived RPTECs, indicating a similar mechanism in the proximal tubules that is responsible for the renal disease phenotype in this family.

In conclusion, in this study, we successfully applied human iPSC-derived cellular model systems to demonstrate how a unique missense mutation in *LRP2* impacts its receptor function as a molecular cause for DBS. In addition, our data provide evidence that LRP2 acts as an endocytosis and trafficking receptor for SHH in neuroepithelial progenitor cells.

3.2 GAS1 enhances SHH activity by facilitating NOTCH signaling

GAS1 has been identified as a co-receptor facilitating SHH signaling in the caudal neural tube and limb buds (Allen et al., 2007, 2011; Martinelli and Fan, 2007). However, loss of GAS1 function in patients carrying mutations in the human *GAS1* gene (Pineda-Alvarez et al., 2012; Ribeiro et al., 2010) results in microforms of HPE and a range of related craniofacial malformations phenocopying aspects of SHH-deficiency in the rostral neural tube (Carreno et al., 2017; Zhao et al., 2012). Phenotypic appearances increase in severity with haploinsufficiency for *Shh* indicating a genetic interaction of *Gas1* and *Shh* in rostral midline formation (Allen et al., 2007; Khonsari et al., 2013; Martinelli and Fan, 2007; Seppala et al., 2007). However, a role for GAS1 in promoting SHH action in the forebrain organizer region of the rostral ventral neuroepithelium was questioned by the observation that GAS1 itself is negatively regulated by SHH action (Allen et al., 2007). Thus, the exact function of GAS1 in SHH signaling during forebrain development remained debated.

In the second publication, I analyzed the role of GAS1 in the cellular response of forebrain neuroepithelial cells to SHH signals by performing comparative studies in GAS1-deficient mouse models and genetically engineered human iPSC-derived *GAS1* KO NPCs. I documented that the induction of the SHH expression domain in the murine RDVM at E8.5 was GAS1 independent (Paper 2, Fig. 1A and B), contrary to the function of LRP2 that is essential for SHH induction in this tissue at this developmental stage (Christ et al., 2012). However, I showed that GAS1 was required for sustaining SHH expression and pathway activity in the ventral forebrain neuroepithelium at later stages (Paper 2, Fig. 1C and D). In line with my observations in mouse embryos, GAS1 also facilitated SHH signaling in human iPSC-derived NPCs while *GAS1* KO cells failed to adapt a SHH-dependent ventral cell fate (Paper 2, Fig. 4). These features recapitulated the ventralizing defects seen in *Gas1* mutant mouse embryos (Allen et al., 2007; Khonsari et al., 2013; Martinelli and Fan, 2007; Seppala et al., 2007).

Performing comparative gene expression analysis by bulk RNA sequencing, I made the surprising observation that, in addition to SHH defects, a defect in NOTCH signaling was apparent in the ventral forebrain midline of GAS1-deficient embryos (Paper 2, Fig. 2). Impaired NOTCH signaling in the rostral ventral neuroepithelium as evidenced by reduced Hes family BHLH transcription factor 5 (*HES5*) transcript levels was confirmed in *Gas1*$^{-/-}$ mutant embryos by *in situ* hybridization as early as E8.5 (Paper 2, Fig. 3). This defect resembled phenotypes described in mice with disruption of the NOTCH pathway component recombinant signal binding protein for Ig kappa J (RBPJ) (Ware et al., 2016).

In line with NOTCH defects seen in mutant mice, iPSC-derived *GAS1* KO NPCs were not able to induce *HES5* expression and to further respond to pathway activation upon treatment with NOTCH ligand delta-like protein 1 (DLL1). This defect manifested in the inability to respond to the ligand with induction of NOTCH intracellular domain (NICD) production as well as *HES5* expression (Paper 2, Fig. 5). Since defective NOTCH signaling in mouse models and mutations in NOTCH pathway components in humans result in forebrain phenotypes that copy defects caused by loss of GAS1 or SHH (Dupé et al., 2011; Khonsari et al., 2013), I suspected a GAS1-dependent functional interaction between the SHH and NOTCH signaling during forebrain development.

Possibly, GAS1-deficient phenotypes may result from a combinatory defect in NOTCH and SHH signaling. In line with my hypothesis, NOTCH facilitates SHH activity and maintains SHH responsiveness in retinal and neural progenitor cells in different animal models by regulating either the availability and stability of GLI proteins (Jacobs and Huang, 2019; Ringuette et al., 2016) or by trafficking of PTCH1 and/or SMO (Huang et al., 2012; Kong et al., 2015; Stasiulewicz et al., 2015). Consequently, disrupting NOTCH signaling in mouse and chick embryos leads to a loss of the SHH activity domain in the rostral ventral forebrain midline (Hamdi-Rozé et al., 2020). Using quantitative real time PCR analyses in iPSC-derived NPCs, I further dissected NOTCH-dependent and NOTCH-independent functions for GAS1 in facilitating SHH signaling. These findings uncovered that GAS1 partially acts on SHH signaling via promoting NOTCH activity. Inhibiting NOTCH by γ-secretase inhibitor DAPT reduced SHH-Np induced expression of SHH downstream targets *GLI1* and *NKX2.1* in WT NPCs to similar levels detected in *GAS1* KO cells (Paper 2, Fig. 7A-C). Overexpressing NICD in *GAS1 KO* NPCs and *Gas1* mutant mouse forebrain explants rescued the loss of *Shh* and downstream target gene expression (Paper 2, Fig. 7D-E and 8) documenting that GAS1-dependent NOTCH signaling contributes to SHH signal strength in this cell type.

Earlier, GAS1 was shown to directly interact with PTCH1 to form a co-receptor complex that facilitates SHH signaling (Izzi et al., 2011). I suspected that GAS1 promotes NOTCH signaling also via direct interaction with NOTCH receptor 1 (NOTCH1) that I confirmed by co-immunoprecipitation studies and proximity ligation assay in iPSC-derived NPCs (Paper 2, Fig. 6A and B). These findings supported a dual role for GAS1 as an independent co-receptor for both PTCH1 and NOTCH1. Since GAS1 is a GPI-anchored protein and promotion of NOTCH1 activation was lost upon GPI anchor deletion (Paper 2, Fig. 6D and E), GAS1 may direct NOTCH1 to lipid raft compartments facilitating close interaction between NOTCH1 and its ligands or promoting receptor processing by secretases as described for the GPI-anchored protein teratocarcinoma-derived growth factor 1 (Cripto-1) (Watanabe et al., 2009).

GAS1 is a negative target of SHH signaling and its expression is downregulated by pathway activity (Allen et al., 2007). Similar to GAS1, the facilitating SHH co-receptor CDO is also negatively regulated by SHH (Tenzen et al., 2006) while the inhibitory co-receptors PTCH1 and HHIP are positive SHH targets (Jeong and McMahon, 2005) resulting in distinct regulatory feedback loops that direct spatial and temporal gradients of SHH signaling and thus modulate the response of target cells to distinct SHH concentrations (Ashe and Briscoe, 2006; Kang et al., 2007; Stamataki et al., 2005). The presented study does not only demonstrate a unique mechanism for GAS1-dependent SHH pathway facilitation via NOTCH signaling but also proposes a potential role for SHH signaling in indirectly regulating NOTCH pathway activity via GAS1. While GAS1-dependent NOTCH activity facilitates SHH signaling, SHH activity downregulates GAS1 expression potentially leading to decreased NOTCH signaling. This feedback would present a new regulatory mechanism to balance different signaling pathways crucial for forebrain development with GAS1 as central modulator. However, this hypothesis needs to be validated by further studies.

3.3 Conclusion

In my thesis, I uncovered specific cellular functions for the two SHH co-receptors LRP2 and GAS1 in forebrain development and the possible reasons for forebrain malformations in receptor-deficient patients using human disease modeling in iPSCs. On the one hand, I identified the molecular mechanisms how a unique missense mutation in *LRP2* in two siblings with DBS impacts the receptor function in iPSC-derived NPCs. In addition, I demonstrated that LRP2 acts as an endocytosis and trafficking receptor for SHH in forebrain neuroepithelial cells corroborating its crucial role for SHH-dependent forebrain development. On the other hand, I discovered a novel function for GAS1 in integrating SHH and NOTCH signaling during early forebrain development by being essential for NOTCH-dependent maintenance of the SHH activity domain in the rostral ventral neuroepithelium. For these studies, iPSC-based cellular model systems of forebrain development have proven indispensable since they faithfully recapitulate developmental processes as well as disease phenotypes and are easily accessible for experimental manipulation and quantitative assessment of the resulting cellular responses.

4 REFERENCES

Abdul-Aziz, N.M., Turmaine, M., Greene, N.D.E., and Copp, A.J. (2009). EphrinA-EphA receptor interactions in mouse spinal neurulation: implications for neural fold fusion. Int J Dev Biol *53*, 559–568.

Allen, B.L., Tenzen, T., and McMahon, A.P. (2007). The Hedgehog-binding proteins Gas1 and Cdo cooperate to positively regulate Shh signaling during mouse development. Genes Dev *21*, 1244–1257.

Allen, B.L., Song, J.Y., Izzi, L., Althaus, I.W., Kang, J.-S., Charron, F., Krauss, R.S., and McMahon, A.P. (2011). Overlapping roles and collective requirement for the coreceptors GAS1, CDO, and BOC in SHH pathway function. Dev Cell *20*, 775–787.

Alvarez, I.S., and Schoenwolf, G.C. (1992). Expansion of surface epithelium provides the major extrinsic force for bending of the neural plate. J Exp Zool *261*, 340–348.

Andoniadou, C.L., and Martinez-Barbera, J.P. (2013). Developmental mechanisms directing early anterior forebrain specification in vertebrates. Cell Mol Life Sci *70*, 3739–3752.

Anglani, F., Terrin, L., Brugnara, M., Battista, M., Cantaluppi, V., Ceol, M., Bertoldi, L., Valle, G., Joy, M.P., Pober, B.R., et al. (2018). Hypercalciuria and nephrolithiasis: Expanding the renal phenotype of Donnai-Barrow syndrome. Clin Genet *94*, 187–188.

Aoto, K., Nishimura, T., Eto, K., and Motoyama, J. (2002). Mouse GLI3 regulates Fgf8 expression and apoptosis in the developing neural tube, face, and limb bud. Dev Biol *251*, 320–332.

Arauz, R.F., Solomon, B.D., Pineda-Alvarez, D.E., Gropman, A.L., Parsons, J.A., Roessler, E., and Muenke, M. (2010). A Hypomorphic Allele in the FGF8 Gene Contributes to Holoprosencephaly and Is Allelic to Gonadotropin-Releasing Hormone Deficiency in Humans. Mol Syndromol *1*, 59–66.

Argraves, W.S., and Morales, C.R. (2004). Immunolocalization of cubilin, megalin, apolipoprotein J, and apolipoprotein A-I in the uterus and oviduct. Mol Reprod Dev *69*, 419–427.

Ashe, H.L., and Briscoe, J. (2006). The interpretation of morphogen gradients. Development *133*, 385–394.

Assémat, E., Châtelet, F., Chandellier, J., Commo, F., Cases, O., Verroust, P., and Kozyraki, R. (2005). Overlapping expression patterns of the multiligand endocytic receptors cubilin and megalin in the CNS, sensory organs and developing epithelia of the rodent embryo. Gene Expr Patterns *6*, 69–78.

Avunduk, A.M., Aslan, Y., Kapicioğlu, Z., and Elmas, R. (2000). High myopia, hypertelorism, iris coloboma, exomphalos, absent corpus callosum, and sensorineural deafness: report of a case and further evidence for autosomal recessive inheritance. Acta Ophthalmol Scand *78*, 221–222.

Baardman, M.E., Zwier, M.V., Wisse, L.J., Gittenberger-de Groot, A.C., Kerstjens-Frederikse, W.S., Hofstra, R.M.W., Jurdzinski, A., Hierck, B.P., Jongbloed, M.R.M., Berger, R.M.F., et al.

(2016). Common arterial trunk and ventricular non-compaction in Lrp2 knockout mice indicate a crucial role of LRP2 in cardiac development. Dis Model Mech *9*, 413–425.

Bachiller, D., Klingensmith, J., Kemp, C., Belo, J.A., Anderson, R.M., May, S.R., McMahon, J.A., McMahon, A.P., Harland, R.M., Rossant, J., et al. (2000). The organizer factors Chordin and Noggin are required for mouse forebrain development. Nature *403*, 658–661.

Bae, G.-U., Domené, S., Roessler, E., Schachter, K., Kang, J.-S., Muenke, M., and Krauss, R.S. (2011). Mutations in CDON, encoding a hedgehog receptor, result in holoprosencephaly and defective interactions with other hedgehog receptors. Am J Hum Genet *89*, 231–240.

del Barco Barrantes, I., Davidson, G., Gröne, H.-J., Westphal, H., and Niehrs, C. (2003). Dkk1 and noggin cooperate in mammalian head induction. Genes Dev *17*, 2239–2244.

Barr, M.J., Hanson, J.W., Currey, K., Sharp, S., Toriello, H., Schmickel, R.D., and Wilson, G.N. (1983). Holoprosencephaly in infants of diabetic mothers. J Pediatr *102*, 565–568.

Belo, J.A., Bouwmeester, T., Leyns, L., Kertesz, N., Gallo, M., Follettie, M., and De Robertis, E.M. (1997). Cerberus-like is a secreted factor with neutralizing activity expressed in the anterior primitive endoderm of the mouse gastrula. Mech Dev *68*, 45–57.

Bendavid, C., Rochard, L., Dubourg, C., Seguin, J., Gicquel, I., Pasquier, L., Vigneron, J., Laquerrière, A., Marcorelles, P., Jeanne-Pasquier, C., et al. (2009). Array-CGH analysis indicates a high prevalence of genomic rearrangements in holoprosencephaly: an updated map of candidate loci. Hum Mutat *30*, 1175–1182.

Bendavid, C., Dupé, V., Rochard, L., Gicquel, I., Dubourg, C., and David, V. (2010). Holoprosencephaly: An update on cytogenetic abnormalities. Am J Med Genet C Semin Med Genet *154C*, 86–92.

Berman, D.M., Karhadkar, S.S., Maitra, A., Montes De Oca, R., Gerstenblith, M.R., Briggs, K., Parker, A.R., Shimada, Y., Eshleman, J.R., Watkins, D.N., et al. (2003). Widespread requirement for Hedgehog ligand stimulation in growth of digestive tract tumours. Nature *425*, 846–851.

Birn, H., Willnow, T.E., Nielsen, R., Norden, A.G.W., Bönsch, C., Moestrup, S.K., Nexø, E., and Christensen, E.I. (2002). Megalin is essential for renal proximal tubule reabsorption and accumulation of transcobalamin-B(12). Am J Physiol Renal Physiol *282*, F408-416.

Bitgood, M.J., Shen, L., and McMahon, A.P. (1996). Sertoli cell signaling by Desert hedgehog regulates the male germline. Curr Biol *6*, 298–304.

Bönnemann, C., and Meinecke, P. (1990). Holoprosencephaly as a possible embryonic alcohol effect: another observation. Am J Med Genet *37*, 431–432.

Brennan, J., Lu, C.C., Norris, D.P., Rodriguez, T.A., Beddington, R.S., and Robertson, E.J. (2001). Nodal signalling in the epiblast patterns the early mouse embryo. Nature *411*, 965–969.

van den Brink, G.R. (2007). Hedgehog signaling in development and homeostasis of the gastrointestinal tract. Physiol Rev *87*, 1343–1375.

Briscoe, J., Pierani, A., Jessell, T.M., and Ericson, J. (2000). A homeodomain protein code specifies progenitor cell identity and neuronal fate in the ventral neural tube. Cell *101*, 435–445.

Burke, R., Nellen, D., Bellotto, M., Hafen, E., Senti, K.A., Dickson, B.J., and Basler, K. (1999). Dispatched, a novel sterol-sensing domain protein dedicated to the release of cholesterol-modified hedgehog from signaling cells. Cell *99*, 803–815.

Cabrera, J.R., Sanchez-Pulido, L., Rojas, A.M., Valencia, A., Mañes, S., Naranjo, J.R., and Mellström, B. (2006). Gas1 is related to the glial cell-derived neurotrophic factor family receptors alpha and regulates Ret signaling. J Biol Chem *281*, 14330–14339.

Carpenter, D., Stone, D.M., Brush, J., Ryan, A., Armanini, M., Frantz, G., Rosenthal, A., and de Sauvage, F.J. (1998). Characterization of two patched receptors for the vertebrate hedgehog protein family. Proc Natl Acad Sci U S A *95*, 13630–13634.

Carreno, G., Apps, J.R., Lodge, E.J., Panousopoulos, L., Haston, S., Gonzalez-Meljem, J.M., Hahn, H., Andoniadou, C.L., and Martinez-Barbera, J.P. (2017). Hypothalamic sonic hedgehog is required for cell specification and proliferation of LHX3/LHX4 pituitary embryonic precursors. Development *144*, 3289–3302.

Cases, O., Joseph, A., Obry, A., Santin, M.D., Ben-Yacoub, S., Pâques, M., Amsellem-Levera, S., Bribian, A., Simonutti, M., Augustin, S., et al. (2015). Foxg1-Cre Mediated Lrp2 Inactivation in the Developing Mouse Neural Retina, Ciliary and Retinal Pigment Epithelia Models Congenital High Myopia. PLoS One *10*, e0129518.

Chassaing, N., Lacombe, D., Carles, D., Calvas, P., Saura, R., and Bieth, E. (2003). Donnai-Barrow syndrome: four additional patients. Am J Med Genet A *121A*, 258–262.

Chen, Z.F., and Behringer, R.R. (1995). twist is required in head mesenchyme for cranial neural tube morphogenesis. Genes Dev *9*, 686–699.

Chen, J.K., Taipale, J., Cooper, M.K., and Beachy, P.A. (2002). Inhibition of Hedgehog signaling by direct binding of cyclopamine to Smoothened. Genes Dev *16*, 2743–2748.

Chen, M.-H., Li, Y.-J., Kawakami, T., Xu, S.-M., and Chuang, P.-T. (2004a). Palmitoylation is required for the production of a soluble multimeric Hedgehog protein complex and long-range signaling in vertebrates. Genes Dev *18*, 641–659.

Chen, W., Ren, X.-R., Nelson, C.D., Barak, L.S., Chen, J.K., Beachy, P.A., de Sauvage, F., and Lefkowitz, R.J. (2004b). Activity-dependent internalization of smoothened mediated by beta-arrestin 2 and GRK2. Science *306*, 2257–2260.

Chen, X., Tukachinsky, H., Huang, C.-H., Jao, C., Chu, Y.-R., Tang, H.-Y., Mueller, B., Schulman, S., Rapoport, T.A., and Salic, A. (2011a). Processing and turnover of the Hedgehog protein in the endoplasmic reticulum. J Cell Biol *192*, 825–838.

Chen, Y., Li, S., Tong, C., Zhao, Y., Wang, B., Liu, Y., Jia, J., and Jiang, J. (2010). G protein-coupled receptor kinase 2 promotes high-level Hedgehog signaling by regulating the active state of Smo through kinase-dependent and kinase-independent mechanisms in Drosophila. Genes Dev *24*, 2054–2067.

Chen, Y., Sasai, N., Ma, G., Yue, T., Jia, J., Briscoe, J., and Jiang, J. (2011b). Sonic Hedgehog dependent phosphorylation by CK1α and GRK2 is required for ciliary accumulation and activation of smoothened. PLoS Biol *9*, e1001083.

Cheung, H.O.-L., Zhang, X., Ribeiro, A., Mo, R., Makino, S., Puviindran, V., Law, K.K.L., Briscoe, J., and Hui, C.-C. (2009). The kinesin protein Kif7 is a critical regulator of Gli transcription factors in mammalian hedgehog signaling. Sci Signal *2*, ra29.

Chiang, C., Litingtung, Y., Lee, E., Young, K.E., Corden, J.L., Westphal, H., and Beachy, P.A. (1996). Cyclopia and defective axial patterning in mice lacking Sonic hedgehog gene function. Nature *383*, 407–413.

Cho, S.-H., and Cepko, C.L. (2006). Wnt2b/beta-catenin-mediated canonical Wnt signaling determines the peripheral fates of the chick eye. Development *133*, 3167–3177.

Christ, A., Christa, A., Kur, E., Lioubinski, O., Bachmann, S., Willnow, T.E., and Hammes, A. (2012). LRP2 is an auxiliary SHH receptor required to condition the forebrain ventral midline for inductive signals. Dev Cell *22*, 268–278.

Christ, A., Christa, A., Klippert, J., Eule, J.C., Bachmann, S., Wallace, V.A., Hammes, A., and Willnow, T.E. (2015). LRP2 Acts as SHH Clearance Receptor to Protect the Retinal Margin from Mitogenic Stimuli. Dev Cell *35*, 36–48.

Christ, A., Herzog, K., and Willnow, T.E. (2016). LRP2, an auxiliary receptor that controls sonic hedgehog signaling in development and disease. Dev Dyn *245*, 569–579.

Christ, A., Marczenke, M., and Willnow, T.E. (2020). LRP2 controls sonic hedgehog-dependent differentiation of cardiac progenitor cells during outflow tract formation. Hum Mol Genet *29*, 3183–3196.

Christensen, E.I., Nielsen, S., Moestrup, S.K., Borre, C., Maunsbach, A.B., de Heer, E., Ronco, P., Hammond, T.G., and Verroust, P. (1995). Segmental distribution of the endocytosis receptor gp330 in renal proximal tubules. Eur J Cell Biol *66*, 349–364.

Christensen, E.I., Moskaug, J.O., Vorum, H., Jacobsen, C., Gundersen, T.E., Nykjaer, A., Blomhoff, R., Willnow, T.E., and Moestrup, S.K. (1999). Evidence for an essential role of megalin in transepithelial transport of retinol. J Am Soc Nephrol *10*, 685–695.

Chuang, P.T., and McMahon, A.P. (1999). Vertebrate Hedgehog signalling modulated by induction of a Hedgehog-binding protein. Nature *397*, 617–621.

Chuang, P.-T., Kawcak, T., and McMahon, A.P. (2003). Feedback control of mammalian Hedgehog signaling by the Hedgehog-binding protein, Hip1, modulates Fgf signaling during branching morphogenesis of the lung. Genes Dev *17*, 342–347.

Clements, M., Pernaute, B., Vella, F., and Rodriguez, T.A. (2011). Crosstalk between Nodal/activin and MAPK p38 signaling is essential for anterior-posterior axis specification. Curr Biol *21*, 1289–1295.

Cobourne, M.T., Miletich, I., and Sharpe, P.T. (2004). Restriction of sonic hedgehog signalling during early tooth development. Development *131*, 2875–2885.

Cohen, M.M.J. (1989). Perspectives on holoprosencephaly: Part I. Epidemiology, genetics, and syndromology. Teratology *40*, 211–235.

Cohen, M.M.J., and Sulik, K.K. (1992). Perspectives on holoprosencephaly: Part II. Central nervous system, craniofacial anatomy, syndrome commentary, diagnostic approach, and experimental studies. J Craniofac Genet Dev Biol *12*, 196–244.

Colak, D., Mori, T., Brill, M.S., Pfeifer, A., Falk, S., Deng, C., Monteiro, R., Mummery, C., Sommer, L., and Götz, M. (2008). Adult neurogenesis requires Smad4-mediated bone morphogenic protein signaling in stem cells. J Neurosci *28*, 434–446.

Cole, F., and Krauss, R.S. (2003). Microform holoprosencephaly in mice that lack the Ig superfamily member Cdon. Curr Biol *13*, 411–415.

Colnot, C., de la Fuente, L., Huang, S., Hu, D., Lu, C., St-Jacques, B., and Helms, J.A. (2005). Indian hedgehog synchronizes skeletal angiogenesis and perichondrial maturation with cartilage development. Development *132*, 1057–1067.

Copp, A.J. (2005). Neurulation in the cranial region--normal and abnormal. J Anat *207*, 623–635.

Copp, A.J., Greene, N.D.E., and Murdoch, J.N. (2003). The genetic basis of mammalian neurulation. Nat Rev Genet *4*, 784–793.

Corbin, J.G., Rutlin, M., Gaiano, N., and Fishell, G. (2003). Combinatorial function of the homeodomain proteins Nkx2.1 and Gsh2 in ventral telencephalic patterning. Development *130*, 4895–4906.

Corcoran, R.B., and Scott, M.P. (2006). Oxysterols stimulate Sonic hedgehog signal transduction and proliferation of medulloblastoma cells. Proc Natl Acad Sci U S A *103*, 8408–8413.

Correa, A., Gilboa, S.M., Besser, L.M., Botto, L.D., Moore, C.A., Hobbs, C.A., Cleves, M.A., Riehle-Colarusso, T.J., Waller, D.K., and Reece, E.A. (2008). Diabetes mellitus and birth defects. Am J Obstet Gynecol *199*, 237.e1-9.

Cowled, P.A., Ciccarelli, C., Coccia, E., Philipson, L., and Sorrentino, V. (1994). Expression of growth arrest-specific (gas) genes in senescent murine cells. Exp Cell Res *211*, 197–202.

Creanga, A., Glenn, T.D., Mann, R.K., Saunders, A.M., Talbot, W.S., and Beachy, P.A. (2012). Scube/You activity mediates release of dually lipid-modified Hedgehog signal in soluble form. Genes Dev *26*, 1312–1325.

Croen, L.A., Shaw, G.M., and Lammer, E.J. (1996). Holoprosencephaly: epidemiologic and clinical characteristics of a California population. Am J Med Genet *64*, 465–472.

Croen, L.A., Shaw, G.M., and Lammer, E.J. (2000). Risk factors for cytogenetically normal holoprosencephaly in California: a population-based case-control study. Am J Med Genet *90*, 320–325.

Crossley, P.H., and Martin, G.R. (1995). The mouse Fgf8 gene encodes a family of polypeptides and is expressed in regions that direct outgrowth and patterning in the developing embryo. Development *121*, 439–451.

Crossley, P.H., Martinez, S., Ohkubo, Y., and Rubenstein, J.L. (2001). Coordinate expression of Fgf8, Otx2, Bmp4, and Shh in the rostral prosencephalon during development of the telencephalic and optic vesicles. Neuroscience *108*, 183–206.

Curtin, J.A., Quint, E., Tsipouri, V., Arkell, R.M., Cattanach, B., Copp, A.J., Henderson, D.J., Spurr, N., Stanier, P., Fisher, E.M., et al. (2003). Mutation of Celsr1 disrupts planar polarity of inner ear hair cells and causes severe neural tube defects in the mouse. Curr Biol *13*, 1129–1133.

Dachy, A., Paquot, F., Debray, G., Bovy, C., Christensen, E.I., Collard, L., and Jouret, F. (2015). In-depth phenotyping of a Donnai-Barrow patient helps clarify proximal tubule dysfunction. Pediatr Nephrol *30*, 1027–1031.

Dai, P., Akimaru, H., Tanaka, Y., Maekawa, T., Nakafuku, M., and Ishii, S. (1999). Sonic Hedgehog-induced activation of the Gli1 promoter is mediated by GLI3. J Biol Chem *274*, 8143–8152.

Dawber, R.J., Hebbes, S., Herpers, B., Docquier, F., and van den Heuvel, M. (2005). Differential range and activity of various forms of the Hedgehog protein. BMC Dev Biol *5*, 21.

Del Sal, G., Ruaro, M.E., Philipson, L., and Schneider, C. (1992). The growth arrest-specific gene, gas1, is involved in growth suppression. Cell *70*, 595–607.

Del Sal, G., Collavin, L., Ruaro, M.E., Edomi, P., Saccone, S., Valle, G.D., and Schneider, C. (1994). Structure, function, and chromosome mapping of the growth-suppressing human homologue of the murine gas1 gene. Proc Natl Acad Sci U S A *91*, 1848–1852.

Del Sal, G., Ruaro, E.M., Utrera, R., Cole, C.N., Levine, A.J., and Schneider, C. (1995). Gas1-induced growth suppression requires a transactivation-independent p53 function. Mol Cell Biol *15*, 7152–7160.

DEMYER, W., ZEMAN, W., and PALMER, C.G. (1964). THE FACE PREDICTS THE BRAIN: DIAGNOSTIC SIGNIFICANCE OF MEDIAN FACIAL ANOMALIES FOR HOLOPROSENCEPHALY (ARHINENCEPHALY). Pediatrics *34*, 256–263.

Dessaud, E., McMahon, A.P., and Briscoe, J. (2008). Pattern formation in the vertebrate neural tube: a sonic hedgehog morphogen-regulated transcriptional network. Development *135*, 2489–2503.

Ding, Q., Motoyama, J., Gasca, S., Mo, R., Sasaki, H., Rossant, J., and Hui, C.C. (1998). Diminished Sonic hedgehog signaling and lack of floor plate differentiation in Gli2 mutant mice. Development *125*, 2533–2543.

Ding, Q., Fukami, S. i, Meng, X., Nishizaki, Y., Zhang, X., Sasaki, H., Dlugosz, A., Nakafuku, M., and Hui, C. c (1999). Mouse suppressor of fused is a negative regulator of sonic hedgehog signaling and alters the subcellular distribution of Gli1. Curr Biol *9*, 1119–1122.

Dipple, K.M., and McCabe, E.R. (2000). Phenotypes of patients with “simple” Mendelian disorders are complex traits: thresholds, modifiers, and systems dynamics. Am J Hum Genet *66*, 1729–1735.

Donnai, D., and Barrow, M. (1993). Diaphragmatic hernia, exomphalos, absent corpus callosum, hypertelorism, myopia, and sensorineural deafness: a newly recognized autosomal recessive disorder? Am J Med Genet *47*, 679–682.

Dorn, K.V., Hughes, C.E., and Rohatgi, R. (2012). A Smoothened-Evc2 complex transduces the Hedgehog signal at primary cilia. Dev Cell *23*, 823–835.

Doss, M.X., and Sachinidis, A. (2019). Current Challenges of iPSC-Based Disease Modeling and Therapeutic Implications. Cells *8*.

Dubourg, C., Lazaro, L., Pasquier, L., Bendavid, C., Blayau, M., Le Duff, F., Durou, M.-R., Odent, S., and David, V. (2004). Molecular screening of SHH, ZIC2, SIX3, and TGIF genes in patients with features of holoprosencephaly spectrum: Mutation review and genotype-phenotype correlations. Hum Mutat *24*, 43–51.

Dubourg, C., Bendavid, C., Pasquier, L., Henry, C., Odent, S., and David, V. (2007). Holoprosencephaly. Orphanet J Rare Dis *2*, 8.

Dubourg, C., Carré, W., Hamdi-Rozé, H., Mouden, C., Roume, J., Abdelmajid, B., Amram, D., Baumann, C., Chassaing, N., Coubes, C., et al. (2016). Mutational Spectrum in Holoprosencephaly Shows That FGF is a New Major Signaling Pathway. Hum Mutat *37*, 1329–1339.

Dupé, V., Rochard, L., Mercier, S., Le Pétillon, Y., Gicquel, I., Bendavid, C., Bourrouillou, G., Kini, U., Thauvin-Robinet, C., Bohan, T.P., et al. (2011). NOTCH, a new signaling pathway implicated in holoprosencephaly. Hum Mol Genet *20*, 1122–1131.

Dwyer, J.R., Sever, N., Carlson, M., Nelson, S.F., Beachy, P.A., and Parhami, F. (2007). Oxysterols are novel activators of the hedgehog signaling pathway in pluripotent mesenchymal cells. J Biol Chem *282*, 8959–8968.

Dyer, M.A., Farrington, S.M., Mohn, D., Munday, J.R., and Baron, M.H. (2001). Indian hedgehog activates hematopoiesis and vasculogenesis and can respecify prospective neurectodermal cell fate in the mouse embryo. Development *128*, 1717–1730.

Echelard, Y., Epstein, D.J., St-Jacques, B., Shen, L., Mohler, J., McMahon, J.A., and McMahon, A.P. (1993). Sonic hedgehog, a member of a family of putative signaling molecules, is implicated in the regulation of CNS polarity. Cell *75*, 1417–1430.

Echevarría-Andino, M.L., and Allen, B.L. (2020). The hedgehog co-receptor BOC differentially regulates SHH signaling during craniofacial development. Development *147*.

Endoh-Yamagami, S., Evangelista, M., Wilson, D., Wen, X., Theunissen, J.-W., Phamluong, K., Davis, M., Scales, S.J., Solloway, M.J., de Sauvage, F.J., et al. (2009). The mammalian Cos2 homolog Kif7 plays an essential role in modulating Hh signal transduction during development. Curr Biol *19*, 1320–1326.

Ericson, J., Muhr, J., Placzek, M., Lints, T., Jessell, T.M., and Edlund, T. (1995). Sonic hedgehog induces the differentiation of ventral forebrain neurons: a common signal for ventral patterning within the neural tube. Cell *81*, 747–756.

Eugster, C., Panáková, D., Mahmoud, A., and Eaton, S. (2007). Lipoprotein-heparan sulfate interactions in the Hh pathway. Dev Cell *13*, 57–71.

Evdokiou, A., and Cowled, P.A. (1998a). Growth-regulatory activity of the growth arrest-specific gene, GAS1, in NIH3T3 fibroblasts. Exp Cell Res *240*, 359–367.

Evdokiou, A., and Cowled, P.A. (1998b). Tumor-suppressive activity of the growth arrest-specific gene GAS1 in human tumor cell lines. Int J Cancer *75*, 568–577.

Feinberg, A.P., and Irizarry, R.A. (2010). Evolution in health and medicine Sackler colloquium: Stochastic epigenetic variation as a driving force of development, evolutionary adaptation, and disease. Proc Natl Acad Sci U S A *107 Suppl 1*, 1757–1764.

Fernandes, M., Gutin, G., Alcorn, H., McConnell, S.K., and Hébert, J.M. (2007). Mutations in the BMP pathway in mice support the existence of two molecular classes of holoprosencephaly. Development *134*, 3789–3794.

Fertuzinhos, S., Krsnik, Z., Kawasawa, Y.I., Rasin, M.-R., Kwan, K.Y., Chen, J.-G., Judas, M., Hayashi, M., and Sestan, N. (2009). Selective depletion of molecularly defined cortical interneurons in human holoprosencephaly with severe striatal hypoplasia. Cereb Cortex *19*, 2196–2207.

Fukuchi-Shimogori, T., and Grove, E.A. (2001). Neocortex patterning by the secreted signaling molecule FGF8. Science *294*, 1071–1074.

Furuta, Y., Piston, D.W., and Hogan, B.L. (1997). Bone morphogenetic proteins (BMPs) as regulators of dorsal forebrain development. Development *124*, 2203–2212.

Gajera, C.R., Emich, H., Lioubinski, O., Christ, A., Beckervordersandforth-Bonk, R., Yoshikawa, K., Bachmann, S., Christensen, E.I., Götz, M., Kempermann, G., et al. (2010). LRP2 in ependymal cells regulates BMP signaling in the adult neurogenic niche. J Cell Sci *123*, 1922–1930.

Galceran, J., Miyashita-Lin, E.M., Devaney, E., Rubenstein, J.L., and Grosschedl, R. (2000). Hippocampus development and generation of dentate gyrus granule cells is regulated by LEF1. Development *127*, 469–482.

Gallagher, H., Oleinikov, A.V., Fenske, C., and Newman, D.J. (2004). The adaptor disabled-2 binds to the third psi xNPxY sequence on the cytoplasmic tail of megalin. Biochimie *86*, 179–182.

Gallet, A., Ruel, L., Staccini-Lavenant, L., and Thérond, P.P. (2006). Cholesterol modification is necessary for controlled planar long-range activity of Hedgehog in Drosophila epithelia. Development *133*, 407–418.

Geelen, J.A., and Langman, J. (1977). Closure of the neural tube in the cephalic region of the mouse embryo. Anat Rec *189*, 625–640.

Geelen, J.A., and Langman, J. (1979). Ultrastructural observations on closure of the neural tube in the mouse. Anat Embryol (Berl) *156*, 73–88.

Geng, X., and Oliver, G. (2009). Pathogenesis of holoprosencephaly. J Clin Invest *119*, 1403–1413.

Goddeeris, M.M., Schwartz, R., Klingensmith, J., and Meyers, E.N. (2007). Independent requirements for Hedgehog signaling by both the anterior heart field and neural crest cells for outflow tract development. Development *134*, 1593–1604.

Goetz, S.C., and Anderson, K.V. (2010). The primary cilium: a signalling centre during vertebrate development. Nat Rev Genet *11*, 331–344.

Golden, J.A., and Chernoff, G.F. (1993). Intermittent pattern of neural tube closure in two strains of mice. Teratology *47*, 73–80.

Gongal, P.A., French, C.R., and Waskiewicz, A.J. (2011). Aberrant forebrain signaling during early development underlies the generation of holoprosencephaly and coloboma. Biochim Biophys Acta *1812*, 390–401.

Goodrich, L.V., Milenković, L., Higgins, K.M., and Scott, M.P. (1997). Altered neural cell fates and medulloblastoma in mouse patched mutants. Science *277*, 1109–1113.

Gripp, K.W., Donnai, D., Clericuzio, C.L., McDonald-McGinn, D.M., Guttenberg, M., and Zackai, E.H. (1997). Diaphragmatic hernia-exomphalos-hypertelorism syndrome: a new case and further evidence of autosomal recessive inheritance. Am J Med Genet *68*, 441–444.

Grove, E.A., Tole, S., Limon, J., Yip, L., and Ragsdale, C.W. (1998). The hem of the embryonic cerebral cortex is defined by the expression of multiple Wnt genes and is compromised in Gli3-deficient mice. Development *125*, 2315–2325.

Gutin, G., Fernandes, M., Palazzolo, L., Paek, H., Yu, K., Ornitz, D.M., McConnell, S.K., and Hébert, J.M. (2006). FGF signalling generates ventral telencephalic cells independently of SHH. Development *133*, 2937–2946.

Hackett, D.A., Smith, J.L., and Schoenwolf, G.C. (1997). Epidermal ectoderm is required for full elevation and for convergence during bending of the avian neural plate. Dev Dyn *210*, 397–406.

Hahn, J.S., and Barnes, P.D. (2010). Neuroimaging advances in holoprosencephaly: Refining the spectrum of the midline malformation. Am J Med Genet C Semin Med Genet *154C*, 120–132.

Hahn, J.S., Barnes, P.D., Clegg, N.J., and Stashinko, E.E. (2010). Septopreoptic holoprosencephaly: a mild subtype associated with midline craniofacial anomalies. AJNR Am J Neuroradiol *31*, 1596–1601.

Hamblet, N.S., Lijam, N., Ruiz-Lozano, P., Wang, J., Yang, Y., Luo, Z., Mei, L., Chien, K.R., Sussman, D.J., and Wynshaw-Boris, A. (2002). Dishevelled 2 is essential for cardiac outflow tract development, somite segmentation and neural tube closure. Development *129*, 5827–5838.

Hamdi-Rozé, H., Ware, M., Guyodo, H., Rizzo, A., Ratié, L., Rupin, M., Carré, W., Kim, A., Odent, S., Dubourg, C., et al. (2020). Disrupted Hypothalamo-Pituitary Axis in Association With Reduced SHH Underlies the Pathogenesis of NOTCH-Deficiency. J Clin Endocrinol Metab *105*.

Hayhurst, M., Gore, B.B., Tessier-Lavigne, M., and McConnell, S.K. (2008). Ongoing sonic hedgehog signaling is required for dorsal midline formation in the developing forebrain. Dev Neurobiol *68*, 83–100.

Hébert, J.M., and Fishell, G. (2008). The genetics of early telencephalon patterning: some assembly required. Nat Rev Neurosci *9*, 678–685.

Hébert, J.M., Mishina, Y., and McConnell, S.K. (2002). BMP signaling is required locally to pattern the dorsal telencephalic midline. Neuron *35*, 1029–1041.

Hellemans, J., Coucke, P.J., Giedion, A., De Paepe, A., Kramer, P., Beemer, F., and Mortier, G.R. (2003). Homozygous mutations in IHH cause acrocapitofemoral dysplasia, an autosomal recessive disorder with cone-shaped epiphyses in hands and hips. Am J Hum Genet *72*, 1040–1046.

Hill, R.E., Heaney, S.J.H., and Lettice, L.A. (2003). Sonic hedgehog: restricted expression and limb dysmorphologies. J Anat *202*, 13–20.

Hobbs, H.H., Brown, M.S., and Goldstein, J.L. (1992). Molecular genetics of the LDL receptor gene in familial hypercholesterolemia. Hum Mutat *1*, 445–466.

Hoch, R.V., Rubenstein, J.L.R., and Pleasure, S. (2009). Genes and signaling events that establish regional patterning of the mammalian forebrain. Semin Cell Dev Biol *20*, 378–386.

Holmberg, J., Clarke, D.L., and Frisén, J. (2000). Regulation of repulsion versus adhesion by different splice forms of an Eph receptor. Nature *408*, 203–206.

Holtz, A.M., Peterson, K.A., Nishi, Y., Morin, S., Song, J.Y., Charron, F., McMahon, A.P., and Allen, B.L. (2013). Essential role for ligand-dependent feedback antagonism of vertebrate hedgehog signaling by PTCH1, PTCH2 and HHIP1 during neural patterning. Development *140*, 3423–3434.

Hong, M., and Krauss, R.S. (2018). Modeling the complex etiology of holoprosencephaly in mice. Am J Med Genet C Semin Med Genet *178*, 140–150.

Hong, M., Srivastava, K., Kim, S., Allen, B.L., Leahy, D.J., Hu, P., Roessler, E., Krauss, R.S., and Muenke, M. (2017). BOC is a modifier gene in holoprosencephaly. Hum Mutat *38*, 1464–1470.

Houart, C., Caneparo, L., Heisenberg, C., Barth, K., Take-Uchi, M., and Wilson, S. (2002). Establishment of the telencephalon during gastrulation by local antagonism of Wnt signaling. Neuron *35*, 255–265.

Huang, P., Xiong, F., Megason, S.G., and Schier, A.F. (2012). Attenuation of Notch and Hedgehog signaling is required for fate specification in the spinal cord. PLoS Genet *8*, e1002762.

Huang, X., Litingtung, Y., and Chiang, C. (2007). Region-specific requirement for cholesterol modification of sonic hedgehog in patterning the telencephalon and spinal cord. Development *134*, 2095–2105.

Huang, Y., Prasad, M., Lemon, W.J., Hampel, H., Wright, F.A., Kornacker, K., LiVolsi, V., Frankel, W., Kloos, R.T., Eng, C., et al. (2001). Gene expression in papillary thyroid carcinoma reveals highly consistent profiles. Proc Natl Acad Sci U S A *98*, 15044–15049.

Hui, C.-C., and Angers, S. (2011). Gli proteins in development and disease. Annu Rev Cell Dev Biol *27*, 513–537.

Humke, E.W., Dorn, K.V., Milenkovic, L., Scott, M.P., and Rohatgi, R. (2010). The output of Hedgehog signaling is controlled by the dynamic association between Suppressor of Fused and the Gli proteins. Genes Dev *24*, 670–682.

Hynes, M., Stone, D.M., Dowd, M., Pitts-Meek, S., Goddard, A., Gurney, A., and Rosenthal, A. (1997). Control of cell pattern in the neural tube by the zinc finger transcription factor and oncogene Gli-1. Neuron *19*, 15–26.

Ihrie, R.A., and Alvarez-Buylla, A. (2011). Lake-front property: a unique germinal niche by the lateral ventricles of the adult brain. Neuron *70*, 674–686.

Incardona, J.P., Gruenberg, J., and Roelink, H. (2002). Sonic hedgehog induces the segregation of patched and smoothened in endosomes. Curr Biol *12*, 983–995.

Izzi, L., Lévesque, M., Morin, S., Laniel, D., Wilkes, B.C., Mille, F., Krauss, R.S., McMahon, A.P., Allen, B.L., and Charron, F. (2011). Boc and Gas1 each form distinct Shh receptor complexes with Ptch1 and are required for Shh-mediated cell proliferation. Dev Cell *20*, 788–801.

Jacobs, C.T., and Huang, P. (2019). Notch signalling maintains Hedgehog responsiveness via a Gli-dependent mechanism during spinal cord patterning in zebrafish. Elife *8*.

Jeong, J., and McMahon, A.P. (2005). Growth and pattern of the mammalian neural tube are governed by partially overlapping feedback activities of the hedgehog antagonists patched 1 and Hhip1. Development *132*, 143–154.

Jessell, T.M. (2000). Neuronal specification in the spinal cord: inductive signals and transcriptional codes. Nat Rev Genet *1*, 20–29.

Jia, J., Tong, C., Wang, B., Luo, L., and Jiang, J. (2004). Hedgehog signalling activity of Smoothened requires phosphorylation by protein kinase A and casein kinase I. Nature *432*, 1045–1050.

Jia, J., Zhang, L., Zhang, Q., Tong, C., Wang, B., Hou, F., Amanai, K., and Jiang, J. (2005). Phosphorylation by double-time/CKIepsilon and CKIalpha targets cubitus interruptus for Slimb/beta-TRCP-mediated proteolytic processing. Dev Cell *9*, 819–830.

Juriloff, D.M., Harris, M.J., Tom, C., and MacDonald, K.B. (1991). Normal mouse strains differ in the site of initiation of closure of the cranial neural tube. Teratology *44*, 225–233.

Kang, J.S., Gao, M., Feinleib, J.L., Cotter, P.D., Guadagno, S.N., and Krauss, R.S. (1997). CDO: an oncogene-, serum-, and anchorage-regulated member of the Ig/fibronectin type III repeat family. J Cell Biol *138*, 203–213.

Kang, J.-S., Mulieri, P.J., Hu, Y., Taliana, L., and Krauss, R.S. (2002). BOC, an Ig superfamily member, associates with CDO to positively regulate myogenic differentiation. EMBO J *21*, 114–124.

Kang, J.-S., Zhang, W., and Krauss, R.S. (2007). Hedgehog signaling: cooking with Gas1. Sci STKE *2007*, pe50.

Kantarci, S., Al-Gazali, L., Hill, R.S., Donnai, D., Black, G.C.M., Bieth, E., Chassaing, N., Lacombe, D., Devriendt, K., Teebi, A., et al. (2007). Mutations in LRP2, which encodes the multiligand receptor megalin, cause Donnai-Barrow and facio-oculo-acoustico-renal syndromes. Nat Genet *39*, 957–959.

Kantarci, S., Ragge, N.K., Thomas, N.S., Robinson, D.O., Noonan, K.M., Russell, M.K., Donnai, D., Raymond, F.L., Walsh, C.A., Donahoe, P.K., et al. (2008). Donnai-Barrow syndrome (DBS/FOAR) in a child with a homozygous LRP2 mutation due to complete chromosome 2 paternal isodisomy. Am J Med Genet A *146A*, 1842–1847.

Kauvar, E.F., Solomon, B.D., Curry, C.J.R., van Essen, A.J., Janssen, N., Dutra, A., Roessler, E., and Muenke, M. (2010). Holoprosencephaly and agnathia spectrum: Presentation of two new patients and review of the literature. Am J Med Genet C Semin Med Genet *154C*, 158–169.

Keller, R., Davidson, L., Edlund, A., Elul, T., Ezin, M., Shook, D., and Skoglund, P. (2000). Mechanisms of convergence and extension by cell intercalation. Philos Trans R Soc Lond B Biol Sci *355*, 897–922.

Keyel, P.A., Thieman, J.R., Roth, R., Erkan, E., Everett, E.T., Watkins, S.C., Heuser, J.E., and Traub, L.M. (2008). The AP-2 adaptor beta2 appendage scaffolds alternate cargo endocytosis. Mol Biol Cell *19*, 5309–5326.

Khalifa, O., Al-Sahlawi, Z., Imtiaz, F., Ramzan, K., Allam, R., Al-Mostafa, A., Abdel-Fattah, M., Abuharb, G., Nester, M., Verloes, A., et al. (2015). Variable expression pattern in Donnai-Barrow syndrome: Report of two novel LRP2 mutations and review of the literature. Eur J Med Genet *58*, 293–299.

Khan, A.O., and Ghazi, N.G. (2018). The distinct optic disk and peripapillary appearance in Donnai-Barrow syndrome. Ophthalmic Genet *39*, 321–324.

Khokha, M.K., Yeh, J., Grammer, T.C., and Harland, R.M. (2005). Depletion of three BMP antagonists from Spemann's organizer leads to a catastrophic loss of dorsal structures. Dev Cell *8*, 401–411.

Khonsari, R.H., Seppala, M., Pradel, A., Dutel, H., Clément, G., Lebedev, O., Ghafoor, S., Rothova, M., Tucker, A., Maisey, J.G., et al. (2013). The buccohypophyseal canal is an ancestral vertebrate trait maintained by modulation in sonic hedgehog signaling. BMC Biol *11*, 27.

Kibar, Z., Vogan, K.J., Groulx, N., Justice, M.J., Underhill, D.A., and Gros, P. (2001). Ltap, a mammalian homolog of Drosophila Strabismus/Van Gogh, is altered in the mouse neural tube mutant Loop-tail. Nat Genet *28*, 251–255.

Kimura, C., Yoshinaga, K., Tian, E., Suzuki, M., Aizawa, S., and Matsuo, I. (2000). Visceral endoderm mediates forebrain development by suppressing posteriorizing signals. Dev Biol *225*, 304–321.

Kinzler, K.W., Bigner, S.H., Bigner, D.D., Trent, J.M., Law, M.L., O'Brien, S.J., Wong, A.J., and Vogelstein, B. (1987). Identification of an amplified, highly expressed gene in a human glioma. Science *236*, 70–73.

Kise, Y., Morinaka, A., Teglund, S., and Miki, H. (2009). Sufu recruits GSK3beta for efficient processing of Gli3. Biochem Biophys Res Commun *387*, 569–574.

Klingensmith, J., Matsui, M., Yang, Y.-P., and Anderson, R.M. (2010). Roles of bone morphogenetic protein signaling and its antagonism in holoprosencephaly. Am J Med Genet C Semin Med Genet *154C*, 43–51.

Kogerman, P., Grimm, T., Kogerman, L., Krause, D., Undén, A.B., Sandstedt, B., Toftgård, R., and Zaphiropoulos, P.G. (1999). Mammalian suppressor-of-fused modulates nuclear-cytoplasmic shuttling of Gli-1. Nat Cell Biol *1*, 312–319.

Kong, J.H., Yang, L., Dessaud, E., Chuang, K., Moore, D.M., Rohatgi, R., Briscoe, J., and Novitch, B.G. (2015). Notch activity modulates the responsiveness of neural progenitors to sonic hedgehog signaling. Dev Cell *33*, 373–387.

Kovacs, J.J., Whalen, E.J., Liu, R., Xiao, K., Kim, J., Chen, M., Wang, J., Chen, W., and Lefkowitz, R.J. (2008). Beta-arrestin-mediated localization of smoothened to the primary cilium. Science *320*, 1777–1781.

Kubo, M., Nakamura, M., Tasaki, A., Yamanaka, N., Nakashima, H., Nomura, M., Kuroki, S., and Katano, M. (2004). Hedgehog signaling pathway is a new therapeutic target for patients with breast cancer. Cancer Res *64*, 6071–6074.

Kudoh, T., Concha, M.L., Houart, C., Dawid, I.B., and Wilson, S.W. (2004). Combinatorial Fgf and Bmp signalling patterns the gastrula ectoderm into prospective neural and epidermal domains. Development *131*, 3581–3592.

Kuwabara, P.E., and Labouesse, M. (2002). The sterol-sensing domain: multiple families, a unique role? Trends Genet *18*, 193–201.

Lammer, E.J., Chen, D.T., Hoar, R.M., Agnish, N.D., Benke, P.J., Braun, J.T., Curry, C.J., Fernhoff, P.M., Grix, A.W.J., and Lott, I.T. (1985). Retinoic acid embryopathy. N Engl J Med *313*, 837–841.

Lapouge, G., Millon, R., Muller, D., Abecassis, J., Eber, M., Bergerat, J.P., and Klein-Soyer, C. (2005). Cisplatin-induced genes as potential markers for thyroid cancer. Cell Mol Life Sci *62*, 53–64.

Lee, C.S., and Fan, C.M. (2001). Embryonic expression patterns of the mouse and chick Gas1 genes. Mech Dev *101*, 293–297.

Lee, S., and Gleeson, J.G. (2020). Closing in on Mechanisms of Open Neural Tube Defects. Trends Neurosci *43*, 519–532.

Lee, C.S., Buttitta, L., and Fan, C.M. (2001a). Evidence that the WNT-inducible growth arrest-specific gene 1 encodes an antagonist of sonic hedgehog signaling in the somite. Proc Natl Acad Sci U S A *98*, 11347–11352.

Lee, J.D., Kraus, P., Gaiano, N., Nery, S., Kohtz, J., Fishell, G., Loomis, C.A., and Treisman, J.E. (2001b). An acylatable residue of Hedgehog is differentially required in Drosophila and mouse limb development. Dev Biol *233*, 122–136.

Lee, K.K., Leung, A.K., Tang, M.K., Cai, D.Q., Schneider, C., Brancolini, C., and Chow, P.H. (2001c). Functions of the growth arrest specific 1 gene in the development of the mouse embryo. Dev Biol *234*, 188–203.

Lee, S.M., Tole, S., Grove, E., and McMahon, A.P. (2000). A local Wnt-3a signal is required for development of the mammalian hippocampus. Development *127*, 457–467.

Leheste, J.R., Rolinski, B., Vorum, H., Hilpert, J., Nykjaer, A., Jacobsen, C., Aucouturier, P., Moskaug, J.O., Otto, A., Christensen, E.I., et al. (1999). Megalin knockout mice as an animal model of low molecular weight proteinuria. Am J Pathol *155*, 1361–1370.

Li, Y., van Kerkhof, P., Marzolo, M.P., Strous, G.J., and Bu, G. (2001). Identification of a major cyclic AMP-dependent protein kinase A phosphorylation site within the cytoplasmic tail of the low-density lipoprotein receptor-related protein: implication for receptor-mediated endocytosis. Mol Cell Biol *21*, 1185–1195.

Li, Y., Klena, N.T., Gabriel, G.C., Liu, X., Kim, A.J., Lemke, K., Chen, Y., Chatterjee, B., Devine, W., Damerla, R.R., et al. (2015). Global genetic analysis in mice unveils central role for cilia in congenital heart disease. Nature *521*, 520–524.

Lim, D.A., Tramontin, A.D., Trevejo, J.M., Herrera, D.G., García-Verdugo, J.M., and Alvarez-Buylla, A. (2000). Noggin antagonizes BMP signaling to create a niche for adult neurogenesis. Neuron *28*, 713–726.

Lundgren, S., Carling, T., Hjälm, G., Juhlin, C., Rastad, J., Pihlgren, U., Rask, L., Akerström, G., and Hellman, P. (1997). Tissue distribution of human gp330/megalin, a putative Ca(2+)-sensing protein. J Histochem Cytochem *45*, 383–392.

Ma, Y., Erkner, A., Gong, R., Yao, S., Taipale, J., Basler, K., and Beachy, P.A. (2002). Hedgehog-mediated patterning of the mammalian embryo requires transporter-like function of dispatched. Cell *111*, 63–75.

Maeda, Y., Nakamura, E., Nguyen, M.-T., Suva, L.J., Swain, F.L., Razzaque, M.S., Mackem, S., and Lanske, B. (2007). Indian Hedgehog produced by postnatal chondrocytes is essential for maintaining a growth plate and trabecular bone. Proc Natl Acad Sci U S A *104*, 6382–6387.

Mann, R.K., and Beachy, P.A. (2004). Novel lipid modifications of secreted protein signals. Annu Rev Biochem *73*, 891–923.

Marcorelles, P., and Laquerriere, A. (2010). Neuropathology of holoprosencephaly. Am J Med Genet C Semin Med Genet *154C*, 109–119.

Marinò, M., Lisi, S., Pinchera, A., Chiovato, L., and McCluskey, R.T. (2003). Targeting of thyroglobulin to transcytosis following megalin-mediated endocytosis: evidence for a preferential pH-independent pathway. J Endocrinol Invest *26*, 222–229.

Martinelli, D.C., and Fan, C.-M. (2007). Gas1 extends the range of Hedgehog action by facilitating its signaling. Genes Dev *21*, 1231–1243.

Maruoka, Y., Ohbayashi, N., Hoshikawa, M., Itoh, N., Hogan, B.L., and Furuta, Y. (1998). Comparison of the expression of three highly related genes, Fgf8, Fgf17 and Fgf18, in the mouse embryo. Mech Dev *74*, 175–177.

Mas, C., and Ruiz i Altaba, A. (2010). Small molecule modulation of HH-GLI signaling: current leads, trials and tribulations. Biochem Pharmacol *80*, 712–723.

Matsumoto, A., Hatta, T., Moriyama, K., and Otani, H. (2002). Sequential observations of exencephaly and subsequent morphological changes by mouse exo utero development system: analysis of the mechanism of transformation from exencephaly to anencephaly. Anat Embryol (Berl) *205*, 7–18.

McMahon, A.P., Ingham, P.W., and Tabin, C.J. (2003). Developmental roles and clinical significance of hedgehog signaling. Curr Top Dev Biol *53*, 1–114.

McWhirter, J.R., Goulding, M., Weiner, J.A., Chun, J., and Murre, C. (1997). A novel fibroblast growth factor gene expressed in the developing nervous system is a downstream target of the chimeric homeodomain oncoprotein E2A-Pbx1. Development *124*, 3221–3232.

Mecklenburg, N., Kowalczyk, I., Witte, F., Görne, J., Laier, A., Mamo, T.M., Gonschior, H., Lehmann, M., Richter, M., Sporbert, A., et al. (2021). Identification of disease-relevant modulators of the SHH pathway in the developing brain. Development *148*.

Mercier, S., David, V., Ratié, L., Gicquel, I., Odent, S., and Dupé, V. (2013). NODAL and SHH dose-dependent double inhibition promotes an HPE-like phenotype in chick embryos. Dis Model Mech *6*, 537–543.

Meyers, E.N., Lewandoski, M., and Martin, G.R. (1998). An Fgf8 mutant allelic series generated by Cre- and Flp-mediated recombination. Nat Genet *18*, 136–141.

Milenkovic, L., Scott, M.P., and Rohatgi, R. (2009). Lateral transport of Smoothened from the plasma membrane to the membrane of the cilium. J Cell Biol *187*, 365–374.

Ming, J.E., and Muenke, M. (1998). Holoprosencephaly: from Homer to Hedgehog. Clin Genet *53*, 155–163.

Ming, J.E., and Muenke, M. (2002). Multiple hits during early embryonic development: digenic diseases and holoprosencephaly. Am J Hum Genet *71*, 1017–1032.

Ming, J.E., Kaupas, M.E., Roessler, E., Brunner, H.G., Golabi, M., Tekin, M., Stratton, R.F., Sujansky, E., Bale, S.J., and Muenke, M. (2002). Mutations in PATCHED-1, the receptor for SONIC HEDGEHOG, are associated with holoprosencephaly. Hum Genet *110*, 297–301.

Miyake, Y., Tajima, S., Funahashi, T., and Yamamoto, A. (1989). Analysis of a recycling-impaired mutant of low density lipoprotein receptor in familial hypercholesterolemia. J Biol Chem *264*, 16584–16590.

Montcouquiol, M., Rachel, R.A., Lanford, P.J., Copeland, N.G., Jenkins, N.A., and Kelley, M.W. (2003). Identification of Vangl2 and Scrb1 as planar polarity genes in mammals. Nature *423*, 173–177.

Monuki, E.S. (2007). The morphogen signaling network in forebrain development and holoprosencephaly. J Neuropathol Exp Neurol *66*, 566–575.

Moradi, S., Mahdizadeh, H., Šarić, T., Kim, J., Harati, J., Shahsavarani, H., Greber, B., and Moore, J.B. 4th (2019). Research and therapy with induced pluripotent stem cells (iPSCs): social, legal, and ethical considerations. Stem Cell Res Ther *10*, 341.

Morales, C.R., Zeng, J., El Alfy, M., Barth, J.L., Chintalapudi, M.R., McCarthy, R.A., Incardona, J.P., and Argraves, W.S. (2006). Epithelial trafficking of Sonic hedgehog by megalin. J Histochem Cytochem *54*, 1115–1127.

Morris, S.M., Tallquist, M.D., Rock, C.O., and Cooper, J.A. (2002). Dual roles for the Dab2 adaptor protein in embryonic development and kidney transport. EMBO J *21*, 1555–1564.

Motoyama, J., Heng, H., Crackower, M.A., Takabatake, T., Takeshima, K., Tsui, L.C., and Hui, C. (1998a). Overlapping and non-overlapping Ptch2 expression with Shh during mouse embryogenesis. Mech Dev *78*, 81–84.

Motoyama, J., Takabatake, T., Takeshima, K., and Hui, C. (1998b). Ptch2, a second mouse Patched gene is co-expressed with Sonic hedgehog. Nat Genet *18*, 104–106.

Mouden, C., Dubourg, C., Carré, W., Rose, S., Quelin, C., Akloul, L., Hamdi-Rozé, H., Viot, G., Salhi, H., Darnault, P., et al. (2016). Complex mode of inheritance in holoprosencephaly revealed by whole exome sequencing. Clin Genet *89*, 659–668.

Moury, J.D., and Schoenwolf, G.C. (1995). Cooperative model of epithelial shaping and bending during avian neurulation: autonomous movements of the neural plate, autonomous movements of the epidermis, and interactions in the neural plate/epidermis transition zone. Dev Dyn *204*, 323–337.

Muenke, M., and Beachy, P.A. (2000). Genetics of ventral forebrain development and holoprosencephaly. Curr Opin Genet Dev *10*, 262–269.

Muenke, M., Gurrieri, F., Bay, C., Yi, D.H., Collins, A.L., Johnson, V.P., Hennekam, R.C., Schaefer, G.B., Weik, L., and Lubinsky, M.S. (1994). Linkage of a human brain malformation, familial holoprosencephaly, to chromosome 7 and evidence for genetic heterogeneity. Proc Natl Acad Sci U S A *91*, 8102–8106.

Mukhopadhyay, M., Shtrom, S., Rodriguez-Esteban, C., Chen, L., Tsukui, T., Gomer, L., Dorward, D.W., Glinka, A., Grinberg, A., Huang, S.P., et al. (2001). Dickkopf1 is required for embryonic head induction and limb morphogenesis in the mouse. Dev Cell *1*, 423–434.

Murdoch, J.N., Doudney, K., Paternotte, C., Copp, A.J., and Stanier, P. (2001). Severe neural tube defects in the loop-tail mouse result from mutation of Lpp1, a novel gene involved in floor plate specification. Hum Mol Genet *10*, 2593–2601.

Murdoch, J.N., Henderson, D.J., Doudney, K., Gaston-Massuet, C., Phillips, H.M., Paternotte, C., Arkell, R., Stanier, P., and Copp, A.J. (2003). Disruption of scribble (Scrb1) causes severe neural tube defects in the circletail mouse. Hum Mol Genet *12*, 87–98.

Naccache, S.N., Hasson, T., and Horowitz, A. (2006). Binding of internalized receptors to the PDZ domain of GIPC/synectin recruits myosin VI to endocytic vesicles. Proc Natl Acad Sci U S A *103*, 12735–12740.

Nachtergaele, S., Mydock, L.K., Krishnan, K., Rammohan, J., Schlesinger, P.H., Covey, D.F., and Rohatgi, R. (2012). Oxysterols are allosteric activators of the oncoprotein Smoothened. Nat Chem Biol *8*, 211–220.

Nadeau, J.H. (2001). Modifier genes in mice and humans. Nat Rev Genet *2*, 165–174.

Nagai, J., Christensen, E.I., Morris, S.M., Willnow, T.E., Cooper, J.A., and Nielsen, R. (2005). Mutually dependent localization of megalin and Dab2 in the renal proximal tubule. Am J Physiol Renal Physiol *289*, F569-576.

Nanni, L., Ming, J.E., Bocian, M., Steinhaus, K., Bianchi, D.W., Die-Smulders, C., Giannotti, A., Imaizumi, K., Jones, K.L., Campo, M.D., et al. (1999). The mutational spectrum of the sonic hedgehog gene in holoprosencephaly: SHH mutations cause a significant proportion of autosomal dominant holoprosencephaly. Hum Mol Genet *8*, 2479–2488.

Nieuwenhuis, E., Motoyama, J., Barnfield, P.C., Yoshikawa, Y., Zhang, X., Mo, R., Crackower, M.A., and Hui, C.-C. (2006). Mice with a targeted mutation of patched2 are viable but develop alopecia and epidermal hyperplasia. Mol Cell Biol *26*, 6609–6622.

Nikaido, H. (2011). Structure and mechanism of RND-type multidrug efflux pumps. Adv Enzymol Relat Areas Mol Biol *77*, 1–60.

Nikolopoulou, E., Galea, G.L., Rolo, A., Greene, N.D.E., and Copp, A.J. (2017). Neural tube closure: cellular, molecular and biomechanical mechanisms. Development *144*, 552–566.

Nüsslein-Volhard, C., and Wieschaus, E. (1980). Mutations affecting segment number and polarity in Drosophila. Nature *287*, 795–801.

Nykjaer, A., Dragun, D., Walther, D., Vorum, H., Jacobsen, C., Herz, J., Melsen, F., Christensen, E.I., and Willnow, T.E. (1999). An endocytic pathway essential for renal uptake and activation of the steroid 25-(OH) vitamin D3. Cell *96*, 507–515.

Odent, S., Le Marec, B., Munnich, A., Le Merrer, M., and Bonaïti-Pellié, C. (1998). Segregation analysis in nonsyndromic holoprosencephaly. Am J Med Genet *77*, 139–143.

Ohkubo, Y., Chiang, C., and Rubenstein, J.L.R. (2002). Coordinate regulation and synergistic actions of BMP4, SHH and FGF8 in the rostral prosencephalon regulate morphogenesis of the telencephalic and optic vesicles. Neuroscience *111*, 1–17.

Ohlig, S., Farshi, P., Pickhinke, U., van den Boom, J., Höing, S., Jakuschev, S., Hoffmann, D., Dreier, R., Schöler, H.R., Dierker, T., et al. (2011). Sonic hedgehog shedding results in functional activation of the solubilized protein. Dev Cell *20*, 764–774.

Okada, A., Charron, F., Morin, S., Shin, D.S., Wong, K., Fabre, P.J., Tessier-Lavigne, M., and McConnell, S.K. (2006). Boc is a receptor for sonic hedgehog in the guidance of commissural axons. Nature *444*, 369–373.

Orioli, I.M., and Castilla, E.E. (2010). Epidemiology of holoprosencephaly: Prevalence and risk factors. Am J Med Genet C Semin Med Genet *154C*, 13–21.

Ortega, M.C., Cases, O., Merchán, P., Kozyraki, R., Clemente, D., and de Castro, F. (2012). Megalin mediates the influence of sonic hedgehog on oligodendrocyte precursor cell migration and proliferation during development. Glia *60*, 851–866.

Panáková, D., Sprong, H., Marois, E., Thiele, C., and Eaton, S. (2005). Lipoprotein particles are required for Hedgehog and Wingless signalling. Nature *435*, 58–65.

Patten, I., and Placzek, M. (2000). The role of Sonic hedgehog in neural tube patterning. Cell Mol Life Sci *57*, 1695–1708.

Pepinsky, R.B., Zeng, C., Wen, D., Rayhorn, P., Baker, D.P., Williams, K.P., Bixler, S.A., Ambrose, C.M., Garber, E.A., Miatkowski, K., et al. (1998). Identification of a palmitic acid-modified form of human Sonic hedgehog. J Biol Chem *273*, 14037–14045.

Perler, F.B. (1998). Protein splicing of inteins and hedgehog autoproteolysis: structure, function, and evolution. Cell *92*, 1–4.

Petryk, A., Graf, D., and Marcucio, R. (2015). Holoprosencephaly: signaling interactions between the brain and the face, the environment and the genes, and the phenotypic variability in animal models and humans. Wiley Interdiscip Rev Dev Biol *4*, 17–32.

Pineda-Alvarez, D.E., Dubourg, C., David, V., Roessler, E., and Muenke, M. (2010). Current recommendations for the molecular evaluation of newly diagnosed holoprosencephaly patients. Am J Med Genet C Semin Med Genet *154C*, 93–101.

Pineda-Alvarez, D.E., Roessler, E., Hu, P., Srivastava, K., Solomon, B.D., Siple, C.E., Fan, C.-M., and Muenke, M. (2012). Missense substitutions in the GAS1 protein present in holoprosencephaly patients reduce the affinity for its ligand, SHH. Hum Genet *131*, 301–310.

Pober, B.R., Longoni, M., and Noonan, K.M. (2009). A review of Donnai-Barrow and facio-oculo-acoustico-renal (DB/FOAR) syndrome: clinical features and differential diagnosis. Birth Defects Res A Clin Mol Teratol *85*, 76–81.

Rahnama, F., Toftgård, R., and Zaphiropoulos, P.G. (2004). Distinct roles of PTCH2 splice variants in Hedgehog signalling. Biochem J *378*, 325–334.

Raible, F., and Brand, M. (2001). Tight transcriptional control of the ETS domain factors Erm and Pea3 by Fgf signaling during early zebrafish development. Mech Dev *107*, 105–117.

Rallu, M., Machold, R., Gaiano, N., Corbin, J.G., McMahon, A.P., and Fishell, G. (2002). Dorsoventral patterning is established in the telencephalon of mutants lacking both Gli3 and Hedgehog signaling. Development *129*, 4963–4974.

Ramírez-Weber, F.A., and Kornberg, T.B. (1999). Cytonemes: cellular processes that project to the principal signaling center in Drosophila imaginal discs. Cell *97*, 599–607.

Rash, B.G., and Grove, E.A. (2007). Patterning the dorsal telencephalon: a role for sonic hedgehog? J Neurosci *27*, 11595–11603.

Razzaque, M.S., Soegiarto, D.W., Chang, D., Long, F., and Lanske, B. (2005). Conditional deletion of Indian hedgehog from collagen type 2alpha1-expressing cells results in abnormal endochondral bone formation. J Pathol *207*, 453–461.

Ribeiro, L.A., Quiezi, R.G., Nascimento, A., Bertolacini, C.P., and Richieri-Costa, A. (2010). Holoprosencephaly and holoprosencephaly-like phenotype and GAS1 DNA sequence changes: Report of four Brazilian patients. Am J Med Genet A *152A*, 1688–1694.

Ringuette, R., Atkins, M., Lagali, P.S., Bassett, E.A., Campbell, C., Mazerolle, C., Mears, A.J., Picketts, D.J., and Wallace, V.A. (2016). A Notch-Gli2 axis sustains Hedgehog responsiveness of neural progenitors and Müller glia. Dev Biol *411*, 85–100.

Robb, L., and Tam, P.P.L. (2004). Gastrula organiser and embryonic patterning in the mouse. Semin Cell Dev Biol *15*, 543–554.

Roessler, E., and Muenke, M. (2010). The molecular genetics of holoprosencephaly. Am J Med Genet C Semin Med Genet *154C*, 52–61.

Roessler, E., Belloni, E., Gaudenz, K., Jay, P., Berta, P., Scherer, S.W., Tsui, L.C., and Muenke, M. (1996). Mutations in the human Sonic Hedgehog gene cause holoprosencephaly. Nat Genet *14*, 357–360.

Roessler, E., Du, Y.-Z., Mullor, J.L., Casas, E., Allen, W.P., Gillessen-Kaesbach, G., Roeder, E.R., Ming, J.E., Ruiz i Altaba, A., and Muenke, M. (2003). Loss-of-function mutations in the human GLI2 gene are associated with pituitary anomalies and holoprosencephaly-like features. Proc Natl Acad Sci U S A *100*, 13424–13429.

Roessler, E., El-Jaick, K.B., Dubourg, C., Vélez, J.I., Solomon, B.D., Pineda-Alvarez, D.E., Lacbawan, F., Zhou, N., Ouspenskaia, M., Paulussen, A., et al. (2009a). The mutational spectrum of holoprosencephaly-associated changes within the SHH gene in humans predicts loss-of-function through either key structural alterations of the ligand or its altered synthesis. Hum Mutat *30*, E921-935.

Roessler, E., Ma, Y., Ouspenskaia, M.V., Lacbawan, F., Bendavid, C., Dubourg, C., Beachy, P.A., and Muenke, M. (2009b). Truncating loss-of-function mutations of DISP1 contribute to holoprosencephaly-like microform features in humans. Hum Genet *125*, 393–400.

Rohatgi, R., Milenkovic, L., and Scott, M.P. (2007). Patched1 regulates hedgehog signaling at the primary cilium. Science *317*, 372–376.

Rojas-Ríos, P., Guerrero, I., and González-Reyes, A. (2012). Cytoneme-mediated delivery of hedgehog regulates the expression of bone morphogenetic proteins to maintain germline stem cells in Drosophila. PLoS Biol *10*, e1001298.

Rolo, A., Savery, D., Escuin, S., de Castro, S.C., Armer, H.E.J., Munro, P.M.G., Molè, M.A., Greene, N.D.E., and Copp, A.J. (2016). Regulation of cell protrusions by small GTPases during fusion of the neural folds. Elife *5*, e13273.

Ronen, G.M., and Andrews, W.L. (1991). Holoprosencephaly as a possible embryonic alcohol effect. Am J Med Genet *40*, 151–154.

Rosenfeld, J.A., Ballif, B.C., Martin, D.M., Aylsworth, A.S., Bejjani, B.A., Torchia, B.S., and Shaffer, L.G. (2010). Clinical characterization of individuals with deletions of genes in holoprosencephaly pathways by aCGH refines the phenotypic spectrum of HPE. Hum Genet *127*, 421–440.

Ruaro, E.M., Collavin, L., Del Sal, G., Haffner, R., Oren, M., Levine, A.J., and Schneider, C. (1997). A proline-rich motif in p53 is required for transactivation-independent growth arrest as induced by Gas1. Proc Natl Acad Sci U S A *94*, 4675–4680.

Rudenko, G., Henry, L., Henderson, K., Ichtchenko, K., Brown, M.S., Goldstein, J.L., and Deisenhofer, J. (2002). Structure of the LDL receptor extracellular domain at endosomal pH. Science *298*, 2353–2358.

Saito, A., Pietromonaco, S., Loo, A.K., and Farquhar, M.G. (1994). Complete cloning and sequencing of rat gp330/"megalin," a distinctive member of the low density lipoprotein receptor gene family. Proc Natl Acad Sci U S A *91*, 9725–9729.

Sasaki, H., Nishizaki, Y., Hui, C., Nakafuku, M., and Kondoh, H. (1999). Regulation of Gli2 and Gli3 activities by an amino-terminal repression domain: implication of Gli2 and Gli3 as primary mediators of Shh signaling. Development *126*, 3915–3924.

Schachter, K.A., and Krauss, R.S. (2008). Murine models of holoprosencephaly. Curr Top Dev Biol *84*, 139–170.

Schneider, C., King, R.M., and Philipson, L. (1988). Genes specifically expressed at growth arrest of mammalian cells. Cell *54*, 787–793.

Schrauwen, I., Sommen, M., Claes, C., Pinner, J., Flaherty, M., Collins, F., and Van Camp, G. (2014). Broadening the phenotype of LRP2 mutations: a new mutation in LRP2 causes a predominantly ocular phenotype suggestive of Stickler syndrome. Clin Genet *86*, 282–286.

Seppala, M., Depew, M.J., Martinelli, D.C., Fan, C.-M., Sharpe, P.T., and Cobourne, M.T. (2007). Gas1 is a modifier for holoprosencephaly and genetically interacts with sonic hedgehog. J Clin Invest *117*, 1575–1584.

Seppala, M., Xavier, G.M., Fan, C.-M., and Cobourne, M.T. (2014). Boc modifies the spectrum of holoprosencephaly in the absence of Gas1 function. Biol Open *3*, 728–740.

Shah, M., Baterina, O.Y.J., Taupin, V., and Farquhar, M.G. (2013). ARH directs megalin to the endocytic recycling compartment to regulate its proteolysis and gene expression. J Cell Biol *202*, 113–127.

Shaheen, I.S., Finlay, E., Prescott, K., Russell, M., Longoni, M., and Joss, S. (2010). Focal segmental glomerulosclerosis in a female patient with Donnai-Barrow syndrome. Clin Dysmorphol *19*, 35–37.

Shanmugalingam, S., Houart, C., Picker, A., Reifers, F., Macdonald, R., Barth, A., Griffin, K., Brand, M., and Wilson, S.W. (2000). Ace/Fgf8 is required for forebrain commissure formation and patterning of the telencephalon. Development *127*, 2549–2561.

Shimamura, K., and Rubenstein, J.L. (1997). Inductive interactions direct early regionalization of the mouse forebrain. Development *124*, 2709–2718.

Shimogori, T., Banuchi, V., Ng, H.Y., Strauss, J.B., and Grove, E.A. (2004). Embryonic signaling centers expressing BMP, WNT and FGF proteins interact to pattern the cerebral cortex. Development *131*, 5639–5647.

Shinya, M., Koshida, S., Sawada, A., Kuroiwa, A., and Takeda, H. (2001). Fgf signalling through MAPK cascade is required for development of the subpallial telencephalon in zebrafish embryos. Development *128*, 4153–4164.

Singh, V.K., Kalsan, M., Kumar, N., Saini, A., and Chandra, R. (2015). Induced pluripotent stem cells: applications in regenerative medicine, disease modeling, and drug discovery. Front Cell Dev Biol *3*, 2.

Smelkinson, M.G., and Kalderon, D. (2006). Processing of the Drosophila hedgehog signaling effector Ci-155 to the repressor Ci-75 is mediated by direct binding to the SCF component Slimb. Curr Biol *16*, 110–116.

Smith, J.L., and Schoenwolf, G.C. (1989). Notochordal induction of cell wedging in the chick neural plate and its role in neural tube formation. J Exp Zool *250*, 49–62.

Solnica-Krezel, L., and Sepich, D.S. (2012). Gastrulation: making and shaping germ layers. Annu Rev Cell Dev Biol *28*, 687–717.

Solomon, B.D., Mercier, S., Vélez, J.I., Pineda-Alvarez, D.E., Wyllie, A., Zhou, N., Dubourg, C., David, V., Odent, S., Roessler, E., et al. (2010a). Analysis of genotype-phenotype correlations in human holoprosencephaly. Am J Med Genet C Semin Med Genet *154C*, 133–141.

Solomon, B.D., Rosenbaum, K.N., Meck, J.M., and Muenke, M. (2010b). Holoprosencephaly due to numeric chromosome abnormalities. Am J Med Genet C Semin Med Genet *154C*, 146–148.

Spoelgen, R., Hammes, A., Anzenberger, U., Zechner, D., Andersen, O.M., Jerchow, B., and Willnow, T.E. (2005). LRP2/megalin is required for patterning of the ventral telencephalon. Development *132*, 405–414.

Stamataki, D., Ulloa, F., Tsoni, S.V., Mynett, A., and Briscoe, J. (2005). A gradient of Gli activity mediates graded Sonic Hedgehog signaling in the neural tube. Genes Dev *19*, 626–641.

Stasiulewicz, M., Gray, S.D., Mastromina, I., Silva, J.C., Björklund, M., Seymour, P.A., Booth, D., Thompson, C., Green, R.J., Hall, E.A., et al. (2015). A conserved role for Notch signaling in priming the cellular response to Shh through ciliary localisation of the key Shh transducer Smo. Development *142*, 2291–2303.

Stebel, M., Vatta, P., Ruaro, M.E., Del Sal, G., Parton, R.G., and Schneider, C. (2000). The growth suppressing gas1 product is a GPI-linked protein. FEBS Lett *481*, 152–158.

Stern, C.D., and Downs, K.M. (2012). The hypoblast (visceral endoderm): an evo-devo perspective. Development *139*, 1059–1069.

St-Jacques, B., Hammerschmidt, M., and McMahon, A.P. (1999). Indian hedgehog signaling regulates proliferation and differentiation of chondrocytes and is essential for bone formation. Genes Dev *13*, 2072–2086.

Stora, S., Conte, M., Chouery, E., Richa, S., Jalkh, N., Gillart, A.-C., Joannis, A.-L. de, and Mégarbané, A. (2009). A 56-year-old female patient with facio-oculo-acoustico-renal syndrome (FOAR) syndrome. Report on the natural history and of a novel mutation. Eur J Med Genet *52*, 341–343.

Storm, T., Tranebjærg, L., Frykholm, C., Birn, H., Verroust, P.J., Nevéus, T., Sundelin, B., Hertz, J.M., Holmström, G., Ericson, K., et al. (2013). Renal phenotypic investigations of megalin-deficient patients: novel insights into tubular proteinuria and albumin filtration. Nephrol Dial Transplant *28*, 585–591.

Storm, T., Heegaard, S., Christensen, E.I., and Nielsen, R. (2014). Megalin-deficiency causes high myopia, retinal pigment epithelium-macromelanosomes and abnormal development of the ciliary body in mice. Cell Tissue Res *358*, 99–107.

Streit, A., Berliner, A.J., Papanayotou, C., Sirulnik, A., and Stern, C.D. (2000). Initiation of neural induction by FGF signalling before gastrulation. Nature *406*, 74–78.

Sulik, K.K., Dehart, D.B., Rogers, J.M., and Chernoff, N. (1995). Teratogenicity of low doses of all-trans retinoic acid in presomite mouse embryos. Teratology *51*, 398–403.

Tabata, T., and Takei, Y. (2004). Morphogens, their identification and regulation. Development *131*, 703–712.

Taipale, J., Cooper, M.K., Maiti, T., and Beachy, P.A. (2002). Patched acts catalytically to suppress the activity of Smoothened. Nature *418*, 892–897.

Takahashi, K., Tanabe, K., Ohnuki, M., Narita, M., Ichisaka, T., Tomoda, K., and Yamanaka, S. (2007). Induction of pluripotent stem cells from adult human fibroblasts by defined factors. Cell *131*, 861–872.

Takeda, T., Yamazaki, H., and Farquhar, M.G. (2003). Identification of an apical sorting determinant in the cytoplasmic tail of megalin. Am J Physiol Cell Physiol *284*, C1105-1113.

Take-uchi, M., Clarke, J.D.W., and Wilson, S.W. (2003). Hedgehog signalling maintains the optic stalk-retinal interface through the regulation of Vax gene activity. Development *130*, 955–968.

Takiguchi-Hayashi, K., Sekiguchi, M., Ashigaki, S., Takamatsu, M., Hasegawa, H., Suzuki-Migishima, R., Yokoyama, M., Nakanishi, S., and Tanabe, Y. (2004). Generation of reelin-positive marginal zone cells from the caudomedial wall of telencephalic vesicles. J Neurosci *24*, 2286–2295.

Taylor, F.R., Wen, D., Garber, E.A., Carmillo, A.N., Baker, D.P., Arduini, R.M., Williams, K.P., Weinreb, P.H., Rayhorn, P., Hronowski, X., et al. (2001). Enhanced potency of human Sonic hedgehog by hydrophobic modification. Biochemistry *40*, 4359–4371.

Tenzen, T., Allen, B.L., Cole, F., Kang, J.-S., Krauss, R.S., and McMahon, A.P. (2006). The cell surface membrane proteins Cdo and Boc are components and targets of the Hedgehog signaling pathway and feedback network in mice. Dev Cell *10*, 647–656.

Thayer, S.P., di Magliano, M.P., Heiser, P.W., Nielsen, C.M., Roberts, D.J., Lauwers, G.Y., Qi, Y.P., Gysin, S., Fernández-del Castillo, C., Yajnik, V., et al. (2003). Hedgehog is an early and late mediator of pancreatic cancer tumorigenesis. Nature *425*, 851–856.

Theil, T., Aydin, S., Koch, S., Grotewold, L., and Rüther, U. (2002). Wnt and Bmp signalling cooperatively regulate graded Emx2 expression in the dorsal telencephalon. Development *129*, 3045–3054.

Thérond, P.P. (2012). Release and transportation of Hedgehog molecules. Curr Opin Cell Biol *24*, 173–180.

Tole, S., Gutin, G., Bhatnagar, L., Remedios, R., and Hébert, J.M. (2006). Development of midline cell types and commissural axon tracts requires Fgfr1 in the cerebrum. Dev Biol *289*, 141–151.

Tseng, T.T., Gratwick, K.S., Kollman, J., Park, D., Nies, D.H., Goffeau, A., and Saier, M.H.J. (1999). The RND permease superfamily: an ancient, ubiquitous and diverse family that includes human disease and development proteins. J Mol Microbiol Biotechnol *1*, 107–125.

Tukachinsky, H., Lopez, L.V., and Salic, A. (2010). A mechanism for vertebrate Hedgehog signaling: recruitment to cilia and dissociation of SuFu-Gli protein complexes. J Cell Biol *191*, 415–428.

Tukachinsky, H., Kuzmickas, R.P., Jao, C.Y., Liu, J., and Salic, A. (2012). Dispatched and scube mediate the efficient secretion of the cholesterol-modified hedgehog ligand. Cell Rep *2*, 308–320.

Tuson, M., He, M., and Anderson, K.V. (2011). Protein kinase A acts at the basal body of the primary cilium to prevent Gli2 activation and ventralization of the mouse neural tube. Development *138*, 4921–4930.

Varjosalo, M., and Taipale, J. (2008). Hedgehog: functions and mechanisms. Genes Dev *22*, 2454–2472.

Veth, K.N., Willer, J.R., Collery, R.F., Gray, M.P., Willer, G.B., Wagner, D.S., Mullins, M.C., Udvadia, A.J., Smith, R.S., John, S.W.M., et al. (2011). Mutations in zebrafish lrp2 result in adult-onset ocular pathogenesis that models myopia and other risk factors for glaucoma. PLoS Genet *7*, e1001310.

Von Ohlen, T., Lessing, D., Nusse, R., and Hooper, J.E. (1997). Hedgehog signaling regulates transcription through cubitus interruptus, a sequence-specific DNA binding protein. Proc Natl Acad Sci U S A *94*, 2404–2409.

Vortkamp, A., Lee, K., Lanske, B., Segre, G.V., Kronenberg, H.M., and Tabin, C.J. (1996). Regulation of rate of cartilage differentiation by Indian hedgehog and PTH-related protein. Science *273*, 613–622.

Vyas, N., Goswami, D., Manonmani, A., Sharma, P., Ranganath, H.A., VijayRaghavan, K., Shashidhara, L.S., Sowdhamini, R., and Mayor, S. (2008). Nanoscale organization of hedgehog is essential for long-range signaling. Cell *133*, 1214–1227.

Wallingford, J.B., and Harland, R.M. (2001). Xenopus Dishevelled signaling regulates both neural and mesodermal convergent extension: parallel forces elongating the body axis. Development *128*, 2581–2592.

Wallingford, J.B., and Harland, R.M. (2002). Neural tube closure requires Dishevelled-dependent convergent extension of the midline. Development *129*, 5815–5825.

Wallis, D.E., Roessler, E., Hehr, U., Nanni, L., Wiltshire, T., Richieri-Costa, A., Gillessen-Kaesbach, G., Zackai, E.H., Rommens, J., and Muenke, M. (1999). Mutations in the homeodomain of the human SIX3 gene cause holoprosencephaly. Nat Genet *22*, 196–198.

Walshe, J., and Mason, I. (2003). Unique and combinatorial functions of Fgf3 and Fgf8 during zebrafish forebrain development. Development *130*, 4337–4349.

Wang, B., Fallon, J.F., and Beachy, P.A. (2000). Hedgehog-regulated processing of Gli3 produces an anterior/posterior repressor gradient in the developing vertebrate limb. Cell *100*, 423–434.

Wang, J., Hamblet, N.S., Mark, S., Dickinson, M.E., Brinkman, B.C., Segil, N., Fraser, S.E., Chen, P., Wallingford, J.B., and Wynshaw-Boris, A. (2006). Dishevelled genes mediate a conserved mammalian PCP pathway to regulate convergent extension during neurulation. Development *133*, 1767–1778.

Wang, Y., Zhou, Z., Walsh, C.T., and McMahon, A.P. (2009). Selective translocation of intracellular Smoothened to the primary cilium in response to Hedgehog pathway modulation. Proc Natl Acad Sci U S A *106*, 2623–2628.

Wang, Y.P., Dakubo, G., Howley, P., Campsall, K.D., Mazarolle, C.J., Shiga, S.A., Lewis, P.M., McMahon, A.P., and Wallace, V.A. (2002). Development of normal retinal organization depends on Sonic hedgehog signaling from ganglion cells. Nat Neurosci *5*, 831–832.

Ware, M., Hamdi-Rozé, H., Le Friec, J., David, V., and Dupé, V. (2016). Regulation of downstream neuronal genes by proneural transcription factors during initial neurogenesis in the vertebrate brain. Neural Dev *11*, 22.

Washington Smoak, I., Byrd, N.A., Abu-Issa, R., Goddeeris, M.M., Anderson, R., Morris, J., Yamamura, K., Klingensmith, J., and Meyers, E.N. (2005). Sonic hedgehog is required for cardiac outflow tract and neural crest cell development. Dev Biol *283*, 357–372.

Watanabe, K., Nagaoka, T., Lee, J.M., Bianco, C., Gonzales, M., Castro, N.P., Rangel, M.C., Sakamoto, K., Sun, Y., Callahan, R., et al. (2009). Enhancement of Notch receptor maturation and signaling sensitivity by Cripto-1. J Cell Biol *187*, 343–353.

Watkins, D.N., Berman, D.M., Burkholder, S.G., Wang, B., Beachy, P.A., and Baylin, S.B. (2003). Hedgehog signalling within airway epithelial progenitors and in small-cell lung cancer. Nature *422*, 313–317.

Weaver, D.D., Solomon, B.D., Akin-Samson, K., Kelley, R.I., and Muenke, M. (2010). Cyclopia (synophthalmia) in Smith-Lemli-Opitz syndrome: First reported case and consideration of mechanism. Am J Med Genet C Semin Med Genet *154C*, 142–145.

van der Westhuyzen, D.R., Stein, M.L., Henderson, H.E., Marais, A.D., Fourie, A.M., and Coetzee, G.A. (1991). Deletion of two growth-factor repeats from the low-density-lipoprotein receptor accelerates its degradation. Biochem J *277 (Pt 3)*, 677–682.

Wicher, G., Larsson, M., Fex Svenningsen, A., Gyllencreutz, E., Rask, L., and Aldskogius, H. (2006). Low density lipoprotein receptor-related protein-2/megalin is expressed in oligodendrocytes in the mouse spinal cord white matter. J Neurosci Res *83*, 864–873.

Willnow, T.E., Hilpert, J., Armstrong, S.A., Rohlmann, A., Hammer, R.E., Burns, D.K., and Herz, J. (1996). Defective forebrain development in mice lacking gp330/megalin. Proc Natl Acad Sci U S A *93*, 8460–8464.

Wilson, S.W., and Houart, C. (2004). Early steps in the development of the forebrain. Dev Cell *6*, 167–181.

Wood, L.R., and Smith, M.T. (1984). Generation of anencephaly: 1. Aberrant neurulation and 2. Conversion of exencephaly to anencephaly. J Neuropathol Exp Neurol *43*, 620–633.

Xavier, G.M., Seppala, M., Papageorgiou, S.N., Fan, C.-M., and Cobourne, M.T. (2016). Genetic interactions between the hedgehog co-receptors Gas1 and Boc regulate cell proliferation during murine palatogenesis. Oncotarget *7*, 79233–79246.

Yamaguchi, Y., and Miura, M. (2013). How to form and close the brain: insight into the mechanism of cranial neural tube closure in mammals. Cell Mol Life Sci *70*, 3171–3186.

Yang, Y.-P., and Klingensmith, J. (2006). Roles of organizer factors and BMP antagonism in mammalian forebrain establishment. Dev Biol *296*, 458–475.

Yang, C., Chen, W., Chen, Y., and Jiang, J. (2012). Smoothened transduces Hedgehog signal by forming a complex with Evc/Evc2. Cell Res *22*, 1593–1604.

Yao, S., Lum, L., and Beachy, P. (2006). The ihog cell-surface proteins bind Hedgehog and mediate pathway activation. Cell *125*, 343–357.

Ybot-Gonzalez, P., Cogram, P., Gerrelli, D., and Copp, A.J. (2002). Sonic hedgehog and the molecular regulation of mouse neural tube closure. Development *129*, 2507–2517.

Ybot-Gonzalez, P., Gaston-Massuet, C., Girdler, G., Klingensmith, J., Arkell, R., Greene, N.D.E., and Copp, A.J. (2007). Neural plate morphogenesis during mouse neurulation is regulated by antagonism of Bmp signalling. Development *134*, 3203–3211.

Ye, W., Shimamura, K., Rubenstein, J.L., Hynes, M.A., and Rosenthal, A. (1998). FGF and Shh signals control dopaminergic and serotonergic cell fate in the anterior neural plate. Cell *93*, 755–766.

Yuseff, M.I., Farfan, P., Bu, G., and Marzolo, M.-P. (2007). A cytoplasmic PPPSP motif determines megalin's phosphorylation and regulates receptor's recycling and surface expression. Traffic *8*, 1215–1230.

Zaidi, S., Choi, M., Wakimoto, H., Ma, L., Jiang, J., Overton, J.D., Romano-Adesman, A., Bjornson, R.D., Breitbart, R.E., Brown, K.K., et al. (2013). De novo mutations in histone-modifying genes in congenital heart disease. Nature *498*, 220–223.

Zamorano, A., Lamas, M., Vergara, P., Naranjo, J.R., and Segovia, J. (2003). Transcriptionally mediated gene targeting of gas1 to glioma cells elicits growth arrest and apoptosis. J Neurosci Res *71*, 256–263.

Zamorano, A., Mellström, B., Vergara, P., Naranjo, J.R., and Segovia, J. (2004). Glial-specific retrovirally mediated gas1 gene expression induces glioma cell apoptosis and inhibits tumor growth in vivo. Neurobiol Dis *15*, 483–491.

Zeng, X., Goetz, J.A., Suber, L.M., Scott, W.J.J., Schreiner, C.M., and Robbins, D.J. (2001). A freely diffusible form of Sonic hedgehog mediates long-range signalling. Nature *411*, 716–720.

Zhang, W., Kang, J.-S., Cole, F., Yi, M.-J., and Krauss, R.S. (2006). Cdo functions at multiple points in the Sonic Hedgehog pathway, and Cdo-deficient mice accurately model human holoprosencephaly. Dev Cell *10*, 657–665.

Zhang, W., Hong, M., Bae, G., Kang, J.-S., and Krauss, R.S. (2011). Boc modifies the holoprosencephaly spectrum of Cdo mutant mice. Dis Model Mech *4*, 368–380.

Zhao, C., Guan, W., and Pleasure, S.J. (2006). A transgenic marker mouse line labels Cajal-Retzius cells from the cortical hem and thalamocortical axons. Brain Res *1077*, 48–53.

Zhao, L., Zevallos, S.E., Rizzoti, K., Jeong, Y., Lovell-Badge, R., and Epstein, D.J. (2012). Disruption of SoxB1-dependent Sonic hedgehog expression in the hypothalamus causes septo-optic dysplasia. Dev Cell *22*, 585–596.

Zhao, Q., Behringer, R.R., and de Crombrugghe, B. (1996). Prenatal folic acid treatment suppresses acrania and meroanencephaly in mice mutant for the Cart1 homeobox gene. Nat Genet *13*, 275–283.

Zhao, S., Chen, Q., Hung, F.-C., and Overbeek, P.A. (2002). BMP signaling is required for development of the ciliary body. Development *129*, 4435–4442.

Zhao, Y., Tong, C., and Jiang, J. (2007). Hedgehog regulates smoothened activity by inducing a conformational switch. Nature *450*, 252–258.

Zhu, A.J., and Scott, M.P. (2004). Incredible journey: how do developmental signals travel through tissue? Genes Dev *18*, 2985–2997.

5 APPENDICES

5.1 Acknowledgement

First and foremost, my gratitude goes to Prof. Dr. Thomas Willnow for giving me the opportunity to do my doctoral studies in his research group, for his constant supervision and guidance, and for always keeping me on my toes.

I want to thank Dr. Annabel Christ for delegating one of her previous research projects to me, for her trust, and for her profound support and advice to work-related as well as non-work-related issues.

I would like to thank my second examiner, Prof. Dr. Ursula Koch who kindly supervised and reviewed my doctoral thesis.

Many thanks go to Dr. Annette Hammes-Lewin and Dr. Nora Mecklenburg who introduced me to all the mouse work at the beginning of my PhD and who were always happy to provide helpful assistance and valuable advice.

I am grateful to all the past and present members of the Willnow group for the great and warm atmosphere in the lab that made my work much more enjoyable. Special thanks go to Verona Kuhle our irreplaceable secretary who has simply solved every little problem.

I would like to express my deepest gratitude to Antonino Asaro, Rishabhdev Sinha, Alexis Zi Le Shih, Izabela Kowalczyk and Kevin Manuel Mendez Acevedo who have been awesome colleagues and even much better friends. We have gone through all the ups and downs of (a PhD) life together and they have become my second family in Berlin.

I am indebted to Alexandro Landshammer for his aid and support during all these years, and for the inspiring discussions and all his ingenious suggestions.

I am thankful for my friends and all the people who accompanied me through this formative phase of my life.

Last but not least, I would like to express my heartfelt gratitude to my family for their encouragement, patience and understanding, and that they have always backed me up and believed in me. Without them I would have come nowhere near to where I am now.

5.2 Selbstständigkeitserklärung

Hiermit erkläre ich, dass ich meine Dissertation mit dem Titel

„Functional characterization of the SHH receptorsome using human induced pluripotent stem cell models“

selbstständig und ohne Hilfe Dritter verfasst habe. Die von mir verwendeten Hilfsmittel sowie Literaturangaben habe ich als solche kenntlich gemacht.

Ich versichere, dass ich meine Dissertation nicht schon einmal in einem anderen Promotionsverfahren eingereicht habe. Außerdem habe ich mich nicht anderweitig um einen entsprechenden Doktorgrad beworben.

Die Promotionsordnung des Fachbereichs Biologie, Chemie und Pharmazie der Freien Universität Berlin habe ich gelesen und akzeptiert.

Berlin, Oktober 2021

Maike Marczenke

5.3 Curriculum Vitae

Der Lebenslauf ist in der Online-Version aus Gründen des Datenschutzes nicht enthalten.

Der Lebenslauf ist in der Online-Version aus Gründen des Datenschutzes nicht enthalten.

Der Lebenslauf ist in der Online-Version aus Gründen des Datenschutzes nicht enthalten.